

DTIC FILE COPY

1

# FIRST INTERNATIONAL SYMPOSIUM ON SPECIAL TOPICS IN CHEMICAL PROPULSION : BASE BLEED

ATHENS, GREECE

NOVEMBER 23, 24, 25 1988

SPONSORS

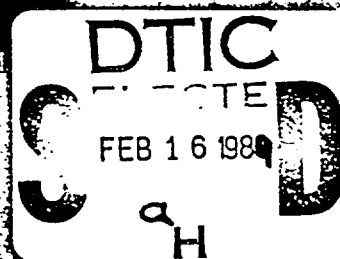


FLEMING  
CONSULTING  
INTERNATIONAL



EUROPEAN  
RESEARCH OFFICE  
OF THE U.S. ARMY

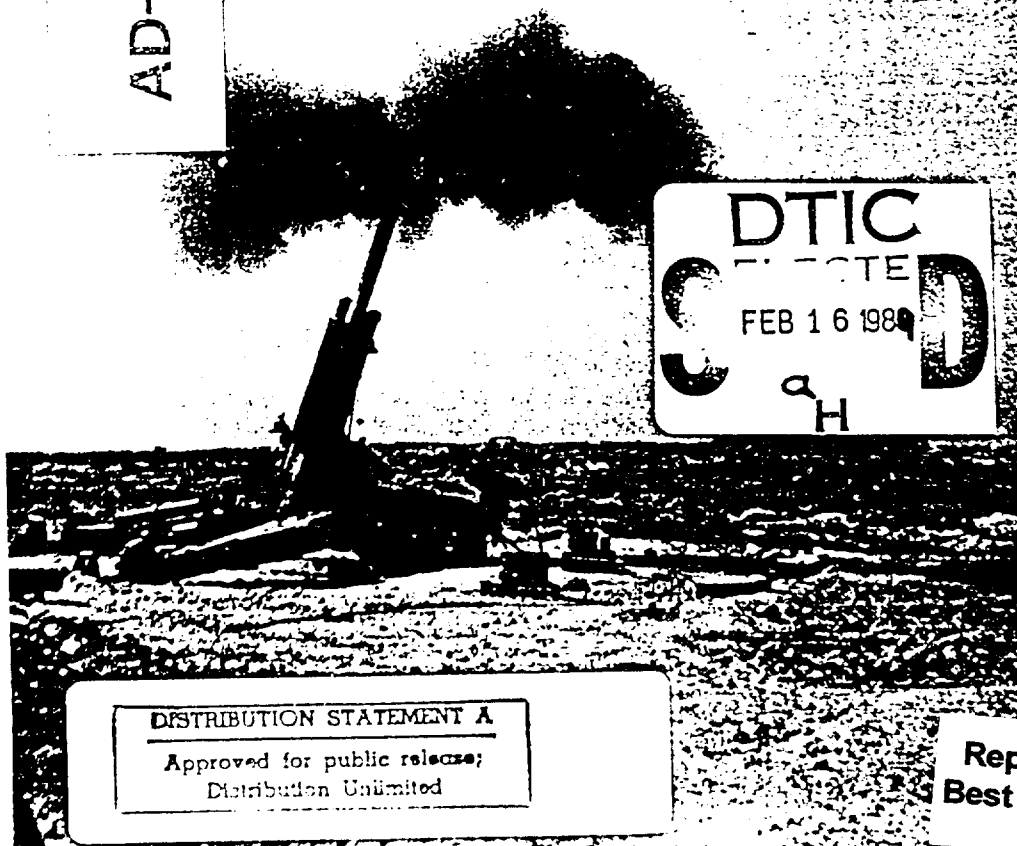
AD-A205 637



DISTRIBUTION STATEMENT A

Approved for public release;  
Distribution Unlimited

Reproduced From  
Best Available Copy



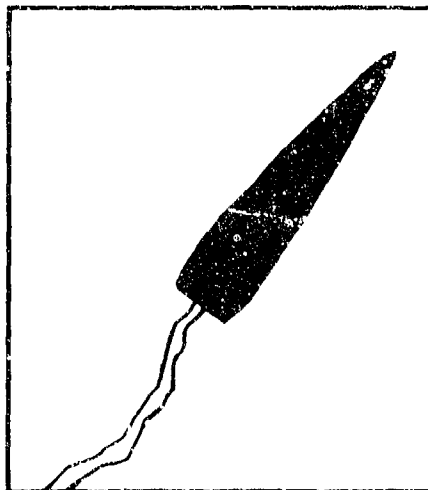
①

PROCEEDINGS  
OF THE  
FIRST INTERNATIONAL SYMPOSIUM ON  
SPECIAL TOPICS IN CHEMICAL PROPULSION :

BASE BLEED

DAJA45-88-M-0128

23 - 25 November 1988, Athens Hilton, Greece.



STEERING COMMITTEE

K. K. Kuo, Penn. State University, Chairman  
B. Zeller, SNPE  
W. C. Strahle, Georgia Technical Institute  
G. V. Bull, SRC  
J. N. Fleming, FCI, Symposium Coordinator

DTIC  
FEB 16 1989  
S H

(Cover photo shows a 155mm Extended Range Base Bleed projectile, being fired from a FGH-155 Howitzer. Photo courtesy of Space Research Corporation).

DTIC  
Approved for Release  
2000

89

2

15

232

## PREFACE

This symposium has been organized to review the state-of-the-art in the development of base bleed projectiles and its related research. It was conceived to fill the gap in the coverage of this new field of major technical and commercial interest. Although other meetings have included a few papers on Base Bleed, it has not previously been possible to devote any depth to this subject. Since base bleed projectiles have recently been seriously considered for production in several countries, and will likely become standard ammunition in the armed forces of many nations in the next decade, the need for such meetings is apparent.

It is intended that a series of symposia on Special Topics in Chemical Propulsion will be held in the future. It is tentatively planned to hold the second meeting in the United States or West Germany, in Spring of 1990, with the provisional subject area being Combustion of Boron and Metal Particles in Solid-Propellant Flames. It is also anticipated that this meeting will be held under the chairmanship of Professor Kenneth K. Kuo, with sponsorship to be provided by interested parties.

Following this meeting we will, with the help of the authors of the various papers, edit these proceedings, which will then be published by, and commercially available from, Hemisphere Publishing Corporation.

We would like to take this opportunity to acknowledge the financial assistance given towards this meeting by the European Research Office of the United States Army (London, U.K.) and by Space Research Corporation (Brussels, Belgium). We would also like to thank Mrs. Ginny Smith for her great help in maintaining excellent records of conference papers, communication between various parties, and in development of the meeting program.

Kenneth K. Kuo  
Symposium Chairman  
Distinguished Alumni Professor of  
Mechanical Engineering  
The Pennsylvania State University

James N. Fleming  
Symposium Coordinator  
F.C.I.



<input checked="checked" type="checkbox"/>	
<input type="checkbox"/>	
<input type="checkbox"/>	
Justification	
By <i>per Form 50</i>	
Distribution/	
Availability Codes	
Dist.	Avail and/or Special
<i>A-1</i>	

## CONTENTS:

### Paper Number

### Title & Author

#### Invited Talk

"Base Bleed Technology in perspective"

G. V. Bull

#### SESSION I:

Chemistry and Ignition / Combustion Behaviour of Base Bleed  
Propellants and Igniter Materials

I - 1

"Base Bleed Solid Propellants,"

M. Lecoustre, J. Gauchoux, and D. Coupez.

I - 2

"Study of the Pyrotechnic Composition Used as the Base Bleed  
Propellant,"

G. Pan, C. Zhu, and Z. Wang.

I - 3

"The Base Bleed Igniter,"

N. Dragoslav.

I - 4

"Ignition and Combustion Behaviour of MTV Igniter Materials  
for Base Bleed Applications,"

B. L. Fetherolf, D. M. Chen, T. S. Snyder, T. A. Litzinger, and K. K.  
Kuo.

I - 5

"Development and Production of Base Bleed Grain for 155 mm  
Guns,"

S. Haugen, A. Oppegard, and K. Melby.



SESSION II: Models and Performance Calculations of Base Bleed Projectiles:

- II - 1 "A Review of the Fluid Dynamic Aspect of the Effect of Base Bleed,"  
J. Sahu, and W. L. Chow.
- II - 2 "Navier - Stokes Computations of Base Bleed Projectiles,"  
C. J. Nietubicz and J. Sahu.
- II - 3 "Computer Codes for Ballistic Performance Calculations of Base Bleed Propellant Grain,"  
Y. Fabignon and D. Coupez.
- II - 4 "A Modification of the Modified Point Mass Trajectory Model for Base Bleed Projectiles,"  
M. M. A. Hasselaar.
- II - 5 "A Model of the Axial Drag Coefficient for Base Bleed Projectiles,"  
N. Bartelsson and S. Linde.
- II - 6 "Effect of Grain Characteristics on Range of Artillery Projectiles with Base Bleed,"  
S. Jaramaz and M. Injac.
- II - 7 "Discussion for Two Important Parameters of a Base Bleeding Projectile,"  
X. Guo.
- II - 8 "A Two - Phase Base Bleed Base Combustion Model and its Calculation,"  
N. -Y. Wang.
- II - 9 "Base - Burn Projectile French Trajectory Model,"  
D. Chargelegue and M. T. Couloumy.
- II - 10 "Trajectory Modeling for Base Bleed Projectiles,"  
G. Laube.

SESSION III: **Experimental and Ballistic Performance of Base Bleed Projectiles and Gas Generators**

- III - 1 "Base Injection and Combustion at Mach 3,"  
W. C. Strahle.
- III - 2 "Structure and Ballistic Properties of the Rheinmetall RH 49 Base Bleed Projectile,"  
L. Borngen and U. Hahn.
- III - 3 "A Study of Drag Reduction by Base Bleed at Subsonic Speeds,"  
Z. S. Ding, Y. F. Liu, and S. S. Chen.
- III - 4 "Testing of Parts and Complete Units of the Swedish Base Bleed System,"  
N. E. Gunners, K. Andersson, and Y. Nilsson.
- III - 5 "Analysis of the Dispersion of the Base Bleed Projectile,"  
X Guo.
- III - 6 "Solution to Base Bleed Projectile Hardware Manufacturing Challenges,"  
L. L. Crowson.
- III - 7 *Handwritten: Solid* Solid Fuel Ramjet Self - Propelled Gun Launched Projectiles, *Handwritten: Keywords:*  
A. Gany.

*Handwritten:*  
Solid Propellants, Gun  
Propellants, Thermochemical  
Thrusting, Rocket assisted  
Projectiles (AR)

## BASE BLEED TECHNOLOGY IN PERSPECTIVE

Dr. G.V. Bull  
Group President, SRC

### INTRODUCTION

In scientific matters, as true in any general relating of human affairs, the versions of historical events often differ radically dependent on the historian. Often there exists a valid basis for the differences; unfortunately, and more frequently, there does not. The twisting of truth to perpetuate unfounded propaganda justifying past actions, or to inflate national or personal roles played, is the common stuff of history. The mixed blessing of alledged journalism, constituting the public media and often used as source references, generally relates more propaganda than reality. A short reference period in any archives reveals to the reader yesterday's "newspapers" filled with yesterday's lies. Probably more wars and chaos have been created by media propaganda than any other single source.

The above may seem somewhat irrelevant to the technical subject of this meeting. However I believe it appropriate in view of the rapid developments that have taken place in the application of the technique of Base Bleed to artillery in the last decade. These accomplishments in the practical application field tend, for a variety of reasons, to overshadow the lengthy historical base on which the technology rests. Since the papers in this conference are dedicated to the status of the applied development, it was felt appropriate to include at the outset a brief review of the history of the relative aerodynamic and aero-mechanical background with, of course, a look at the presently unresolved, complex problems.

### FLOW ABOUT BODIES OF REVOLUTION

#### The General Flow Field

By simple application of the conservation of momentum principle, Sir Isaac Newton deduced the general relation that a flat plate inclined at an angle to the airstream would have forces acting on it parallel and perpendicular to the flow velocity vector of the general form :

$$\text{Force} = \text{Constant} \cdot \frac{1}{2} \rho V^2$$

where  $\rho$  is the air density and  $V$  is the freestream velocity. (The constant for the vertical component being proportional to the sine of the angle of inclination to the flow stream).

This deduction failed to take into account the potential nature of flow fields wherein the disturbance to the flow by the body is propagated throughout the surrounding flow fields. For the case of irrotational, inviscid flow, the potential field defines streamlines which must satisfy the Laplace equation :

$$\nabla^2 \phi = 0$$

with the flow being affected significantly at large distances from the body. Early attempts by mathematicians to determine the effect on bodies immersed in irrotational flow fields resulted in D'Alembert's paradox (1744) that no net forces could be developed. The introduction of the concept of circulation (Helmholtz) implying vorticity and rotational flow led to the solution of the inviscid, incompressible flow equations yielding the relations :

$$L = \rho K V, D = 0$$

where  $L$  is the lift force,  $D$  is the drag force and  $K$  is the circulation.

The resolution of this paradox was accomplished by Prandtl (1904) by the introduction of the boundary layer, which essentially divided the flow about a body into two regimes. A thin layer adjacent to the body surface had to satisfy the no-slip condition, so that the fluid velocity went from a zero value on the wall surface to full free stream value a short distance away from the surface. This viscous flow layer, the boundary layer, had to satisfy the general Navier-Stokes equations. Outside this layer the field would behave as irrotational, inviscid flow.

As the flow progresses along a body, the boundary layer increases in thickness; against an increasing pressure gradient, the boundary layer flow momentum can fall below the value required to sustain the flow. Reversed flow inside the boundary layer can occur, with eventual separation of the boundary layer from the surface, such as the case of a wing profile at high angle of attack.

While the general aerodynamic problem is not directly relevant, at least in passing we should observe that the aircraft aerodynamicist expended enormous effort in overcoming boundary layer separation. This work included injecting energy into the boundary layer, boundary layer suction, etc. In this case, he was primarily interested in high lift-to-drag ratios and preventing the onset of stalling.

In relation to bodies of revolution, the axisymmetric flow can be divided into five distinct, but connected flow

regimes if consideration is restricted to bodies at essentially zero angle of attack. These are illustrated in Figure 1(a) in the case of supersonic flight and may be noted as :

1. The inviscid flow field outside of the boundary layer.
2. The viscous boundary layer flow to the rear edge.
3. The "dead zone" or cavity region terminated by a rear stagnation point.
4. The separated boundary layer merging behind the rear stagnation point into a neck, with the turbulent wake flow after the neck carrying the fluid downstream and expanding, causing a recompression shock to form in the outer inviscid flow region.
5. The far wake region.

The flow illustrated in Figure 1(a) becomes considerably more complex when examined in detail, and of virtually unlimited complexity for the case of interest here, namely a yawing body with surface protrusions and a high spin rate.

The bow shock is curved through interaction with the expansion field about the ogival shape. The boundary layer grows as the flow proceeds over the body, its thickness and nature a function of the Reynolds number and Mach number. The Reynolds number dominates the boundary layer characteristics, and is the ratio of the fluid momentum to viscous forces given by the dimensionless relation :

$$\frac{vl}{\nu} \quad \text{or} \quad \frac{\rho vl}{\mu}$$

where  $v$  is the local velocity,  $l$  the characteristic flow length and  $\nu$  is the kinematic viscosity, the viscosity,  $\mu$ , divided by the density,  $\rho$ . Surface roughness, temperature,

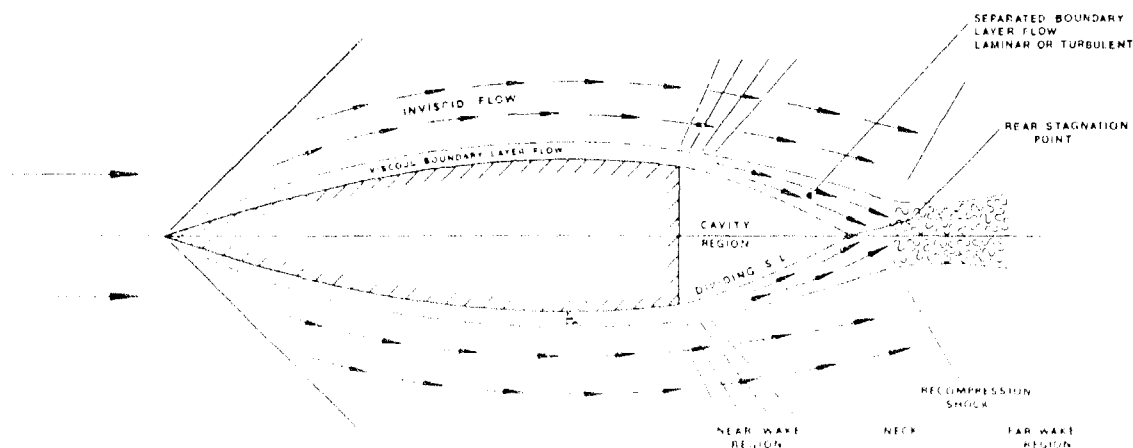


FIGURE 1(a). Simplified illustration of flow about an axisymmetric body at zero angle of attack.

protuberances (driving bands, nubs etc) add to determining the boundary layer and general flow nature.

### The Wake Flow

At very high Reynolds numbers, the boundary layer will be extremely thin; at low Reynolds numbers, it will be of appreciable thickness at the base of normal axisymmetric shapes of interest. A generally accepted, overall model of the wake flow is shown in Figure 1(b) for the case of no yaw. Restricting our interest to the supersonic Mach number regime, we should note that boundary layer flow will consist of numerous internal layers which as traversed will pass from supersonic adjacent to the free stream, through the transonic regime to subsonic flow in the region adjacent to the surface. As separation takes place the inner subsonic layer will turn generating a Prandtl-Meyer type expansion throughout the supersonic portion of the flow field. Within the supersonic portion of the boundary layer, a lip shock may form due to boundary layer expansion and be propagated into the inviscid flow field.

The expanding boundary layer will be bounded by a separation streamline delineating the viscous region from the main inviscid flow on its outer surface and by what has been termed the Dividing Streamline (DSL) on its inner surface. The Dividing Streamline separates the inner cavity flow region from the viscous boundary layer, and terminates in the rear stagnation point which closes off the near wake cavity region adjacent to the base. Within the cavity region low pressure, low velocity circulatory flow is postulated.

Beyond the aft stagnation point a neck occurs in the boundary layer flow, with subsequent expansion into the far wake region. This causes the formation of the wake shock as shown.

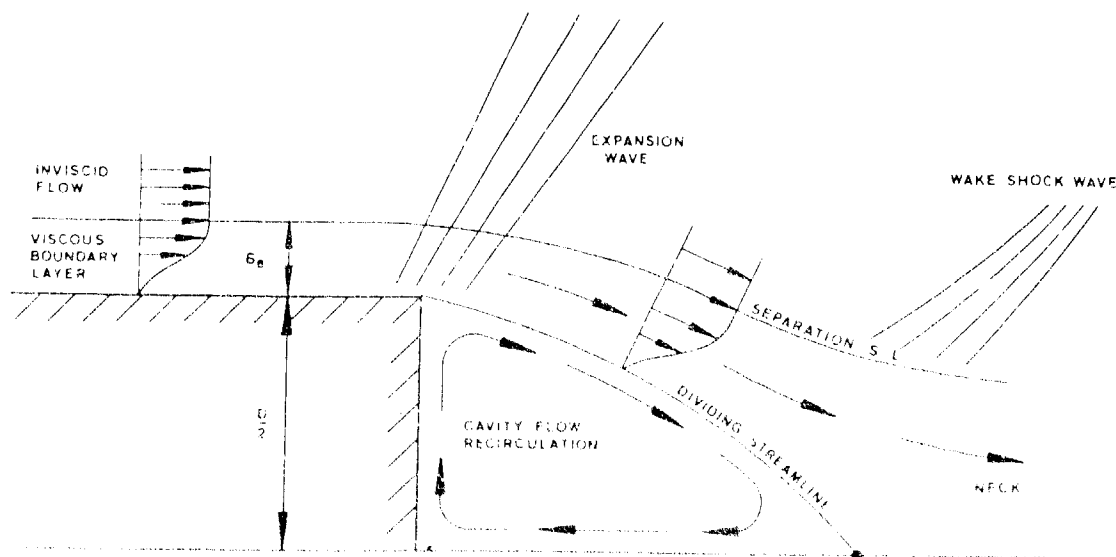


FIGURE 1(b). Details of postulated supersonic base flow.

The flow illustrated is in as simple a form as possible. In the more general case the boundary layer at the base prior to or even after separation, may be all turbulent, or a mixture of turbulent and laminar layers. After separation, the boundary layer may have viscous mixing regions, entraining gas both from the cavity zone and the inviscid flow zone.

Thus the detailed calculation of the base flow even for the case of zero yaw and spin, is beyond any generalized treatment. Clearly there will exist a significant scale effect, where  $\delta_B/D$ , the ratio of base boundary layer thickness to body base diameter, is important.

#### DRAG OF AXISYMMETRIC BODIES

The total drag of a non-yawing axisymmetric body such as considered in Figure 1(a), is generally considered as consisting of three main components :

1. Profile (form or wave) drag
2. Skin friction drag
3. Base drag

The objective of the designer is to minimize each of these components to obtain maximum range for a given shell muzzle velocity.

The exact theoretical determination of all drag components for long range shell firings is well beyond our present ability. As will be discussed in more detail, the real trajectory conditions involve a spinning-yawing shell traversing rapidly a large Reynolds number range and a significant Mach number range. Semi-empirical codes have been developed which of course are force-fitted to experimental long range trajectory observations.

The aerodynamic problem embraces the most complex fields of fluid mechanics. Compressible inviscid flow solutions are rather well understood until we get into the region of "rarefied aerodynamics" or free molecular flow. For the boundary layer we can start with the classical text book of Schlichting (1), and note the incomplete but lengthy Bibliography of Reference (2), a reference to be discussed in more detail subsequently. The general fluid mechanic treatises of wakes may be considered as starting with the subsonic case studied by von Karman and leading to the now classical von Karman vortex street. But the general solution to the wake problem still presents a major hurdle in fluid mechanic analyses.

#### MINIMIZING AERODYNAMIC DRAG

##### Profile Drag

Starting as early as 1874, ballisticians began studying

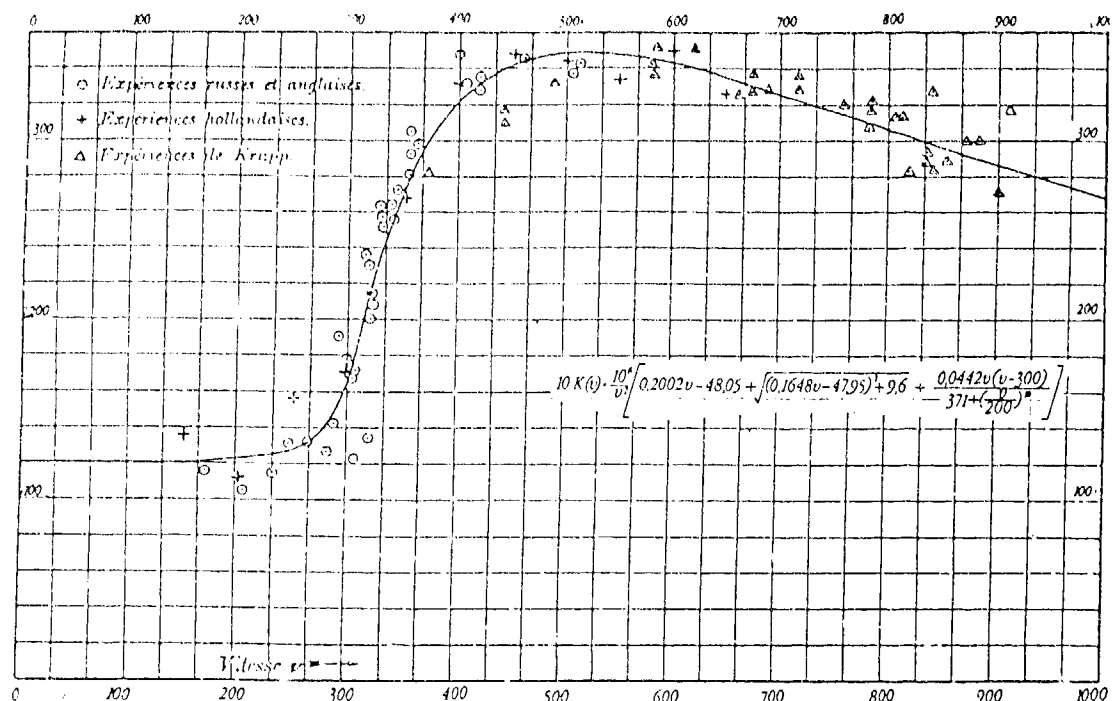


FIGURE 2. Experimentally determined drag-velocity variation. (From Reference (3)).

spark photographic techniques to measure the drag of small calibre bullets. By 1912 extensive data on the drag of various shape bullets existed as shown in Figure 2. In spite of this, the general major calibre artillery shell employed a rather blunt nose profile (approximately a 3:1 circular ogive) until October 1914 when Rausenberger and Ebernard of Krupp tried a 10:1 circular ogive nose cap on the 35 centimeter naval shell. This resulted in a range increase of approximately 50%, enabling the 38 cm Lange Max gun to reach Dover from Cap Gris Nez (37 km).

Both theoretical studies and supersonic wind tunnel tests were conducted during World War 2 by the Germans (4) to determine minimum drag profiles. In general these are obtained by using an all ogival body. In practice this leads to problems. A front bourrelet must be provided either by canted nubs or by a discarding front sabot (bore rider). An interesting aside is that the World War 2 German artillery effort had started investigating nubs; an example may be seen in the museum at Picatinny Arsenal. The second problem is that of gyroscopic stability. The ogive cannot be completed at the aft end of the body without encountering stability problems that cannot be resolved in terms of permissible normal shell design parameters.

#### Skin Friction Drag

The skin friction drag is a function of the wetted area and any particular rough areas, such as in the vicinity of the



driving band. In general, the designer has little control over this component of the total drag.

### The Base Drag

This component represents an appreciable portion of the total drag of any shell configuration. The blunt rear end configuration shown in Figure 1 represents (normally) the worst case, or the case of maximum base drag. By boat-tailing the base drag can be reduced appreciably. However base drag remains an appreciable percentage of the total as shown by the drag coefficient break down for the nubbed, low drag profile boat-tailed round shown in Figure 3.

### Reducing the Base Drag

Theoretical concepts for the reduction of base drag date back prior to World War 2. However serious interest may be considered to have started shortly after the war. The groups that sparked interest in shell base drag reduction were of course those working in ballistics. It was well known among external ballisticians that the velocity retardation of small calibre shells carrying tracers was less than the same shell without a tracer. It would be futile to enter into a debate as to whether German, French, Russian, English or American ballisticians were the first to observe this. As Figure 2 clearly illustrates, European small arms ballisticians were measuring shell retardation with differing shapes by the beginning of the present century.

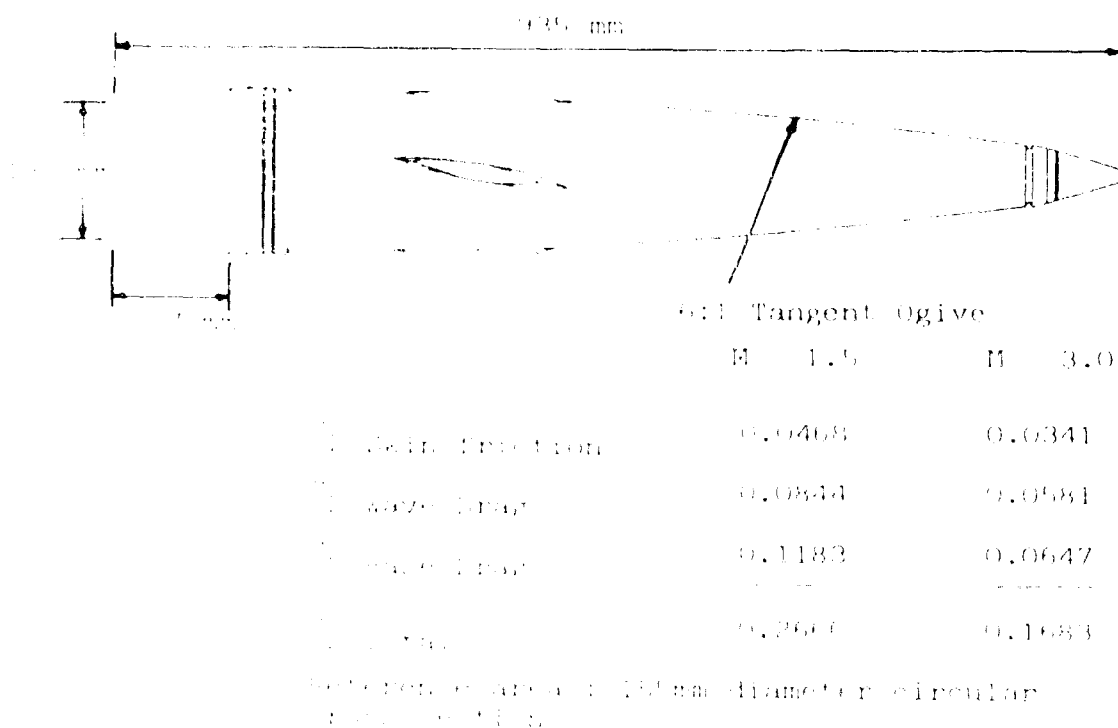


FIGURE 1. 155mm ERFB MK10 MOD2 drag coefficient components.

After World War 2 the general interest in Western countries in major calibre ordnance declined in favour of other systems. The decision of the Westerveld Board of 1932 became established dogma. This cast field artillery into the role of a close support weapon, resulting in no serious requirement for long range firings. However the advent in the field of long range Soviet artillery such as the 130mm system (27.5 km) and the 152 system, created a NATO requirement of 30 km for the 155 system. With limitations placed on barrel length (39 calibres), this range could be obtained only by absolute minimization of shell drag or by rocket boosting after muzzle exit (RAP).

With the relative abundance of supersonic/hypersonic wind tunnels that appeared in North America in the early post-war years as a direct result of the wartime German developments, compressible aerodynamics experienced an enormous increase in scientific interest, both theoretically and experimentally. Inviscid, steady state compressible fluid flow mechanics was relatively well advanced and understood by 1950. Theoreticians then concentrated on the extremely complex areas of the compressible flow boundary layer and wake flows.

Theoretical concepts for the reduction of base drag date back well prior to World War 2. However serious technical effort on this problem may be considered to have started shortly after the war. Estimates of base drag from fitting observed firing range data were formulized as early as 1931 by Gabeaud (5) in the form :

$$C_{D_b} = 0.25 \text{ for supersonic flow}$$

while von Karman and Moore derived (1932, Reference (6)) a value:

$$C_{D_{b \max}} = 2 / \gamma M^2$$

while Hoerner (7) showed that a good correlation with firing results in the supersonic range was given by

$$C_{D_b} = 0.7 / M^2$$

These are effective total contributions of the base pressure distribution to the drag for blunt based bodies.  $C_{D_b}$  is the base drag coefficient based on base area, and M is the freestream Mach number.

Before considering the complex problem of examining base and wake flows in order to look at the general problems of base drag reduction, it is necessary to review the general aero mechanical aspects of shell flight.

## THE TRAJECTORY CHARACTERISTICS OF LONG RANGE SHELLS

### General

A typical major calibre artillery shell leaves the muzzle of the gun with some angular (yaw) acceleration. This acceleration comes from mass and geometrical misalignments of the shell during bore travel and grows in magnitude with tube wear. The muzzle disturbance results in the excitation of two free-flight oscillatory modes, with the disturbance equally divided between them. The relatively low frequency precessional mode is damped out normally after several cycles, with the maximum yaw usually occurring within 50 to 100 meters of the muzzle. The high frequency nutational mode is damped out much earlier than the precessional mode, and is normally negligible at the point of first maximum yaw.

For well designed systems the maximum induced muzzle yaw generally is less than 3 degrees in the new barrel case. However as tubes enter the third and fourth quarter of their life, this initial yaw can be large. The effect of the initial yaw on range increases with the range of the shell, and for the very long range case, introduces a considerable correction factor. Clearly the reduction in range must then consider the shell at an angle of attack, with large Reynolds number and maximum Mach number values.

The shell proceeds through its flight trajectory with aerodynamic forces producing moments which result, through gyroscopic action, in a shell displacement angle in the plane at  $90^\circ$  to that of the applied aerodynamic moment. This displacement results in a gyroscopic moment causing the shell to maintain alignment with the flight velocity vector.

However as the shell traverses the large range of Reynolds and Mach number as it approaches apogee, permanent angles of yaw (in the side plane) can be present. In effect the density decreases to a value where gyroscopic moments dominate. On re-entry, the shell recovers through damped precessional mode oscillations as it traverses the increasing density atmosphere.

As interest increases in shells with increasing ranges, (ranges of up to 60 km are currently becoming of interest), the flight modes along the trajectory must be considered and it is obvious that effect of angle of attack on drag cannot be ignored. This of course, vastly increases the complexity of the aerodynamic analytical problem.

To illustrate the above comments two cases of long range shell trajectories will be presented.

### The Paris Gun Shell Trajectory

This 210mm 106 kg spin stabilized shell was developed in 1917, and fired against Paris from Crépy-en Laon starting on



FIGURE 4. Paris Gun 210mm Shell.

March 23, 1918. During these firings it attained an altitude of 43 km and a maximum range of 127 km.

A recovered shell, with the nose cap replaced, is shown in Figure 4. A typical trajectory (taken from Reference (8)) is shown in Figure 5. It will be noted that the shell starts to develop significant permanent yaw (in the side plane) above 20 km, reaching an angle of repose of approximately 40' during traverse over apogee. The angular recovery mode is shown in the plot labelled (b) in Figure 5.

#### The 45 calibre ERFB MK10 MOD2 Trajectories

With a muzzle velocity of 897 meters per second and no base bleed, this shell attains a range of 30 km. A typical trajectory plot for this case is shown in Figure 6(a), where it may be noted that the maximum yaw angle achieved is approximately 2 degrees. When the range is extended to 39

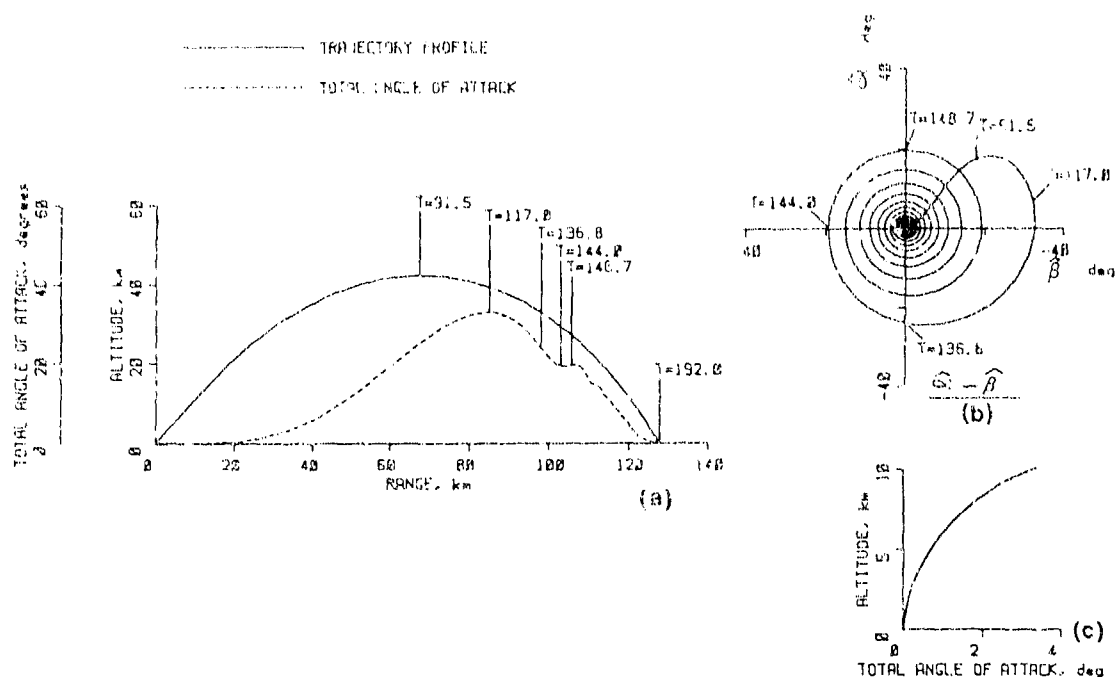


FIGURE 5. Paris Gun shell computed trajectory. Muzzle velocity = 1646 m/s, quadrant elevation = 50°.

km using base bleed the corresponding plot is shown in Figure 6(b).

The previous discussion illustrates the necessity of considering the entire trajectory when considering drag optimization for range. Among the complexities added to the simple consideration of axisymmetric body drag at zero degrees and a fixed Reynolds number - Mach number combination, must be added the drag component due to yaw and the optimization over the range of Reynolds number and Mach number while aerodynamic effects are still significant. The range of Reynolds number,  $P_r$ , and Mach number,  $M$ , experienced by the two projectiles can be seen in Figures 6(a) and 6(b).

#### REDUCTION OF BASE DRAG : BASE BLEED

Reference (9), dedicated to establishing the state of knowledge on wake flows and base drag reduction, published in 1976, must be studied as a base line work on this topic. It covers at least all the major work up to that time, including injection through the boundary layer ahead of the base, the effect on base drag of plates mounted downstream from the base on stings attached to the base, cold gas injection into the wake through the base, and base injection with combustion in the wake.

At the time this study was being compiled, no practical system had been devised (excluding tracers on small

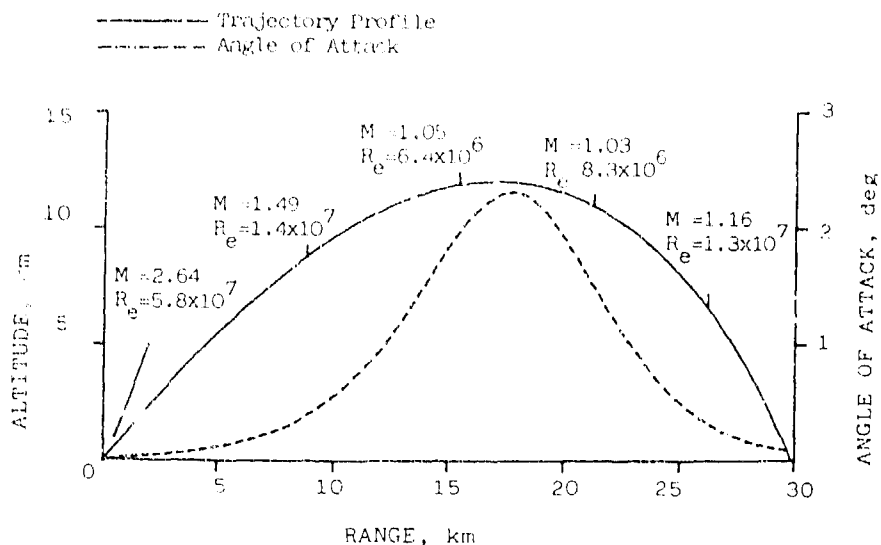


FIGURE 6(a). 155mm ERFB MK10 MOD2 maximum range trajectory

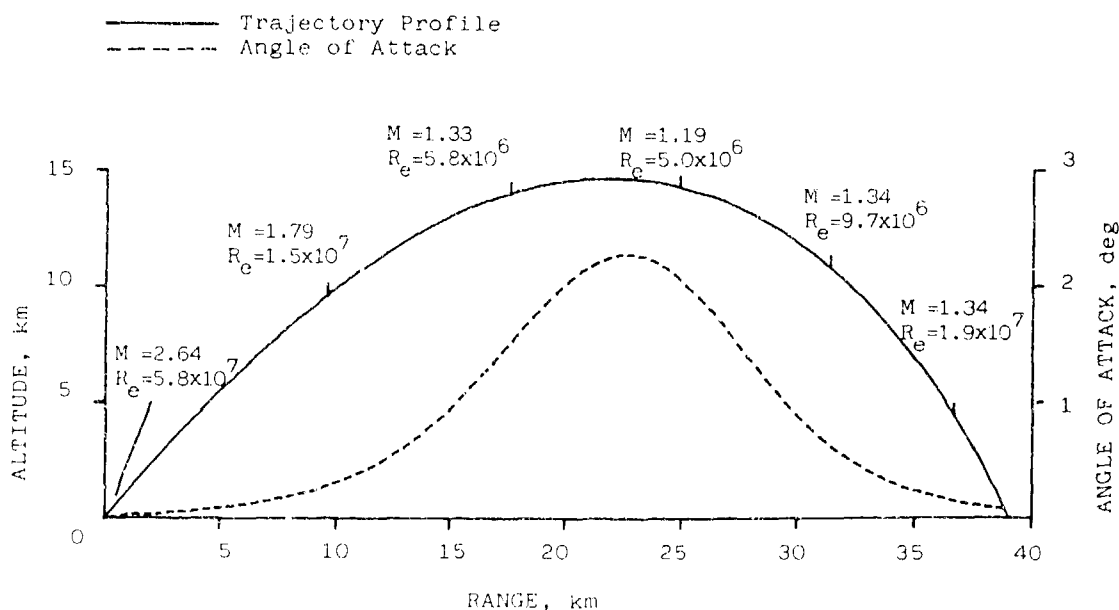


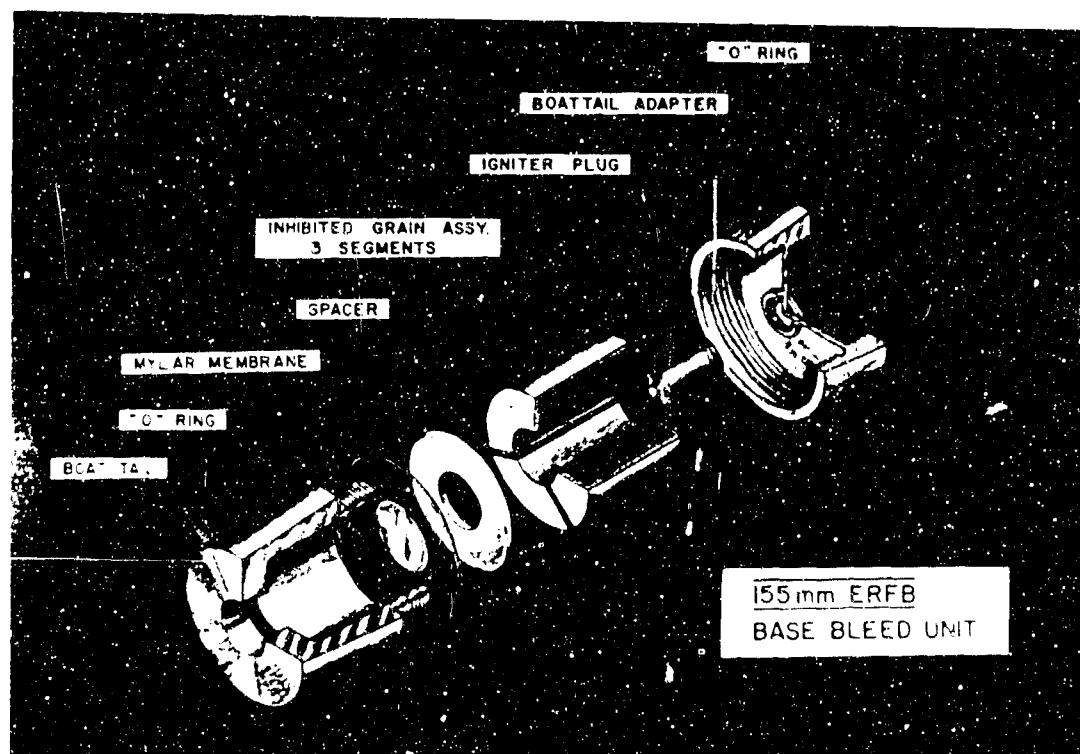
FIGURE 6(b). 155mm ERFB/BB maximum range trajectory.

calibres) to apply this to major calibre artillery shells. The first successful system in fact, was then in the test and development stage in Sweden. It was brought to North America with the major firing series in Antigua conducted in 1978 (10). The grains used were carboxyl terminated polybutadiene/ammonium perchlorate manufactured in Sweden to fit the SRC ERFB MK10 MOD2 projectile. Swedish engineers supervised the tests, which yielded the almost 30% increase in range predicted. Because of its assigned carcinogenic nature, the Swedes switched to hydroxyl terminated polybutadiene/ammonium perchlorate grains which for all

practical purposes are identical in performance.

The method used in mounting these grains in the base of the ERFB MK10 MOD2 projectile is illustrated in Figure 7. This simply involved replacing the boattail by a conical section with a closed end cap and a central orifice of sufficiently large diameter to ensure subsonic flow into the cavity wake. The inside geometry was such as to accept the cylindrical shaped, sectioned grain, inhibited on all surfaces other than the central annulus and the section cut surfaces. A diaphragm seals the grain; as the pressure builds up to the shot-start value, the diaphragm is ruptured and the hot gun gas flows through the orifice and about the grain. Some indications exist that the grains are floating in the hot gas, and do not build up to the full spin rate of the projectile. The in-bore and muzzle exit conditions are of a complexity that while some effects can be observed, detailed analysis is beyond the present state of the art. The grain and igniter begin burning probably at or near the seating position, and then experience the full in-bore gas pressure during shot travel down the bore. At exit, the sudden pressure drop causes quenching of the grain burning, but only sporadically. The igniter ensures continued grain burning after muzzle exit.

Returning to the flow models of the wake, the optimum condition would be when the momentum flux is such as to restore the base pressure to the full freestream value. The temperatures of the products of complete combustion lie in the



range of 1000 to 2000°C, dependent on composition. Photographic evidence shows the presence of combustion in the wake during at least the early, and most critical part of the trajectory. Thus in practice, a satisfactory theoretical model must include combustion-heat transfer across the dividing streamline, through the separated boundary layer flow and into the main stream.

Various models can be postulated, and solutions to the wake flow presented under severely restrictive assumptions, at this time not adequate to describe the real case. In Figure 8 we look at various idealized conditions. In Figure 8(a) the base bleed mass flow is shown for the less than optimum case; in (b) the optimum case is sketched from the simplified assumption that the momentum flux into the cavity wake restores the pressure at the dividing streamline to freestream value, so that the mixing processes cause the boundary layer to be simply a thin dividing shear layer between the mainstream flow and the lower velocity wake flow. Heat transfer across the shear layer to the mainstream flow will add considerable complexity to the analytical model. Typical smear photographs illustrating a wide range of base bleed wake flow conditions are shown in Figures 9, 10 and 11.

#### TRAJECTORY OPTIMIZATION

In any long range trajectory, the projectile is traversing rapidly a large Reynolds number range during its ascent.

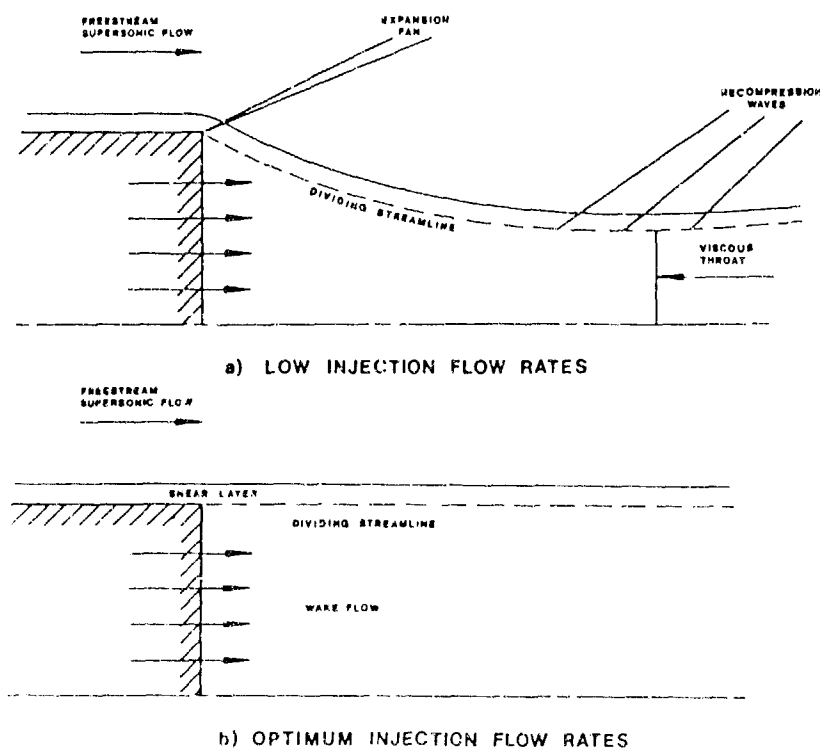


FIGURE 8. Schematic of base flow with base bleed.





FIGURE 9. Smear photograph of base bleed projectile showing less than optimum base bleed mass flow.

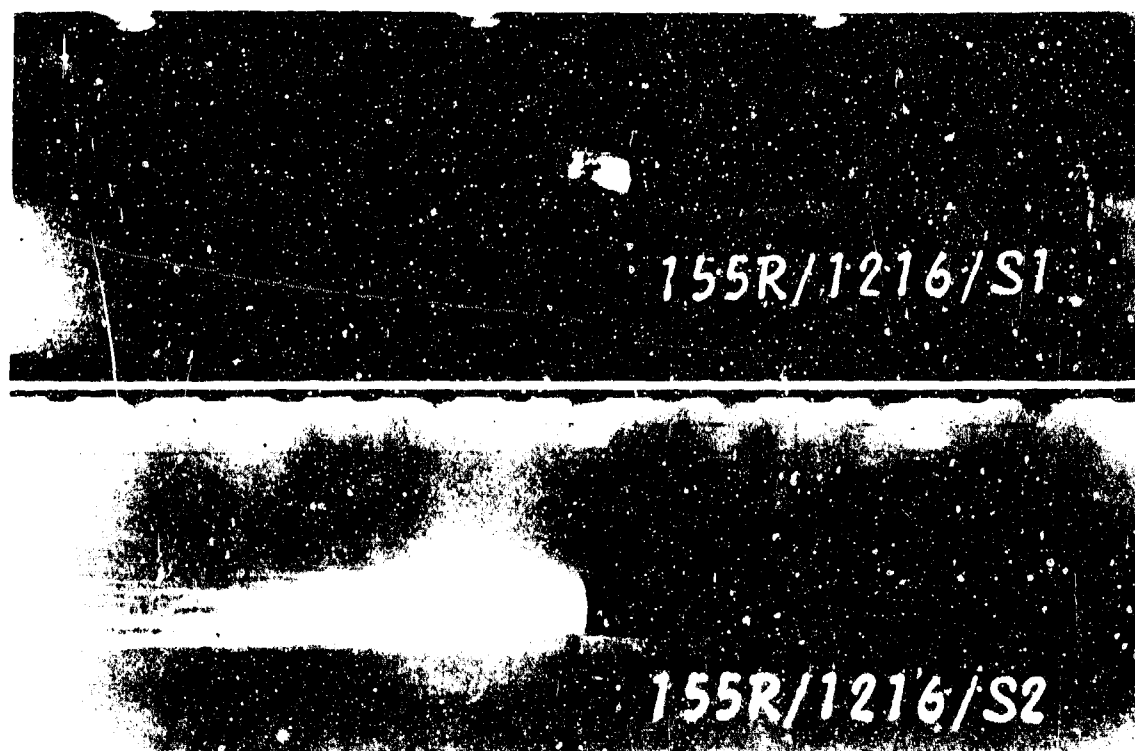


FIGURE 10. Smear photograph of base bleed projectile showing optimum base bleed mass flow.



FIGURE 11. Smear photograph showing greater than optimum, supersonic type, base bleed mass flow.

Assuming that the optimum conditions could be achieved, this would imply a continuously varying mass-momentum flux from the base to the wake. Furthermore it would imply a detailed knowledge of base bleed - wake flow characteristics. To date the optimization is a trial and error proposition based on fixed grain properties and any variation in combustion rate caused by the change in the surrounding ambient air.

During the last decade, the base bleed concept has been applied to a wide range of projectiles in many different countries. One might say that the state of the applied field has advanced far ahead of the derivation of satisfactory fluid dynamic models. Contrary to the conclusions of Reference (11), range increases in the order of 30% have been achieved, well exceeding the 10% estimate (matching RAP) he concludes as a limit on base bleed systems.

#### Firing Results

Hoping not to appear parochial, but because of the simple reason that this is the only projectile for which the author has access to data, the performance of the base bleed version of the ERFB MK10 MOD2 projectile will be presented in concluding this presentation, and as typical of all systems. At the outset, it should be noted that the base bleed system only reduces projectile drag, and does not apply thrust. Thus dispersion is not affected, other than malfunctions causing the base bleed drag reduction to vary. This results in increased range dispersion, but no variation in deflection dispersion. For fully developed systems, the reproducibility of drag reduction by base bleed is such that no increase is observed in range dispersion, the values for

TABLE 1. Results of Typical Firing Series.

	Muzzle Velocity, m/s	Range, m	Probable error	
			Range	Deflection
ERFB	897.6	30577	.376%	.97 mils
ERFB/BB	899.9	39153	.324%	1.03 mils

probable error in range using the data reduction techniques of Reference (12) lying between 0.3 and 0.45. Table 1 shows typical firing results of the ERFB MK10 MOD2 projectile, and of the base bleed version.

#### CONCLUDING DISCUSSION

In no way can this paper claim to be more than a superficial scanning over the difficult subject of wake flows and trajectory analyses. However, hopefully, the papers to follow covering the current work in the many practical aspects of manufacture, supported by advances in theory, will at least allow it to qualify as an acceptable introduction to these more qualified, specific treatments.

#### REFERENCES

1. Schlichting, R., *Boundary Layer Theory*, 4th ed., McGraw-Hill, New York, 1960.
2. Murthy, S.N.B., and Osborn, J.R., Base Flow Phenomena with and without Injection, in *Aerodynamics of Base Combustion*, Ed. S.N.B. Murthy, pp. 7-210, AIAA, New York, 1976.
3. Becker, K., and Cranz, C., Messungen über den Luftwiderstand für grosse Geschwindigkeiten, *Artilleristische Monatshefte*, Nr. 69, September 1912.
4. Ferri, A., Supersonic Tunnel Tests of Projectiles in Germany and Italy, NACA Wartime Report L5H08, October 1945.
5. Gabeaud, A., Sur la Resistance de l'Air aux Vitesses Balistique, *Comptes-Rendus de l'Académie des Sciences*, No. 192, p. 1630, 1931.
6. von Karman, Th., and Moore, N.B., Resistance of Slender Bodies Moving with Supersonic Velocities, with Special Reference to Projectiles, *American Society of Mechanical Engineers Transactions*, Vol. 54, p. 303, 1932.

7. Hoerner, S.F., *Fluid Dynamic Drag*, 2nd ed., published by the author, New Jersey, 1965.
8. Bull, G.V., and Murphy, C.H., *Paris Kanonen - The Paris Guns (Wilhelmsgeschütze) and Project HARP*, Mittler, Herford, 1983.
9. *Aerodynamics of Base Combustion*, Ed. S.N.B. Murthy, AIAA, New York, 1976.
10. Anon, Data Analysis Report, 155mm ERFB MK10 MOD2 and ERFB Base Bleed Tests. Antigua Test Range, March 5-7, 1978, SRC-R-103, March 1978.
11. Hudgins, H.E., Range Increase of Projectiles by Heat and/or Mass Addition to Base or External Flow, in *Aerodynamics of Base Combustion*, Ed. S.N.B. Murthy, pp. 495-521, AIAA, New York, 1976.
12. NATO STANAG N° 4106, Procedure for the Determination of External Ballistic Performance of Shell.

# STUDY OF THE PYROTECHNIC COMPOSITION USED AS THE BASE BLEED PROPELLANT

Pan Gongpei, Zhu Changjiang and Wang Zhaoqun  
Department of Chemical Engineering, East China Institute  
of Technology, Nanjing, China

## INTRODUCTION

The recent base bleed propellants used in base bleed projectiles are usually the composite propellants of which essential components are hydroxy terminal polybutadiene (HTPB) and ammonium perchlorate (AP). However, our research completely bases upon the pyrotechnic field and aims at selecting the optimum formulation of pyrotechnic composition as a base bleed propellant. It would make the shooting range-increasing effect for base bleed projectiles to raise and have good igniting property, simple process of manufacture and low cost.

A series of tests were carried out which include the wind tunnel test, the dynamic analogue test and the live ammunition flight test for the compositions with  $\text{Sr}(\text{NO}_3)_2$ -Mg-CaRes\*-additive or  $\text{Sr}(\text{NO}_3)_2$ -Mg-AP-additive. And satisfying results of the tests have been obtained.

## EXPERIMENT METHODS AND CONDITIONS

### 1. Samples

In the live ammunition flight survey test, the samples are processed according to the bullet structure. The sample used in laboratory is shown in Figure 1.

\* CaRes--Calcium resin

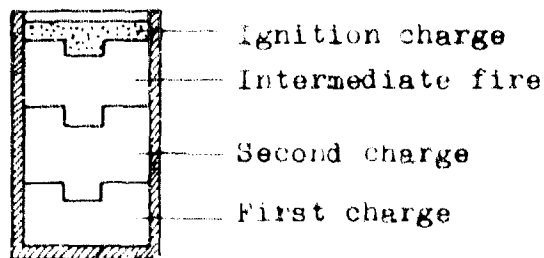


Figure 1. Sample used in laboratory

## 2. Measurement of Temperature

The temperature sensor is a W-Re thermocouple. Figure 2 shows the schematic drawing of measuring the combustion temperature of the sample.

## 3. Amount of the Ejected Gas

Its measuring device is shown in Figure 3.

## 4. Dynamic Analogue Test

In this test, the 14.5mm machine gun is used to shoot live ammunition. The flight velocity of the bullets is measured by means of a velocity radar. And we evaluate the effect of drag reduction on the attenuation of the velocity.

## 5. Live Ammunition Flight Survey Test

Under the same conditions, the effect of drag reduction or the shooting range-increasing effect is to be determined through the comparative flight test in which the bullets load with the base bleed agent and without it.

## THE RESULTS OF THE TESTS

### 1. Selection of the Formulations

Test result for  $\text{Sr}(\text{NO}_3)_2$ -Mg-Ca-Res formulation. Under the static conditions, the test result for this type of formulation in terms of combustion temperature and velocity is shown in Table 1.

It can be seen from Table 1 that the formulation with  $k=0.47$  has relatively high temperature. The observed value of the gas produced according

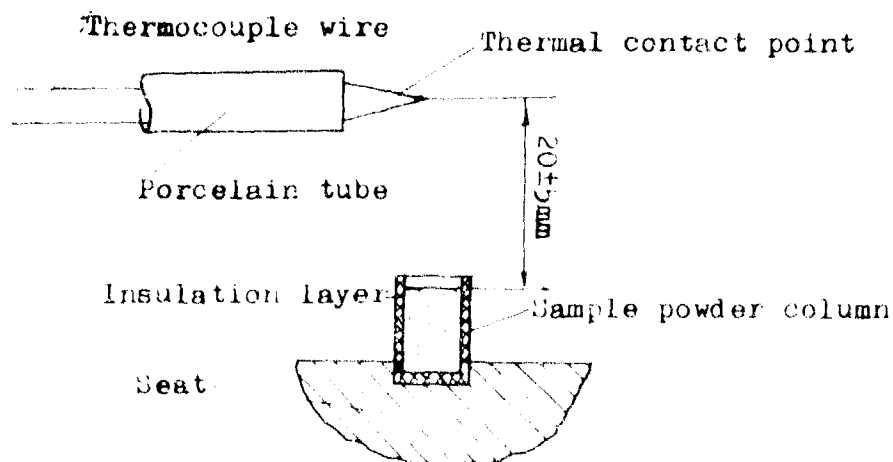


Figure 2. Schematic drawing of measuring the combustion temperature

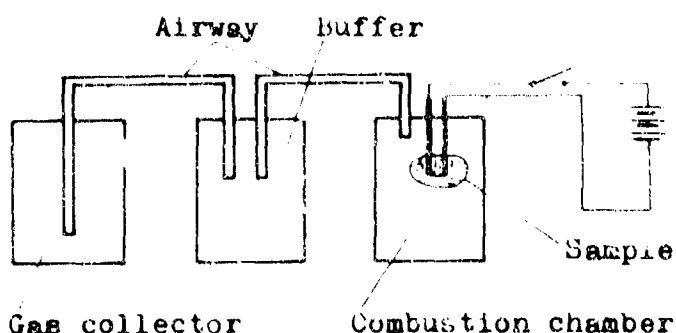


Figure 3. Device of measuring amount of the ejected gas

to this formulation is 348.8ml/g. The average molecular weight is 33.15.

The wind tunnel test showed that the formulation with  $k=0.47$  has poor performance of combustion at the low pressure as well as poor effect on the reduction of drag (see Table 2).

Adjustment test for the formulation of  $\text{Sr}(\text{NO}_3)_2\text{-Mg-CaRes}$  type. The adjustment tests for the formulation were carried out with the addition of AP and the removal of DOP(dioctylephthalate) so as to keep the fluctuation of the oxygen balance within a small range ( $k=0.40\text{-}0.48$ ). The

Table 1. Formulation Test for  $\text{Sr}(\text{NO}_3)_2\text{-Mg-CaRes}$

No.	Formulation				Oxygen diff. n	Guaranteed coeff. K	Combustion temp. $T(^{\circ}\text{C})$	Combustion velocity $\bar{u}(\text{mm/s})$
	$\text{Sr}(\text{NO}_3)_2$	Mg	CaRes	DOP				
1	69	20	10	1	-15.0	0.63	1905	2.77
2	64	25	10	1	-20.2	0.54	1942	2.80
3	61.5	27.5	10	1	-22.6	0.50	2058	2.96
4	59	30	10	1	-25.4	0.47	2100	3.28
5	54	35	10	1	-30.5	0.40	1942	3.26
6	49	40	10	1	-35.7	0.34	1835	2.59

Table 2. Result of the wind Tunnel Test for  $\text{Sr}(\text{NO}_3)_2\text{-Mg-CaRes}$  Formulations

No.	Stable pressure in the wind tunnel ( $\text{kg/cm}^2$ )		Pressure after combustion ( $\text{kg/cm}^2$ )		Remarks
	Excess pressure	Absolute pressure	Excess pressure	Absolute pressure	
1	-0.4453	+0.5567	-0.3645	+0.6355	
2	-0.4531	+0.5469	-	-	unignited
3	-0.4650	+0.5350	-	-	unignited
4	-0.4453	+0.5567	-	-	unignited
5	-0.4534	+0.5466	-0.3446	+0.6554	
6	-0.4451	+0.5549	-	-	unignited
7	-0.4453	+0.5547	-	-	unignited

Table 3. Adjustment Test for the formulation of  $\text{Sr}(\text{NO}_3)_2$ -Mg-Cates Type

No.	Formulation				Oxygen diff. n	Guaranteed coeff. K	Combustion temp. T(°C)	Combustion time t(s)
	$\text{Sr}(\text{NO}_3)_2$	Mg	AP	Cates				
1	41.4	25.9	19.7	15	-32.85	0.40	1700	7.7
2	35.0	35.0	20.0	10	-29.31	0.41	2975*	3.4*
3	33.5	26.8	25.7	12	-29.11	0.42	1852	7.4
4	30.6	32.2	27.2	10	-26.67	0.44	1990	6.1
5	29.4	33.3	27.7	9	-25.04	0.45	2034	5.2
6	28.2	35.6	26.2	8	-24.21	0.46	2168	4.9
7	26.0	39.0	29.0	6	-21.24	0.48	2218	4.95

\* Data obtained under the conditions of rotating at 18,000 rpm.

result of the adjustment test is shown in Table 3.

It has been proved by the tests that the adjusted formulation has made improvement in the performance of combustion and also increased the combustion temperature in a certain degree. In particular, for the No.2 formulation, the combustion temperature has been raised by a considerable margin under the conditions of rotation.

The gas yield out of the composition with this formulation is 448ml/g. The average molecular weight is 29.46.

Test 1 on the formulation of AP-Mg-Cates type. To reduce the molecular weight still further,  $\text{Sr}(\text{NO}_3)_2$  is entirely replaced by AP, and the characteristic curves obtained from the tests are shown in Figure 4.

The observed quantity of the gas yield out of this type of composition is 576-690ml/g. The average molecular weight has been lowered below 25. However, its mechanical sensitivity is rather high, hence the difficulty in manufacture.

Test for the formulation of  $\text{Sr}(\text{NO}_3)_2$ -Mg-AP-additive type. In order to further raise the combustion temperature, low the average molecular weight and especially promote the secondary combustion of the product,

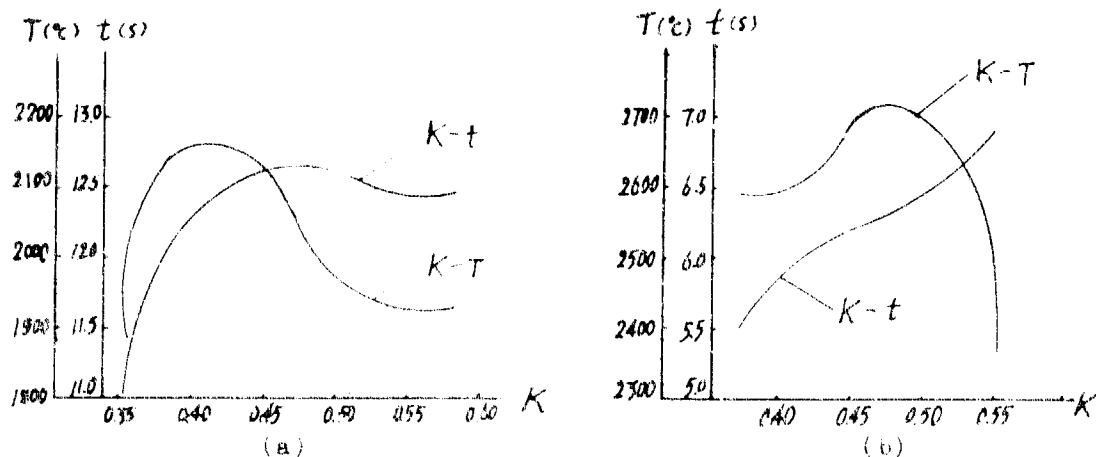


Figure 4. Characteristic curves of the relationship between combustion temperature, time and ingredient ratio of the AP-Mg-Cates composition, (a) during static combustion; (b) during rotational combustion



tests have been performed for the formulation of  $\text{Sr}(\text{NO}_3)_2\text{-Mg-AP-additive}$  type.

By selecting the suitable additive, this type of formulation will make the gas ejection agent with a low combustion velocity. As an example in which naphthalene was chosen as the additive, the result of the wind tunnel test is illustrated in Table 4.

Figure 5 shows the result for present composition and the HTPB-AP composite propellant in the wind tunnel test when the Mach number is respectively 1.3, 1.73 and 2.5.

With the increase of the Mach number, the base bleed composition with the formulation of  $\text{Sr}(\text{NO}_3)_2\text{-Mg-AP-additive}$  can produce more excellent effect of drag reduction. Figure 6 gives the curves of the change of the bullet base pressure with that of the combustion time ( $P_b\text{-}t$  curve) for this pyrotechnic composition with the additive naphthalene when  $M=1.3$  and  $M=2.5$ .

## 2. Dynamic Analogue Test

In this test according to the aforementioned method, the reentrant on

Table 4. Amount of the Base Drag Reduction in Wind Tunnel Tests

No.	Mass flow rate (kg/s)	Mach number M	Jet parameter I	Rate of base drag reduction $\Delta\bar{C}_{Db}(\%)$
1	$2.70 \times 10^{-3}$	1.72	$1.58 \times 10^{-3}$	50
2	$4.05 \times 10^{-3}$	1.72	$2.35 \times 10^{-3}$	61
3	$5.90 \times 10^{-3}$	1.72	$3.43 \times 10^{-3}$	69.9
4	$6.15 \times 10^{-3}$	1.72	$7.65 \times 10^{-3}$	78
5	$8.26 \times 10^{-3}$	1.72	$10.00 \times 10^{-3}$	88.9

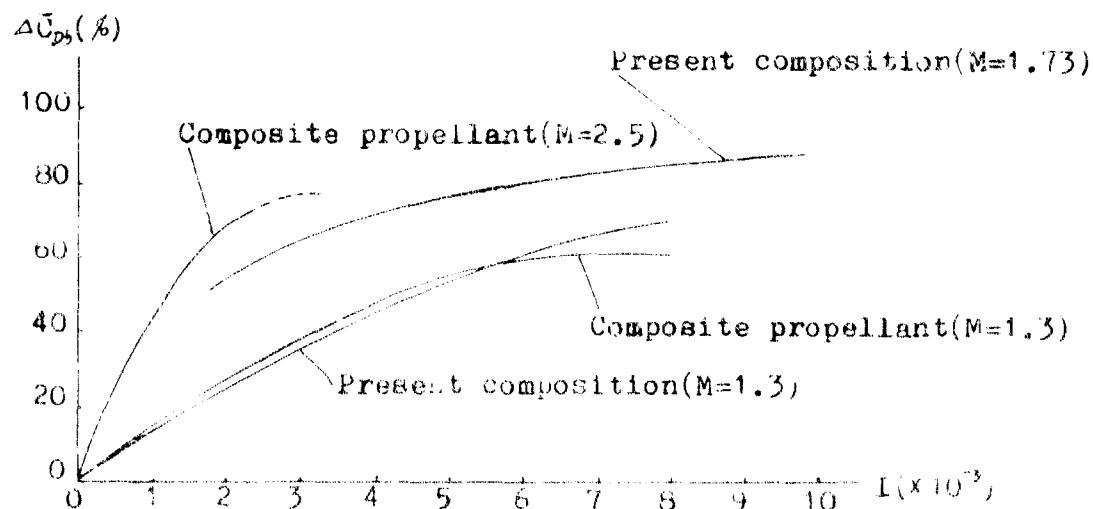


Figure 5. The test result in the wind tunnel

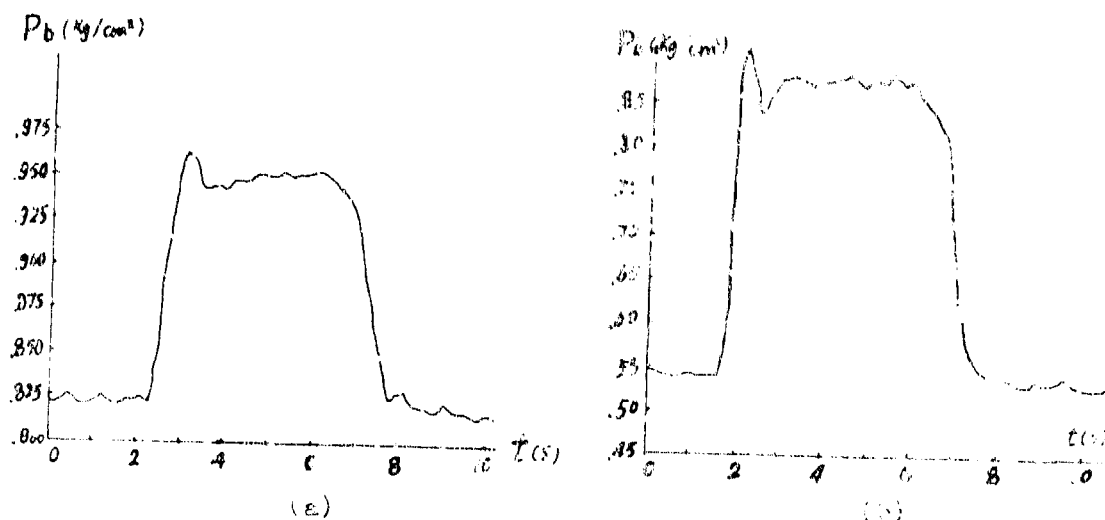


Figure 6. Curves of change of the base pressure with the combustion time when (a)  $M=1.3$ ; (b)  $M=2.5$

the analogue bullet base is loaded with the gas ejection agent of  $\text{Sr}(\text{NO}_3)_2$ -Mg-AP-additive by pressing. The test result is shown in Figure 7. The curve B illustrates the change of the bullet drag coefficient ( $C_D$ ) with that of Mach number for the formulation of which additive is naphthalene.

### 5. Live Ammunition Flight Survey Test

Test result on small-calibre bullets. The test was performed by means of a 37mm aerogun. The result indicated that the 37mm base bleed bullet loaded with present base bleed composition had slow attenuation of remaining velocity ( $V_p$ ) (see Table 5) and good effect on drag reduction (see Figure 8).

Test result on medium-calibre bullets. A 122mm homizer was used in

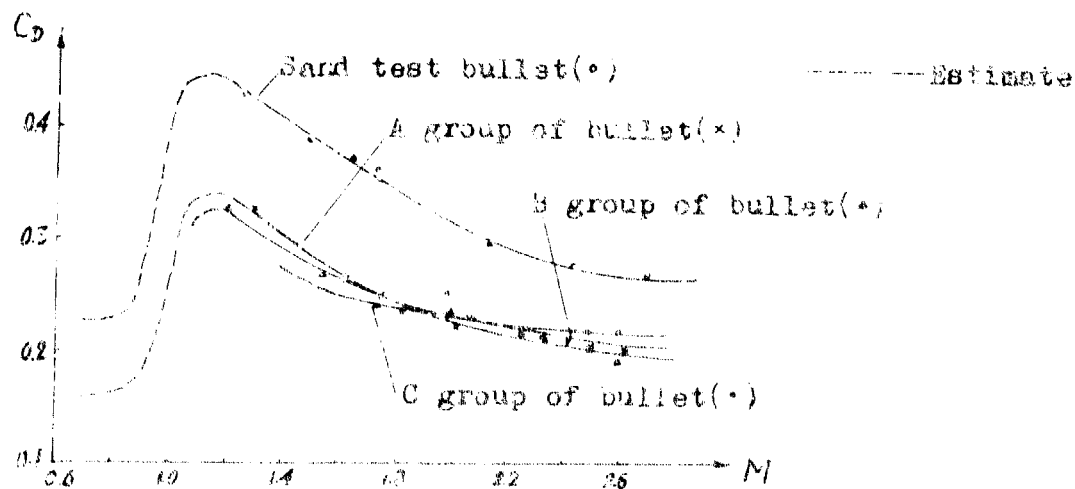


Figure 7. bullet drag curves in dynamic analogue test

Table 5. The Remaining Velocity of the Bullets in the Live Ammunition Flight Survey Test

Bullet kind	37mm bullet without base bleed agent	37mm bullet with base bleed agent	35mm bullet (foreign)			
bullet weight (g)	740	640	550			
Initial velocity $V_i$ (m/s)	1000	1162	1175			
Slant range(m)	$t(s)^a$	$V_R(m/s)$	$t(s)$	$V_R(m/s)$	$t(s)$	$V_R(m/s)$
2000	2.67	633	2.09	796	2.18	720
3000	4.75	446	3.48	658	3.78	530
4000	7.70	324	5.15	543	5.96	385
5000	11.75	244	7.18	444	9.15	292
5500			8.46	391		
6000			9.71	357		

a)  $t$ --flight time

this test. Its result is shown in Table 6.

#### DISCUSSIONS

1. Basing on the design principle of the base bleed propellant<sup>2</sup>, our research must take the following into consideration: (a) relatively low combustion velocity or mass ejection rate; (b) relatively high temperature of ejected gas; (c) relatively low molecular weight of the ejected gases; (d) combustion in the wake, i.e., the secondary combustion. It is considerable that the pyrotechnic composition consisted of  $Br(NO_3)_2$ - $Mg$ - $Al$ -additive can essentially conform to the above principle as the base bleed propellant. Its combustion velocity is low, combustion

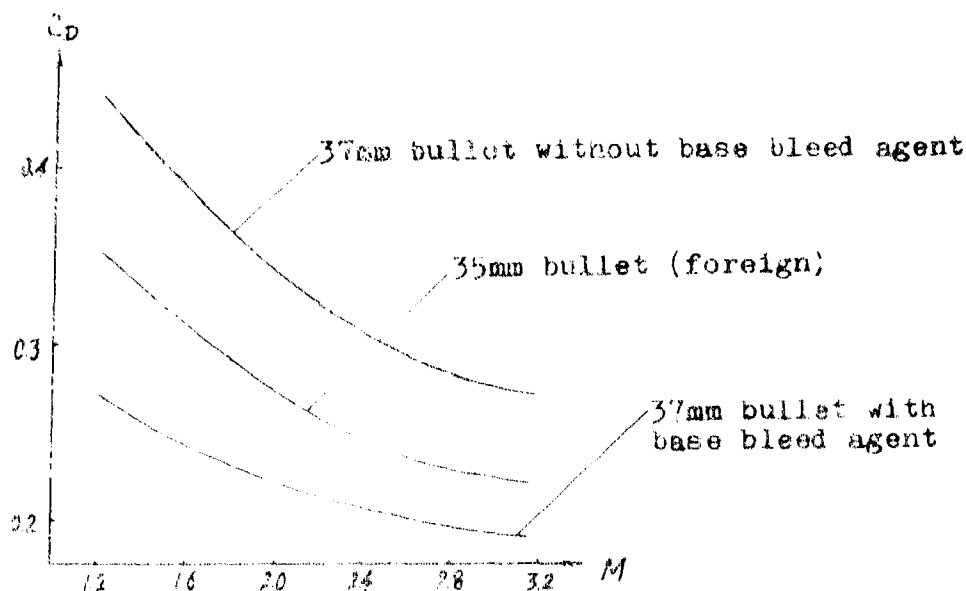


Figure 6. The  $C_d$ - $M$  curves of small-calibre bullets.

Table 6. Shooting Range-Increasing Effect in Live Ammunition Flight Survey Test

kind of base bleed agent	$V_i$ (m/s)	Shooting range		Precision		Shooting range increasing rate (%)
		Bullet A <sup>a)</sup>	Bullet B <sup>b)</sup>	Deflection(m)	Range	
$Sr(NO_3)_2$ -mg-AP-additive	550	11008	15031	7.5	1/237	18.4
Ditto	520	12877	15027	3.1	1/233	16.7
Ditto	690	17500	21887	12.7	1/279	25.1
HTPB-AP	550	11008	12528	17.5	1/220	12.0

a) the original bullet; b) the bullet loaded with the base bleed composition

temperature is high because of the  $SrO$ ,  $MgO$  in its combustion product, and the  $Mg$  powder with low molecular weight easily evaporates as its low boiling point(1100 $^{\circ}C$ ) and makes the secondary combustion in the wake of the bullets in flight. By comparison, the HTPB-AP composite propellant is not as good as it at all. As a result, the practical effect of the present composition as a base bleed propellant all is better than the HTPB-AP composite propellant in both the wind tunnel test and the live ammunition flight survey test.

2. With the pyrotechnic composition as the gas ejection agent, it is possible to reduce the average molecular weight of the combustion product in the same type of formulations. Table 1 and Table 2 list the same type of formulations. In Table 1, the average molecular weight of the adjusted formulation No.4 is 33.15, while in Table 2 the average molecular weight of the adjusted formulation No.2 goes down to 29.46. If all the oxidizer is to be replaced by AP, the average molecular weight of this type of formulation can be reduced to less than 25.

3. The application of the pyrotechnic composition to increase the shooting range of the bullet is feasible. Under certain conditions, it can raise the shooting range by a big margin and has such characteristics as being simple in process of manufacture and being low in cost. It can be anticipated that the use of the pyrotechnic composition as a base bleed propellant has great potentialities.

#### REFERENCES

1. Nils-Erik Gunners, Rune V. Hellgren and Torsten Liljergren, Gun Projectile Arranged with a Base Drag Reducing System, U.S. Patent 4,213,593, Jul. 1980.
2. Ward., J. R., Baltakis, F. P. and Pronchick, D. W., Wind Tunnel Study of Base Drag Reduction by Combustion of Pyrotechnics, BRL-R-1745, AD-B000431, April 1974.

# THE BASE BLEED IGNITER

Negoiciu mr Dragoslav

## 1. INTRODUCTION

This paper presents some problems connected with the designing and development of igniters, some examples of existing igniters, the base bleed propellant ignition in static conditions and the possibility of the base bleed propellant ignition with Mg/PTFE pyrotechnic mixture.

The autor is concerned much more with the pyrotechnic part of the igniter. The base bleed propellant is AP/HTPB composite solid propellant. The grain is cylindrical in shape with central hole and three slits arranged by angle of  $120^\circ$ .

Such configuration ensures the desired degressive (pattern) of burning surface, and the burning rate for propellant compositions used so far is about 1 mm/s at atmospheric pressure which gives the burning time of base bleed from 25 to 30 seconds [1].

## 2. THE BASE BLEED DESIGN REQUIREMENTS

To satisfy the function of base bleed unit successfully the igniter must fill out the following requirements:

- it must be hermetic,
- it must have compact construction to withstand extreme conditions of firing,
- it must be ignited by hot gun gas,
- it must not quench after firing during the decompression,
- it must reignite the base bleed propellant and bring it to the stable burning,
- after igniter functioning its remaining parts must not fall down and disturb the flight of projectile.

In this paper only the pyrotechnic mixture, which is the main part of the igniter, is considered.

### 3. THE IGNITER PYROTECHNIC MIXTURE RESEARCH

In order to satisfy the basic requirements the pyrotechnic mixture must be pressed in the steel body of the igniter with high consolidation pressures. The igniter has four holes at the bottom through which the pyrotechnic mixture is ignited and the combustion products flow out after ignition. The opposite side of the igniter is coated with resin for increasing the mechanical strength of pressed pyrotechnic mixture and hermetization.

During the igniter preliminary researches the well known pyrotechnic mixtures were used. The characteristics of these mixtures are shown in table 1.

TABLE 1.

M I X T U R E	$T_p$ /°C/	(t) (/s/)	Q (J/g)	$P \cdot 10^{-8}$ /Pa/	$v_l$ /mm/s/	$v_m$ /g/s/
B KNO <sub>3</sub> Phenolformaldehyde resin (I)	500	(4,5)	12980	3,268	9,5	7,4
Mg KNO <sub>3</sub> Ba(NO <sub>3</sub> ) <sub>2</sub> Phenolformaldehyde resin (II)	500	(4,0)	8780	3,268	6,4	5,7
Mg KClO <sub>4</sub> Ba(NO <sub>3</sub> ) <sub>2</sub> Phenolformaldehyde resin (III)	560	(4,5)	9640	3,266	7,3	5,7

The used symbols denote:

- Q - heat output of the pyrotechnic mixture
- $T_p$  - autoignition/temperature of the pyrotechnic mixture
- t - induction time
- P - consolidation pressure
- $V_l$  - linear burning rate in the igniter body
- $V_m$  - mass burning rate in the igniter body

Although these pyrotechnic mixtures give satisfactory performance with propellant /2/, yet they had some disadvantages which required to find more convenient mixtures. Mixture I is almost gasless and most of its products are solid, remaining in the body of the igniter. Thus, it is assumed that in some cases, the hot combustion products, which flow out through holes at the igniter bottom, could not ignite the base bleed propellant. The burning rate of mixture II and III is low and this affecting irregular burn-

ng of propellant during igniter functioning (increased burning pressure and erosion of propellant).

In order to shorten the burning time the experiments were performed in the shortened igniter's body and with pyrotechnic mixtures which have the higher burning rates. The most part of this results are presented in table 2.

TABLE 2.

MIXTURE	$T_p$ /°C/	( $\tau$ ) /(s)/	Q /J/g/	$P \cdot 10^{-8}$ /Pa/	$v_1$ /mm/s/	$v_m$ /g/s/
Mg (IV)				2,177	5,00	4,05
KClO <sub>4</sub>	590	(6)	9300	3,268	4,95	4,29
Phenolformaldehyde resin				4,354	4,90	4,52
Mg (V)				2,177	7,70	6,78
KNO <sub>3</sub>	510	(4,5)	8300	3,268	7,70	6,92
Phenolformaldehyde resin				4,354	7,50	7,10
Mg (VI)				2,177	10,0	10,50
Ba (NO <sub>3</sub> ) <sub>2</sub>	560	(4,5)	6380	3,268	9,66	10,62
Phenolformaldehyde resin				4,354	9,01	10,3

All mixtures from table 2 gave well results both in static and dynamics igniter examinations. However, the best results and the shortest burning time gave the mixture VI. It is assumed that the optimal ingiter burning time is between 2 and 3 seconds.

The change in the consolidation pressure in designated range had a little influence on both linear and mass burning rates, and all examined samples had withstood the conditions of firing.

The base bleed unit gave good performance, and expected increasing of a range capability and decreasing of a dispersion in range were achieved. (2,3).

#### 4. THE BASE BLEED IGNITION IN STATIC CONDITIONS

In order to carry out the base bleed examination in a static conditions the problem of propellant ignition must be solved. The ignition with complete igniter is very expansive and the autor decided to find the simplest and cheaper way of ignition. Ignition with the black powder of large particle size and unpressed pyrotechnic mixtures didn't give satisfactory results. Namely, a large number of failures had complicated the examinations.

The satisfactory solution was found using the pressed tablet (mixture III from table 1) activated with suitable igniter. The longer burning time lead to the better propellant igni-

tion and enabled the propellant to reach the stable burning. Figure 1 shows the  $p(T)$  curve of base bleed unit during static firing.

#### 5. THE BASE BLEED PROPELLANT IGNITION WITH Mg/PTFE MIXTURE

The purpose of these examinations was to study the possibility of use Mg/PTFE mixtures for the base bleed propellant ignition. According to the literature data (4,5) five Mg/PTFE mixtures was selected and examined in the igniter body. The results of this experiments are shown in table 3.

TABLE 3.

M I X T U R E*		$v_1$	$v_m$	Q
( )		/mm/s/	/g/s/	/J/g/
Mg - 70	(VII)	1,90	1,80	4642
PTFE - 30				
Mg - 60	(VIII)	1,25	1,18	6002
PTFE - 40				
Mg - 50	(IX)	1,20	1,14	7349
PTFE - 50				
Mg - 40	(X)	1,06	1,00	8763
PTFE - 60				
Mg - 30	(XI)	0,85	0,81	8445
PTFE - 70				

\*In these mixtures was used as a binder 2,5 g of flourel FC-2175 on 100 g of mixture, and consolidation pressure was  $3,268 \cdot 10^8 \text{ Pa}$ .

On the bases of these results the mixtures VII and X were selected and examined with base bleed propellant in static conditions.

Experiments were performed both with complete igniter and pressed tablet, where the ignition was activated with fuse mase up of unpressed mixture I (table 1) and electric squib. The satisfactory results confirmed the possibility of the use Mg/PTFE mixtures for base bleed propellant ignition.

#### CONCLUSION

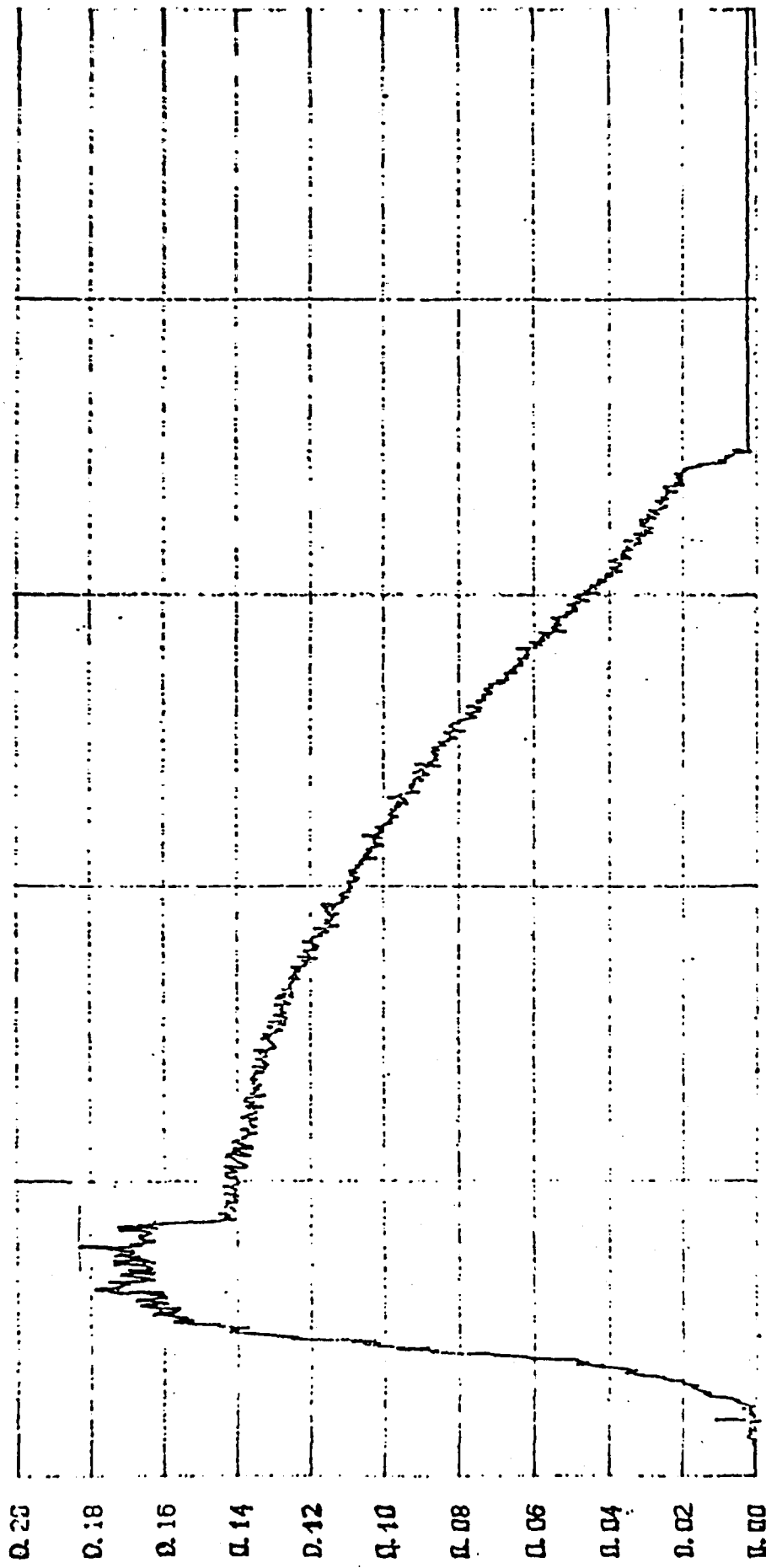
This paper deals with some problems connected with the design and development of the base bleed igniters and reports the results of igniter examination loaded with different pyrotechnic mixtures.

The selected pyrotechnic mixtures give satisfactory performance (results) both in static and dynamic conditions. The solution of ignition was proposed for the base bleed propellant examinations in static conditions.



# KRIVA P(t) GAS GENERATORA

Opit : 13 Datum : 23.08.1983 Mesto : ZARADVO  
 Pm(bar) : 0.183



0.0 8.0 16.0 24.0 32.0 40.0(s)

FIGURE 1. THE P(t) CURVE OF BASE BLEED

It was confirmed, according to the results of the examinations in the static conditions, that successful ignition may be achieved with Mg/PTFE mixture. However, it must be confirmed through examinations in dynamic conditions.

#### L I T E R A T U R E

- 1/ INTERNAL REPORT, Vogošća - SFRJ, May 1986. PP 171-180.
- 2/ INTERNAL REPORT, VT1-02-27-117, Beograd, SFRJ, 1984.
- 3/ INTERNAL REPORT, VT1-02-24-444, Beograd, SFRJ, 1985.
- 4/ ŠILDOVSKIJ, A.A., GORBUNOV, V.V., Fizika gorenja i vrziva, vol.14, no. 1, PP 157, 1978.
- 5/ PERETZ, A., J.SPACECRAFT, vol.21, no. 2, PP 222, 1984.

# IGNITION AND COMBUSTION BEHAVIOR OF MIV IGNITER MATERIALS FOR BASE BLEED APPLICATIONS

B. L. Fetherolf, D. M. Chen, T. S. Snyder,  
T. A. Litzinger, and K. K. Kuo

Department of Mechanical Engineering  
The Pennsylvania State University  
University Park, PA 16802 U.S.A.

## ABSTRACT

The pyrolysis and ignition characteristics of an igniter material composed of magnesium, Polytetrafluorethylene, and Viton A have been studied using a high-power CO<sub>2</sub> laser as the radiative heating source. Methods of analysis and the instrumentation employed were high-speed direct and schlieren photography to visualize the flame structure and gas-phase dynamics, near-infrared photodiodes to obtain ignition delay data, and probe sampling and a gas chromatograph/mass spectrometer to analyze the gaseous products evolved. Important test variables were incident heat flux, chamber pressure, and oxygen concentration. In addition, the effect of boron addition on the ignition behavior of the igniter charge was studied.

Ignition occurred on the sample surface under all test conditions. A primary flame, attached to the surface, with a height of 1.2-1.5 mm for ignition in air was observed. A gas-phase flame of less intensity was observed directly above the primary flame, and the magnitude of this flame was considerably reduced as the ambient oxygen concentration decreased. At low pressures ( $\approx 0.1$  atm), no evident luminous plume evolution and gas-phase dynamics were observed, and the propellant decomposed in large fragments evolved at high speeds after ignition. Experimental results for the ignition delay as a function of heat flux indicated that the delay time decreases monotonically as heat flux increases, and that decreasing the ambient pressure or the ambient oxygen percentage also decreased the ignition delay time. For combustion of the propellant in air and in an inert helium atmosphere, only hydrocarbon compounds [primarily ethylene (C<sub>2</sub>H<sub>4</sub>), propylene (C<sub>3</sub>H<sub>6</sub>), and benzene (C<sub>6</sub>H<sub>6</sub>)] and CO and CO<sub>2</sub> for combustion in air were observed. However, in an inert atmosphere, pure PTFE  $(-C_2F_4-)_n$  pyrolyzed into many fluorocarbon compounds, and Viton A  $(-C_5H_3.5F_6.5-)_n$  pyrolyzed into a variety of hydrofluorocarbons and fluorocarbons. It is believed that these primary pyrolysis species are consumed to form the aforementioned hydrocarbon species plus undetected HF and the observed MgF<sub>2</sub> solid products.

## 1. INTRODUCTION

The development of a reliable and efficient base bleed system to increase the range of artillery projectiles is currently of great

interest. This system is designed to inject gases into the wake behind the projectile, increasing the base pressure and reducing the profile drag, which accounts for 50-75% of the total drag. This reduction of the drag will increase the range capabilities of the projectile. To insure sustained ignition of the base bleed propellant during the transition from the severe gun barrel environment to the ambient air and also during the subsequent flight, a supplementary, redundant igniter system is required. Thus, the base bleed igniter propellant must be able to sustain burning over a wide range of pressures, temperatures, and gaseous environments. It must also be durable enough to withstand the tremendous forces ( $\approx 10,000$  G's) of setback acceleration and the centrifugal forces of high-speed rotation (16,000 rpm).<sup>1</sup>

Most of the work to date on base bleed has concentrated on the aerodynamics and selection of candidate propellants. Several researchers have done theoretical calculations of the effect of base bleed systems on the aerodynamics of a projectile.<sup>2-6</sup> Experimental simulations have also been conducted to validate the effectiveness of base injection.<sup>7,8</sup> Kloeckner and Rassinfosse have written a paper on the manufacture of base bleed propellants.<sup>9</sup> However, very few papers have been published to date on studies of the performance of practical base bleed motors and their supplementary redundant igniter systems.

Magnesium/PTFE/Viton A (MTV) propellants have been considered in solid rocket motor igniters and are now being tried experimentally as base bleed igniter propellants. Peretz<sup>10</sup> stated that the use of magnesium as the metal counterpart is beneficial because it ignites and burns readily, thus promoting efficient combustion, and requires small amounts of oxidizing agent to burn. Viton A ( $-(C_5H_3.5F_6.5-)_n$ ), a copolymer of vinylidene fluoride and perfluoropropylene, is often added to Mg/PTFE formulations to increase homogeneity and facilitate fabrication. Because of its chemical similarity to Polytetrafluoroethylene,  $[PTFE + (C_2F_4-)_n]$ , significant amounts of Viton A can be added without altering the combustion characteristics.

Peretz<sup>11</sup> listed the following advantages of the MTV formulation for use as an igniter material: high energy content, high degree of safety in preparation, low temperature and pressure dependence of the burning rate, ease and low cost of igniter pellet or grain fabrication, favorable aging characteristics, and stable burning at low pressures. He also listed several advantages of metal-fluorocarbon compositions in comparison with metal-hydrocarbon propellants: higher volumetric heat release, higher rate of reaction, much higher density, excellent thermal stability (due to the high C-F bond strength), higher activation energy, and much lower production of soot due to the lower content of carbon. For magnesium, the standard gravimetric and volumetric heats of fluorination [producing  $MgF_2(s)$ ] are almost exactly twice as much as those for oxidation [producing  $MgO(s)$ ].

Kubota and Serizawa have published two of the more comprehensive papers on experimental studies of the combustion of Mg/PTFE propellants.<sup>12,13</sup> Their propellant also contained 3% Viton A. Chen et al.<sup>14</sup> have conducted studies of the thermophysical properties and combustion of metal-based solid fuels in a strand burner, including the propellant that is the subject of this paper. They found that the burning rate was consistently higher in a nitrogen atmosphere than in air, and they also measured the thermal diffusivity to be  $1.6 \times 10^{-2}$  cm<sup>2</sup>/sec. However, to

the authors' knowledge, no experimental papers have been published to date on the ignition behavior of MTV propellants.

Characterization of the ignition behavior of the MTV propellant under a wide range of conditions is critical for determining the feasibility, applicability, and subsequent performance of the igniter. Radiative ignition has been often used in the studies of ignition behavior of solid propellants. The high-power CO<sub>2</sub> laser is now the prevailing choice for the radiant energy source due to its advantages of precise control of lasing time and energy flux, and a high level of beam intensity that simulates energy fluxes found in igniters and propulsive devices.

The overall objective of this research was to investigate the ignition behavior of a Mg/PTFE/Viton A propellant under various ambient conditions, to gain a better understanding of the processes governing ignition, and to correlate this data with conditions experienced by a base bleed igniter. Specific objectives were: (1) to investigate the flame structure and gas-phase dynamics during the ignition transient under various pressures and ambient oxygen concentrations, (2) to study the variation of ignition delay time as a function of pressure, ambient oxygen concentration, and incident heat flux, and (3) to analyze the gaseous species produced during pyrolysis and ignition of the MTV propellant and during pyrolysis of PTFE and Viton A individually.

## 2. EXPERIMENTAL APPROACH

A diagram of the overall experimental set-up is given in Figure 1. The radiative energy source was a high-power Coherent Super 48 CO<sub>2</sub> Laser, capable of producing 800 watts of power in the continuous wave mode and 3500 watts in the pulsed mode with precise control of the power output and lasing time. A beam profile, uniform within  $\pm 10\%$  across the propellant sample surface, was obtained using an aperture with a diameter of 7 mm to allow only the most uniform center section of the beam to irradiate the surface. For all tests, the actual heat flux was measured with a calorimeter. A cubic Plexiglass test chamber, 25 cm on a side, with a stainless steel top cover was used for ignition delay tests and schlieren visualization. Two high-quality glass windows were installed in opposite sides of the chamber for the schlieren flow visualization. For the species sampling tests, in order to have considerable species concentrations, a smaller Plexiglass test chamber, 10 cm long by 5 cm in diameter with aluminum end caps, was employed. A septum, installed in the side of the chamber, allowed for gas sampling with a syringe. The top covers of both chambers were fitted with potassium chloride windows, which are highly transmissive in the infrared range, for beam entrance. Pressure and composition of the initial gas in the chamber was controlled using a vacuum pump, a pressure/vacuum gauge, and an inert gas supply system.

Both the direct and schlieren images were recorded with a Spin Physics 2000 video recording system. As seen in Fig. 1, the system consists of a controller, video monitor, and two camera heads. Maximum recording speed is 12000 pps, but a 2000 pps recording rate was employed for this research. The controller can display both the schlieren and direct images simultaneously, allowing direct comparison of the flame structure and gas-phase dynamics. The schlieren system is a "Z-type" configuration, employing 15 cm parabolic mirrors to direct a parallel light beam through the test chamber from a 100 watt continuous

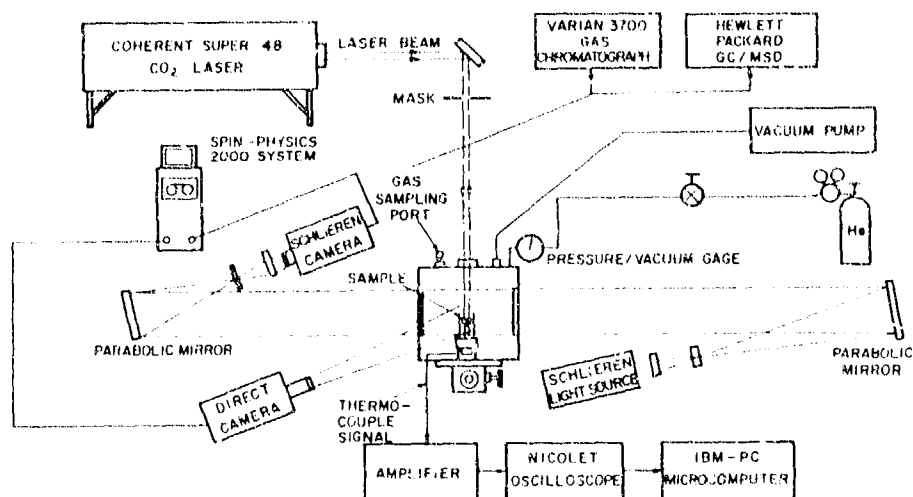


FIGURE 1. Experimental Setup for CO<sub>2</sub> laser pyrolysis and ignition research

Tungsten-halogen lamp. The beam is directed and shaped by lenses and rectangular apertures at each end as it travels from the light source, through the chamber, and into the video camera at the other end.

Ignition delay times were determined using two near-infrared photodiodes (spectral response: 0.35-1.15  $\mu\text{m}$ ) to sense the first light emission from a flame or heat production from chemical reactions. One photodiode was positioned seven cm from the sample and aimed directly at its surface while the other one was positioned in an upper corner of the chamber and aimed 2.5 cm above the surface to observe the gas-phase infrared emission. To signal "zero-time" on both the photodiode traces and the direct video image, a strobe light was employed. The data was recorded on a Nicolet oscilloscope and transferred to an IBM PC for processing.

After a test, samples of gaseous products were drawn from the test chamber with a one milliliter syringe. These gaseous product species were then analyzed using a Hewlett/Packard gas chromatograph/mass spectrometer. Most of the samples were analyzed with a Carboxen B/5% Fluorocel column. The temperature program employed was isothermal at 50°C for the first 5 minutes and then ramped at 15°C per minute up to 200°C for the remainder of the run. A column with Porapak Q&R in series was also used to obtain data on hydrocarbon species.

### 3. FLAME STRUCTURE AND GAS-PHASE DYNAMICS

Figure 2 is a sequence of images depicting the ignition transient for a sample ignited in air at 1 atmosphere. Both the direct and schlieren photographs of the ignition sequence are shown. The times below each pair of images represent the time elapsed from the onset of laser heating. In each pair of images, the sample surface is at the same height; however, the magnification of the direct image is slightly less than that of the schlieren image.

Ignition occurs in Fig. 2a after a delay time of 19 milliseconds. The faint light emission seen on the sample surface in the direct image corresponds to the abrupt rise in the photodiode signal (within 2 milliseconds) that was used as the criterion for ignition. The initial evolution of a gaseous sphere on the schlieren image occurs slightly off the center of the sample due to minor variations in the laser beam intensity profile. The gaseous sphere expands upward in Fig. 2b and a ball of flame is established within the dark outer gradients of the sphere. The flame and evolved gases continue to propagate through Figs. 2c-2f. A mushroom-shaped gas-phase structure can be seen inside the outer gradient in the schlieren picture in Fig. 2e. The cap of the mushroom is due to the formation of a vortex resulting from the propagation of the initial sphere of gases evolved, and the stem is formed by the continued evolution of a stream of gases normal to the surface. The actual steady-state flame shape has not yet been established in Fig. 2f, but it is quite similar in size to the inner flame region that can be seen in the schlieren image. Large particles can be seen in both the direct and schlieren images in this figure.

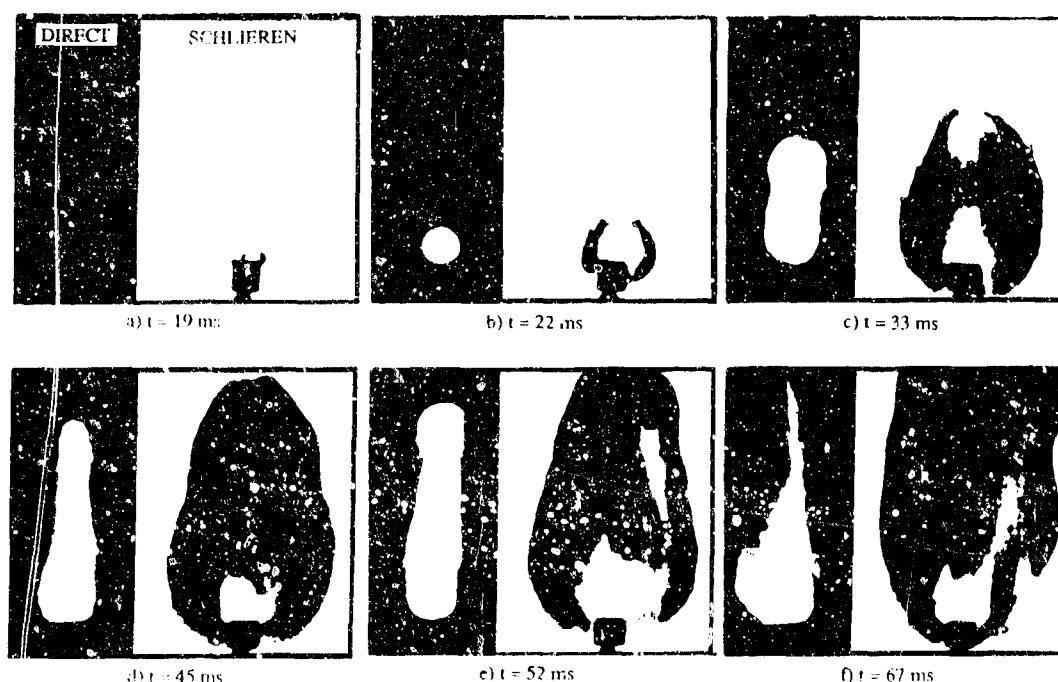


FIGURE 2. Ignition sequence of the MTV propellant in air at 1 atmosphere  
( $q'' = 640 \text{ W/cm}^2$ )

An ignition test conducted at a low pressure of  $\sim 0.1$  atmosphere is displayed in Fig. 3. Clearly, this ignition process is much less vigorous than the rather explosive dynamics observed in the higher pressure ignition. The first emission of visible light does not occur until 108 milliseconds, but the photodiode signal abruptly increased at 32 milliseconds. Evidently, the rise in the photodiode signal was caused by a significant amount of heat (infrared emission) begin evolved well before the visible light of a flame was observed. Thus, the ignition at low pressure is correlated with the significant evolution of heat from reactions; the heat evolution does not directly correspond to the onset of a visible flame.

Two distinct phenomena observed in Fig. 3 are the abundance of very large particles and fragments evolved from the sample and the lack of any gas-phase structure in the schlieren pictures. Figures 3b and 3c depict the evolution and transport of two large fragments from the surface, and Fig. 3d shows the first sign of a substantial flame zone established on the surface. Then in Figs. 3e and 3f, huge amounts of very large particles are evolved as the sample "burns". In this test, the side surfaces of the sample were not inhibited, and particles evolved horizontally in Fig. 3f are a result of side burning. After the test, these particles fully coated the schlieren windows 15 cm from the sample and blocked the schlieren image by the time the sample had been completely burned.

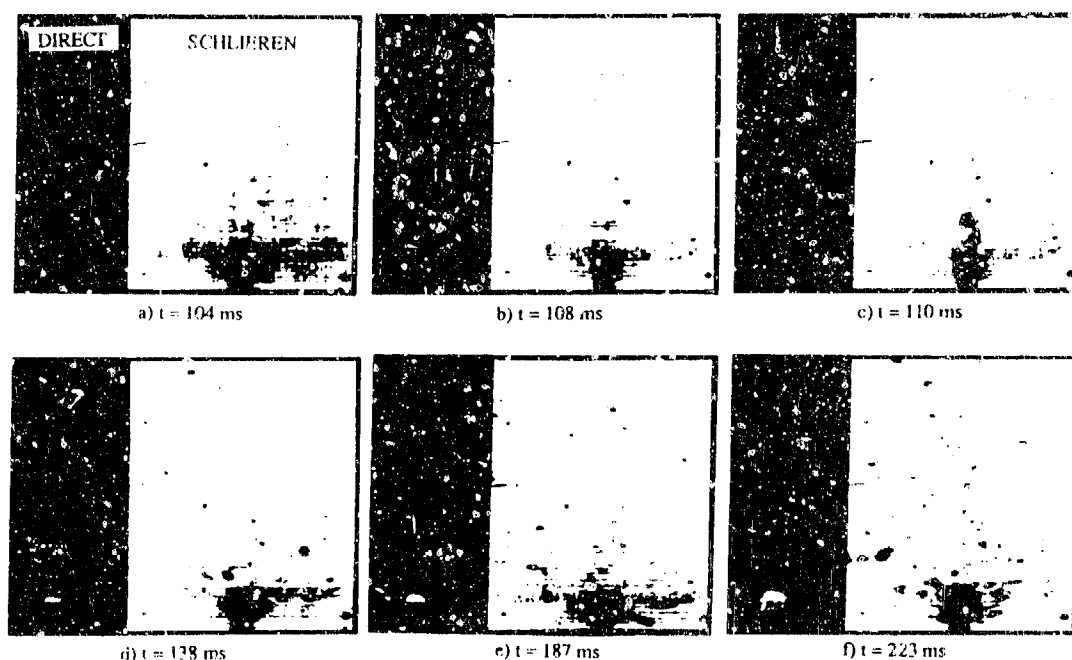


FIGURE 3. Ignition sequence of the MTV propellant in air at 0.1 atmosphere ( $q'' = 430 \text{ W/cm}^2$ )

A set of images depicting ignition in an inert atmosphere of nitrogen ( $\sim 0.5\% \text{ O}_2$ ) is given in Fig. 4. The gas-phase dynamics follow roughly the same progression as those for tests in air. The gradients are noticeably darker, though, indicating stronger density and/or temperature gradients, and the flame structure is obviously quite different from the ignition tests in air at one atmosphere. The flame initially propagates to a height around 1.0 centimeter above the sample surface and then recedes to the steady-state shape seen in Fig. 4f. Comparing Figs. 2 and 4, it can definitely be concluded that oxygen plays a significant role in the reactions that produce a large luminous plume during ignition. The final steady-state flame is also larger for the case of air. Finally, Fig. 5 displays two schlieren images with different levels of magnification that were obtained using different focal lengths of collimating lenses in front of the camera. The lenses used for Figs. 5a and 5b provide magnifications of 1.8 and 4.5, respectively, of the images displayed in Figs. 2-4. Both images in Fig. 5 represent ignition in air at 1 atmosphere. Measurements taken from all the images, irrespective of



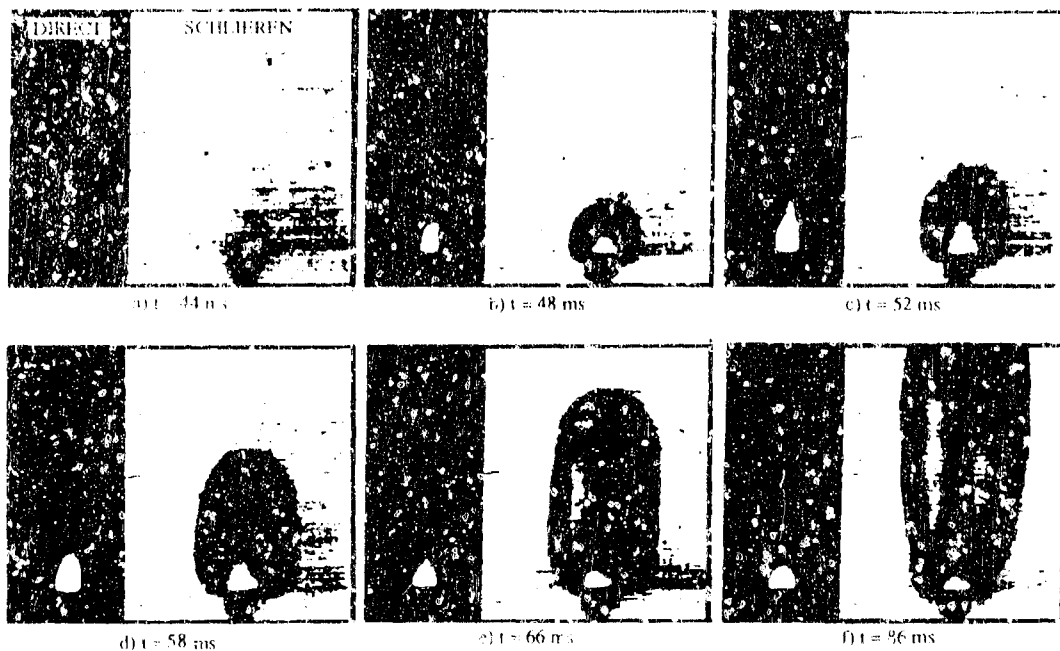
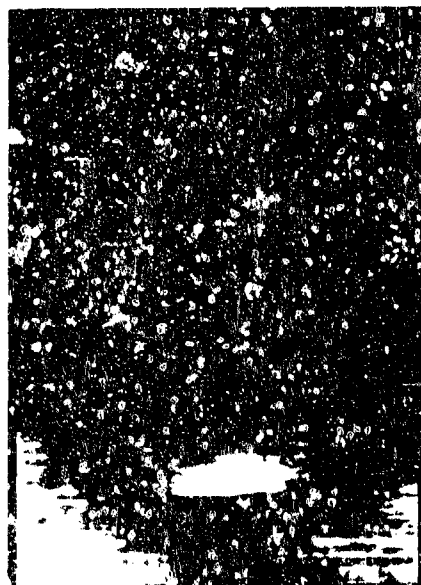


FIGURE 4. Ignition sequence of one MIV propellant in an inert  $H_2$  environment at 1 atmosphere ( $q^* = 430 \text{ W/cm}^2$ )



(a) Magnification  $\times 1.3$ ,  $t = 90 \text{ ms}$



(b) Magnification  $\times 1.5$ ,  $t = 90 \text{ ms}$

FIGURE 5. Primary flame, and attached to sample surface; two different magnifications of the size of the flame image in Figure 4d.

the level of magnification, corresponded very well, confirming the accuracy and reproducibility of the schlieren system. These measurements showed that the primary flame zone established on the sample surface is 1.2-1.5 mm in height.

#### 4. IGNITION DELAY BEHAVIOR

The ignition delay behavior of the MTV propellant was investigated as a function of pressure, heat flux, and ambient oxygen concentration. The ignition delay times were determined from the photodiode traces as the elapsed time from the initiation of laser heating to the distinct point where the signal rose very abruptly, evidenced by the typical photodiode trace given in Fig. 6. There is a very abrupt "spike" in the signal which drops and then rises again to a relatively steady state. This ignition delay time was normally within 2-3 milliseconds of the time lapsed until the first light emission observed in the direct image. After ignition, combustion of the samples was sustained until they were totally consumed, regardless of the ambient conditions.

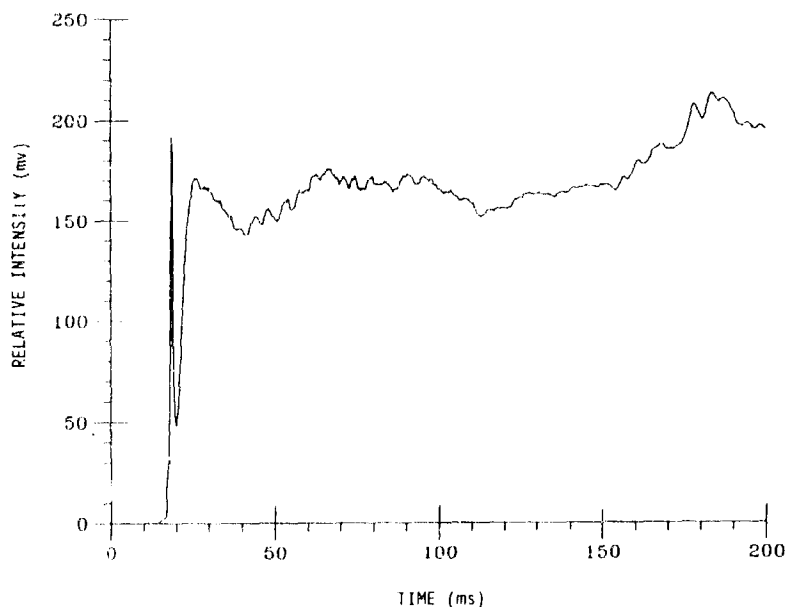


FIGURE 6. Near-field photodiode trace of ignition in air at 1 atmosphere ( $q'' = 670 \text{ W/cm}^2$ )

Figure 7 exhibits the ignition delay behavior as a function of ambient pressure and incident heat flux. The two curves indicate the pressure dependence, one for ignition at 1 atmosphere and the other in a relative vacuum of  $<0.1$  atmosphere. Most importantly, it can be seen that the ignition delay times are shorter at lower pressure. Also, the profiles of both curves as a function of the radiative heat flux from the  $\text{CO}_2$  laser are quite similar. In other words, lowering the pressure merely serves to shift the curve down while maintaining the same flux-dependent profile. However, the reason for the shorter delays at lower pressures can most likely be explained by the results given in Fig. 8.

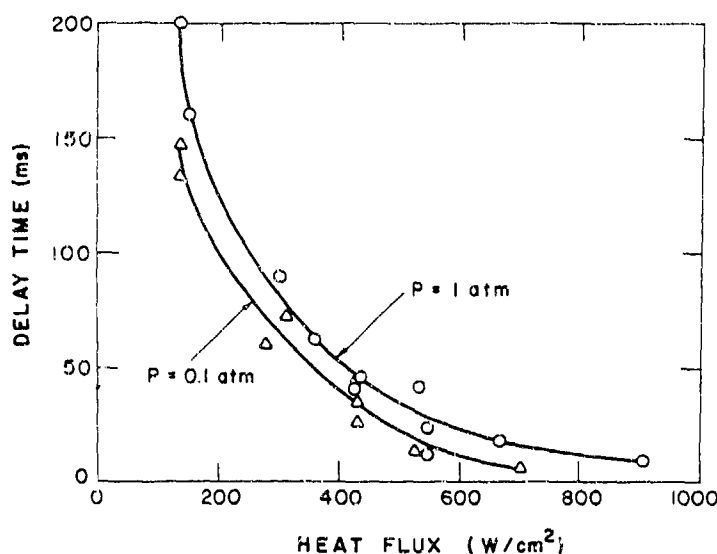


FIGURE 7. Effect of pressure and incident heat flux on ignition delay time of MTV propellant in air

Figure 8 illustrates the effect of the ambient oxygen concentration on the ignition delay behavior at a constant heat flux. Although more data is needed to confirm this behavior, the trend is believed to be correct, and it represents a significant point in understanding the ignition mechanisms. The curve shows that the ignition delay time increases with an increase in the ambient oxygen concentration. This behavior is also the most likely justification for the lower ignition delays at lower pressures observed in Fig. 7, since as pressure decreases, the concentration of ambient oxygen also decreases.

Some interesting results relative to understanding the inhibiting effect of oxygen were presented by Griffiths and Robertson.<sup>15</sup> They did simultaneous DTA/DTG experiments on the decomposition of PTFE powder and Mg/PTFE powder mixtures in different ambient gases. They observed that the decomposition of PTFE was endothermic in N<sub>2</sub> and argon but was exothermic in air, suggesting that the PTFE decomposition products react with the oxygen in the air. They also observed significant differences in the DTA curves for the decomposition of Mg/PTFE (1:1) mixtures in air and in argon but did not discuss the mechanisms that may produce this behavior.

In this work, it was believed initially that the inhibiting effect of oxygen observed in Fig. 8 was due to the reaction with Mg to form MgO and thus prevent the fluorine from reacting with the Mg. Since the gravimetric heats of oxidation and fluorination of Mg are 24.75 KJ/g and 46.25 KJ/g, respectively,<sup>11</sup> the reaction of oxygen with magnesium would generate less thermal energy than the reaction of fluorine with magnesium, producing a longer ignition delay in air. However, ignition delay tests performed on a pellet composed of a 1:1 mixture of PTFE and Mg without any Vilon A showed that the ignition delay was approximately

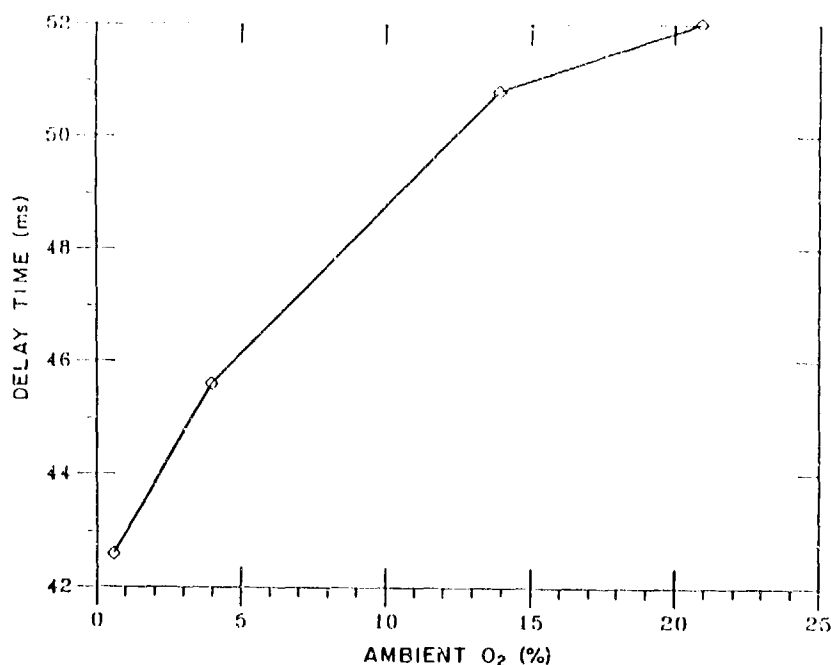


FIGURE 8. Effect of oxygen concentration on ignition delay time of MTV propellant at 1 atmosphere ( $q'' = 400 \text{ W/cm}^2$ )

twice as much as that of the MTV propellant under the same conditions, leading to the conclusion that Viton A is the rate-controlling ingredient for the MTV formulation. Properties of these polymers that would seem to substantiate this behavior are the decomposition of Viton A at  $589 \text{ K}^{16}$  versus  $803 \text{ K}^{13}$  for the PTFE, and activation energies of  $210 \text{ KJ/mol}$  and  $350 \text{ KJ/mol}$ , respectively. The effect of oxygen on the ignition delay of the MTV propellant should then be a result of its effect on Viton A, not magnesium. As will be discussed in the next section, many of the major gaseous species evolved in the decomposition of PTFE are also observed in the pyrolysis of Viton A. Therefore, the effect of  $\text{O}_2$  on the decomposition of PTFE observed by Griffiths and Robertson might also apply to the effect of  $\text{O}_2$  on Viton A and thus explain the longer delay times in air.

In an attempt to improve the ignition and combustion of the MTV propellant, boron was added to several different formulations of Mg and PTFE. The ignition delay results are presented in Fig. 9. The results indicate that increasing the amount of boron in an Mg/PTFE formulation significantly reduces the ignition delay time, with the shortest delay observed for a 50/50 formulation of Boron/PTFE without any magnesium. Two factors considered in explaining this trend were radiation reflectivity at the  $10.6 \text{ m}$  wavelength of the  $\text{CO}_2$  laser and thermal diffusivity. The reflectivity of magnesium is about  $0.75$ ,<sup>17</sup> which is much greater than that of boron. Therefore, a large part of the laser energy may be reflected away from the surface of samples containing significant amounts of magnesium. It was considered that the ignition enhancement by boron observed in Fig. 9 may be an artifact of the laser and not a practical consideration for the improvement of the ignition of Mg/PTFE propellants. However, the combustion after laser cutoff of the

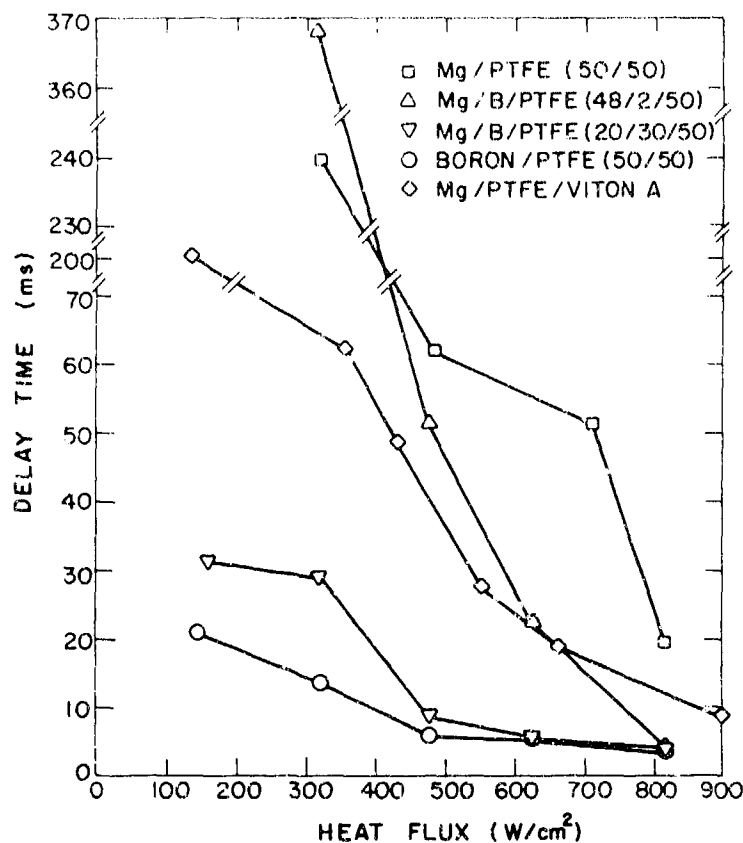


FIGURE 9. Effect on ignition delay of the addition of boron and Viton A to a Mg/PTFE propellant (ignition in air at 1 atmosphere)

Mg/B/PTFE formulation with 30% boron was much more vigorous than the formulation without any boron, indicating that the addition of boron does have a significant physicochemical effect. Also, the thermal diffusivity of magnesium is  $0.876 \text{ cm}^2/\text{sec}$ , which is eight times higher than boron. Consequently, in a sample containing magnesium, in-depth heat transfer is much higher. This phenomenon lowers the rate of increase of the surface temperature, which in turn, increases the delay time to ignition.

Another important observation from Fig. 9 is that the replacement of PTFE in the 50/50 Mg/PTFE formulation with an amount of Viton A significantly reduces the ignition delay time. Kubota and Serizawa<sup>13</sup> reported that the addition of 3% Viton A to their Mg/PTFE propellant did not alter the burning rate. However, the MTV propellant tested here contained a higher percentage of Viton A, and the effect on the ignition delay time was obviously significant. The lower delay times are believed to be caused by the lower decomposition temperature and lower activation energy of Viton A, in comparison with those of PTFE, that was reported earlier.

## 5. PYROLYSIS AND IGNITION PRODUCT SPECIES ANALYSIS

The gaseous species evolved during the pyrolysis of PTFE and Viton A, and the ignition of the MTV propellant, were analyzed with a gas chromatograph/mass spectrometer. Tests were conducted in both an inert atmosphere and in air to investigate the role of oxygen in the ignition processes. Solid ignition products were also analyzed with a Scanning Electron Microscope.

The pyrolysis of PTFE in an inert  $N_2$  environment at one atmosphere produced the total ion chromatograph given in Fig. 10. The sample was heated twice by a heat flux of  $430 \text{ W/cm}^2$  for two seconds each time. The most abundant species evolved are  $C_2F_6$ ,  $C_2F_4$  (the monomer),  $C_3F_6$  (two isomers),  $CF_4$ , and two isomers of  $C_4F_8$ . Interestingly, the most abundant species, perfluoroethane ( $C_2F_6$ ), was not listed in a depolymerization/degradation chart for PTFE presented by Elias,<sup>18</sup> but was the most abundant compound observed in the pyrolysis of both PTFE and Viton A.

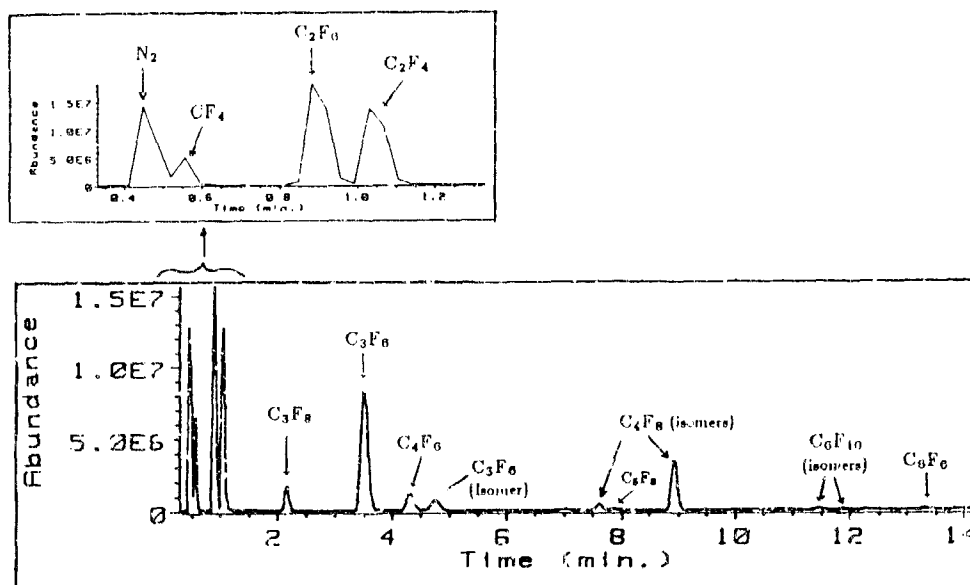


FIGURE 10. Chromatograph of the pyrolysis of PTFE in an inert  $N_2$  environment at 1 atm ( $q'' = 430 \text{ W/cm}^2$  for 2 heatings of 2 sec)

Figure 11 compares the inert pyrolysis of PTFE (shown in Figs. 10 and 11a) with the reaction of PTFE in air at 1 atmosphere. Figure 11 shows that the amounts of  $C_3F_6$  and  $C_4F_8$  decreased slightly for pyrolysis and reaction in air (Fig. 11b), compared to pyrolysis in nitrogen (Fig. 11a). The amount of  $C_2F_6$  appears to remain the same. The amount of  $CF_4$  appeared to increase in Fig. 11b, but the mass spectrometric breakdown of that peak indicated that CO and  $CO_2$  were also eluted at that time, and the three compounds could not be individually resolved. Griffiths and Robertson<sup>15</sup> reported that  $CO_2$  and  $CF_2O$  had been found by several other researchers for the reaction of PTFE in air. However, the existence of  $CF_2O$  could not be confirmed by the present apparatus. Using a microburner to study the premixed burning of several fluorocarbon-oxygen mixtures, Matula<sup>19</sup> reported significant burning of mixtures containing  $C_3F_6$  and  $C_4F_8$ . He also reported that  $C_2F_6-O_2$  and  $CF_4-O_2$  mixtures could not be ignited at one atmosphere of air. These results are consistent with the results presented in Fig. 11.

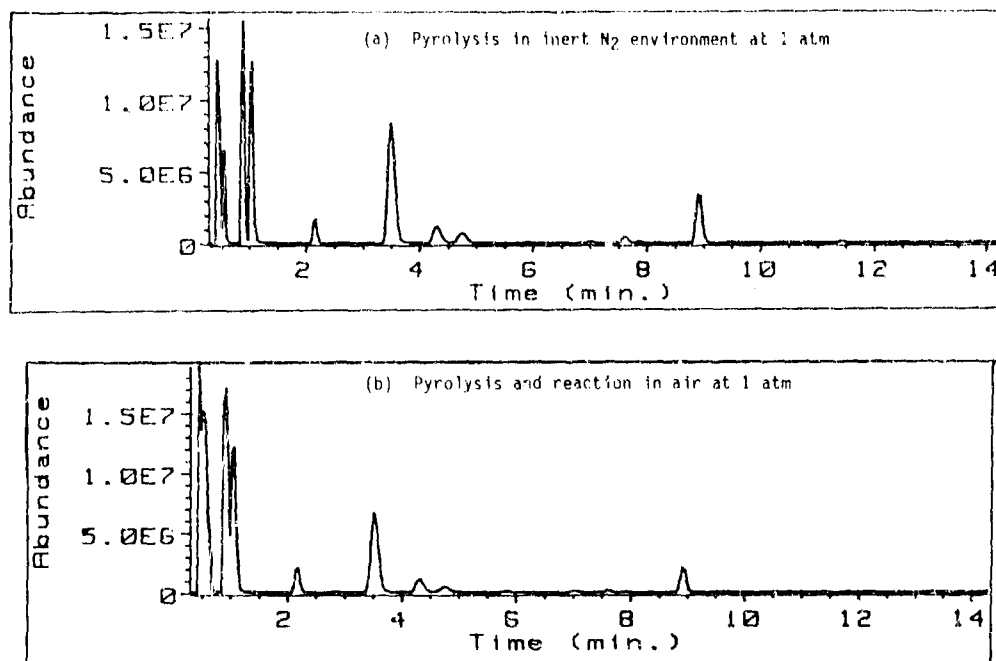


FIGURE 11. Chromatograph of the pyrolysis of PTFE ( $q'' = 430 \text{ W/cm}^2$  for 2 heatings of 2 sec)

Figure 12 gives the total ion chromatograph for the pyrolysis of Viton A in an inert  $\text{N}_2$  atmosphere. The major species evolved were  $\text{CF}_3\text{H}$ ,  $\text{C}_2\text{F}_6$ ,  $\text{C}_2\text{F}_4$ ,  $\text{C}_2\text{F}_3\text{H}$ ,  $\text{C}_2\text{F}_5\text{H}$ ,  $\text{C}_3\text{F}_4\text{H}_2$ ,  $\text{C}_3\text{F}_6$ ,  $\text{C}_3\text{F}_5\text{H}$ ,  $\text{C}_4\text{F}_6\text{H}_2$ ,  $\text{C}_5\text{F}_{10}$ ,  $\text{C}_5\text{F}_7\text{H}$ , and  $\text{C}_4\text{F}_6$ . The two most abundant species evolved were  $\text{C}_2\text{F}_6$  and  $\text{C}_3\text{F}_6$ , which were also the most abundant species, along with the monomer, that were evolved from PTFE. The similarity of products between PTFE and Viton A substantiates the claim that the effect of oxygen on the decomposition products for Viton A and PTFE may be quite similar. Interestingly, no  $\text{CF}_4$  was observed for Viton A, but a peak observed at the same time it is normally eluted contained  $\text{CF}_3\text{H}$ . A trend was observed where fluorine atoms were replaced by hydrogen atoms in some of the more common  $\text{C}_m\text{F}_n$  structures (i.e.,  $\text{C}_3\text{F}_6 \Rightarrow \text{C}_3\text{F}_5\text{H}$ ).

The chromatographs of the gaseous product species evolved for the ignition and combustion of the MTV propellant are presented in Figs. 13 and 14. Since the 5 millimeter cubes of propellant were totally consumed after ignition and the gas samples were taken after the test was over, the species analyzed were the products of sustained combustion and not just ignition. Figure 13a displays the results of tests conducted in air, and the tests for Fig. 13b were conducted in an inert nitrogen atmosphere. Magnesium compounds were not observed in the gaseous state in either case. As was seen in Fig. 11, tests run in air also produced  $\text{CO}$  and  $\text{CO}_2$  as well as most of the other products identified in the combustion in an inert atmosphere.

The rest of the peaks observed in these chromatographs establish an important point to be considered in the mechanisms of ignition and subsequent combustion of the propellant. Almost all of the species observed for combustion in both air and an inert  $\text{N}_2$  atmosphere were  $\text{C}_a\text{H}_b$

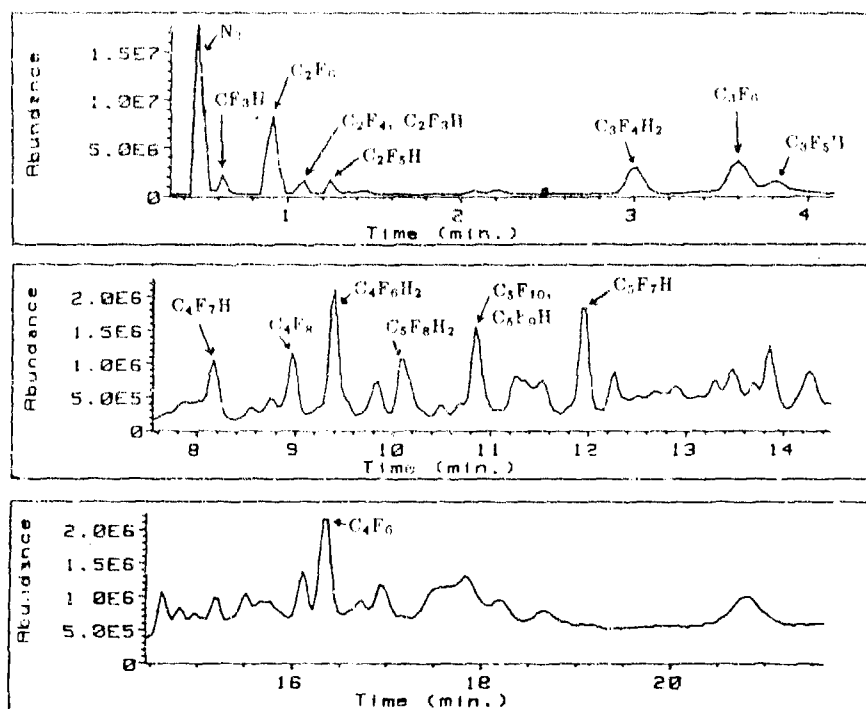


FIGURE 12. Chromatograph of the pyrolysis of Viton A in an inert  $N_2$  environment at 1 atmosphere ( $q'' = 430 \text{ W/cm}^2$  for 2 heatings of 2 seconds)

compounds, and the numerous  $C_mF_n$  and  $C_xH_yF_z$  observed in the pyrolysis of Teflon and Viton A were not found in the combustion of the MTV propellant. A probable explanation is that the primary pyrolysis species are consumed to form undetected HF or to form the observed  $MgF_2$  solid products. Also, the small peaks from 8-13 minutes observed in the inert combustion tests are not evident in the combustion in air; clearly, the combustion in an inert atmosphere is not as complete as that in air.

In Fig. 14, gas samples of the MTV propellant ignition and combustion in air were also run through a series of Porapak Q and R columns for species identification. These columns are more applicable to detecting  $C_nH_m$  compounds. However, only a few compounds of this type were detected, though, in small amounts, as well as a significant amount of CO and  $CO_2$ . These results verify the results given in Fig. 13a for the same experimental conditions using the Carboxack B/5% Fluorcol column for analysis.

X-ray diffraction analysis was also used to investigate the composition of the condensed-phase species evolved during the combustion of the propellant.  $MgF_2$ ,  $MgO$ , and carbon were detected in varying amounts, depending on the test conditions. Of course,  $MgO$  was only detected in significant amounts for the combustion in air.



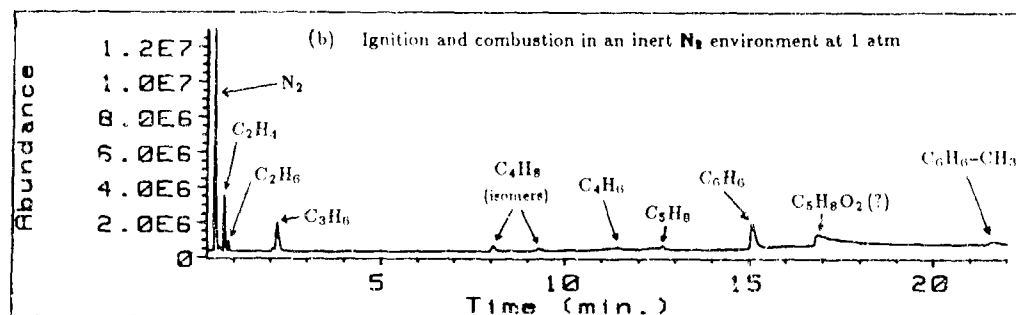
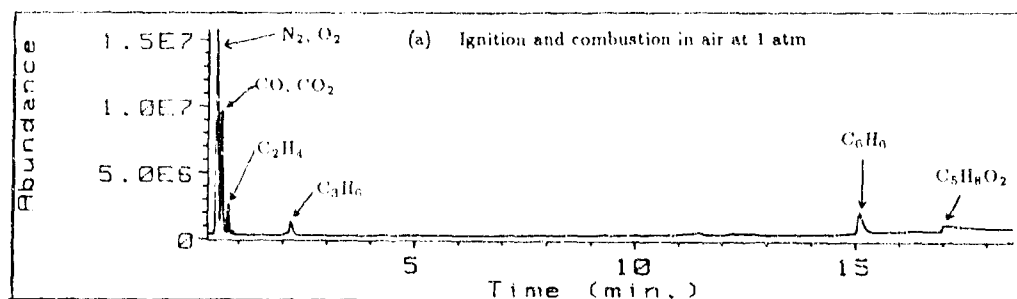


FIGURE 13. Chromatograph using Carbowack B/5% Fluorcol column to analyze the gaseous products of ignition and combustion of the MTV propellant ( $q'' = 430 \text{ W/cm}^2$ )

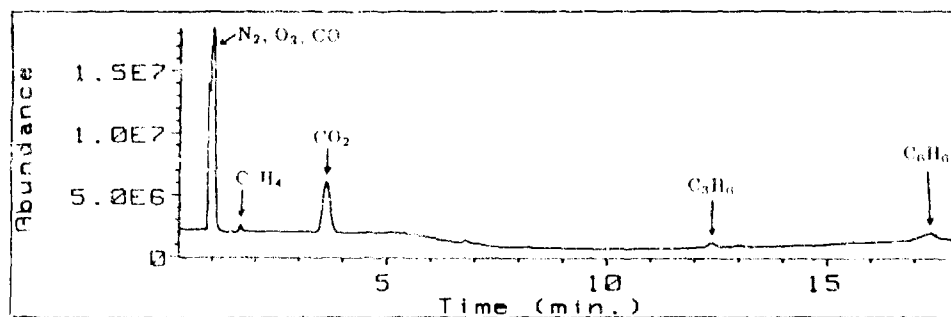


FIGURE 14. Chromatograph using a series of Porapak Q and R columns to analyze the gaseous products of the ignition and combustion of the MTV propellant in air at 1 atmosphere ( $q'' = 430 \text{ W/cm}^2$ )

## 6. SUMMARY AND CONCLUSIONS

The pyrolysis and ignition characteristics of a Mg/PTFE/Viton A igniter material were studied under radiative heating by a high-power CO<sub>2</sub> laser. The ignition sequence was recorded by both direct high-speed video photography of the flame structure and schlieren flow visualization of the gas-phase dynamics. Ignition delay times were obtained as a function of incident heat flux, pressure, and ambient oxygen concentration. A gas chromatograph/mass spectrometer was used to analyze the pyrolysis and ignition products of the test sample and its constituents.

High-speed video photography showed that ignition always occurred on the sample surface. A primary flame zone attached to the surface with a height of 1.2-1.5 millimeters was observed in both air and inert gas environments at one atmosphere. The size of the luminous gas-phase plume above the primary flame decreased with a decrease in ambient oxygen concentration for tests conducted at one atmosphere. However, at a pressure of  $\approx 0.1$  atmosphere, no evident plume evolution and gas-phase dynamics were observed, and the igniter material decomposed in large fragments.

Ignition delay times decreased monotonically as heat flux increased, pressure decreased, or ambient oxygen concentration decreased. The effect on ignition delay of adding boron or Viton A to a basic composition of Mg/PTFE was also investigated. The addition of boron significantly lowered the ignition delay time and greatly enhanced combustion. The addition of Viton A, which has a much lower decomposition temperature and activation energy than PTFE, greatly lowered the ignition delay time, which led to the conclusion that Viton A is the rate-controlling constituent for ignition of the MTV igniter material.

For combustion of the propellant in both inert N<sub>2</sub> and air environments at one atmosphere, the only gaseous product species detected were several hydrocarbons, with the addition of CO and CO<sub>2</sub> in air. However, for pyrolysis of PTFE and Viton A individually in an inert N<sub>2</sub> environment, numerous fluorocarbon species, and hydrofluorocarbons for Viton A, were detected. It was concluded that these primary pyrolysis species are consumed to form the detected hydrocarbons, CO and CO<sub>2</sub>, for combustion in air, undetected HF, and solid MgF<sub>2</sub> and carbon. These condensed phase products were identified with a scanning electron microscope. Solid MgO was also observed for combustion in air.

In summary, the MTV igniter material with the addition of boron is highly recommended for base bleed applications, due to its suitable ignition behavior under various gas and low-pressure environments.

## ACKNOWLEDGMENT

This work was sponsored by the Office of Naval Research, Contract No. N00014-86-K-0468, under the management of Drs. Richard S. Miller and Gabriel D. Roy. We would like to express our appreciation to them, and also to NWC for providing the igniter material that was used in this research.

## REFERENCES

1. Brody, F., Snelling, L., Steinle, M., "A High Volume Cost Effective Manufacturing Process for the Production of Propellant Grains for Base Burning Artillery Projectiles," 1986 JANNAF Propulsion Meeting, CPIA Publication 455, New Orleans, LA, August 26-28, 1986.
2. Sahu, J., "Supersonic Flow Over Cylindrical Afterbodies with Base Bleed," Final Report, BRL-TR-2742, June 1986.
3. Hellgren, R., "Base Bleed Projectiles: Range Calculation Program and Efficiency Comparisons," FOA-C-20516-D2, November 1983.
4. Fox, J. H., "A Generalized Base-Flow Analysis with Initial Boundary-Layer and Chemistry Effects," Final Rept., October 1, 1976-May 18, 1979, AEDC-TR-79-46.
5. Bauer, R. C., Fox J. H., "An Application of the Chapman-Korst Theory of Supersonic Nozzle-Afterbody Flows," Final Rept. July 1, 1975-Sept. 30, 1976, AEDC-R-76-158.
6. Peters, C. E., Phares, W. J., "Analytical Model of Supersonic, Turbulent, Near-Wake Flows," Final Rept. July, 1973-Dec., 1975, AEDC-TR-76-127.
7. Strahle, W. C., Hubbart, J. E., Walterick, R., "Base Burning Performance at Mach 3," AIAA Paper 81-1469, AIAA/SAE/ASME 17th Joint Propulsion Conference, July 27-29, 1981.
8. Kayser, L. D., "Effects of Base Bleed and Supersonic Nozzle Injection on Base Pressure," Final Rept., BRL-MR-2456, March 1975.
9. Kloehn, R., Rassinfosse, A., "Base Bleed Solid Propellants Containing Thermoplastic Elastomers as Binders," Joint Symposium (3rd) on Compatibility of Plastics/Materials with Explosives, Propellants, and Pyrotechnics Ingredients Processing, Phoenix, AZ, May 31-June 2, 1982.
10. Peretz, A., "Investigation of Pyrotechnic MTV Compositions for Rocket Motor Igniters," Journal of Spacecraft and Rockets, Vol. 21, 1984, pp. 222-224.
11. Peretz, A., "Some Theoretical Considerations of Metal-Fluorocarbon Compositions for Ramjet Fuels," 8th International Symposium on Air-Breathing Engines, Cincinnati, OH, June 15-19, 1987.
12. Kubota, N., Serizawa, C., "Combustion Process of Mg/TF Pyrotechnics," Propellants, Explosives, Pyrotechnics, Vol. 12, 1987, pp. 145-148.
13. Kubota, N., Serizawa, C., "Combustion of Magnesium/Polytetrafluoroethylene," Journal of Propulsion, Vol. 3, No. 4, July-Aug. 1987, pp. 303-307.
14. Chen, D. M., Hsieh, W. H., Snyder, T. S., Yang, V., Kuo, K. K., "Study of the Thermophysical Properties and Combustion Behavior of Metal-Based Solid Fuels," AIAA/ASME/SAE/ASEE 24th Joint Propulsion Conference, Paper No. AIAA-88-3041, Boston, MA, July 11-13, 1988.

15. Griffiths, T. T., Robertson, J., "Thermal Decomposition of PIFE in the Presence of Magnesium," 10th International Pyrotechnics Seminar, July 2-5, 1985, Karlsruhe, Germany.
16. Haaf, F., "Occasional Exothermic Decompositions During Processing of 'Viton' Fluoroelastomer," Dupont Bulletin VT-1001, April, 1983.
17. Siegel, R., Howell, J. R., Thermal Radiation Heat Transfer, 2nd Edition, McGraw-Hill, New York, 1981, pp. 129-137.
18. Elias, H. G., Organic and Macromolecular Chemistry, 1972.
19. Matula, R. A., Orloff, D. I., Agnew, J. T., "Burning Velocities of Fluorocarbon-Oxygen Mixtures," Combustion and Flame, Vol. 14, 1970, pp. 97-102.

## DEVELOPMENT AND PRODUCTION OF BASE BLEED GRAIN FOR 155 MM GUN

Haugen, Steinar      Melby, Knut      Oppegård, Arthur

Defence Products Division  
RAUFOSS A/S  
2830 Raufoss Norway

### 1. INTRODUCTION

Raufoss A/S first involvement in the basebleed system was production of basebleed grains for BOFORS in Sweden. The first deliveries were for 75 mm guns in 1983. Shortly after production of grains for 120 mm followed.

The baseline propellant was a composite type with hydroxylterminated polybutadiene (HTPB) binder system and with 80% ammonium perchlorate (AP).

A central patent which covers several aspects of the basebleed concept including propellant type, is a Swedish patent held by Mr. Gunners, Hellgren and Liljegren (ref. 1).

The development of the composite propellant basebleed grain was performed mainly at the Swedish National Defence Research Institute (known as FOA in Sweden).

The results from the development work are published in public reports mainly. Some of the main reports which also will serve as a source of references to other work are: Liljegrens study of the combustion of fuel-rich HTPB-propellants with ammonium perchlorate as oxidizer (ref. 2) reported in 1979, Gunners, Hellgren, Liljegren and Nilssons report dated 1979 on designing and testing of a basebleed system for 155 mm gun (ref. 3), Liljegrens report from 1980 on experience from production of composite propellant basebleed grains for 105 mm gun rounds (ref. 4), Nilsson and Sandens report from 1981 on ageing studies of HTPB composite propellants and liners for rubberbased inhibitors (ref. 5) and Schwartz' report dated 1982 on methods and results from testing of propellant mechanical properties and bond strength between inhibitor and propellant (ref. 6).

For the time being, RAUFOSS is producing composite propellant basebleed grains for 155 mm gun ammunition for BOFORS. The present production is based on a revised

concept for the basebleed system. This is a result of development work performed after a problem was encountered in upscaling to 155 mm ammunition.

## 2. INITIAL BASEBLEED DEVELOPMENT ACTIVITIES AT RAUFOS

### 2.1 Background

The initial production of basebleed grains for 75 and 120 mm guns was based on a complete data package submitted by BOFORS. There were some discrepancies with RAUFOS' production knowhow. Changes were proposed to and accepted by BOFORS. Propellant changes during that period will be described in the following.

### 2.2 Bonding Agent

The propellant contained a bonding agent. A production process for that agent was developed by Mr. Nilsson and Sanden, FCA, for HTPB/AP propellants (ref. 7). Bonding agents improve the mechanical properties of composite propellants by increasing the adhesive strength between the AP particles and the polymer, and are recognized as necessary ingredients in HTPB composite propellants.

The specified agent was a condensation product of tartaric acid and methyl-aziridyl-phosphine oxide (MAPO) which is a curing agent for carboxylterminated polybutadienes. RAUFOS proposed to use another bonding agent from the amine family of chemicals. The rationale for this change was mainly to prevent personnel from exposure to carcinogenic agents in the processing of bonding agent and propellant. The new agent, according to our knowledge, also had better ageing properties in a humid environment.

Tests were performed where propellant samples with different bonding agents were exposed to air with varied relative humidity. The shape of the samples were standard JANNAF dogbones which have a moisture diffusion web of approximately 3.5 mm. After exposure the samples were dried. The mechanical properties were measured before and after the treatment. Results are given in fig. 1.

Even this short duration test indicated differences in moisture sensitivity. When exposed to moist air, the propellant with the new bonding agent seems to be able to regain its initial properties when it is dried. The previously used bonding agent seems to become irreversibly deteriorated after exposure to moisture, but is less sensitive to shorttime exposure. This difference in properties is important to realize when establishing procedures for handling of grains during processing and by the user.

However, moisture access to composite propellants is always a problem when mechanical properties are concerned. This is illustrated by fig. 2. It is a plot of the relation between mechanical properties of a propellant versus relative humidity in the air with which the propellant is in equilibrium. The propellant contains the amine bonding agent.

### 2.3 Antioxidant

A number of antioxidants are available for HTPB. RAUFOSSE produce a number of propellant formulations, and strive for a reduction of the number of chemicals stored inhouse for economical reasons. We proposed to change the antioxidant in the basebleed propellant.

Ageing tests at elevated temperature were performed to verify that no reduction in propellant shelflife was introduced by these changes in the formulation. The effect of humidity on ageing was included in the tests. Propellant samples were stored in contact with air with a range of different relative humidities up to 75%.

## 3. DEVELOPMENT OF BASEBLEED GRAIN FOR 155 MM GUN

### 3.1 Problem definition and development resources

Inside the gun barrel the grain is exposed to an environment with extreme deformation potential. Deformation of the grain is a result of the combined forces from gas pressure and linear and rotational acceleration. A main design goal for basebleed systems consequently is to avoid that the grain is strained beyond its failure limits.

A strain problem was encountered in the 155 mm basebleed unit with unchanged propellant and upscaled grain configuration.

At RAUFOSSE a propellant development program was initiated. A problem in propellant development was that the deformation forces acting on the grain was of a magnitude far outside the range of normal test equipment as to deformation rates and pressures.

BOFORS had access to special test equipment and simulation computer programs, which to some degree gave valid data. But final verification of the quality of the basebleed grains could only be proved by expensive gun testing.

BOFORS solved the problem for the ongoing production of basebleed systems for 155 mm gun by special mechanical designs combined with a slightly modified baseline propellant. RAUFOSS continued the development of the propellant for a possible revision of the basebleed system in the future.

### 3.2 Description of special test equipment

BOFORS has equipment to test propellant samples exposed to high rate of compression. Small cylinders are compressed at a predetermined rate. A number of samples are compressed to different preset values with registration of load vs. compression. After the test, the samples are visually inspected to determine cracking. In this way the failure limits for a propellant are established.

An example of compression force versus deformation curves is given in fig. 3. In this example the line represents test data for a sample which is compressed 64% of its initial height. The points in squares are calculated from uniaxial tensile test data, and agrees very well with the experimental curve up to about 35% compression.

The Swedish government has special equipment for testing of propellant grains exposed to axial acceleration of the same magnitude as in the guns, and subsequent retrieval of the grain for visual inspection. Fig. 4 is a sketch of this equipment. Its main components are a 120 mm gun and a long tube. The projectile, which contains the test object, is fired into the tube, and braked by the air in front of it. The compressed air is vented out at a rate giving an unharmed retardation of the test object.

Fig. 5 is a test projectile with a basebleed grain. To measure maximum deformation during acceleration, a witness rod is positioned in the grain bore. It is covered with wet paint which will be transferred to the grain where contact has been established during the test. By varying the witness rod diameter, the deformation can be registered. The grain also is visually inspected for cracks after the test. Limitations in this tests validity for what is happening in gun firings, are the lack of rotation and exposure to gas pressure.

The high rotation rate of spin-stabilized projectiles may have an influence on the burning characteristics of a basebleed grain. Possible effects of propellant changes were tested on BOFORS' spinstand. Fig. 6 are examples of pressure - time traces for baseline propellant grains burned with and without rotation. In this example the rotation increases the pressure in the middle of the burntime.



### 3.3 Propellant development

The main goal for the propellant development was to improve the mechanical properties. The main limitations to be observed in the development are the requirement of fuelrich propellant (max. 80% solids) and stable burning at low pressure which as a general rule determines a lower limit for oxidizer content.

The initial studies were mainly variation of particle size distribution and cure level. Binder system was not changed. This is conventional techniques, and will not be discussed here. The novel parameter we introduced, is the use of fibers to obtain a tougher propellant.

Previous use of fibers is described by L.J. Van de Kieft et.al. (ref 7). In 1982 published investigations on the effect of fiber reinforcement of gun propellants.

Screening activities comprises of mixing in a 1 gallon mixer to obtain processing data, dogbone samples for tensile testing and strands for burning testing. Some promising formulation has been tested by BOFORS in the special test equipment for basebleed grains.

Different fiber types of short fibers, some coated types, has been added to AP/HTPB propellants. We have found that just very small additions of fibers to propellants with low solids loading has a significant effect on the mechanical properties of the propellant. Some may have an effect on burning properties.

As an example we have chosen some effects of carbon fibers added to the baseline propellant for the basebleed system. Fig. 7 - 9 are plots of the effect of carbon fiber concentration on mechanical properties. Fig. 10 - 12 are plots of carbon fiber length vs. mechanical properties.

Fig. 13 demonstrates the effect of fibers in high rate compression tests. Four samples are compressed to different degrees. The broken line represents the baseline 80% solids propellant.

Basebleed grains with 0.2 % carbon fibers were burned in BOFORS' spin-stand. Carbon fibers did not have asignificant effect on burning properties on neither static nor rotating grains.

### 3.4 Conclusions

Fiber addition. Small amounts of well distributed fibers added to a composite propellant with low solids loading have a significant effect on mechanical properties. Variation of fiber type, size, coating and amount added is a powerful tool in tailoring mechanical properties of such propellants.

Burn tests of 155 mm grains on spinstand revealed no significant change in the burning properties when carbon fibers was added to the propellant.

Propellant for 155 mm basebleed. The ongoing production is a slightly modified baseline propellant without fibers. The grain overstraining problem was solved by BOFORS by introducing a special mechanical design.

#### 4. PRODUCTION OF BASEBLEED GRAINS FOR 155 MM GUN AT RAUFOSS

Fig. 14 is a flowchart for the present basebleed grain production at RAUFOSS. A blend of coarse and ground AP is mixed with polymer, additives and curing agent in a 300 gallon Baker-Perkins vertical mixer. Propellant is cast and cured according to standard procedures.

Grains are machined to correct dimensions and inhibited with curable inhibitor according to RAUFOSS processes. Special production equipment was designed and built by RAUFOSS for the production of basebleed grains for 155 mm gun ammunition.

Quality control of the propellant and the grains are testing of

- Mechanical properties
- Burn rate at ambient pressure and no rotation
- Peel test of propellant/inhibitor bond
- Weight and dimensions.

#### REFERENCES

1. Swedish patent no. 340.076:  
N-E Gunners, R.V.Hellgren, T.Liljegren,  
Kanonprojektil med anordning för ökning av dess skottvidd.
2. Torsten Liljegren, Bert Anderson,  
Forbränningsegenskaper för bränslerika HTPB-krut  
med ammoniumperklorat (AP) som oxidator,  
FOA-rapport C 20299-D1, Mars 1979.
3. Nils-Erik Gunners, Rune Hellgren, Torsten  
Liljegren, Yngve Nilsson, Basflödesaggregat för 155  
mm SGR M/77 för haubits F, FOA-rapport C 20305-D3  
Maj 1979.
4. Torsten Liljegren, Erfarenheter från tillverkning  
av krut för basflödeladdningar till 105 mm STGR M  
40/74, FOA-rapport C 20350-D1, April 1980.

5. Bengt Nilsson, Roland Sanden,  
Åldringsundersökningar av HTPB-baserade  
kompositkrut och bindeskiktmaterial, FOA-rapport C  
20405-D1, April 1981.
6. Anders Schwartz, Provning av basflödesladdningar,  
FOA-rapport C 20452-D1, April 1982.
7. Bengt Nilsson, Roland Sanden, Framställning av ett  
medel som ökar hållfastheten hos kompositkrut med  
hydroxylterminerad polybutadien (HTPB) som  
bindemedel, FOA rapport C 20033-D1, November 1975.
8. L.J.Van de Kieft, B.J.Pacanowsky, W.W.Hillstrom,  
Fiber Reinforcement of Gun Propellants, ADPA  
Meeting, USA, May-June 1982.

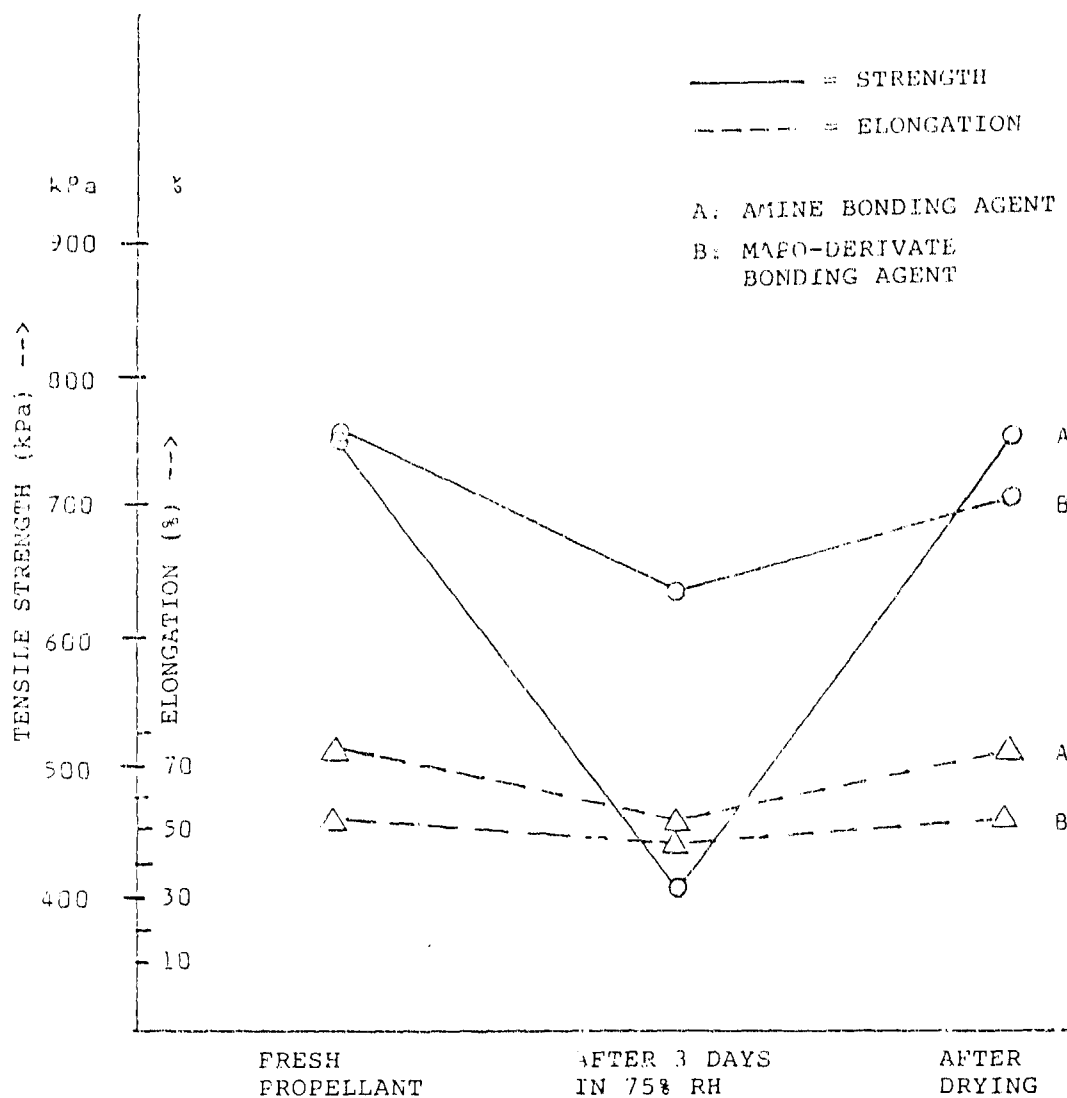


FIGURE 1. Changes in mechanical properties of 2 composite propellants with different bonding agents after short-time exposure to moist air, and after drying.  
 Sample type: Dogbones, 7 mm thickness.

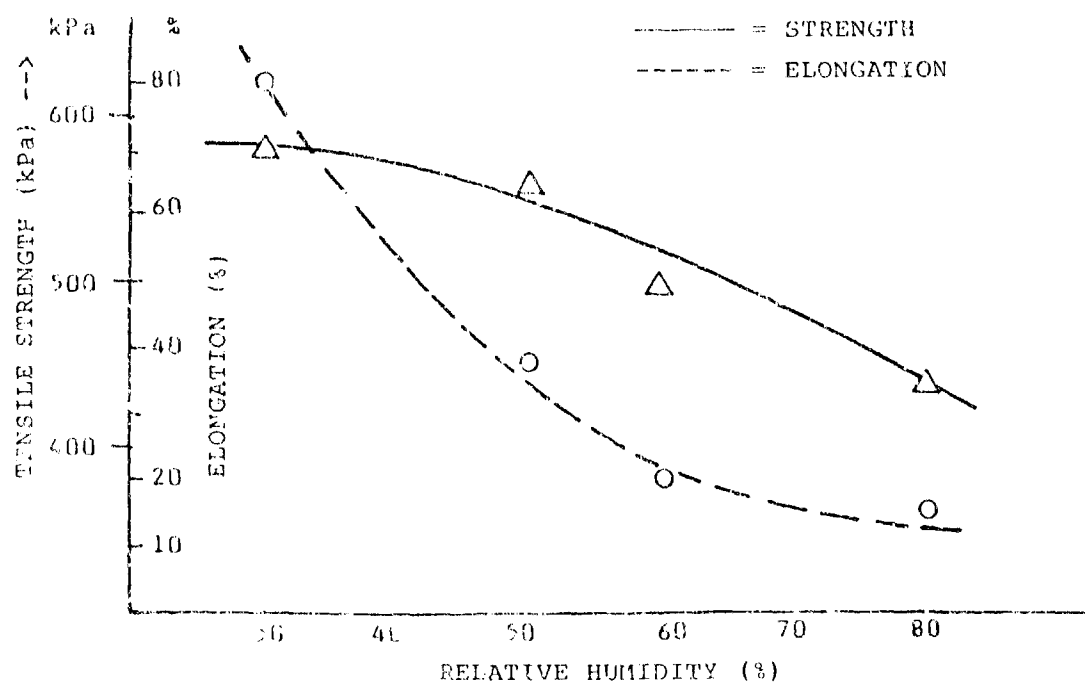


FIGURE 2. Effect of humidity on mechanical properties of a composite propellant.

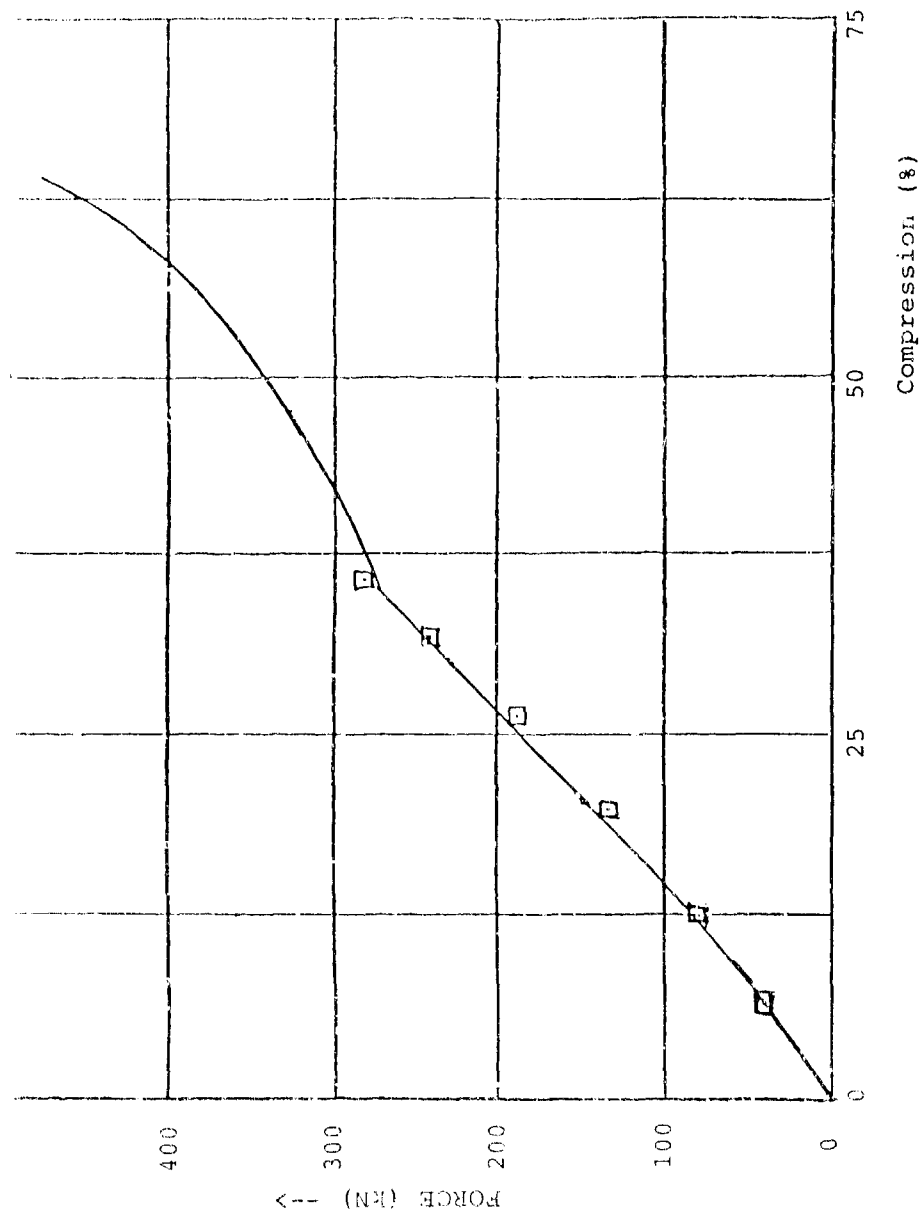


FIGURE 3 Compression force versus compression of a cylindrical propellant sample. (Rate: 500% per second, temp. 65°C).  
 □ Calculated values based on tensile testing of dogbone samples.

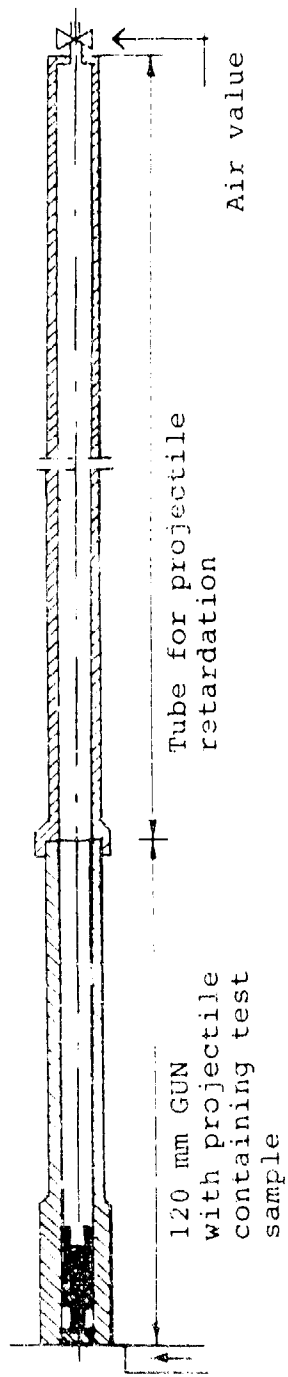
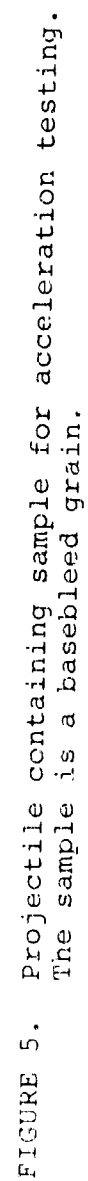


FIGURE 4. Acceleration testing arrangement.





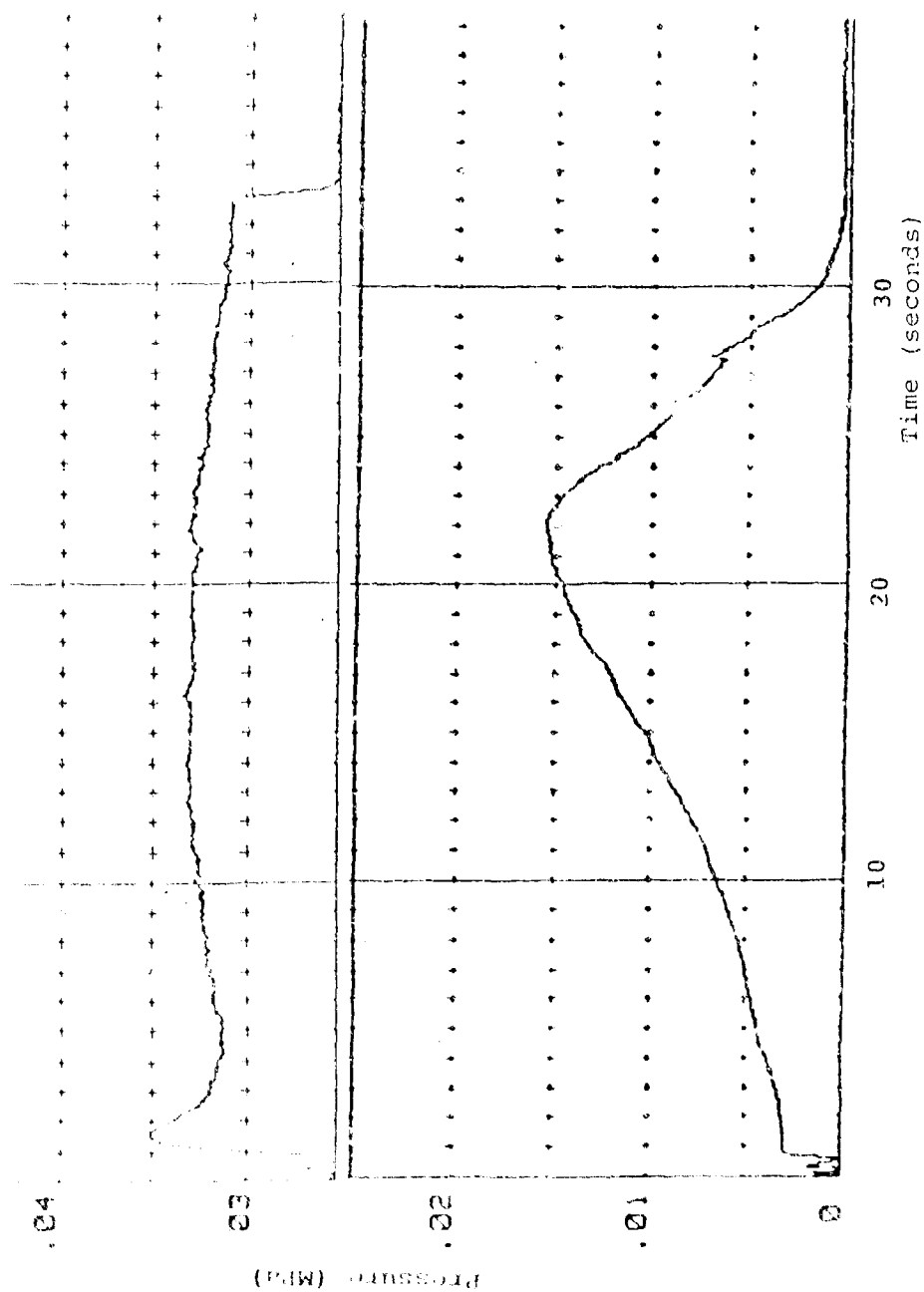


FIGURE 6. Overpressure versus time traces for burning of 155 mm gun basebleed grains at sea level pressure and 20°C.  
Upper: Static test.  
Lower: Rotation test, 16000 rpm.

FIG. 7

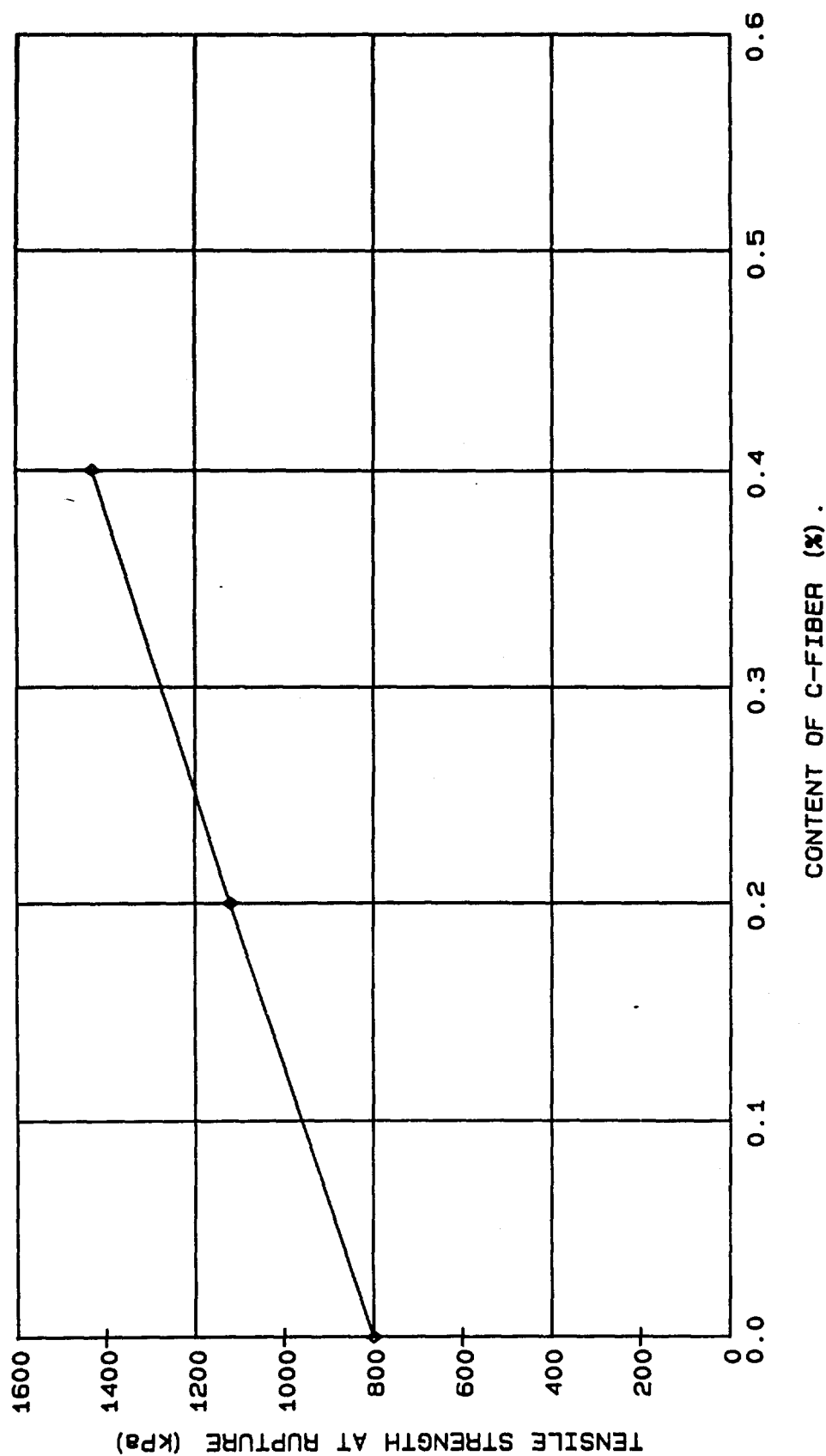


FIG. 7 TENSILE STRENGTH (AT RUPTURE) VERSUS CONCENTRATION OF C-FIBERS  
IN COMPOSITE PROPELLANT (6 MM FIBERS, TEMP. = 20 C)

FIG. 8

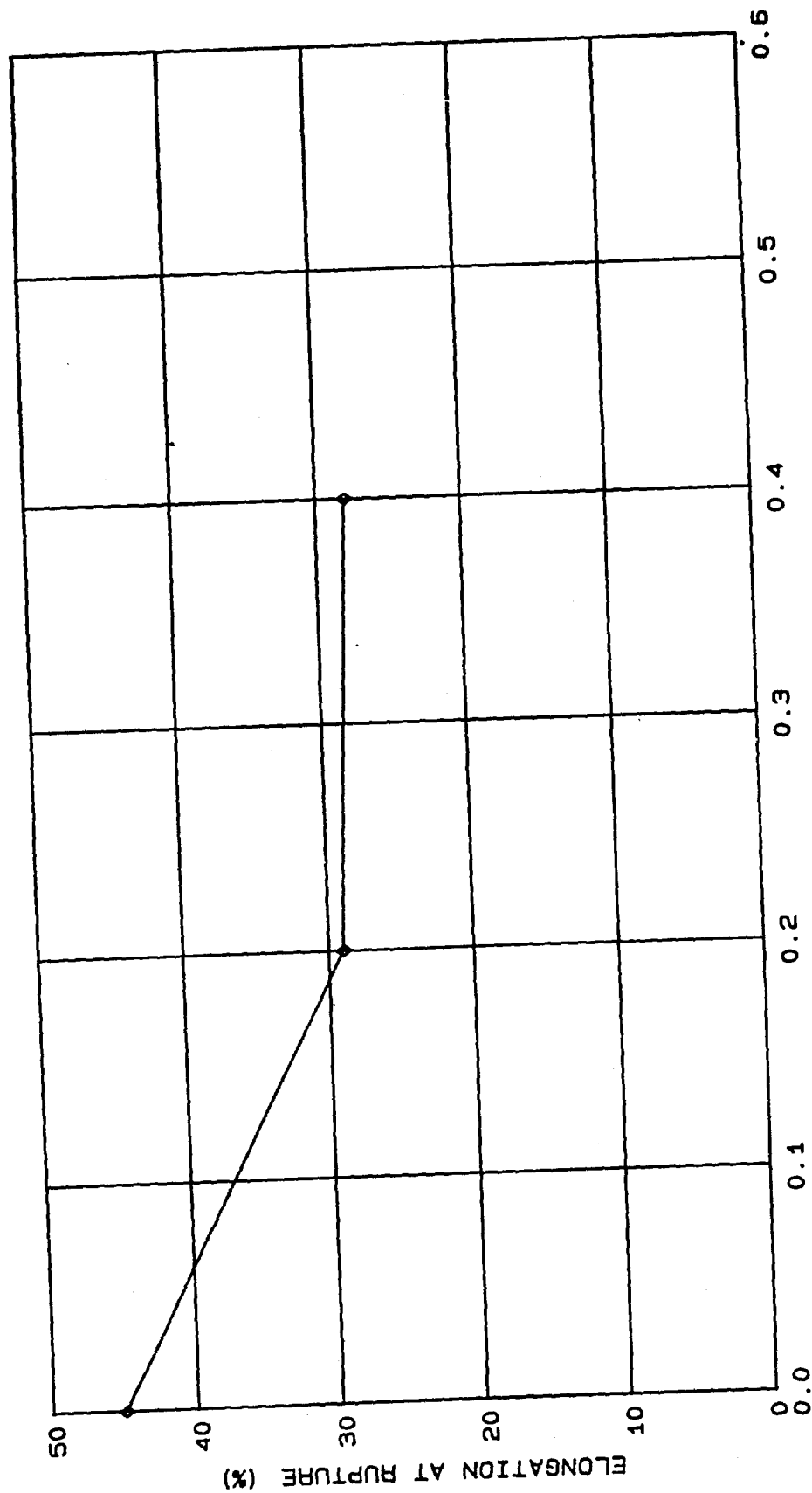


FIG. 8 ELONGATION (AT RUPTURE) VERSUS CONCENTRATION OF C-FIBER IN COMPOSITE PROPELLANT (6 MM FIBERS, TEMP. = 20 C)

FIG. 9

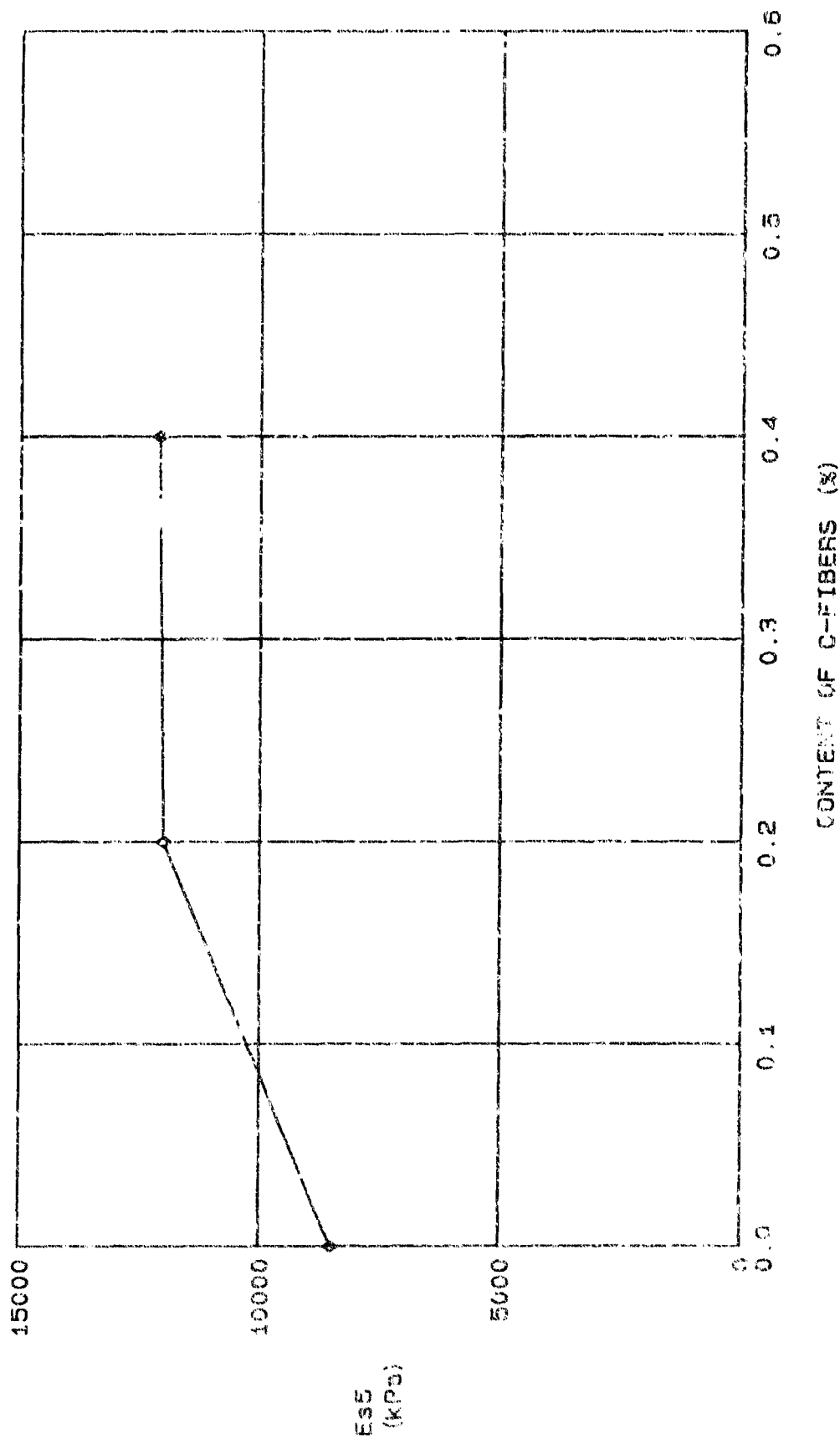


FIG. 9. MODULUS OF ELASTICITY (AT 5 % ELONGATION) VERSUS CONCENTRATION OF C-FIBER IN COMPOSITE PROPELLANT (6 MM FIBERS, TEMP. = 20 °C)

FIG. 10

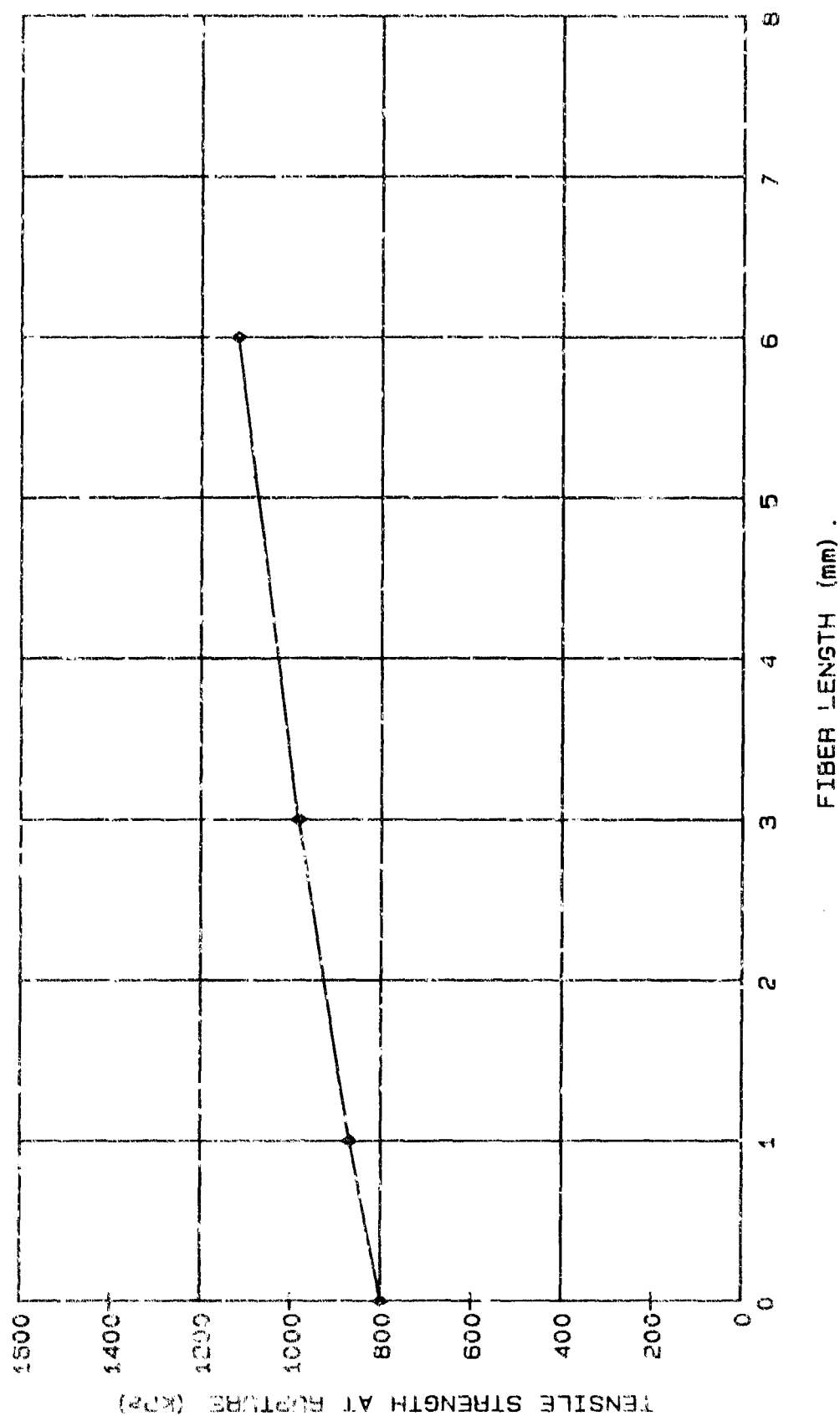


FIG. 10 MAXIMUM TENSILE STRENGTH VERSUS LENGTH OF C-FIBERS IN COMPOSITE PROPELLANT (CONS. OF FIBERS = 0.2 %, TEMP. = 20 C)

FIG. 11

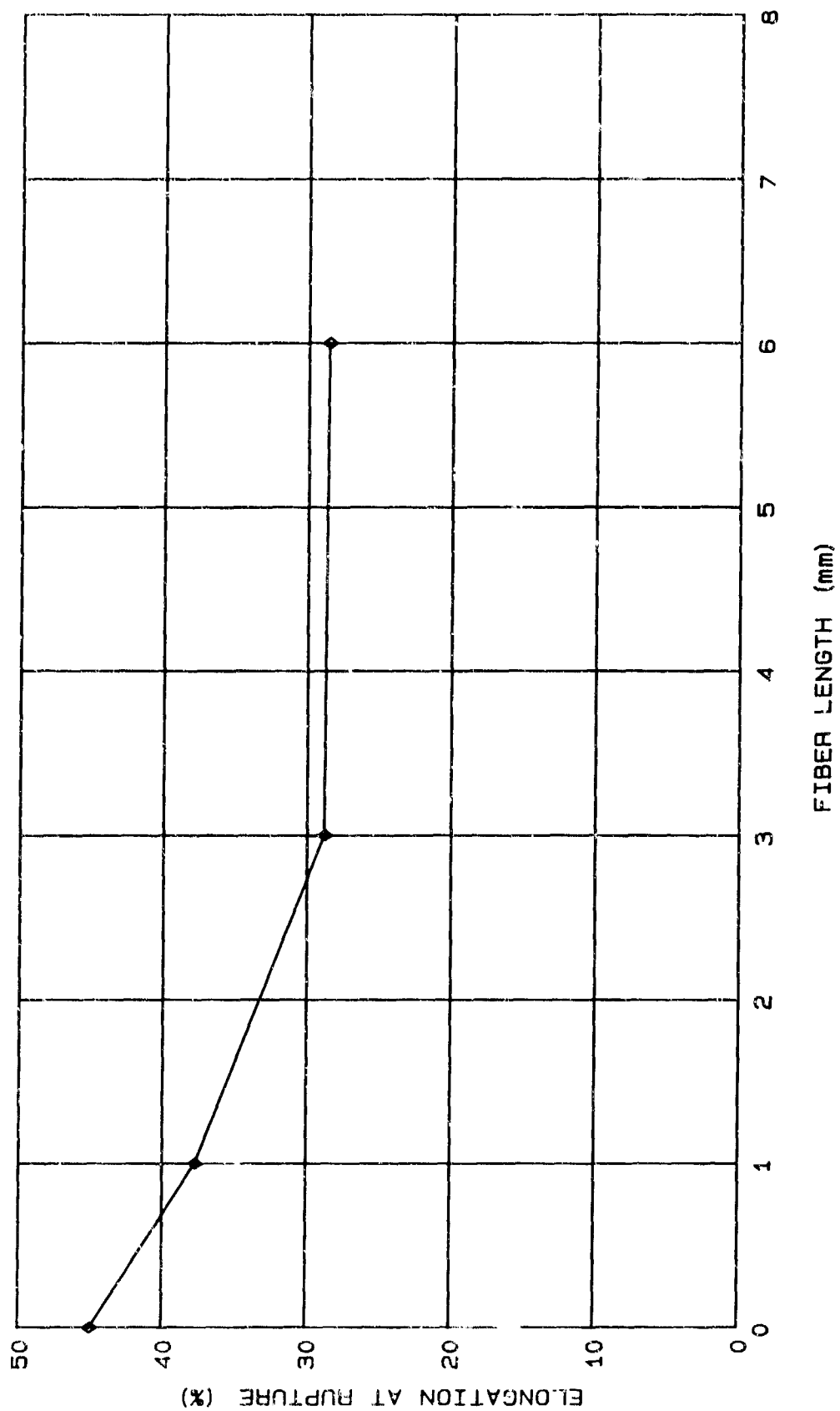


FIG. 11 ELONGATION (AT RUPTURE) VERSUS LENGTH OF C-FIBERS IN COMPOSITE PROPELLANT (CONS. OF FIBERS = 0.2 % . TEMP. = 20 C)

FIG. 12

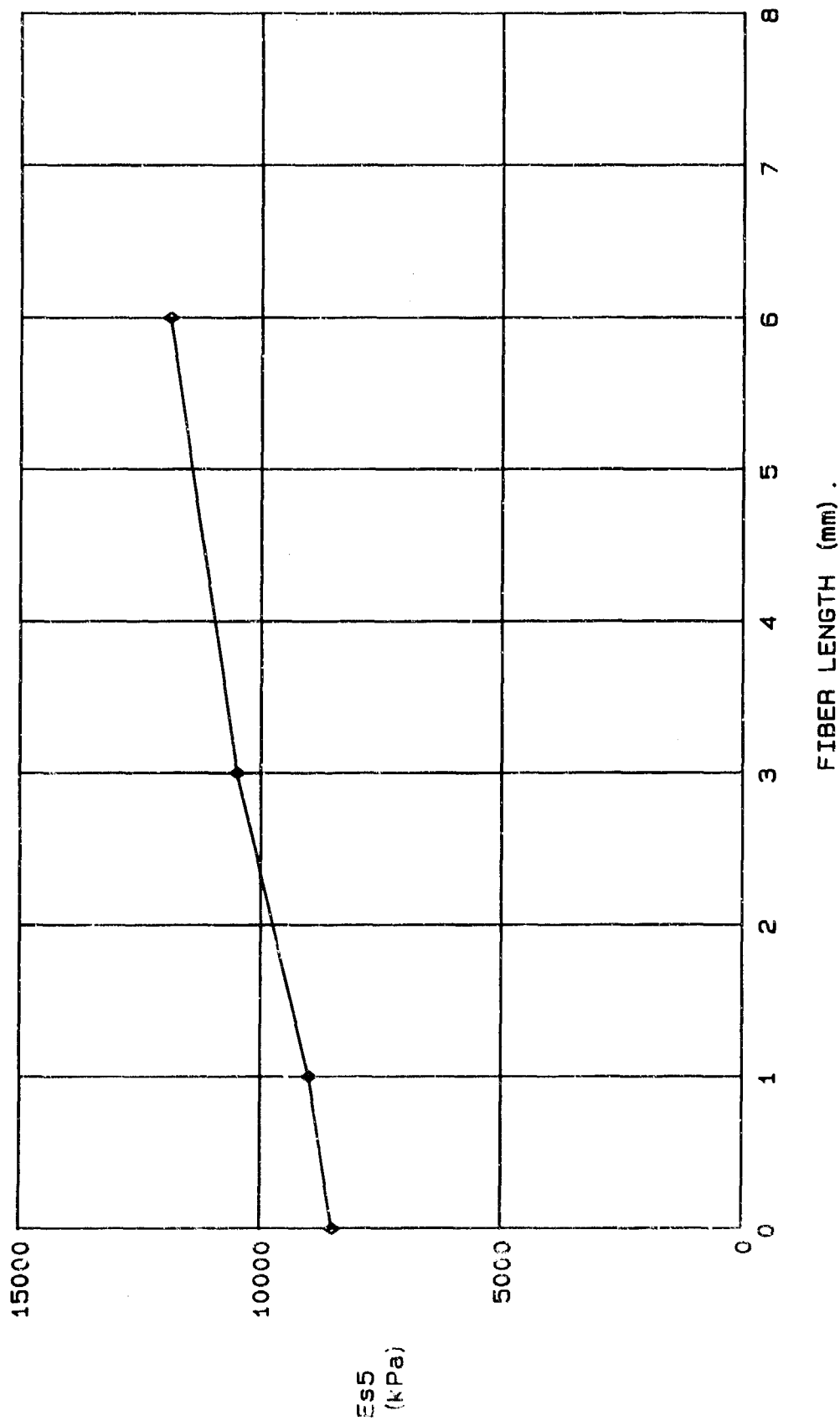


FIG. 12 MODULUS OF ELASTICITY VERSUS LENGTH OF C-FIBERS IN COMPOSITE PROPELLANT (CONS. OF FIBERS = 0.2 %, TEMP. = 20 C)

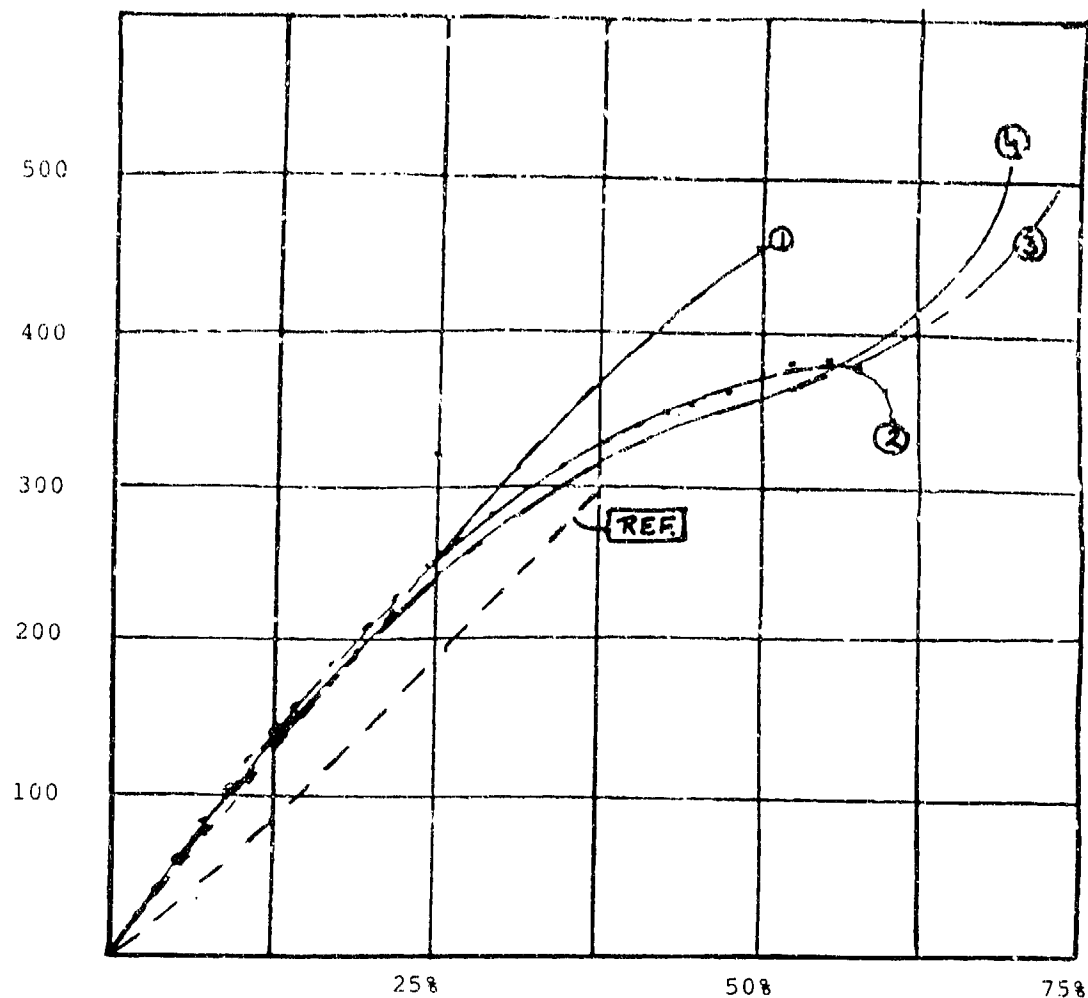


FIGURE 13. High-speed compression (500%/min) reinforced propellant samples. Broken line represents baseline propellant.

1 : 50% compression, no cracks.

2-4: 56-70% compression, cracks.



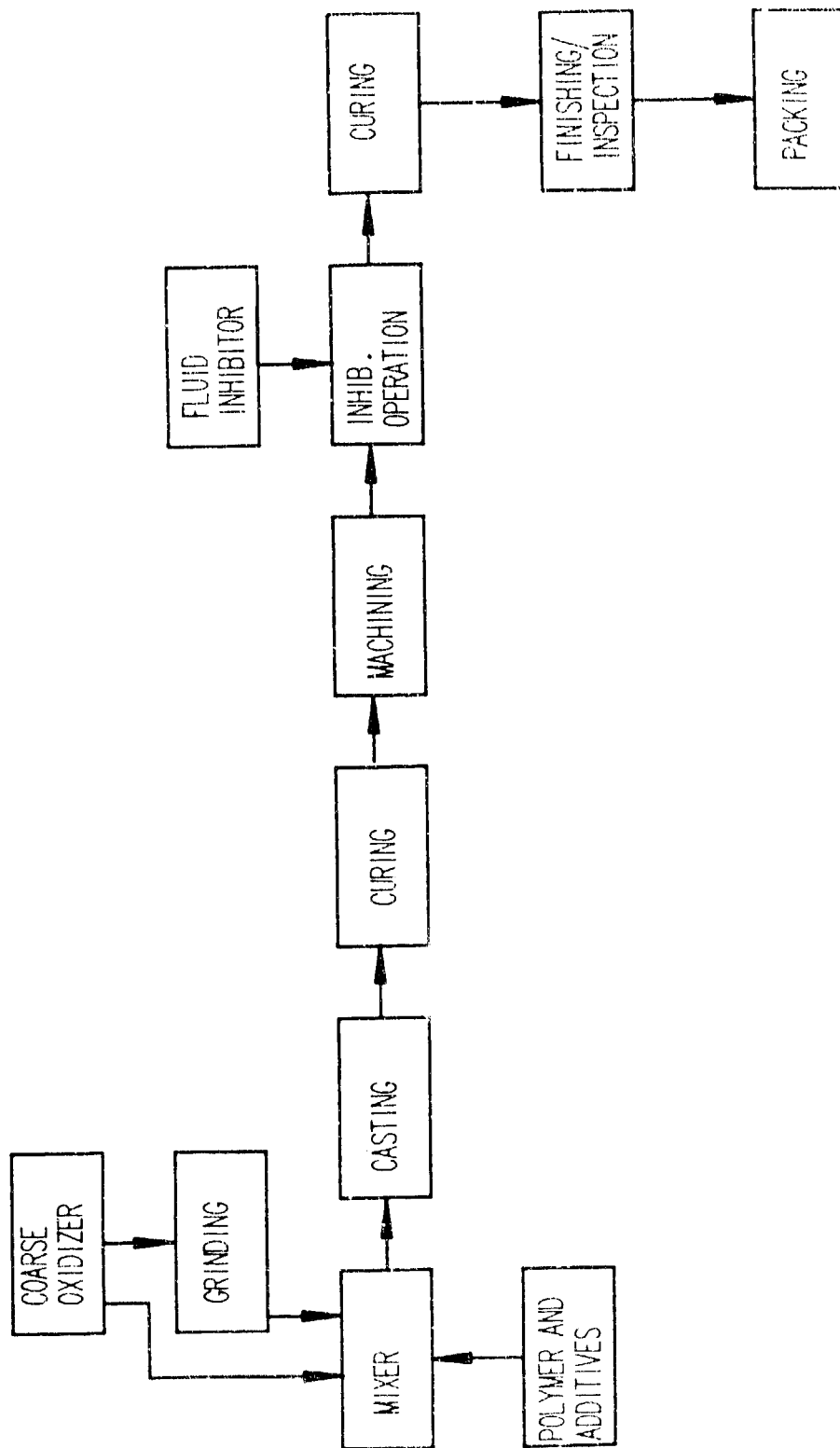


FIGURE 14. Process Flow Chart for BASEBLEED Grains.

# A REVIEW OF THE FLUID DYNAMIC ASPECT OF THE EFFECT OF BASE BLEED

J. Sahu  
Aerospace Engineer  
Computational Aerodynamics Branch  
U.S. Army Ballistic Research Laboratory  
Aberdeen Proving Ground, MD 21105

and

W. L. Chow\*  
Professor of Mechanical Engineering  
Department of Mechanical and Industrial Engineering  
University of Illinois at Urbana-Champaign  
1206 West Green Street  
Urbana, IL 61801

## ABSTRACT

The fluid dynamic aspect of the effect of base bleed is briefly reviewed. Earlier understandings on the basis of interaction between the viscous and inviscid streams can adequately explain the three different flow regimes as results of base bleed. The effect of energy addition to the wake has also been ascertained from this approach. With the detailed numerical computations of the flow by solving the Navier-Stokes Equations becoming available, the effect of base bleed can be illustrated by providing appropriately boundary conditions of the bleed at the base.

## INTRODUCTION

Flow studies on the pressure prevailing behind the blunt based bodies in flight have been prompted by the considerable importance in its practical applications. Since this pressure--the base pressure, is usually much lower than that of the free stream, it constitutes a major portion of the overall drag experienced by the body. Although early studies of low speed flow around blunt based bodies tended to be overshadowed by the phenomenon of vortex shedding, research initiated since the advent of high speed flight resulted in a slow unraveling of the processes and mechanisms which control and establish these flows. The essentially inviscid external stream establishes and determines the overall flow pattern including the low pressure prevailing within the major portion of the wake. On the other hand the viscous flow processes, such as the jet mixing along the wake boundary, recompression at the end of the wake and the ensuing process of flow redevelopment, establish and determine the "corresponding inviscid body geometry." Thus, a low base pressure is the result of the strong interaction between the inviscid and viscous flows; the latter being attached to the inviscid flow in the sense of the boundary layer concept. Naturally the method of controlling and reducing the base drag becomes also part of these investigations.

\*Present Address: Department of Mechanical Engineering, Florida Atlantic University, Boca Raton, FL 33431

One of the effective ways of reducing the base drag is to increase the base pressure through base bleed. It has been learned that by bleeding a certain amount of relatively hot fluid in the wake, the base drag can be reduced. It is the intention of this paper to present a brief review on the fluid dynamic aspect of the base bleed. Flow models for such studies and the influence of base bleed from the early crude analyses up to the sophisticated approach through solving the Navier-stokes equations are presented in the following sections.

#### STUDIES ON THE BASIS OF STRONG INTERACTION

Nearly three decades ago, the second author had the opportunity of examining the effect of base bleed with a small scaled model (Fig. 1) simulating a projectile in supersonic flight [1]. For increasing stagnation pressures of the bleeding jet issuing from the center portion of the base into the wake, it was learned that three distinctly different flow regimes exist (Fig. 2). Starting from the no-bleed condition, where a low base pressure prevails throughout the base-wake region, the base pressure would increase as the stagnation pressure of the base bleed increases. Under this condition, all the mass of bleed is entrained into the mixing region along the wake boundary of the slip stream, and the flow condition (indicated as Regime I) is depicted in Fig. 3. This trend of increase of the base pressure persists until a maximum base pressure is reached. Thereafter, as the stagnation pressure increases, the momentum of the bleed is strong that the part of the jet can overcome the high pressure prevailing at the end of the wake as a result of flow-recompression, and the base pressure would decrease. This type of flow pattern is shown in Fig. 4 (identified as Regime II). The base pressure would continue to decrease as the stagnation pressure of the base bleed increases until a relative minimum is reached. Thereafter for higher stagnation pressure ratios, the jet is so strong that it becomes a supersonic stream itself and the base pressure increases again relative to the pressure of the slip stream. The flow pattern pertaining to this region (Regime III) of the flow is depicted in Fig. 5. The interaction between the two supersonic streams is such that an equilibrium base pressure is reached. In Fig. 5b, where detailed flow field at the end of the wake is shown, the slip stream is pumping out a certain amount of fluid from the wake while the jet stream is feeding an equal amount into the wake so that an equilibrium situation can be maintained. For unusually high jet stagnation pressure ratios, the base pressure may even be higher than that of the approaching free stream, and the plummig jet may even cause separation of the slip stream away from the wall ahead of the base (plum-induced separation).

The above description on the effect of base bleed has been observed and supported by many experimental investigations [2-5]. The theoretical description and explanation of the phenomena [1] were based on a simple, crude, yet effective component analysis originally developed by Korst [6]. By studying the constant pressure turbulent mixing process in conjunction with an "escape" criterion at the end of the wake, an equilibrium base pressure solution can be reached by imposing the principle of mass conservation within the wake. Although this study [1] was carried out with a two-dimensional model with a supersonic slip stream, it is equally applicable to an axisymmetric configuration as the separated flow field is governed by the same flow mechanisms of viscous

interactions. It may also be conjectured that similar phenomenon also exists for other flow regimes of the slip stream.

Through a similar consideration, the effect of heat addition into the wake through conducting walls on the base pressure has also been examined [7]. Figure 6 presents a set of results for a flow past a backward facing step showing the influence of heat addition (or extraction) on the base pressure ratio without any mass addition, while Fig. 7 shows the effect of both mass and heat addition for the same problem. Experimental verification on the effect of heat addition is also presented in Fig. 8 [7]. Obviously heat addition provides the same favorable influence as the mass bleed.

The methods of analysis on viscous flow recompression and redevelopment were improved and developed later [8-12]. These more refined analyses have been employed to study base pressure problems in supersonic, incompressible and transonic flow regimes. Specifically, the study of transonic flow past a projectile based on an equivalent body concept yielded the detailed breakdown of the fore-body drag, the skin friction, and the base drag. Indeed, the base drag is always a major portion of the total drag experienced by the projectile (see Fig. 9). The merit of boattailing has also been substantiated and explained [12]. It is conceivable that the effect of base bleed may be examined with these improved analyses. Since the schemes of large scaled numerical computations have been developed, this effort has not been pursued.

#### STUDIES THROUGH SOLVING THE NAVIER-STOKES EQUATIONS

As more powerful (both in speed and memory space) digital computers become available, it is quite popular to examine flow problems by solving the Navier-Stokes equations with adequate turbulence modeling. Indeed one of the major research activities of the first author has been the study of base pressure problems with or without bleed, by solving the Navier-Stokes equations in the transformed coordinates. Upon adopting a thin-layer approximation of the transformed Navier-Stokes equation, the phenomena of base bleed in any of the foregoingly described flow regimes can be completely predicted from this approach by simply providing the appropriate boundary conditions in the base region (conditions of the bleeding jet). Results obtained by the first author and his colleagues [13-17] have supported the observed influences of the base bleed throughout all three flow regimes. Figure 10 shows the detailed streamline pattern of the flow within the regime I, where all mass of bleed has been entrained into the mixing region. It can be easily observed from this figure that i) the horizontal bleed core flow persists farther downstream within the wake for a larger mass bleed parameter ( $J$ ) before it is completely entrained into the mixing region, and ii) judging from the shade simulating the Prandtl-Meyer expansion at the corner, larger mass bleed parameter corresponds to a higher base pressure ratio. Indeed, this increase in pressure is also observed in the early phase of the bleed for the case shown in Fig. 11. Figure 11 also shows a drop in the base pressure ratio for a higher stagnation pressure of the bleeding jet (or a larger bleed parameter) which corresponds to the flow conditions within the Regime II. A detailed streamline plot does indicate that some of the bleed flow can penetrate the downstream region of a higher pressure (see Fig. 12). Figure 13 shows the case of higher jet stagnation pressure ratios, where the bleed

stream becomes a plummig jet. This is obviously the flow condition in Regime III. The base pressure increases as the stagnation pressure (or the static pressure) of the jet is increased. A detailed streamline flow pattern of the plummig jet is shown in Fig. 14. The interaction between the jet and the free stream results in a pair of recirculating bubbles in the near wake. Many other investigators have also computed the popular MICOM problem [18-20] within this flow regime.

For all these numerical computations, there is only the effect of mass bleed if the stagnation temperature of the jet,  $T_{0j}$ , equals to that of the free stream,  $T_{0\infty}$ . Should  $T_{0j} > T_{0\infty}$ , the results corresponds to the combined influences of both the mass and energy additions. Such a simulation can easily be produced by simply changing the temperature boundary condition at the bleed exit.

## CONCLUSIONS

A short review of the fluid dynamic aspect of the effect of base bleed is given. From the interactive study, it was observed that depending upon the relative level of the stagnation pressure of the bleed stream, its influence to the base pressure ratio can be classified into three distinctively different flow regimes. The effect of energy addition to the wake can also be extracted from a simple component analysis. However, since the schemes of large scaled numerical computation of the Navier-stokes equation became available, it has been shown that the effect of base bleed can be effectively simulated by providing the appropriate boundary conditions of the bleeding stream at the base. It may be anticipated that the effect of combustion by bleeding fuel into the wake may be interpreted in terms of the effects of mass and energy additions. Again, when chemical reactive computer code is incorporated into the present Navier-Stokes solver, this phenomenon can be simulated by simply specifying the concentration of various reactive species at the bleed exit.

## ACKNOWLEDGMENT

The authors are grateful to Dr. W. B. Sturek and Mr. C. J. Nietubicz at the Ballistic Research Laboratory for their continued interest and guidance on the numerical computations of the base pressure problems. The second author wishes to acknowledge the support of the U.S. Army Grant DAAL03-87-K-0010, and NSF Grant No. MSM-8603985 so that large scaled numerical computations are possible.

## REFERENCES

1. Chow, W. L., "On the Base Pressure Resulting from the Interaction of a Supersonic External Stream with a Sonic or Subsonic Jet," *J. Aero. Sci.*, Vol. 26, No. 3, pp. 176-180, 1959.
2. Fuller, L., and Reid J., "Experiments on Two-Dimensional Base Flow at  $M = 2.4$ ," *Br. RAE Report Aero*, 2569, 1956.
3. Wimbrow, W. R., Effect of Base Bleed on the Base Pressure of Blunt-Trailing Edge Airfoils at Supersonic Speeds, NACA RM A54A 07, 1954.

4. Bowman, J. E., Clayden, W. A., "Cylindrical Afterbodies in Supersonic Flow with Gas Ejection," AIAA Journal, Vol. 5, pp. 1524-1525, 1967; "Cylindrical Afterbodies at  $M_\infty = 2$  with Hot Gas Ejection," AIAA Journal, Vol. 6, pp. 2429-2431, 1968.
5. Schilling, H. (1984), "Experimental Investigation on the Base-Bleed-Effect for Body-Tail-Combinations. Proc., 8th Intern. Symp. Ballistics, Amsterdam.
6. Korst, H. H., "A Theory for Base Pressures in Transonic and Supersonic Flow, Journal of Applied Mechanics, Vol. 23, pp. 593-600, 1956.
7. Page, R. H., and Korst, H. H., "Non-Isoenergetic Compressible Jet Mixing with Consideration of its Influence on the Base Pressure Problem," Proc., Fourth Midwestern Conference on Fluid Mechanics, Purdue Univ., pp. 45-68, Sept. 1955.
8. Chow, W. L., "Recompression of a Two-Dimensional Supersonic Turbulent Free Shear Layer," Development of Mech., Vol. 6, Proc., 12th Midwestern Mech. Conf., University of Notre Dame Press, 1971, pp. 319-332.
9. Chow, W. L., and Spring, D. J., "The Viscous Interaction of Flow Redevelopment after Reattachment with Supersonic External Streams," AIAA Journal, Vol. 13, No. 12, pp. 1576-1584, 1975.
10. Chow, W. L., and Spring, D. J., "Viscid-Inviscid Interaction of Two-Dimensional Incompressible Separated Flows," J. Applied Mech., Vol. 43, Series E, Sept. 1976, pp. 387-395.
11. Chow, W. L., "Base Pressure of a Projectile within the Transonic Flight Regime," AIAA Paper 84-230, presented in the AIAA 22nd Aerospace Sciences Meeting, Reno, Nevada, Jan. 1984, also AIAA J., Vol. 23, No. 3, 1985, pp. 388-395.
12. Chow, W. L., "The Effect of Boattailing of a Projectile in Transonic Flow," Proc., of the Third Symposium on Numerical and Physical Aspects of Aerodynamic Flows, California State University, Long Beach, CA, Jan. 1985, 9-15 to 9-23.
13. Sahu, J., Nietubicz, C. J., and Steger, J. L., "Numerical Computation of Base Flow for a Projectile at Transonic Speeds," U.S. Army Ballistic Research Laboratory, Aberdeen Proving Ground, MD, ARBRL IR-02495, June 1983. (AD A130293) (See also, AIAA Paper No. 82-1358, August 1982.)
14. Sahu, J., Nietubicz, C. J., and Steger, J. L., "Navier-Stokes Computations of Projectile Base Flow at Transonic Speeds With and Without Mass Injection," ARBRL-IR-02532, U.S. Army Ballistic Research Laboratory, Aberdeen Proving Ground, MD, Nov. 1983 (see also AIAA Journal, Vol. 23, No. 9, Sept. 1985, pp. 1348-1355).
15. Sahu, J., and Nietubicz, C. J., "Numerical Computation of Base flow for a Missile in the Presence of a Centered Jet," ARBRL-MR-3397, U.S. Army Ballistic Research Laboratory, Aberdeen Proving Ground, MD, October 1984. (AD A148734) (See also, AIAA Paper No. 84-0527, January 1984.)

16. Sahu, J., "Supersonic Flow over Cylindrical Afterbodies with Base Bleed," U.S. Army Ballistic Research Laboratory, ARRADCOM, Tech. Report BRL-TR-2742, June 1986 (see also Computational Mechanics, No. 2, 1987, pp. 176-184).
17. Sahu, J., "Computations of Supersonic Flow over a Missile Afterbody Containing an Exhaust Jet," J. of Spacecraft and Rockets, Vol. 24, No. 25, Sept.-Oct., 1987, pp. 403-410.
18. Petrie, H. L., and B. J. Walter, "Comparisons of Experiment and Computations for a Missile Base Region Flow Field with a Centered-Propulsive Jet," AIAA Paper 85-1618, 1985.
19. Venkatapathy, E., C. K. Lombard, and C. C. Luh, "Accurate Numerical Simulation of Supersonic Jet Exhaust Flow with CSCM on Adaptive Overlapping Grids," AIAA Paper 87-0465.
20. Hoffman, J. J., Birch, S. F., Hopcroft, R. G., and Holcomb, J. E., "Navier-Stokes Calculations of Rocket Base Flows," AIAA-Paper 87-0466.

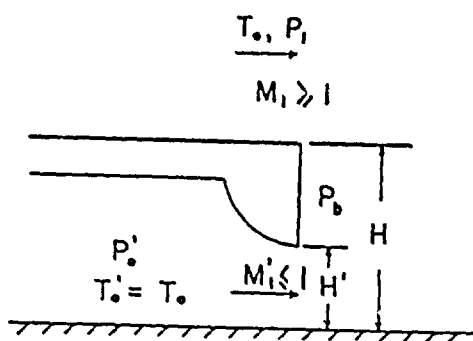


Fig. 1 Two-dimensional model

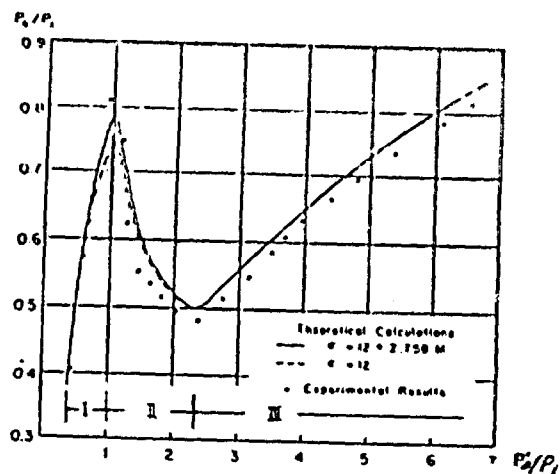


Fig. 2 The relation between  $P_0/P_1$  and  $P_0'/P_1$  for  $M_1 = 1.92$ ,  $H/H_0 = 1.94$

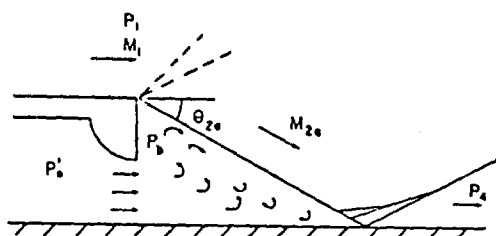


Fig. 3 Flow model for Regime 1

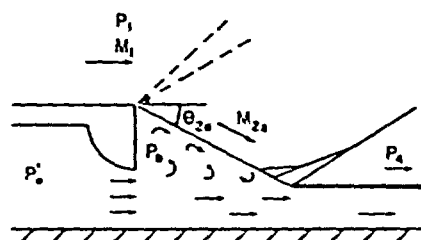


Fig. 4 Flow model for Regime 2

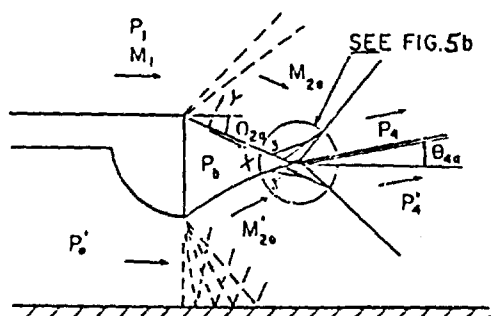


Fig. 5 Inviscid flow model for Regime III

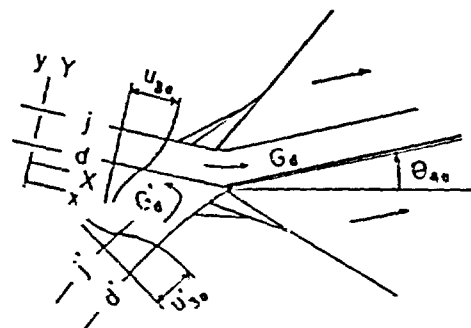


Fig. 5b Details in dissipative flow near the end of the wake



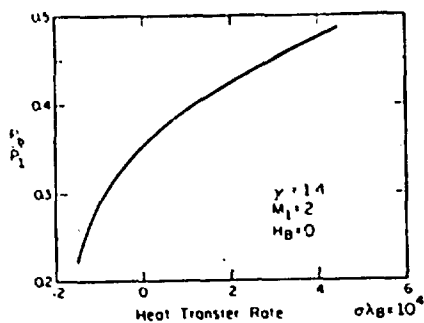


Fig. 6 The effect of heat addition on base pressure

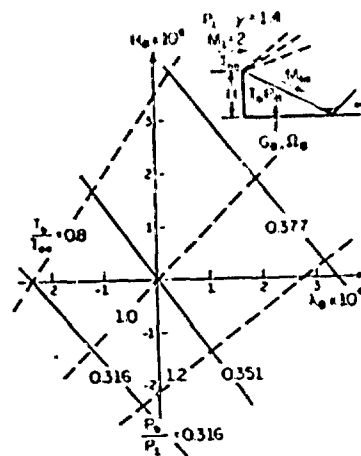


Fig. 7 The effect of both mass and heat additions

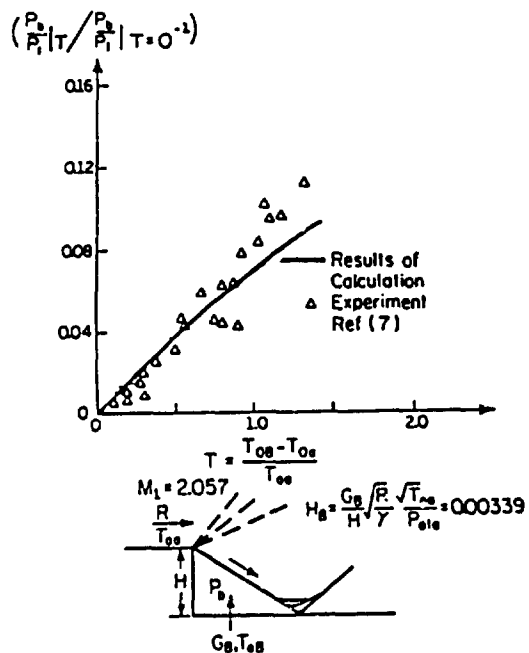


Fig. 8 Base pressure as influenced by energy addition

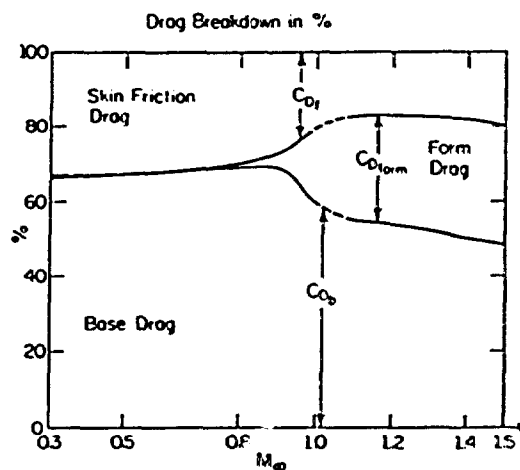


Fig. 9 Breakdown of drag characteristics of a SOC-6 projectile (based on the results obtained from Ref. [11])

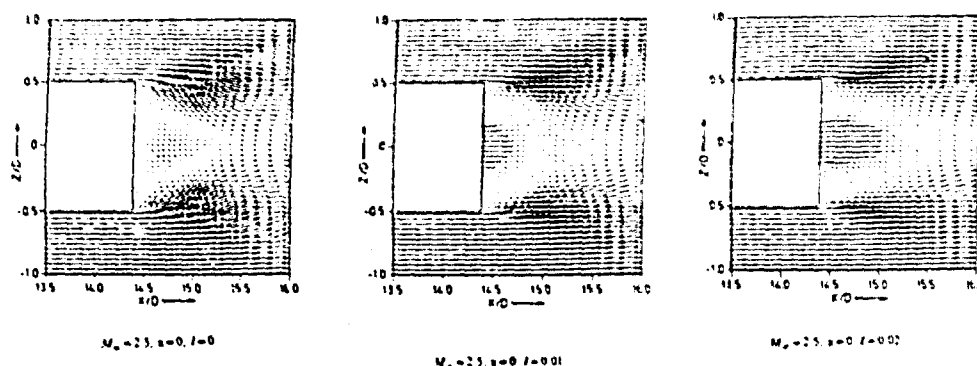


Fig. 10 Velocity vectors in the base region (from Ref. [16])

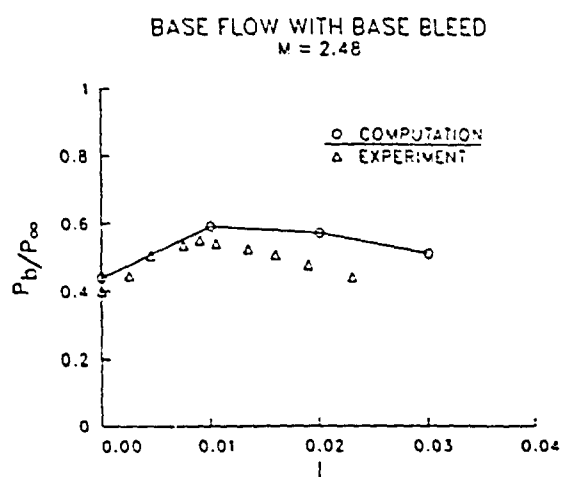


Fig. 11 Base pressure as influenced by the bleed parameter I (showing both regimes I and II)

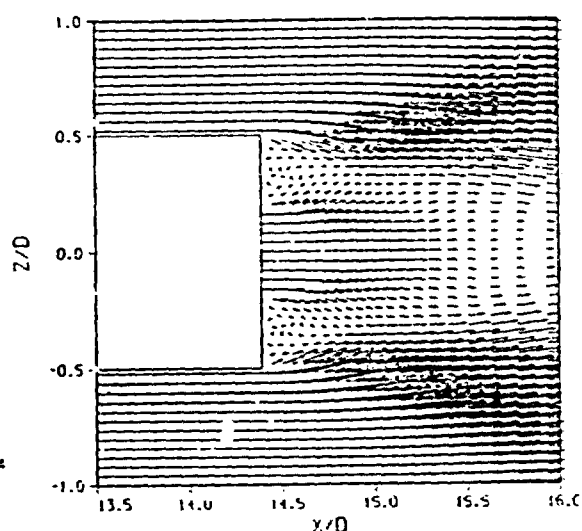


Fig. 12 Detailed velocity vectors diagram in Regime II

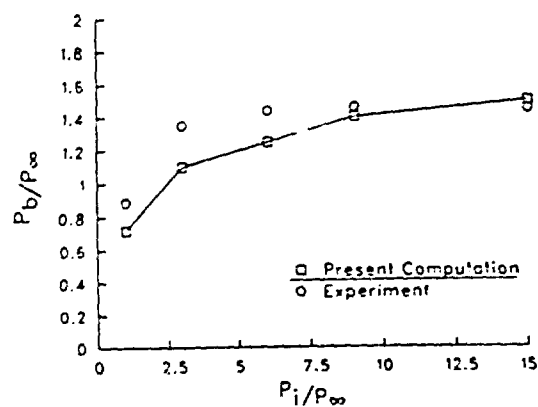


Fig. 13 Base pressure as influenced by the jet pressure ratio--Regime III

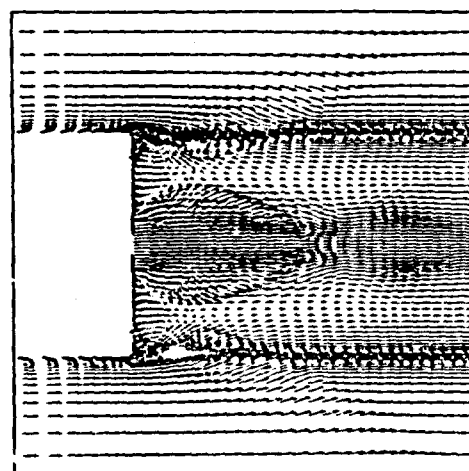


Fig. 14 Detailed velocity vectors diagram--Regime III

## NAVIER-STOKES COMPUTATIONS OF BASE BLEED PROJECTILES

Charles J. Nietubicz and Jubaraj Sahu  
Launch and Flight Division  
U.S. Army Ballistic Research Laboratory  
Aberdeen Proving Ground, Maryland 21005-5066

### INTRODUCTION

The ability to compute the base region flow field for projectile configurations using Navier-Stokes computational techniques has been developed over the past few years. This capability is most important for determining aerodynamic coefficient data and in particular the total aerodynamic drag. The total drag as described in this paper consists of the pressure drag (excluding the base), viscous drag and base drag components. At transonic and low supersonic speeds the base drag component is the major contributor to the total aerodynamic drag.

The majority of base flow calculations to date have modeled the base region as a flat solid surface. Many of the actual configurations have some form of base cavity. General opinion has been that the inclusion of a base cavity or modifications to the interior cavity of a projectile base would have little or no effect on the overall flight performance parameters. In addition to base cavities projectiles are currently being designed which include base bleed and base burning.

The M864 base burn projectile is a configuration of current interest and includes both a dome base cavity and a base burn capability. A schematic is shown in Figure 1. The shape of the M864 is similar to that of the product improved M825 which also contains a base cavity.<sup>1</sup> Very limited data exists for the M864 and the effects of both the dome base and the addition of base bleed are not well understood. Range firings have been conducted for the M864 with an inert base burn motor and active motors. Reductions in base drag of between 30-50% have been found during the 30 second motor burn.<sup>2</sup>

A Navier-Stokes computational study is in progress to determine the aerodynamic coefficients for the M864 both with and without base bleed. A flat base M864 calculation was performed to determine the effect of the base cavity. The use of Navier-Stokes codes can provide a detailed description of the flow field associated these configurations as well as the integrated aerodynamic coefficients. The work to date has been accomplished using an axisymmetric base flow code. Numerical computations have been completed for a Mach number range of  $0.7 \leq M \leq 2.5$ . The computed aerodynamic drag show a small reduction in the total aerodynamic drag for the dome configuration. Additional drag reduction was found by modeling cold mass addition in the base region. Further reduction in drag was found with hot mass injection. Qualitative features of the

## INTRODUCTION

computed flow fields are presented in the form of velocity vectors, and particle paths.

## GOVERNING EQUATIONS AND SOLUTION TECHNIQUE

### Governing Equations

The complete set of time-dependent, thin-layer, Navier-Stokes equations is solved numerically to obtain a solution to this problem. The numerical technique used is an implicit finite difference scheme. Although time-dependent calculations are made, the transient flow is not of primary interest at the present time. The steady flow, which is the desired result, is obtained in a time asymptotic fashion.

The time-dependent, thin-layer, Navier-Stokes equations written in strong conservation law form for the axisymmetric formulation<sup>3</sup> are:

$$\frac{\delta \hat{Q}}{\delta \tau} + \frac{\delta \hat{E}}{\delta \xi} + \frac{\delta \hat{G}}{\delta \zeta} + \hat{H} = \frac{1}{Re} \frac{\delta \hat{S}}{\delta \zeta} \quad (1)$$

The general coordinate transformations are defined as:

$\xi = \xi(x, y, z, t)$  - is the longitudinal coordinate

$\zeta = \zeta(x, y, z, t)$  - is the near normal coordinate

$\tau = t$  - is the time

The vector  $\hat{Q}$  contains the dependent variables  $[p, \rho u, \rho v, \rho w, e]$  and the flux vectors  $\hat{E}$ ,  $\hat{G}$  contain terms which arise from the conservation of mass, momentum and energy. The source vector  $\hat{H}$ , in Equation (1), contains terms which result from an analytic determination of the circumferential flux vector given the assumption of axisymmetric flow and constant angular velocity.<sup>3</sup> The viscous terms are contained in the vector  $\hat{S}$  which is seen to have variation in the  $\zeta$  direction only. This is representative of the thin-layer approximation.

### Solution Technique

The numerical algorithm used for the solution of Equation (1) is the Beam and Warming<sup>4</sup> implicit, approximately factored, finite-difference scheme which uses central differencing in both  $\xi$  and  $\zeta$  directions. Code improvements have been made to include a variable time step, numerical smoothing based on local solution gradients and code vectorization.<sup>5</sup> The Beam-Warming implicit algorithm has been used in various applications for the equations in general curvilinear coordinates. The algorithm is first-order accurate in time and second- or fourth-order accurate in space. Central difference operators are employed; the algorithm produces a block tridiagonal system for each space coordinate. The main computational work is contained in the solution of these block tridiagonal systems of equations.

To suppress high frequency components that appear in regions containing severe pressure gradients e.g., shocks or stagnation points, artificial dissipation terms are added. In the present application, a switching dissipation model is used which is a blend of second- and fourth-order dissipation terms. This is similar to the model used by Pulliam<sup>6</sup> which uses a fourth-order dissipation in smooth regions and switches to a second-order dissipation in regions containing high pressure or density gradients. Incorporation of this dissipation model has resulted in an improvement in the quality of the results and has made the code more robust.

The axisymmetric code that solves Equation (1) uses a unique flow field segmentation procedure to compute the full flow field over a projectile or a missile including the base region. The details of this can be found in Reference.<sup>7</sup> For the computation of turbulent flows, the two-layer algebraic, Baldwin-Lomax, turbulence model<sup>8</sup> is used over the projectile body.

#### BOUNDARY CONDITIONS

The outer computational boundary was kept at approximately 12 body diameters from the body surface. This allows free stream conditions to be imposed at the outer boundary. At the downstream boundary extrapolated outflow conditions were used.

Viscous boundary conditions were imposed on the surface using no slip at the wall. The normal momentum equation is solved at the wall for  $p_n$ , the normal pressure gradient. The free flight wall temperature is specified. Using the time lagged pressure, the density at the wall is determined.

The base bleed boundary conditions initially used were as described in Reference 9, where the bleed conditions are iteratively set. The current boundary conditions do not require iteration and follow from knowing the computed pressure and flow field variables at each time step. The bleed boundary conditions are thus lagged in time. The bleed conditions  $(\rho u)_j$ , and  $T_{0j}$  are specified while  $p_j = p_1$  is the pressure at the interface

boundary at time step  $n$ . The bleed stagnation pressure,  $p_{0j}$ , is defined

and the bleed properties of  $p_j$  and  $T_j$  are known. By specifying the mass injection rate as:

$$\dot{I} = \frac{\rho_j u_j A_j}{\rho_\infty u_\infty A_b}$$

the bleed Mach number ( $M_j$ ) can be directly solved by:

$$M_j^2 = -1 + \sqrt{1 + \frac{2(\gamma-1) a_\infty^2 T_{0j} \rho_\infty u_\infty A_b}{p_j^2 \alpha^2 T_\infty A_j}}$$

## BOUNDARY CONDITIONS

where  $A_b$  and  $A_j$  are the area of the base and bleed opening respectively. Using isentropic relations the bleed stagnation pressure  $p_{0j}$  and static temperature  $T_j$  can be calculated. Given the temperature and pressure the density is computed and the boundary conditions for the next time step are obtained.

## MODEL GEOMETRY AND COMPUTATIONAL GRID

The computational model of the M864 is shown in Figure 2. The features of this projectile which have not been modeled exactly are the meplat on the fuze and the rotating band near the base. The rotating band was eliminated. The meplat was modeled as a hemisphere cap. The model nose is a combination of ogive and conical sections. The cylindrical section is slightly undercut, and the boattail length is 0.524 calibers with a  $3^\circ$  angle. The general shape of the internal base cavity is shown as a dotted line on the boattail. The base burn motor is located internally with the exhaust port centered on the model axis.

The solution technique requires the discretization of the entire flow region of interest into a suitable computational grid. The grid outer boundary has been placed at 1.5 body lengths upstream and surrounding the projectile. The downstream boundary was placed at 2 body lengths. Since the calculations are in the subsonic/transonic regime, the computational boundaries must extend out beyond the influence of the body. This ensures that the specified boundary conditions are satisfied.

Figure 3 shows the grid generated over the projectile body including the base. It consists of 265 longitudinal points and 50 points in the normal direction. This is broken down into two sections: a body region, and a base region. The surface points for each region are selected using an interactive design program. Each grid section is then computed separately using a hyperbolic grid generation program.<sup>10</sup> Figures 4a and 4b show an expanded view for both the flat and dome base configurations. The flat base grid was routinely generated. However, due to the extreme concavity, the grid for the dome base required an increase in the smoothing values used by the hyperbolic grid generator as well as the addition of a grid cell averaging technique.

## RESULTS

A series of calculations have been run for both the flat base and the actual domed M864 with and without base bleed. The Mach number range computed was  $0.7 < M < 2.5$  with  $\alpha = 0^\circ$ . Figures 5a and 5b show the computed velocity vectors in the wake region for the flat base and domed base, respectively. The effect of the dome base is to generate a second, low speed recirculation in the recessed cavity. This recirculation bubble is in the opposite direction of the primary recirculation pattern. This is significantly different than the recirculation pattern found for the flat base and other dome base configurations.

Computations have also been performed for the dome base with the inclusion of base bleed. The mass injection parameter,  $I_j$ , defined as

## RESULTS

$I_j = \dot{m}_j / \rho_\infty u_\infty A$ ; was used to vary the mass flow rate. The computations to date have been for cold and hot mass flow, with mass injection values of up to 0.04. Using the propellant mass and a burn time of 30 seconds the estimated  $I_j = 0.004$ . Although the actual mass flow rate varies over the course of the trajectory, the present calculations were run to see the effect on drag across a Mach number range. Figure 6 shows the computed velocity vectors for the dome M864 with  $I = 0.01$ . The addition of base bleed has increased both the size and strength of the secondary recirculation region.

Recent ground tests have been completed for the spinning M864 base burn motor assembly. Pressure taps and a thermocouple were contained within the base cavity. The temperature varied as a function of spin and burn time. A maximum temperature level of 1700°F was obtained. A second set of computations were run to see the effects of hot mass addition. The results shown in Figures 7a and 7b show particle traces in the vicinity of the base region for the bleed gas temperature of 70°F and 1700°F cases, respectively. The red traces are particles which originate from the bleed ejection hole. The other colors were released in various parts of the flow field. The effect of temperature is rather dramatic in changing the recirculation pattern within the base flow field. At the lower temperature, the bleed gas is shown to be captured by the recirculation region near the base. As the temperature is increased, all of the bleed gas moves downstream. The higher temperature gives rise to an increased velocity and thus an effective increase in the mass injection parameter. The resultant effect of temperature on total drag is shown in Figure 8. The increased temperature shows a net reduction in drag across a range of mass injection rates.

Figure 9 is a plot of the computed drag coefficient,  $C_{D_0}$ , for the flat base and dome base with and without base bleed. The computed drag coefficient is the summation of the pressure, viscous and base drag components. The results show a decrease in total drag for the dome base configuration for all Mach numbers. When the base bleed is initiated a further reduction in drag is evident.

Recent tests performed in the BRL Transonic Aerodynamics Range have provided some limited drag data<sup>11</sup> for the M864. This experimental data is also shown in Figure 9. The experimental data is for the M864 without base burn using an inert burn motor. The computed results are in general agreement at the supersonic velocities, however, in the transonic and subsonic regions, the comparison is poor. The underprediction of the drag in this region has been noticed before and at present lacks a full explanation. Grid refinement studies, turbulence modeling and alternate solution techniques are currently in progress.

## CONCLUDING REMARKS

Numerical computations have been performed for the M864 projectile at supersonic and transonic speeds. The addition of base bleed with a dome base cavity has also been computed. Additional results were also obtained for hot mass addition.

The computed drag coefficients showed an overall decrease in drag between the flat and dome base configuration. An additional decrease in drag was

## CONCLUDING REMARKS

found for cold mass flow addition at the base. Further reductions were found for hot mass addition. A comparison of the computed drag and limited experimental data, for a case with no base bleed, indicates a fair agreement at the supersonic speeds. As the Mach number approaches  $M = 1$  and into the subsonic regime, the comparison becomes poor. Grid refinement work and alternate solution techniques are currently being employed in an attempt to provide more accurate solutions in the subsonic and transonic area.

## REFERENCES

1. D'Amico, W. P., "Transonic Range Testing of the 155mm M825 Projectile with Standard and Dome Steel Bases," U.S. Army Ballistic Research Laboratory, Aberdeen Proving Ground, Maryland, report is forthcoming.
2. Lieske, R. F., private communications, Firing Tables Branch, Launch and Flight Division, U.S. Army Ballistic Research Laboratory, September 1987.
3. Nietubicz, C. J., Pulliam, T. H., and Steger, J. L., "Numerical Solution of the Azimuthal-Invariant Navier-Stokes Equations," U.S. Army Ballistic Research Laboratory, Aberdeen Proving Ground, Maryland, ARBRL-TR-02227, March 1980. (AD A085716) (Also see AIAA Journal, vol. 18, no. 12, pp. 1411-1412, December 1980.)
4. Beam, R., and Warming, R. F., "An Implicit Factored Scheme for the Compressible Navier-Stokes Equations," AIAA Paper No. 77-645, June 1977.
5. Sahu, J., and Nietubicz, C. J., "Improved Numerical Prediction of Transonic Flow," Proceedings of the 4th Army Conference on Applied Mathematics and Computing, Cornell University, May 1986.
6. Pulliam, T. H., and Steger, J. L., "On Implicit Finite-Difference Simulations of Three-Dimensional Flow," AIAA Journal, vol. 18, no. 2, pp. 159-167, February 1980.
7. Sahu, J., Nietubicz, C. J., and Steger, J. L., "Navier-Stokes Computations of Projectiles Base Flow with and without Base Injection," U.S. Army Ballistic Research Laboratory, Aberdeen Proving Ground, Maryland, ARBRL-TR-02532, November 1983. (AD A135738) (Also see AIAA Journal, vol. 23, no. 9, pp. 1348-1355, September 1985.)
8. Baldwin, B. S., and Lomax, H., "Thin-Layer Approximation and Algebraic Model for Separated Turbulent Flows," AIAA Paper No. 78-257, 1978.
9. Sahu, J., "Supersonic Flow Over Cylindrical Afterbodies with Base Bleed," U.S. Army Ballistic Research Laboratory, Aberdeen Proving Ground, Maryland, BRL-TR-2742, June 1986.
10. Nietubicz, C. J., Heavey, K. R., and Steger, J. L., "Grid Generation Techniques for Projectile Configurations," Proceedings of the 1982 Army Numerical Analysis and Computers Conference, ARO Report 82-3, February 1982.



## REFERENCES

11. Oskay, V., private communications, Free Flight Branch, Launch and Flight Division, U.S. Army Ballistic Research, September 1987.

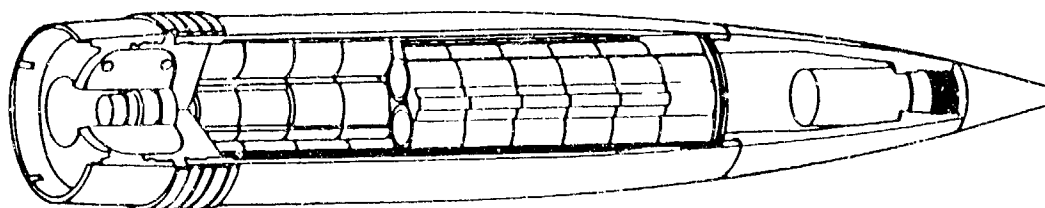


FIGURE 1. Schematic of M864

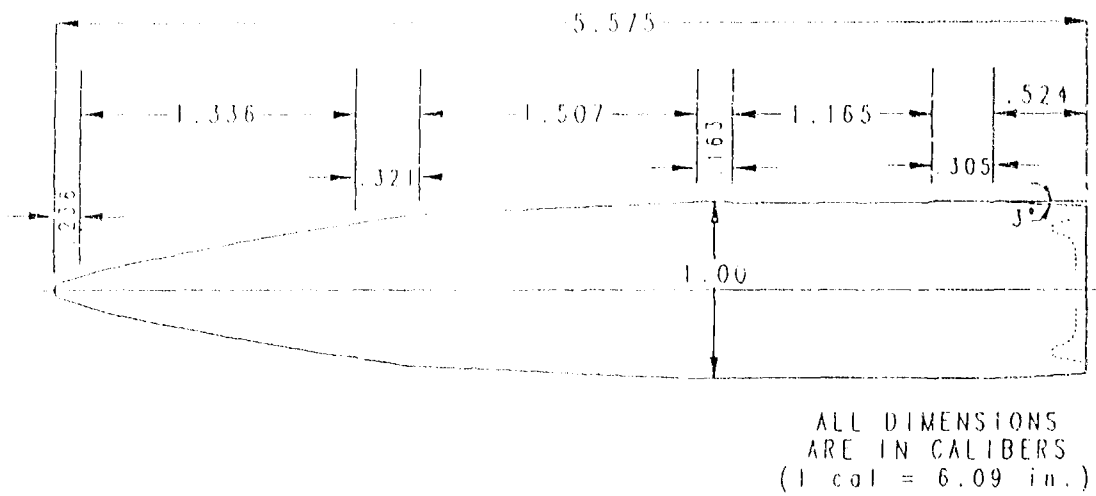


FIGURE 2. Computational model, M864

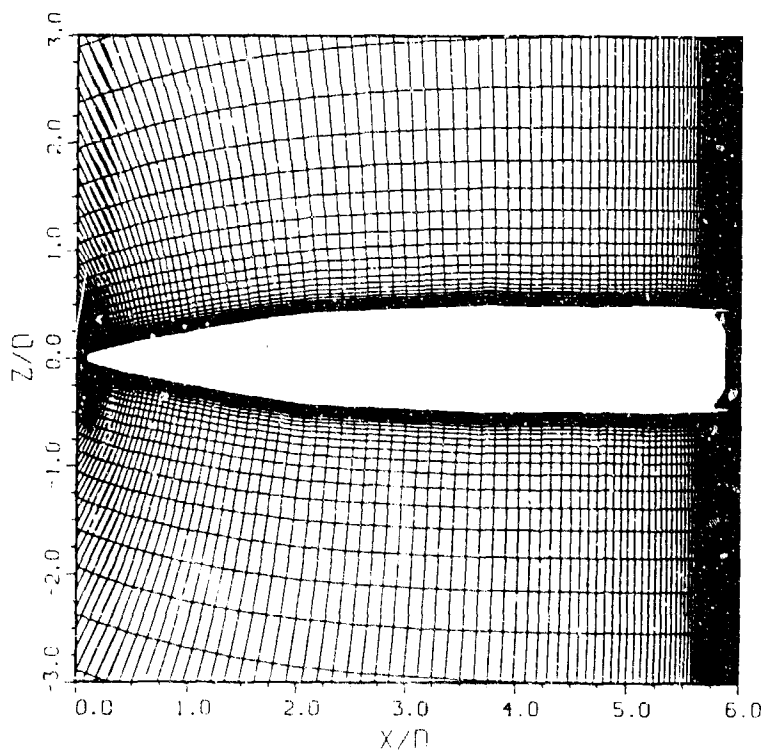


FIGURE 3. Computational grid expanded near the model, M864

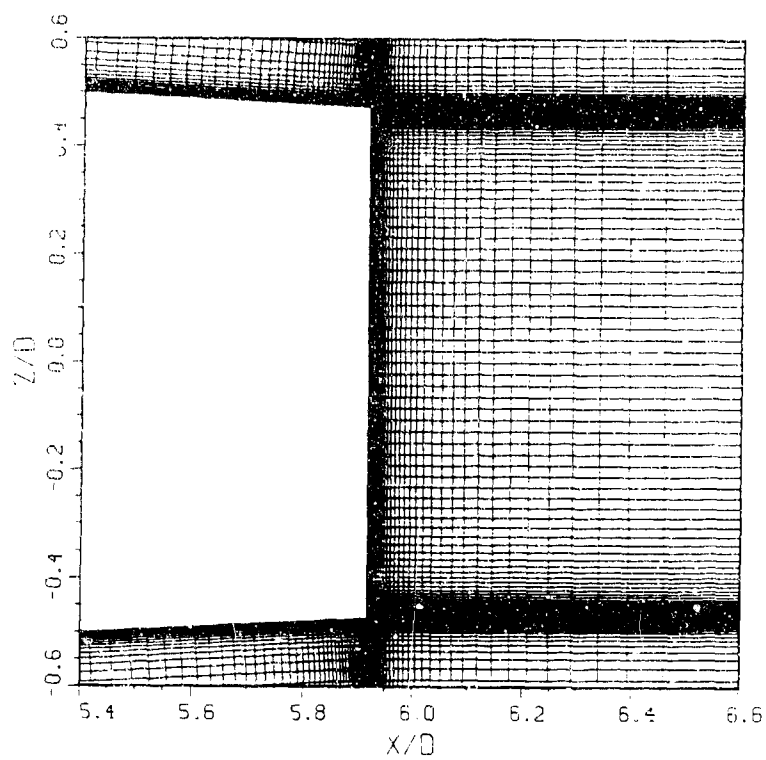


FIGURE 4a. Base region grid, flat base, M864

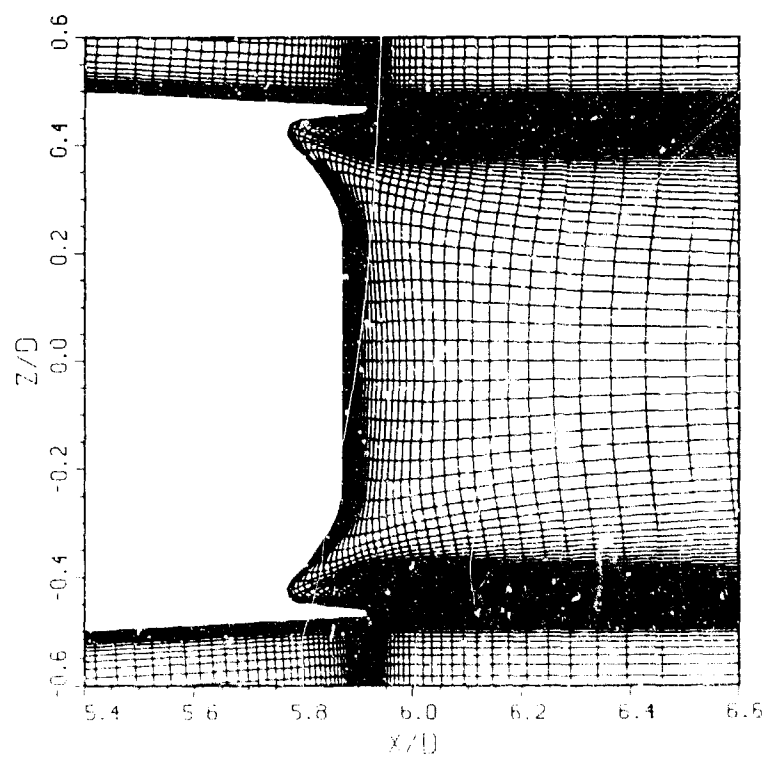


FIGURE 4b. Base region grid, dome base, M864

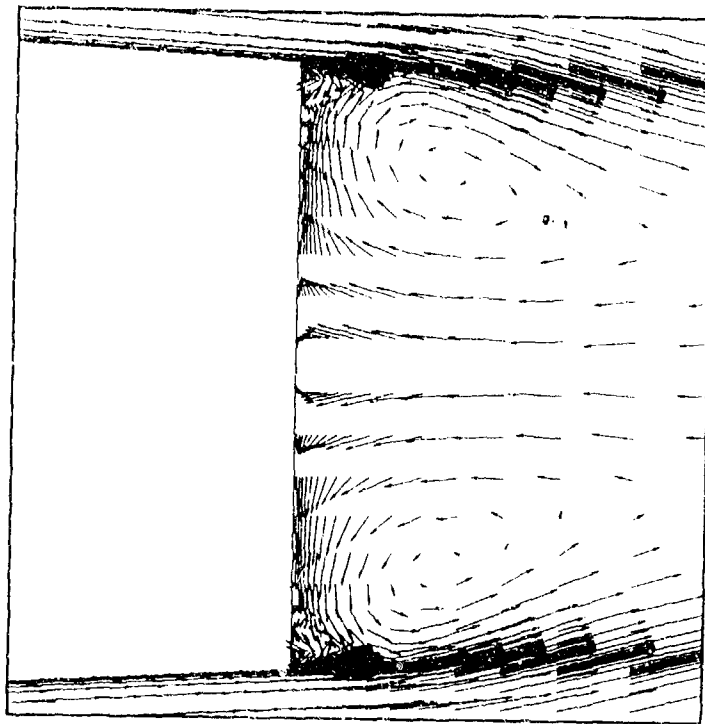


FIGURE 5a. Velocity vectors in base region for flat base M864,  
 $M = 1.4$ ,  $\alpha = 0^\circ$

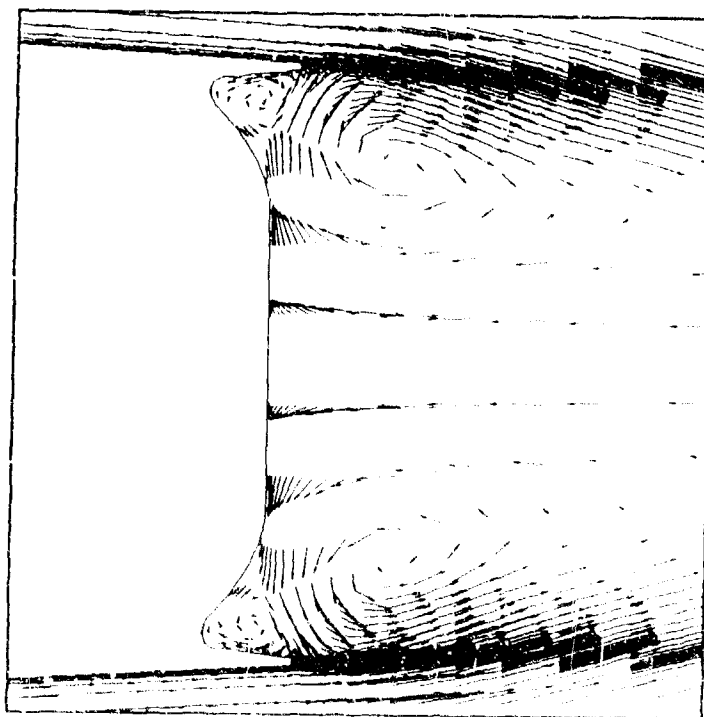


FIGURE 5b. Velocity vectors in base region for dome base M864,  
 $M = 1.4$ ,  $\alpha = 0^\circ$

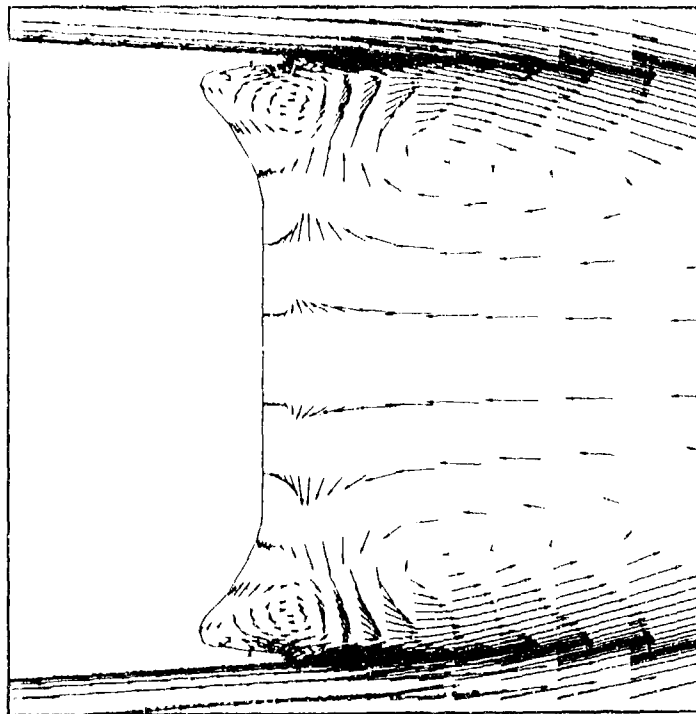


FIGURE 6. Velocity vectors in base region for dome base M864,  
 $M = 1.4$ ,  $\alpha = 0^\circ$ ,  $I = .01$

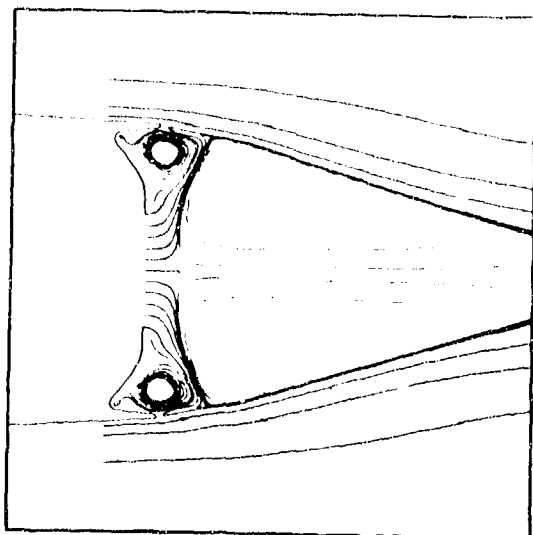


FIGURE 7a. Particle traces in base region,  $\alpha = 0^\circ$ ,  $M = 2.0$ ,  $T = 70^\circ\text{F}$

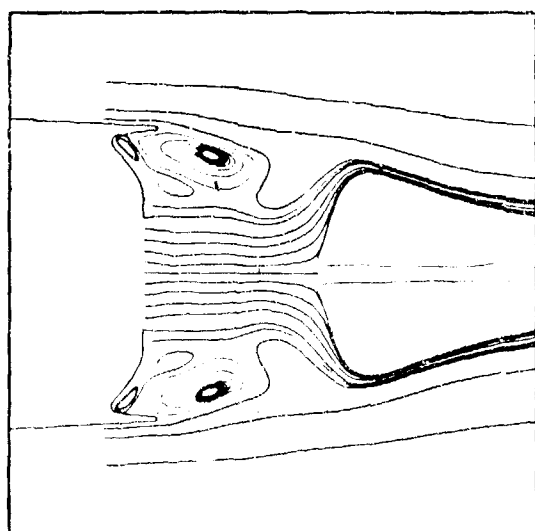


FIGURE 7b. Particle traces in base region,  $\alpha = 0^\circ$ ,  $M = 2.0$ ,  $T = 1700^\circ\text{F}$

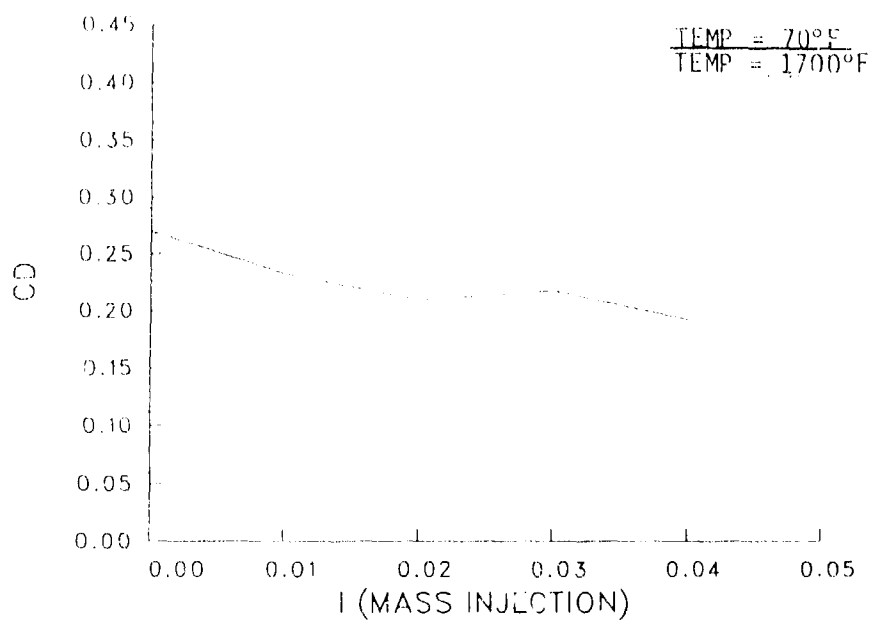


FIGURE 8. Total drag vs mass injection rate at  $T = 70^{\circ}\text{F}$  and  $1700^{\circ}\text{F}$ ,  $M = 2.0$

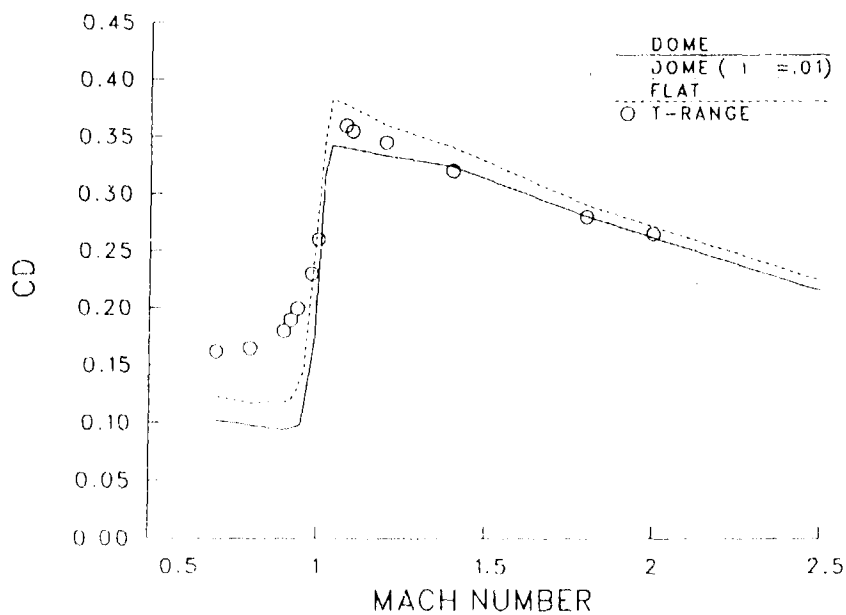


FIGURE 9. Comparison of computed and experimental drag, M864,  $\alpha = 0^{\circ}$

# A MODIFICATION OF THE MODIFIED POINT MASS TRAJECTORY MODEL FOR BASE BLEED PROJECTILES

by

Drs M.M.A. Hasselaar  
Royal Netherlands Army  
Directorate of Material  
Material Test Department 1

## 1. INTRODUCTION

In the 1970s the RNLA expressed the aim to extend the Artillery range to 30 km. The most obvious way to achieve this goal is to increase the muzzle velocity of the projectiles. Therefore a charge 9 and a new 155mm Howitzer were necessary.

Another approach in the range extension project was found in the field of exterior ballistics. In particular the aerodynamic performance of the projectile in flight has been improved. Therefore a new 155 mm projectile has been developed in the late 1970s. This projectile, the HE nr 123 is a slender boosted shell with nubs and a base bleed grain. For an illustration of this projectile see next page.

By means of a mass flow at the base of the projectile, the base drag is reduced with as consequence a range increase of about 20 %. A more detailed description of the base bleed effect will be given below.

In the standard Nato MPM trajectory model<sup>1</sup> (for more details see section 4) an aerodynamic pack is used in which the drag functions depend on the Mach number  $M$  only. For base bleed projectiles this does not hold any more; the MPM model must be modified to describe the reduction of (base) drag. Therefore a base bleed burning model has to be included.

## 2. BASE BLEED EFFECT

The base drag as a component of the total drag arises from vortices and turbulence in the air. These vortices produce a lowering of the air pressure behind the projectile. The base bleed effect can be described as follows. An introduction of a mass flow at the base of the projectile leads to a local rise of the air pressure and this results in a reduction of the base drag. As mentioned above, this reduction is not solely dependent on the Mach number. The mass flow of the base bleed grain, for example, must also be treated as an explanatory variable.



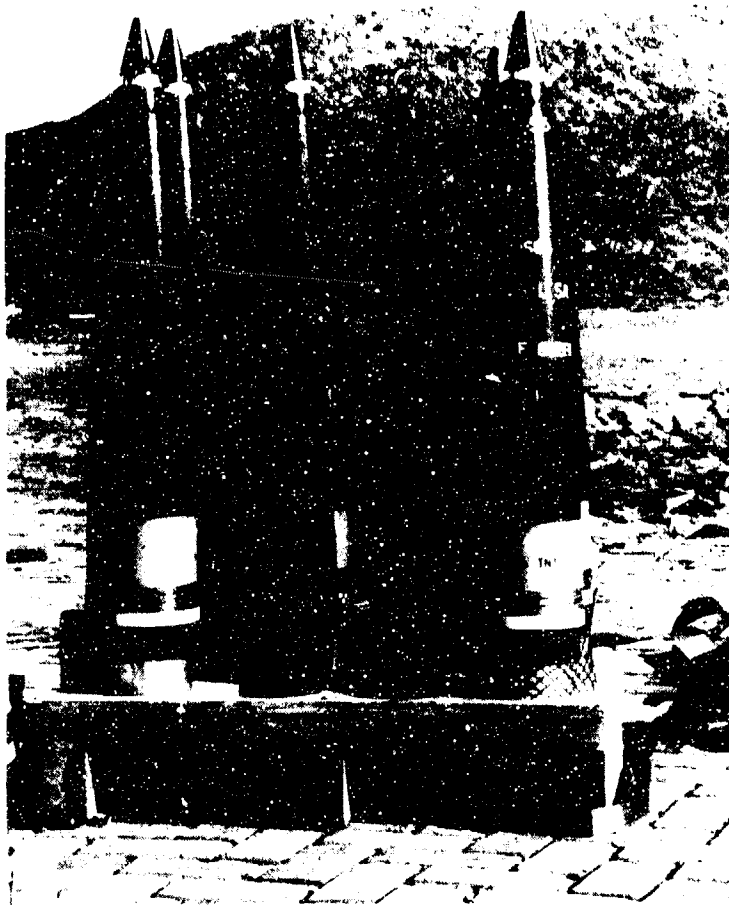


FIGURE 1. THE HE nr 123

### 3. EFFECTS TO BE MODELLED

The most important effect we want to model is the base drag reduction above mentioned. Of lesser importance is the mass reduction of the projectile. A simple theoretical parameter analysis has shown that effects like for instance changes in the center of gravity can be neglected for ballistic purposes<sup>2</sup>.

### 4. MPM MODEL

The classical Point Mass (PM) model is a 2-dimensional trajectory model (XY-space) in which the projectile is treated as a point mass. The forces considered acting on the projectile are Drag and Gravitation and Coriolis (only in X and Y direction) due to the rotation of the earth. There are a number of factors the PM model does not deal with.

The most important ones are the yaw angle of the projectile and its spin. We may conclude that the PM model is not capable of matching all flight data. Therefore a modified 3-dimensional (XYZ-space) trajectory model is developed: the Modified Point Mass (MPM) model<sup>1</sup>. Apart from the forces considered in the PM model, this model considers for example Magnus force and Magnus moment due to the spin of the projectile and Lift force caused by the yaw angle. The result is a rather large aerodynamic package for the MPM model containing several coefficients determined from windtunnel data.

The equation of the projectile acceleration  $\dot{u}$  in the MPM model is given by:

$$\dot{u} = D + L + Ma + G + Labda, \quad (1)$$

where  $D$ ,  $L$ ,  $Ma$ ,  $G$  and  $Labda$  represent respectively the acceleration due to Drag, Lift, Magnus, Gravitation and Coriolis.

The Drag-function  $D$  is given by

$$D = d_0 \cdot (C_{d0} + C_{da} (Q \cdot \alpha_a)^2) \cdot v^2 \quad (2)$$

where  $d_0$  is a constant,  $\alpha_a$  is the yaw angle,  $v$  is the projectile velocity,  $C_{d0}$  is the total drag coefficient at zero yaw and  $C_{da} (Q \cdot \alpha_a)^2$  is the yaw of repose drag term. The trajectory equation must be solved numerically. Often the predictor/corrector algorithm is used for this purpose<sup>3</sup>.

## 5. MODEL DESCRIPTION

Consider the total drag coefficient  $C_{d0}$ :

$$C_{d0} = C_{db} + C_{df} + C_{dw} \quad (3)$$

We distinguish three different components; base drag, frictional drag and wave drag. The burning of the base bleed leads to a reduction of the base drag coefficient only. We define the base drag factor for a projectile with working base bleed as equal to the base drag factor for a projectile with inert base bleed minus a reduction factor, so

$$C_{db} = (C_{db})_{inert\ bb} - \delta C_{db} \quad (4)$$

The reduction factor  $\delta C_{db}$  is not only dependent on the Mach number  $M$ ; it is also dependent on the mass flow  $\dot{m}_r$  of the base bleed grain defined as the mass reduction per time unit. A general form often used for the reduction factor<sup>4</sup> is

$$\delta C_{db}(M, \dot{m}_r) = C_{db0}(M) [1 - \exp(-j(M) \cdot \dot{m}_r / \dot{m}_a)], \quad (5)$$

where  $j(M)$  is an empirical function of the Mach number and  $\dot{m}_a$  is the quantity of displaced air by the projectile per time unit (air stream).

We have now reduced the problem to the modelling of the mass flow  $\dot{m}_r$  since all other factors are known or can be fitted.

## 6. PRESENTATION OF THE BASE BLEED BURNING FORMULAS

At this stage the base bleed burning model can be described completely. We have chosen a model in which the base bleed burning proces is to a large extend based on the geometry of

the grain. The burn direction is assumed to be perpendicular to the exposed base bleed surface according to Piobert's Law. Given the instantaneous burn distance  $s_{bb}$  of the grain, it is possible to calculate the burning base bleed grain surface  $O_{bb}$  and the remaining base bleed grain volume  $Vol_{bb}$ .

This remaining base bleed grain volume is sufficient to model the projectile mass reduction  $m_r$  simply by

$$m_r = \{(Vol_{bb})_{in} - Vol_{bb}\} \cdot \rho_g, \quad (6)$$

where  $\rho_g$  is the density of the grain and  $(Vol_{bb})_{in}$  the initial base bleed grain volume.

Of course the instantaneous burn distance can be determined by the burn velocity  $v_{bb}$  according to

$$(s_{bb})_{new} = (s_{bb})_{old} + v_{bb} \cdot \Delta t \quad (7)$$

So we have reduced the problem to the modelling of the burn velocity  $v_{bb}$ . Static tests have shown<sup>3</sup> that the burn velocity can be given as a function of the pressure in the base bleed unit  $p_g^*$ . The modelling of this pressure  $p_g^*$  is crucial. It depends on the undisturbed air pressure  $p$  and the burning surface  $O_{bb}$ . We assume the following relationship, based on Vieille's Law:

$$p_g^* = b_0(p/101325)^{b_1} + b_2 \cdot O_{bb} \quad (8)$$

Since we have found a relation between the total time of burning of the grain and the spin of the projectile we define an effective pressure  $p_g$  that depends on the spin of the projectile ( $S$ ):

$$p_g = p_g^* + b_3 \cdot S, \quad (9)$$

where  $b_0, \dots, b_3$  are parameters to be estimated. The burn velocity is given by

$$v_{bb} = c_0 \cdot (p_g/101325)^{c_1}, \quad (10)$$

where  $c_0$  and  $c_1$  are known coefficients from static tests<sup>5</sup>.

Finally, given these equations the mass flow is determined by

$$\dot{m}_r = -\rho_g \cdot O_{bb} \cdot v_{bb} \quad (11)$$

To illustrate the application of the model: given the start values of  $s_{bb}$ ,  $O_{bb}$  and  $Vol_{bb}$ , we are able to calculate  $v_{bb}$  by equation (9) and (10) and the mass flow  $\dot{m}_r$  by (11). Finally the base drag reduction is given by (5). The next calculation step can be started by using (7).

## 7. PARAMETER ESTIMATION

After this description of the model, the next problem is to find correct estimates for the parameters  $b_i$ ,  $i=0, \dots, 3$ . We can obtain these estimates from static and in flight test data on the total burning time of the base bleed grain. This can be done numerically using (7)-(10). Right here the problem of underidentification occurs. That is, each time four parameters have to be estimated from one measured trajectory.

Next we have to estimate the empirical function  $j(M)$  in (5) by comparing  $C_a$  data from projectiles with working base bleed and  $C_a$  data from projectiles with inert base bleed. These data will be available in the very near future when the results of the rounds fired in the type classification program of the HE nr 123 are available.

## 8. CONCLUDING REMARKS

The RNLA has developed a model in order to describe the base bleed effect described in section 2. A base bleed burning model is included in this model. It is based on physical considerations. The total burning time of the base bleed grain is not treated as an input variable but is calculated by the model. On the other hand, the modelling of the base reduction itself might seem arbitrary. We have based our functional relationship on literature<sup>4</sup> and make use of a fitting function  $j(M)$ . The parameter estimation has not yet been completed. The complete model incorporated in the original MPM-model describes the trajectory of the projectile accurately. Its first application will be the production of the firing table of the HE nr 123.

## LIST OF SYMBOLS

$\alpha_e$	yaw angle
$b_i$	parameters to be estimated
$c_i$	known coefficients
$C_{d0}$	total drag coefficient at zero yaw
$C_{da}(Q \cdot a_e)^2$	yaw of repose drag term
$C_{db}$	base drag coefficient
$C_{df}$	frictional drag coefficient
$C_{dw}$	wave drag coefficient
$\delta C_{db}$	base drag reduction factor
$D$	acceleration due to drag
$G$	acceleration due to gravitation
$j(M)$	empirical function
$L$	acceleration due to lift
$\text{Lamda}$	acceleration due to Coriolis
$M$	mach number
$M_a$	acceleration due to Magnus
$\dot{m}_a$	displaced air per time unit, airstream

$m_r$	mass reduction per time unit, massflow
$m_r$	projectile mass reduction
$O_{bb}$	exposed base bleed grain surface
$p_g$	grain pressure
$p_g$	effective grain pressure
$Q$	yaw drag factor
$\rho_g$	density of the base bleed grain
$S$	spin of the projectile
$S_{bb}$	burn distance
$t$	current time
$u = v - w$	projectile velocity w.r.t. earth-fixed coordinate system
$\ddot{u}$	projectile acceleration
$v$	projectile velocity w.r.t air
$v_{bb}$	burn velocity
$Vol_{bb}$	remaining base bleed grain volume
$(Vol_{bb})_{in}$	initial base bleed grain volume
$w$	wind speed

#### REFERENCES

1. R.F. Lieske, M.L. Reiter (1966) Equations of motion for a Modified Point Mass Trajectory, BRL Report no.1314
2. T.D. de Witte (1984) Adaption of MPM model to Base Bleed and Development of FCI for nos 122 and 123 HE projectile, Report Material Test Department no 1, RNLA
3. F. de Cock (1983) Comparison of Modern Integration Methods and Codes with built-in tests for Accuracy, Applied to the System of Equations in Exterior Ballistics, Proceedings of the 7th International Symposium on Ballistics, The Hague
4. J.E. Bowman, W.A. Clayden (1969) Reduction of Base Drag by Gas Ejection, RARDE Report 4/69
5. H.F.R. Schöyer, P.A.O.G. Korting (1986) Propellant Combustion at Low Pressures, Combustion and Flame 63 pp 317-327

# A Model of the Axial Drag Coefficient for Base Bleed Projectiles

Nils Bartelson \*)  
Sven Linde \*+)

## SUMMARY

The axial drag on a projectile is usually expressed in terms of the axial drag coefficient  $C_D$ . For a conventional projectile  $C_D$  is often regarded as a function of the Mach number only. For base bleed projectiles, in their bleed phase, ballistic range data indicate that some factor beside the Mach number has a significant influence on  $C_D$ . It is reasonable to expect that the ambient atmospheric pressure is one such factor.

We attempt to relate, in an empirical way, the drag of a base bleed projectile to the geometry of its trajectory and the state of the atmosphere. The relations are not derived from physical principles - our approach is descriptive and statistical. The purpose is to summarize observations of flight performance in a way that permits us to predict a trajectory from its initial conditions and from a picture of the atmosphere.

We propose a functional relation between the Mach number, the ambient atmospheric pressure and the drag coefficient (Section 2). Its parameters are determined by a regression procedure based on time-of-flight recordings from a Doppler radar instrument. In Section 3 we apply the model to a set of experimental data. It proves capable of reproducing  $C_D$  estimates along trajectories of widely differing shapes. As a side effect some light is thrown upon the extinction of the bleed charge (Section 4). It turns out to be a more drawn-out process than is often assumed. We report on a

---

\* Furusundsgatan 12, S-11537 Stockholm, Sweden

\*+ Studsvik AB, Studsvik Data, S-61182 Nyköping, Sweden

verification of the model in Section 5 and also touch upon the problems of modelling the transition from active to inert base bleed. In Section 6 we exemplify the use of the model by studying how the shell temperature will influence the burning of the base bleed charge. We conclude, in Section 7, that the model may be used as a tool for the construction of fire control equipment and ballistic range tables, and also point out some areas for further investigation.

## 1. INTRODUCTION

Artillery ammunition has been in a state of rapid change in Scandinavia for several years. New ideas have emerged and enough funding has been received to result in significant improvements in range and precision.

Ballistic measuring equipment has been developed by a Danish company, OPOS Electronics AS; new methods for analysing data have been formulated by the Royal Swedish Navy together with the National Defence Research Institute and Studsvik AB.

This paper is concerned with long range ammunition. For the designer of a long range projectile the main task is to keep the drag as low as possible, thus increasing the range or decreasing the time of flight.

The axial drag on a projectile depends on the shape, diameter and velocity of the projectile and on the physical state of the ambient atmosphere. The shape dependency is usually expressed in terms of a few dimensionless aerodynamic coefficients, in particular the axial drag coefficient  $C_D$ . For a conventional projectile  $C_D$  is found to depend mainly on the projectile shape and the ratio of the projectile velocity  $v$  to the local sound velocity in air,  $a$ . The ratio  $v/a$  is referred to as the Mach number.

In the early stages of the development of what is now called base bleed ammunition it was found that the simple relationships which are good approximations for a conventional projectile, were no longer valid. It was concluded that experimental resources and manpower for modelling were required to study this phenomenon. A reliable tool was needed to predict trajectories for the design of fire control equipment and for the calculation of range tables.

The objective of this paper is to formulate the problem and to propose a solution, given experimental data.

The tools used are of two kinds, namely:

- Doppler radar records from the firing in Sweden of slender-bodied 120 mm and 155 mm ammunition with inert and active base bleed,
- computer programs written at Studsvik AB identifying the drag function from recorded radar data, atmospheric conditions, gun elevation, the mass of the projectile and its loss of mass during time of flight etc.

We attempt to relate, in a simple, empirical fashion, the drag of a gun-fired base bleed projectile to the geometry of its trajectory and the state of the atmosphere. The relations are not derived from physical principles - our approach is descriptive and statistical. Our purpose is to summarize observations of flight performance in a way that permits us to predict a trajectory from its initial conditions and from a picture of the atmosphere.

The proposed ballistic model is the aerodynamic point mass or modified point mass model extended to account for base bleed effects. It should be possible to identify the parameters from observations at the proving ground using ground-based instruments. The model should be accurate enough to serve as the basis for the design of range tables and data to the fire control equipment for a specific projectile design. We do not aim to model the burning of the base bleed charge or the dynamics of the injection of mass into the base flow region.

The essential results of the study were published in a Studsvik report [1].

## 2. FORMULATION OF THE PROBLEM

The theoretical basis is the aerodynamic law and its proportionality factor, called the drag coefficient.

The drag of a projectile is usually written

$$D = \frac{1}{2} A \rho C_D v^2$$

where

- A is a reference area
- $\rho$  the air density
- $C_D$  the drag coefficient, in German literature often denoted  $C_W$
- v the projectile velocity



In the aerodynamic point mass model the drag coefficient of a conventional projectile is usually regarded as a function of the Mach number only. Experience from the proving ground indicates, however, that this simple model does not generally apply to base bleed projectiles in their bleed phase. The  $C_D$  curves reproduced in Fig 1 testify to this. They are estimated from two sets of trajectories in quadrant elevations  $20^\circ$  and  $50^\circ$ . The average distance between the curves is large compared to the standard deviations of the estimated  $C_D$ 's, at most 0.001 for  $1.3 \leq \text{Mach} \leq 1.9$ .

Some factor beside the Mach number has evidently had a significant influence on the drag coefficient. It is reasonable to expect that the ambient atmospheric pressure may be one such factor.

Thus we are led to consider a functional relation of the form

$$C_D(M, p) = u(M) + \lambda(M) \frac{p - \bar{p}}{\bar{p}}$$

where

$M$  is the Mach number  
 $p$  is the local atmospheric pressure  
 $\bar{p}$  a reference pressure  
 $\left. \begin{matrix} u \\ \lambda \end{matrix} \right\}$  are functions to be identified

The reference pressure is introduced to improve the numerical properties of the estimation procedure. The main reason for using the relative deviation from the reference pressure as a predictor is to become independent of pressure units. The form chosen is essentially a first order Taylor expansion of  $C_D$  in terms of  $p$ .

Next we have to describe the unknown functions  $u$  and  $\lambda$  with a reasonably small set of parameters. Since we have no physical theory to indicate a suitable functional form, we have chosen  $u(M)$  and  $\lambda(M)$  as cubic spline functions with knots to be prescribed by the analyst. The knots will be denoted

$$x_i, i=0..n \quad \text{for } u(M),$$

$$z_i, i=0.. \quad \text{for } \lambda(M).$$

The end-point conditions for the splines are chosen to be

$$u''(x_0) = u''(x_n) = 0;$$

$$\lambda''(z_0) = \lambda''(z_v) = 0.$$

Now let

$$\begin{aligned} b_0 &= u(x_0) & b_{n+1} &= \lambda(z_0) \\ b_n &= u(x_n) & b_{n+l+1} &= \lambda(z_l) \end{aligned}$$

be the regression parameters. By the theory of spline functions we construct a linear estimator

$$C_D(M,p) = \sum_{j=0}^{n+l+1} a_j(M,p) b_j$$

The  $a_j$ 's are functions of the local Mach number and atmospheric pressure.

At this point it is appropriate to remark that our use of spline functions to express  $u(M)$  and  $\lambda(M)$  is one of several alternatives. We could as well have chosen a piecewise linear function or a Lagrange interpolator of higher order. The advantage of the spline functions is their inherent smoothness.

In practice the same (time, space) data will be used to estimate both  $M$  and  $C_D$ . So  $M$  is a stochastic variable with a certain dispersion, and  $p$  is of course not known exactly. Moreover,  $M$  and  $C_D$  are not independent. The deviations of  $M$  and  $p$  propagate to the carriers  $a_j$ . However, we expect  $M$ , which is essentially a first derivative of space data, to be less contaminated with noise than  $C_D$ , which is essentially a second derivative. Also, small errors in  $p$  will not influence the carriers too much. Thus it seems reasonable to choose the common least squares criterion to find the regression parameters  $b_j$ , i.e. to minimize the sum of squared deviations of the observed  $C_D$ 's from the estimated ones.

### 3. APPLICATION TO EXPERIMENTAL DATA

Our first approach is to apply the assumed model on tests conducted at Torhamn and in the isle of Öland, Sweden, in October 1984. 36 rounds of a 155 mm projectile were fired, 11 of which were inert to provide baseling drag data. The quadrant elevations ranged from  $18^\circ$  to  $70^\circ$ . Occasionally data will be taken from a second set of experiments conducted with a 120 mm projectile at the Torhamn experimental range in April 1985.

The projectiles were tracked by a Doppler radar system. Recordings of (time, space) values were processed by a drag

analyser program providing tables of  $M$ ,  $p$  and  $C_D$  for 35-65 time of flight points dispersed along each trajectory.

A few rounds have been omitted from the data set. Observed  $C_D$  values for one such projectile are shown in Figure 2. For illustrative purpose, although prematurely, curves of estimated  $C_D$ 's for inert and active base bleed are displayed in the graph. It is seen that the ignition of the base bleed charge was delayed and that the bleed effect was reduced during the first five seconds. The range to point of impact was 18.0 kms for this round compared to an average range of 18.5 kms for similar projectiles fired in the same elevation. No omission from the experimental data has been accepted unless a suspected malfunctioning of the bleed charge was confirmed by a deviation in range.

The regression analysis for inert projectiles is based on data from 11 trajectories comprising 321 observations. The  $C_D$  estimator was a spline function with 12 knots in the range  $0.7 \leq M \leq 2.3$ . The result is summarized in Table 1.

Table 1  
Estimated  $C_D$  function for inert projectile

$M$	$C_D$	s dev
.700	.1619	.0059
.850	.1689	.0023
.900	.1713	.0030
.950	.1946	.0031
.000	.2910	.0013
.050	.3068	.0009
.100	.3026	.0006
1.200	.2937	.0005
1.400	.2764	.0004
1.700	.2528	.0005
2.000	.2338	.0006
2.300	.2145	.0025

The standard error of estimate is 0.0036.

The regression analysis for active base bleed is founded on flight performance data from 22 trajectories for which  $(M, p, C_D)$  triplets have been calculated at 771 time of flight points. Three trajectories were set aside for later verification of the parameter estimation. For  $u(M)$  a spline function with 6 knots was used, for  $\lambda(M)$  a spline function with 3 knots.

The first question to be asked is whether the model is appropriate, and, in particular, if the addition of a pressure term improves the fit. Its significance can be assessed by an analysis of variance (Table 2), in which we test the hypothesis

$$H_0: \lambda = 0.$$

Table 2  
C<sub>D</sub> regression  
Analysis of variance

Source	Sum of squares	Degrees of freedom	Mean square	Mean square ratio
Regression				
mean	21.76161	1		
u(M)	0.00415	5	0.00083	64
$\lambda$ (M)	0.00923	3	0.00308	239
Residual	0.00982	762	0.000013	
Total	21.78481	771		

The last column is the ratio of the mean square to the residual mean square.

The mean square due to regression on  $\lambda$  should be compared to the residual mean square, and its size is found to be quite large. If the hypothesis is true and under some additional assumptions on the normality of the observations, the test variable for the component  $\lambda$ , i.e. the mean square ratio, will have an F distribution with (3,762) degrees of freedom. The probability of a value  $\geq 239$  is small, indeed. However, we do not wish to stress this formal aspect too much, since little is known about the distribution of the original data.

Anyhow, this exploratory data analysis indicates that the hypothesis  $H_0: \lambda = 0$  should be rejected and that the pressure term is significant.

The estimates of the regression parameters are shown in Table 3.

Table 3.  
 $C_D$  components, active base bleed

M	$u(M)$	s dev of $u(M)$	$\lambda(M)$	s dev of $\lambda(M)$
1.1	0.1745	0.0027	0.0096	0.0038
1.3	0.1797	0.0006	0.0151*	0.0015
1.5	0.1707	0.0003	0.0192	0.0009
1.7	0.1663	0.0003	0.0209*	0.0010
1.9	0.1650	0.0004	0.0207*	0.0020
2.2	0.1612	0.0022	0.0184	0.0056

The values marked by asterisk are interpolations, not actual regression parameters.

The standard error of estimate is 0.0038, close to the value obtained for projectiles with inert base bleed. This may be regarded as another indication that the model is appropriate.

The  $C_D$ ,  $u$  and  $\lambda$  functions are shown in Figure 3.

Standard deviations of the parameter estimates are low, as a rule. They do not, however, tell the whole story. A glance at the correlation matrix reveals that the parameters defining  $u(M)$  are loosely coupled, as are those defining  $\lambda(M)$ . But correlation between the two parameter classes may be considerable, indicating that the problem is not so well conditioned as one might wish.

The degree of ill-conditioning depends on the experimental design. To some extent ill-conditioning is inherent in the physical situation on the proving ground. All projectiles set out at a high Mach number  $M$ , close to the muzzle, and a high atmospheric pressure  $p$ , at ground level. As they proceed to altitudes where  $p$  is lower, the Mach number will also decrease, broadly following a common pattern often tempered only by differences in elevation. Information from other regions of the  $(M,p)$ -plane, e.g. combinations of large  $M$  and low  $p$  values, is missing.

A somewhat better design is achieved by reducing the muzzle velocity for some rounds. The pattern of observations from such an experiment is illustrated in fig 4.

The effects of ill-conditioning may be puzzling to the beginning analyst. The values of  $u(M)$  and  $\lambda(M)$  may be rather sensitive to perturbations in the observed data and,

not least, to contamination from extinct base bleed. Nevertheless the fit is quite good, as a rule. Therefore the method outlined here is not reliable to determine, say,  $\delta C_D / \delta p$  but is quite useful to predict  $C_D$  for those  $p$  and  $M$  values which occur in ballistic applications.

Three trajectories were excluded from the set used for regression analysis; thus they may be regarded as new and independent experiments. These projectiles were fired in quadrant elevations  $20^\circ$ ,  $35^\circ$  and  $50^\circ$ . We will compare the  $C_D$ 's obtained from these trajectories with the predictions of the model. As a by-product this provides an opportunity to study the extinction of the base bleed charge.

In Figures 5-7 are shown, as functions of time,

- the predicted  $C_D$  for inert base bleed,
- the predicted  $C_D$  for active base bleed,
- the observed  $C_D$  values,
- a confidence band within which the observed  $C_D$ 's are expected to fall with 95% probability.(1)<sup>D</sup>

It is seen that up to a certain point in time the observed  $C_D$ 's fall well within the confidence band. This is true for all the three trajectories, which span a wide range of elevations. So the new experiments verify the model and confirm the significance of the pressure term.

---

(1) The width of the band must not be interpreted as a measure of the uncertainty of the estimated  $C_D$ 's. The confidence interval for the outcome of a new experiment is in this case much wider than that for the "true  $C_D$ ", at the same confidence level. This is just an instance of the familiar rule that the outcome of any one experiment is more variable than the mean outcome of, say, ten experiments.

#### 4. THE EXTINCTION OF THE BASE BLEED

The point where the observed  $C_D$ 's depart from the predicted values coincides with a rough a priori estimate of the burning time of the base bleed charge. The graphs show, however, that the extinction process is slow and continues for 6-7 seconds. During this time interval the actual  $C_D$  values will climb gradually from the low active base bleed curve to the higher curve for the inert projectile. We deem it necessary to take the gradual change-over into account in trajectory calculation programs. However, no such program is available to us, and the best we can do is to define an extinction point somewhere in the middle of the extinction interval and use a trajectory program that assumes the active  $C_D$  curve to be applicable up to the extinction point, after which a sudden rise to the inert curve will take place.

#### 5. VERIFICATION OF CALCULATED RANGES

Using such a  $C_D$  model we can calculate trajectories and find for instance the points of impact. Two questions arise:

- How sensitive is the calculated point of impact to a perturbation of the assumed extinction point?
- How does the calculated range compare with the observed one?

Since range observations for the previously treated trajectories are not available, we have to introduce another projectile design including also a new type of base bleed charge. The material as a whole comprises data from more than 20 rounds.

Figure 8 shows the change-over from active to inert base bleed for a 120 mm projectile, fired in a quadrant elevation of  $30^\circ$ .

The bleed is seen to be more sustained and the rise of the  $C_D$  curve steeper than in the previous cases. Nevertheless the extinction process is extended over 5-6 seconds. The data for the trajectory shown in the graph was not used for the regression analysis; the round can thus be regarded as an independent experiment.

From the graph the midpoint of the extinction interval can be roughly estimated at 29 seconds. In order to study the sensitivity of the calculated range to this estimate we have performed trajectory calculations with the extinction point set to 27, 29 and 31 seconds.

The ranges obtained are shown in table 4.

Table 4  
Range sensitivity to postulated extinction time

Extinction time, s	Calculated range, m
27	25437
29	25580
31	25740

The mean observed range for five rounds was 25539 m. It is evident, that the positioning of the assumed extinction point has an influence on the calculated ranges which is far from negligible. The fact that it also depends on the trajectory geometry further complicates the task of trajectory prediction.

#### 6. INFLUENCE OF BASE BLEED CHARGE TEMPERATURE

The influence of the bleed charge temperature on the  $C_D$  function has been studied for 155 mm ammunition. Typical results are shown in figures 9 and 10.

Figure 9 illustrates the  $C_D$  function for a projectile fired with the bleed charge at  $-40^\circ\text{C}$ . It is seen that the  $C_D$  values lie on the upper edge of the 95% confidence band; the low temperature seems to retard the burning. Figure 10 shows the opposite effect. At  $60^\circ\text{C}$  the bleed charge burns rapidly and the actual  $C_D$  turns out to be low. The burning is not sustained, however.

Since this point is outside the scope of this paper, we summarize our conclusions:

- the influence of the charge temperature depends on the composition of the base bleed charge,
- in the studied cases the influence is far from negligible,
- if the actual bleed charge temperature may differ widely from the normal temperature, the influence must be given as corrections in the fire control and the range table.



## 7. CONCLUSIONS

The experiments and analyses reported in this document indicate strongly that for slender bodied base bleed ammunition the drag coefficient  $C_D$  cannot be represented as a function of the Mach number only. It has been demonstrated that an expression which is essentially a first order Taylor expansion in the ambient pressure, provides a means of predicting the  $C_D$  value in a trajectory point where the Mach number and the atmospheric pressure are known.

For ballistic applications a few consequences are obvious.

- For trajectory calculations for range tables, in the fire control etc, the influence of atmospheric pressure on  $C_D$  in the bleed phase must be taken into account.
- The transition from bleed phase to inert phase may be of considerable length; some kind of intermediate  $C_D$  function is required.
- Means are needed to find, for a particular trajectory, the beginning and the end of the transition period.
- If the bleed charge is to be used at widely differing temperatures, the influence of this temperature on range, time of flight etc must be recorded in range tables and programmed into fire control equipment.

## REFERENCE

1. Nils Bartelson, Sven Linde:  
A Model of the Axial Drag Coefficient for Base Bleed Projectiles.  
Report STUDSVIK/SD-87/67 (1987).

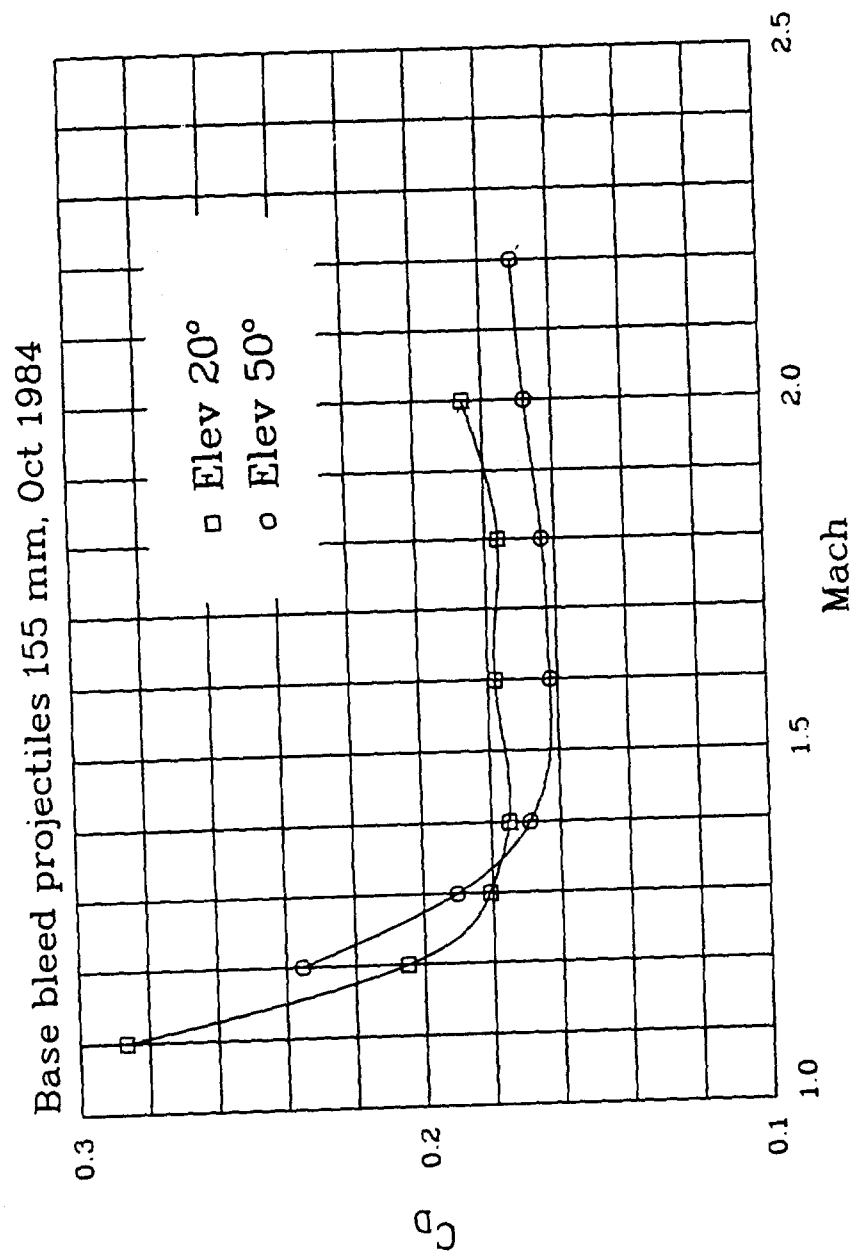


Figure 1

# Base bleed projectile 120 mm, April 1985

Delayed ignition of base bleed charge

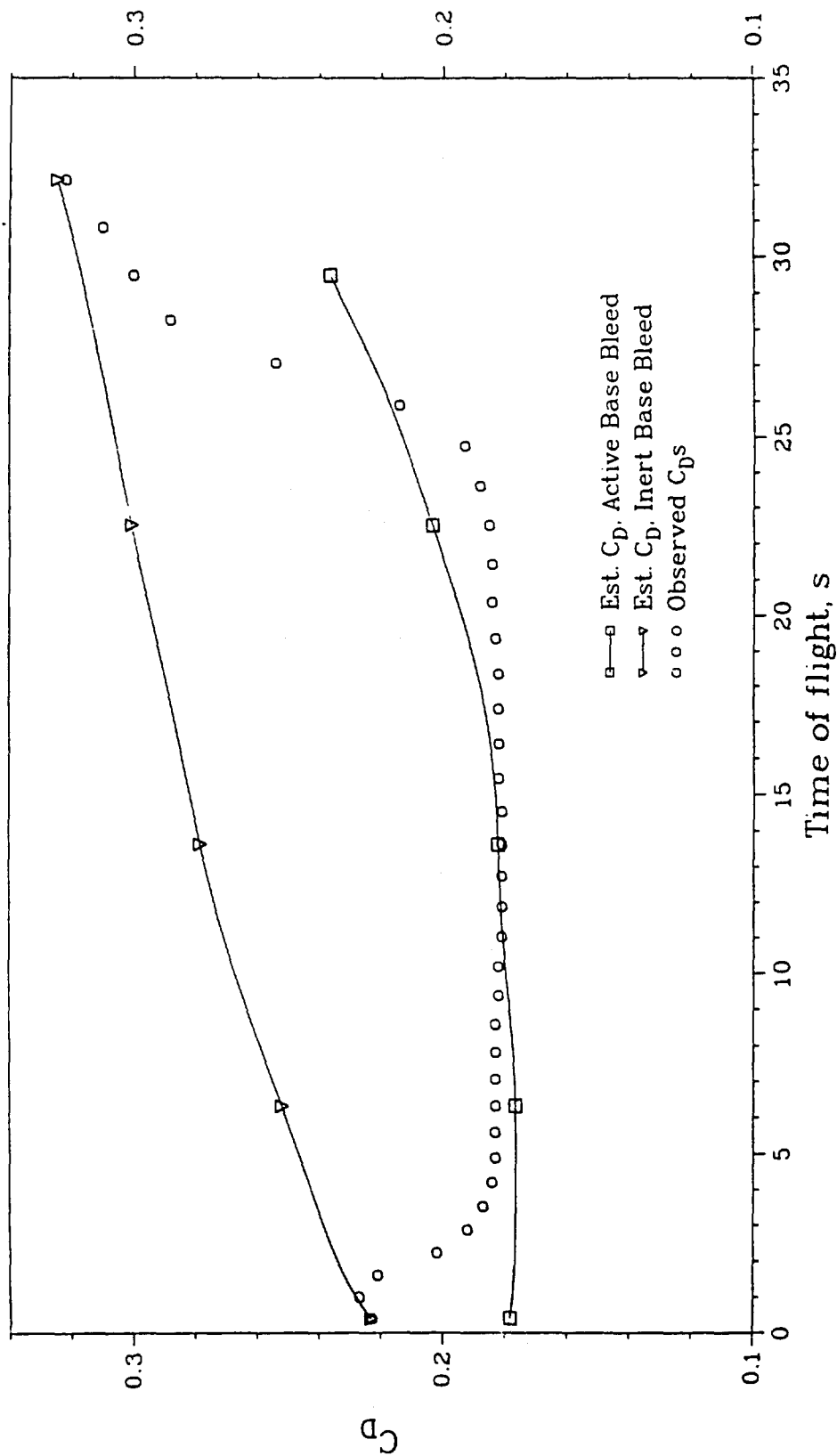


Figure 2

Base bleed projectiles 155 mm, Oct 1984

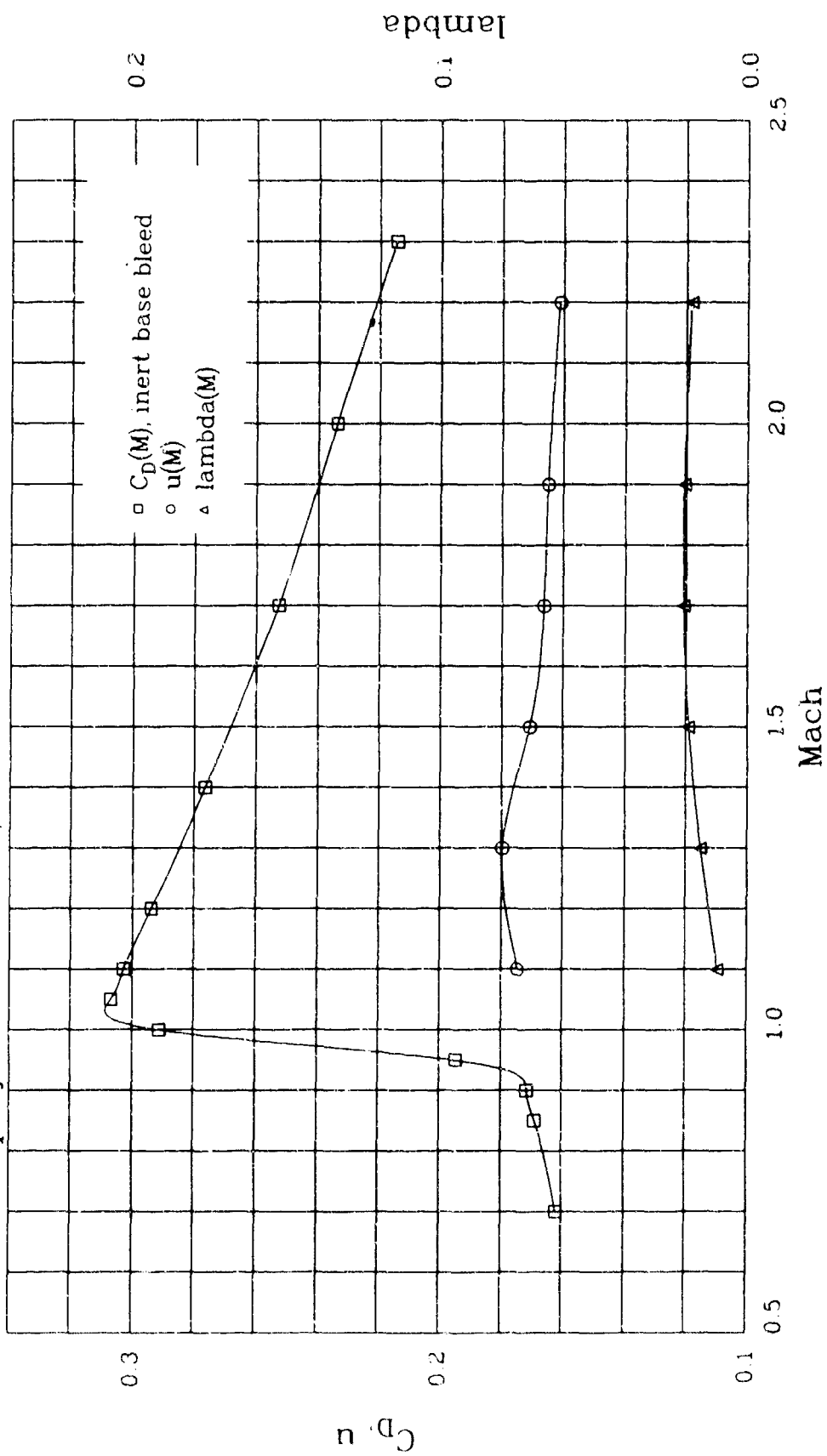


Figure 3

Base bleed projectiles 155 mm, Oct 1984  
Pattern of observations

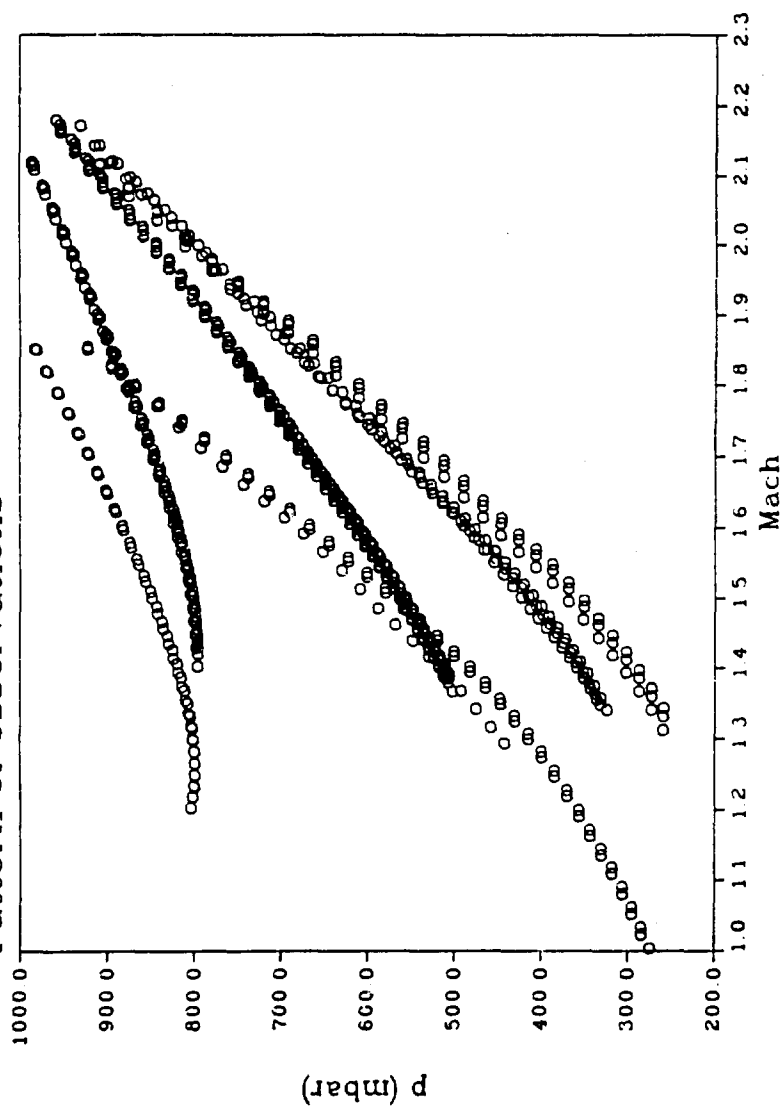


Figure 4

# Base bleed projectile 155 mm, Oct 1984

Quadrant Elevation 20°

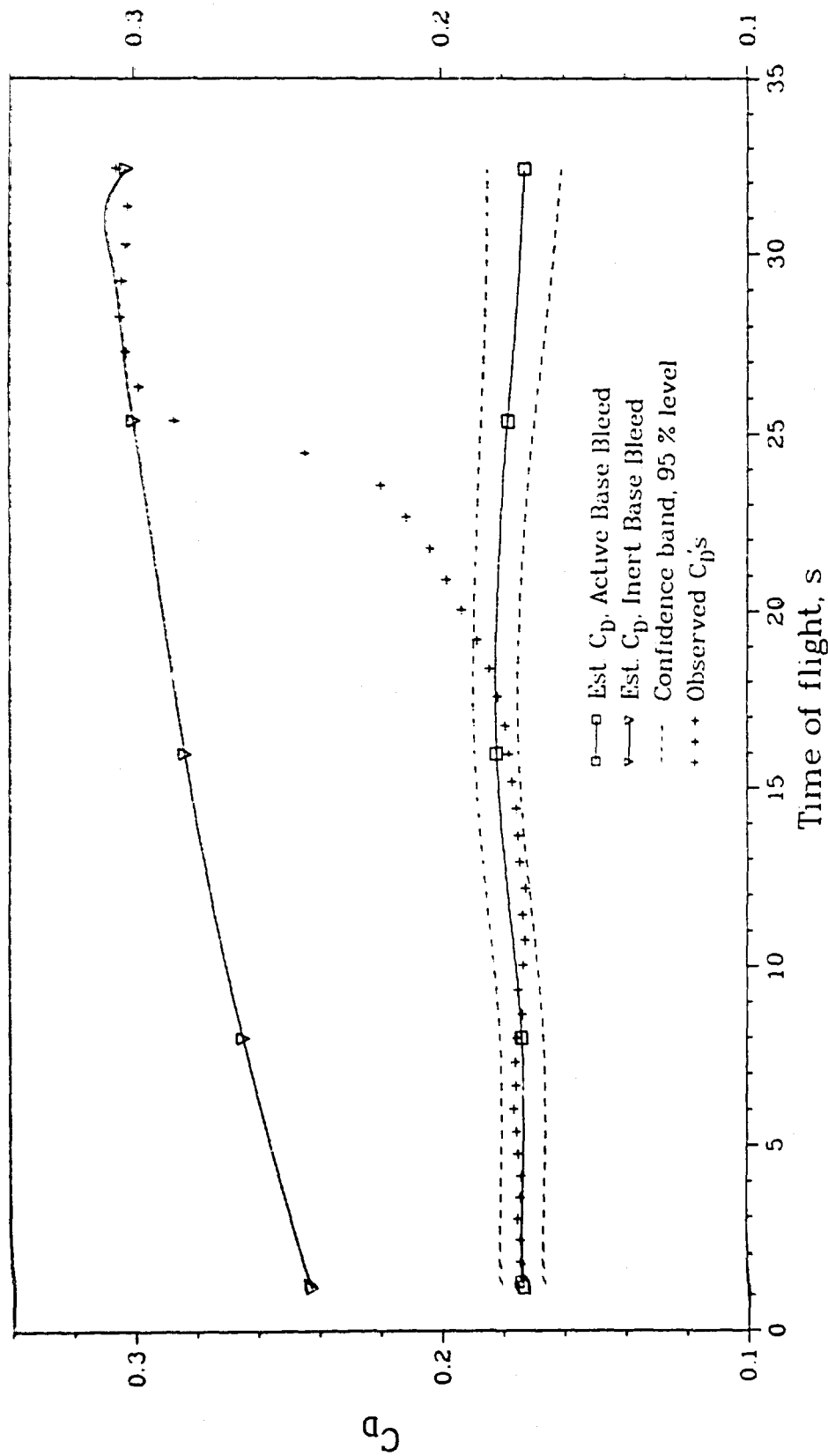


Figure 5

Base bleed projectile 155 mm, Oct 1984

Quadrant Elevation: 35°

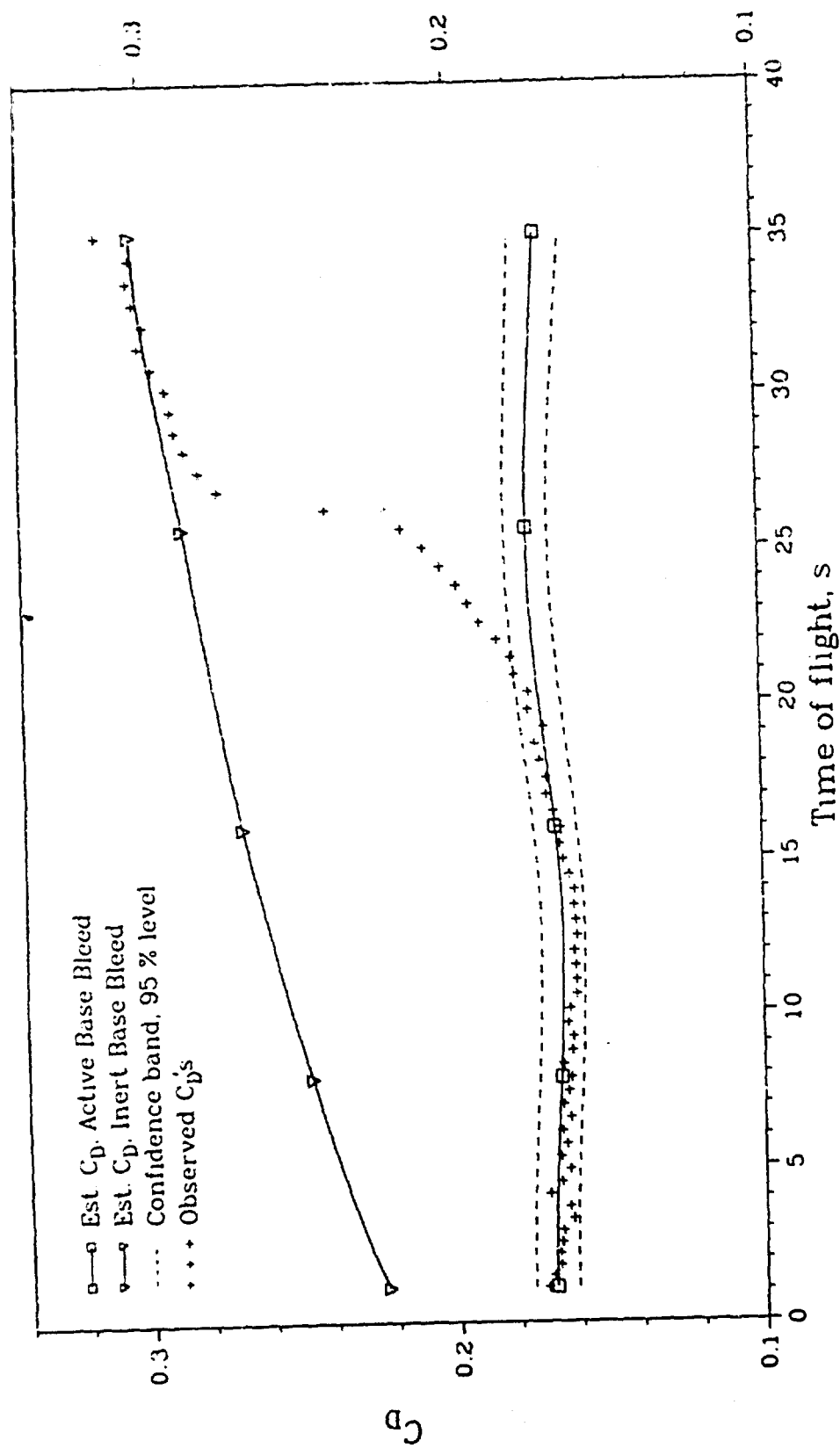


Figure 6

# Base bleed projectile 155 mm, Oct 1984

Quadrant Elevation 50°

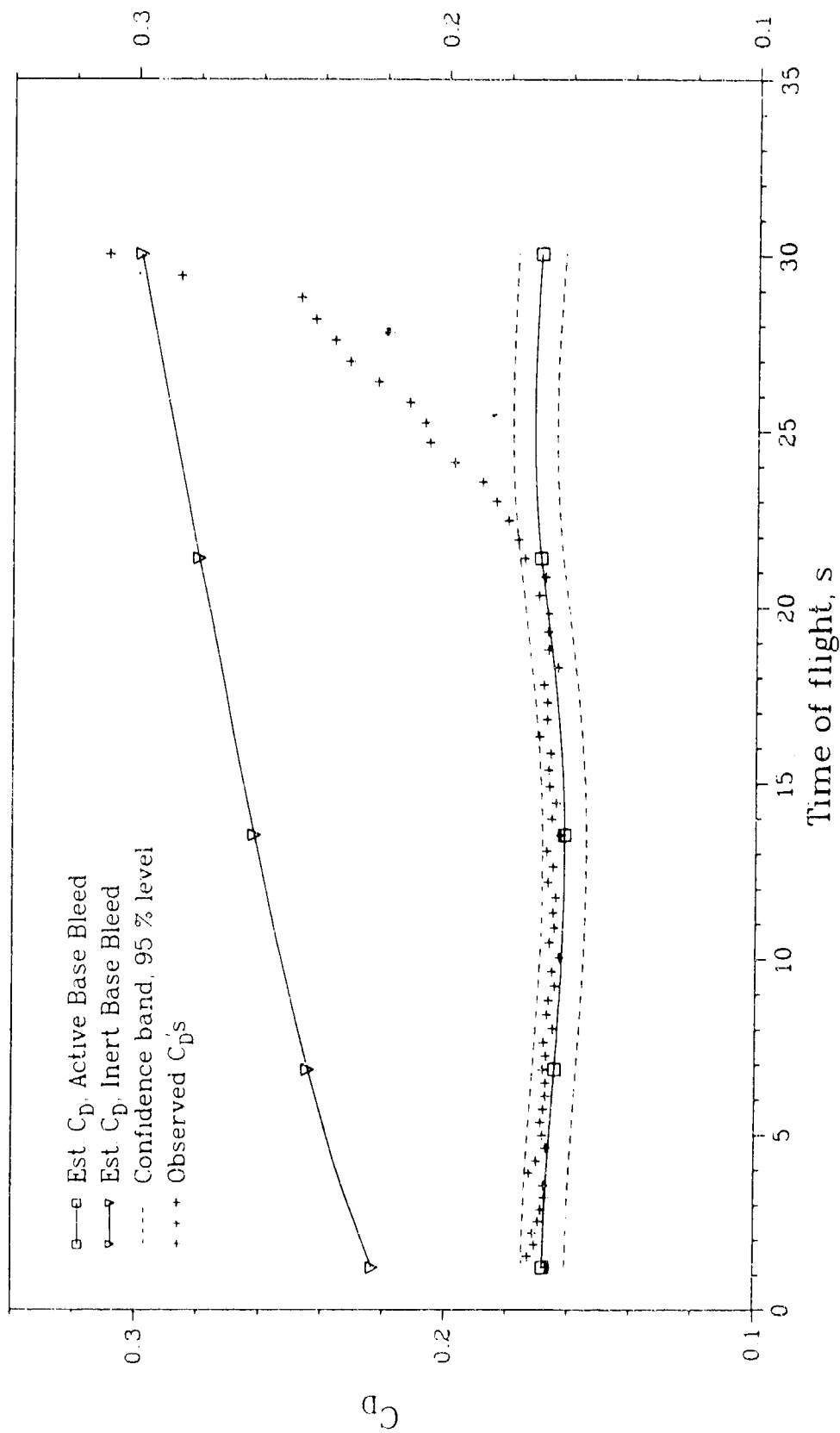


Figure 7



# Base bleed projectile 120 mm, April 1985

Quadrant Elevation: 30°

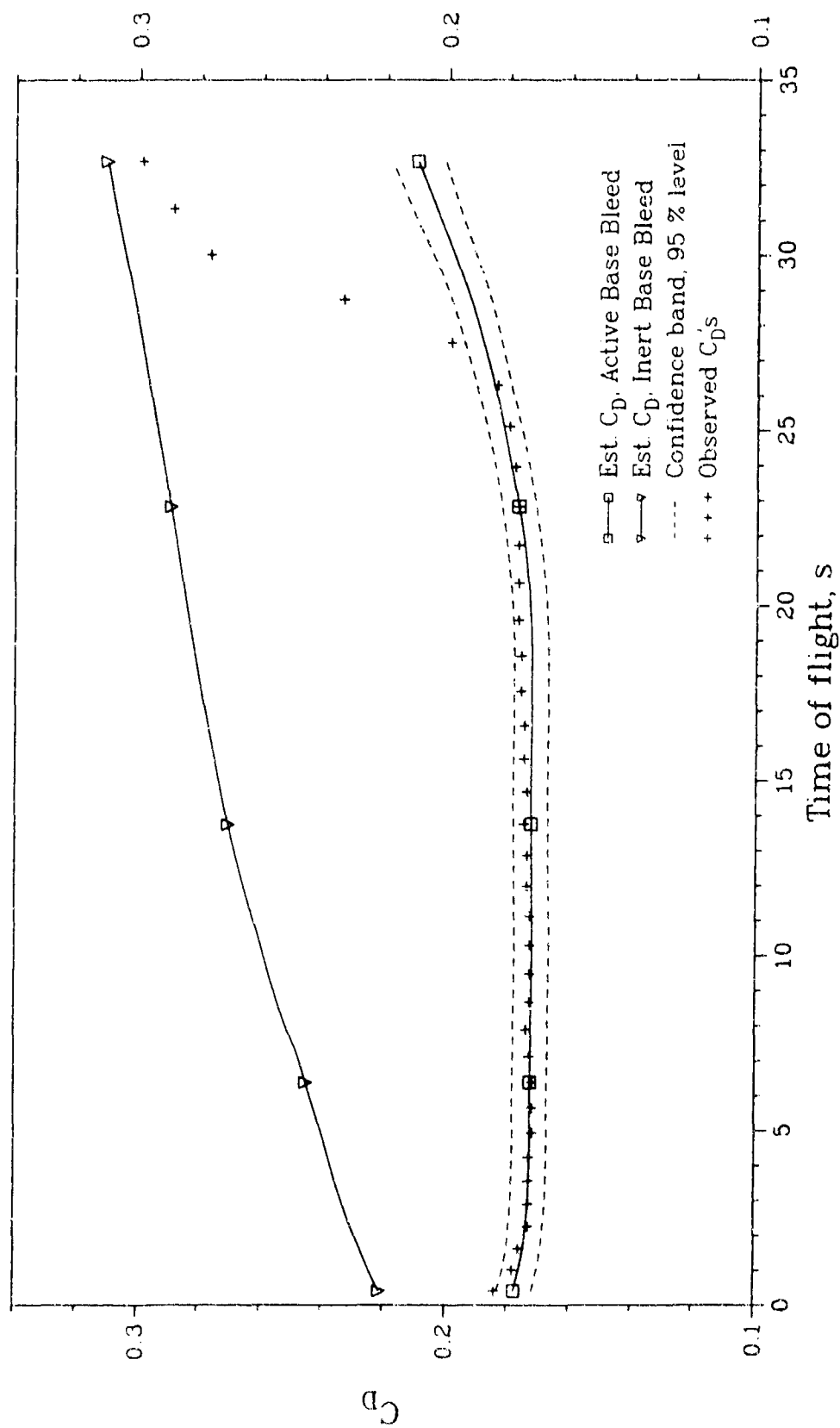


Figure 8

Base bleed projectile 155 mm, Oct 1984

Shell temperature  $-40^{\circ}\text{C}$

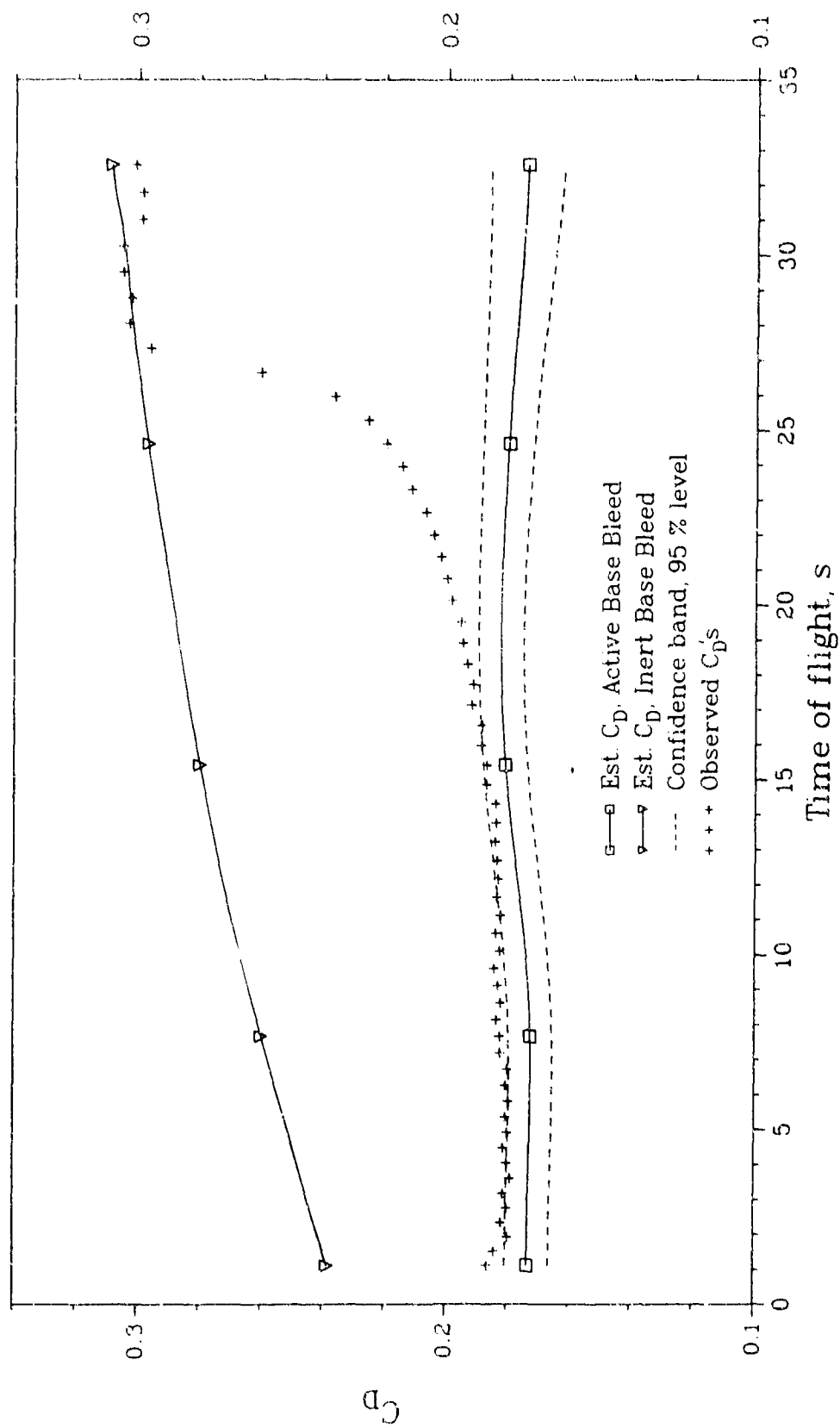


Figure 9

# Base bleed projectile 155 mm, Oct 1984

Shell temperature +60°C

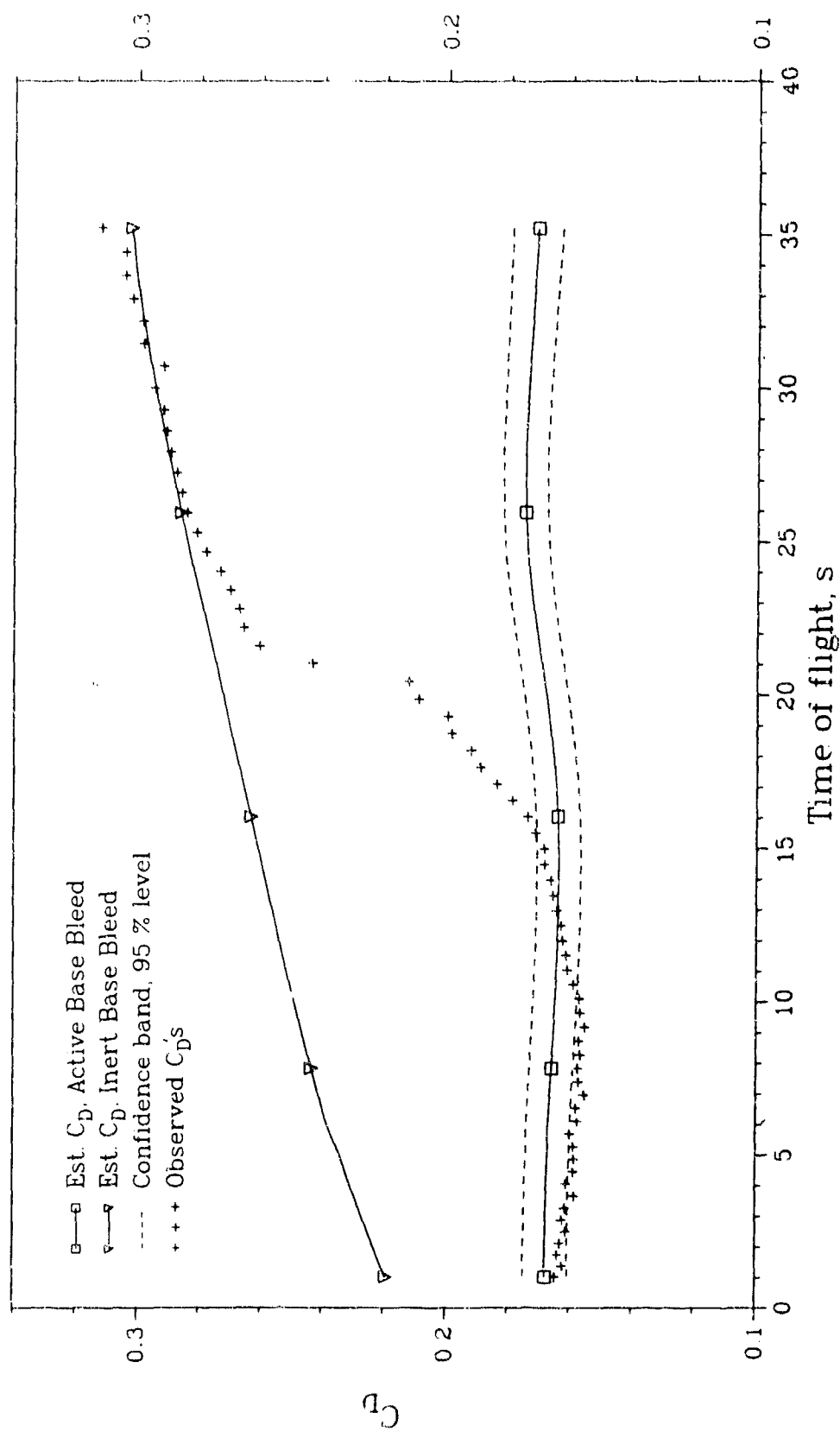


Figure 10

EFFECT OF GRAIN CHARACTERISTICS  
ON RANGE OF ARTILLERY PROJECTILES  
WITH BASE BLEED

Slobodan Jaramaz, Milojko Injac  
Military Technical Institute, Belgrade Yugoslavia

Abstract In this paper the basic points of mathematical model for determining range of artillery projectiles with base bleed are presented. After verification of given model by comparison computational results with experimental data, calculations effects of some characteristics of base bleed on range have been carried out. The range dependence of given projectile on number of grain segments, burning rate, internal diameter and grain length are determined. Presented model can be used for selecting characteristics of grain that will give the maximum range of projectile and for decreasing number of experimental testing for determining that characteristics.

Nomenclature

$a$	- burning law constant
$A_B$	- surface of projectile base
$A_g$	- area of burning surface
$A_i$	- surface of base bleed orifice
$A_{ref}$	- reference projectile surface
$B$	- constant given by equation (15)
$b$	- coefficient in burning law
$C_D$	- total drag coefficient
$C_{DBB}$	- projectile base drag coefficient during burning of grain
$\Delta C_D$	- decreasing of projectile base drag
$C_{D0}$	- projectile total drag coefficient without working of base bleed
$C_{LIM}$	- constant in equation (10)
$C_K$	- quantity given by equation (10)
$D$	- drag
$d_i$	- diameter of base bleed orifice
$d_u$	- internal diameter of grain
$e$	- burnt web of grain at time $t$
$e_0$	- total web of grain
$e_1$	- burnt web in the first phase of burning
$e_2$	- burnt web in the second phase of burning
$I$	- impuls defined by equation (6)
$I_{LIM}$	- limited value of impuls
$J$	- experimental constant
$k$	- specific heat ratio of burning products
$l$	- arc corresponding to the angle
$l_z$	- grain length

$\dot{m}_B$	- mass flux of the air at the base of projectile
$\dot{m}_g$	- mass flux of burning products from burning surface
$M$	- molecular weight of burning products
$M_\infty$	- Mach flight number
$n$	- exponent in burning law
$N$	- number of grain segments
$D$	- burning surface circumference
$p_B$	- pressure in base bleed
$p_d$	- base pressure
$R$	- external grain radius
$r$	- burning rate
$r_0$	- internal grain radius
$R_1$	- grain radius at the crossing of burning from the first into the second phase
$R_g$	- gas constant of burning products
$t$	- time
$t_g$	- vorkig time of base bleed
$t_z$	- ignition delay
$T_g$	- burning products temperature
$V_\infty$	- projectile velocity
$x_1$	- half distance between grain segments
$y$	- geometric parameter defined on figure 3
$y_2$	- geometric parameter defined on figure 4
$\alpha$	- angle at time $t$ defined on figure 2
$\beta$	- half angle of projectile afterbody
$\rho_b$	- grain density
$\rho_\infty$	- air density

## 1. Introduction

Increasing of range of artillery projectiles by base bleed unit is the subject of many theoretical and experimental investigations in past few years [1, 2, 3, 4, 5, 6, 7, etc]. Projectiles with base bleed increase their range as a consequence of decreasing their base drag. Base bleed unit blow burning products of grain into recirculation zone behind the projectile and increase pressure in it. Effect of increasing projectile range is in so much as expressive as the fraction of base drag in total drag is bigger, that is, as the projectile is of better aerodynamical shape.

Selecting of geometrical and physico-chemical characteristics of grain of base bleed is the basic problem which should be solved during the design of such projectiles. For that purpose in this paper the mathematical model which enable selecting of these characteristics is developed. Special attention is dedicated to the effect of some grain characteristics (shape, dimensions, burning rate etc.) on the expected range.

## 2. Mathematical model

The mathematical model, developed in this paper is based on the engineering point of view on selecting of grain characteristics. In continuation of this paper, the basic points of mathematical model connected with the general considerations about

problem, determining of pressure in base bleed unit, changing of burning surface as a function of burnt web and procedure for range calculation are given.

### 3. General considerations about problem

For the projectile trajectory calculation differential equations of projectile motion according the modified point mass trajectory model are used [9]. As a consequence of existing base bleed unit, in the equation of motion projectile drag given by

$$D = C_D \cdot \frac{\rho_\infty V_\infty^2}{2} A_{ref} \quad (1)$$

relation is changed. During the working time of base bleed unit ( $t_g$ ), drag coefficient is changed for  $\Delta C_D$  t.e.

$$\Delta C_D = C_{DB0} - C_{DB8} \quad (2)$$

On that way the total drag coefficient during the time  $t_g$  is given by relation

$$C_D = C_{D0} - \Delta C_D \quad (3)$$

In general case base drag coefficient for the projectile with base bleed is function of several parameters:

$$C_{DB8} = f(M_\infty, I, T_g, A_i, \beta, M, \dots) \quad (4)$$

From the equations (2), (3) and (4) it is obvious that for determining value of  $C_D$  it is necessary to know values for  $C_{D0}$ ,  $C_{DB0}$  and  $C_{DB8}$ . Assuming that values for  $C_{D0}$  and  $C_{DB0}$  are known from theoretical calculations, windtunnel or firing testings, the relation for  $\Delta C_D$  is [7]

$$\Delta C_D = C_{DB0} (1 - e^{jI}) C_K \quad (5)$$

Impuls  $I$  is given by equation:

$$I = \frac{\dot{m}_g}{\dot{m}_B} \quad (6)$$

Here mass fluxes  $\dot{m}_g$  and  $\dot{m}_B$  are

$$\dot{m}_g = r A_g \rho_g \quad (7)$$

$$\dot{m}_B = V_\infty A_B \rho_\infty \quad (8)$$

In the expression (7) burning rate  $r$  is a function given by:

$$r = a + b p_g^n \quad (9)$$

In relation (5)  $j$  is function of Mach number, t.e.,  $j = f(M_\infty)$  and its value is determined from firing testings while for first approximation data for  $j$  can be taken from [7] and [1].

From experimental results it could be seen that when impuls  $I$

is bigger than some limited value, effect of base bleed is decreasing. Based on that fact in expression (5) exists parameter  $C_K$  which can be defined as [7]:

$$\begin{aligned} C_K &= 1.0 & I &\leq I_{\text{LIM}} \\ C_K &= 1 - \left( \frac{I}{I_{\text{LIM}}} - 1 \right)^2 C_{\text{LIM}} & I &> I_{\text{LIM}} \end{aligned} \quad (10)$$

Constants  $I_{\text{LIM}}$  and  $C_{\text{LIM}}$  should be defined for every projectile. For instance, for projectile 155 mm ERFB/BB these values are:  $I_{\text{LIM}} = 0.007$  and  $C_{\text{LIM}} = 0.25$  [7].

From equations (2) through (10) it is obvious that decreasing of base drag  $\Delta C_D$ , in general case, is complex function and for given projectile it can be expressed by relation [3]:

$$\Delta C_D = f(I, p_g, M_\infty) \quad (11)$$

For defining  $\Delta C_D$  it is useful to consider theoretical calculations instead of using only time consuming and expensive experimental testings. We'll first consider the way for determining impuls, t.e., the pressure  $p_g$  in base bleed chamber.

#### Pressure in base bleed chamber

Pressure in base bleed chamber is defined using the equality of mass flux of burning products through the orifice and mass flux of gas formed due to the grain burning. Mass flux of gas due to the grain burning is given by expression (7).

Mass flux of burning products through the base bleed orifice is a function of ratio of pressure on projectile base during the flight and pressure in base bleed chamber. For the case when the following inequality is satisfied

$$p_d/p_g > \left( \frac{2\kappa}{\kappa+1} \right)^{\frac{\kappa}{\kappa-1}} \quad (12)$$

flow of gas from the chamber is subsonic. Then the mass flux of burning products is given by equation

$$\dot{m}_i = \rho A_i \left( \frac{p_d}{p_g} \right) \sqrt{\frac{2\kappa}{\kappa-1} R_g T_g \left[ 1 - \left( \frac{p_d}{p_g} \right)^{\frac{\kappa-1}{\kappa}} \right]} \quad (13)$$

When the inequality is not satisfied flow of gas from the chamber is supersonic and mass flux is defined by expression

$$\dot{m}_i = \frac{B \cdot p_g \cdot A_i}{\sqrt{R_g T_g}} \quad (14)$$

In the expression constant  $B$  is defined as:

$$B = \sqrt{\kappa} \left( \frac{2}{\kappa+1} \right)^{\frac{\kappa+1}{2(\kappa-1)}} \quad (15)$$

It should be emphasized that occurring of supersonic flow in the orifice is undesirable phenomenon for increasing the range. The supersonic flow make impossible recirculation of burning products behind projectile and increasing of projectile base pressure. This is the fact which should be given special care during the selection of grain characteristics.

Equalizing mass fluxes  $\dot{m}_g$  and  $\dot{m}_i$  we get the equation for the pressure in the base bleed chamber which is solved iteratively.

#### Change of grain burning surface as a function of burnt web

Existing base bleed grains have a cylindrical shape with certain number of segments. External and end grain surfaces are inhibited so that burning is performed on internal surfaces and slots. View of one grain with three segments is presented on figure 1.

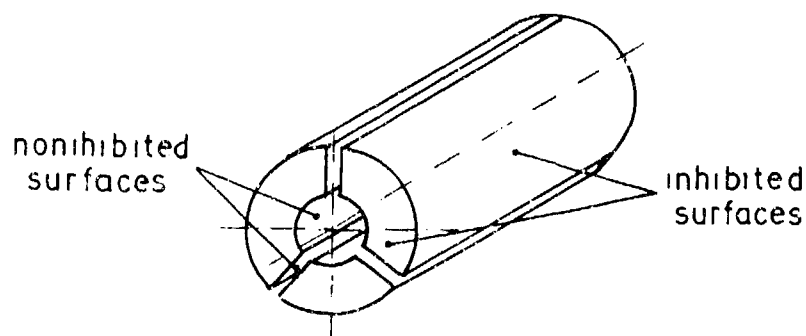


Figure 1. View of base bleed grain

Number of grain segments can be different and change of burnt surface as a function of burning web will be given for the case of grain with three segments. Given relations are valid also for grain with  $N$  segments but in the next relations value for angle  $60$  should be replaced with value of  $360/(2N)$  and number of individual elements of burning surface is also function of  $N$ .

Cross section of grain with three segments is given on figure 2.

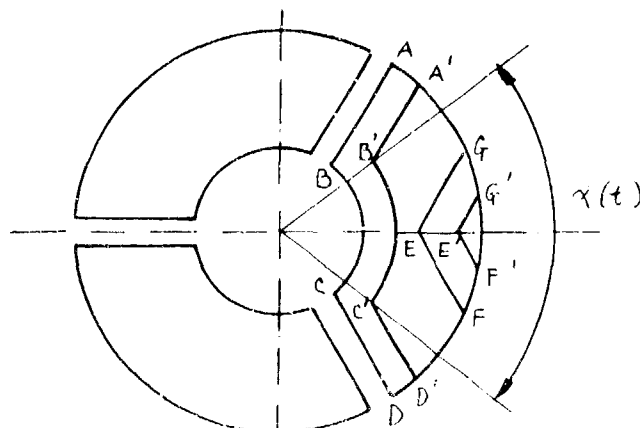


Figure 2. Grain burning phases

In general case grain burning is performing in two phases. Each phase has its own shape of grain cross section. At the beginning of the first phase grain cross section is composed from three equal segments with contours ABCD. Circumference of cross



section of burning surface for one segment at some moment of first phase is composed from two straight lines  $A'B'$  and  $C'D'$  and arc  $B'C'$ . At the end of the first phase arc  $B'C'$  and angle  $\alpha(t)$  disappear. At the beginning of the second phase circumference of cross section of burning surface is composed from two straight lines  $GE$  and  $EF$ . At the some moment of the second phase circumference of cross section of burning surface is composed from two straight lines  $G'E'$  and  $E'F'$ .

Burnt web thickness  $KA(e)$  at the some moment at the first phase should be equal to the thickness  $AG$  (Figure 3). Then it follows:

$$x_1 + e = (r_0 + e) \sin \left( 60^\circ - \frac{\alpha}{2} \right) \quad (16)$$

From equation (16) it follows that the burnt web thickness in the first phase is:

$$e = \frac{r_0 \sin(60^\circ - \frac{\alpha}{2}) - x_1}{1 - \sin(60^\circ - \frac{\alpha}{2})} \quad (17)$$

The first phase end occur when  $\alpha = 0$ . The total burnt web thickness in the first phase is:

$$e_1 = \frac{r_0 \sin 60^\circ - x_1}{1 - \sin 60^\circ} \quad (18)$$

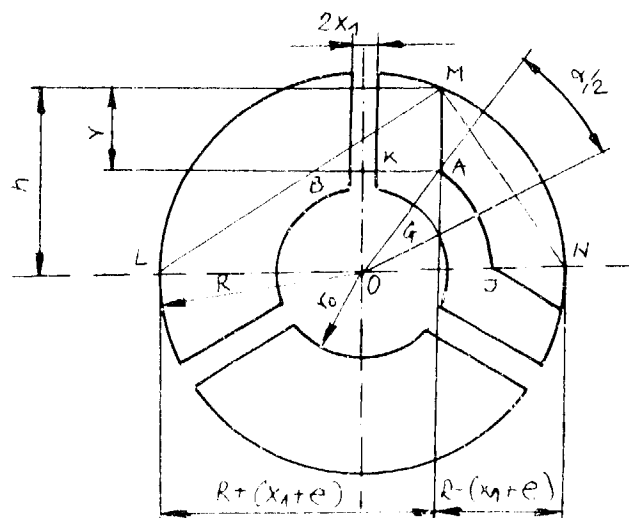


Figure 3. First phase of burning

We should calculate the circumference of segment cross section at one moment of the first phase. The height ME at the triangle LMN is the mean geometrical value of  $LE = R + (x_1 + e)$  and  $EN = R - (x_1 + e)$

$$l_n = \sqrt{R^2 - (x_1 + e)^2} \quad (19)$$

From the triangle ADB it follows that  $\sin(60^\circ - \frac{\alpha}{2}) = \frac{x_1 + e}{r_0 + e}$   
Then  $\frac{\alpha}{2} = 60^\circ - \arcsin \frac{x_1 + e}{r_0 + e}$ . Beside that

$$AE = (r_0 + e) \cos(60^\circ - \frac{\alpha}{2}) \quad (20)$$

PAGE 7

$$y = ME - AE = \sqrt{R^2 - (r_0 + e)^2 \sin^2(60^\circ - \frac{\alpha}{2})} - (r_0 + e) \cos(60^\circ - \frac{\alpha}{2}) \quad (21)$$

The arc length AJ is

$$l = \frac{2\pi}{360^\circ} \alpha (r_0 + e) \quad (22)$$

Now, the circumference of grain cross section in the first phase is given by expression:

$$O_I(t) = 6y + 3l \quad (23)$$

The area of grain burning surface of length  $l_2$  is:

$$A_{gI} = O_I(t) l_2 \quad (24)$$

From the figure 4 it can be seen that the total thickness of burnt web in the second phase is:

$$e_2 = (R - R_1) \sin 60^\circ \quad (25)$$

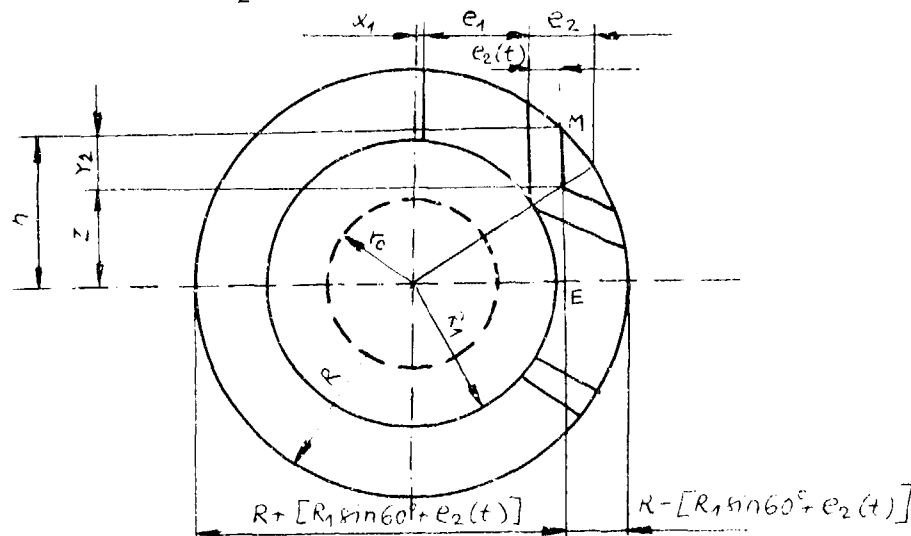


Figure 4. Second phase of burning

In the last equation  $R$  is radius on which arc disappear from the cross section profile and this radius is equal

$$R_1 = r_0 + e_1 \quad (26)$$

Here  $e_1$  is given by expression (18).

By the procedure similar that which is applied for burning in the first phase we get:

$$y_2(t) = h - z_1 - \sqrt{R^2 - [R_1 \sin 60^\circ + e_2(t)]^2} - [R_1 \cos 60^\circ + e_2(t) \tan 60^\circ] \quad (27)$$

$$O_{II}(t) = 6 y_2(t) \quad (28)$$

$$A_{gII}(t) = O_{II}(t) l_2 \quad (29)$$

It should be emphasized that the second phase of grain burning of this geometry need not occur depending on dimensions and

number of segments. Then the contour of grain segment cross section for the whole time of burning is composed of straight lines and the arc.

#### Procedure for determining range

For determining decreasing of projectile base drag coefficient during the grain burning it is necessary to know several different quantities. First, we should know quantities which are dependant on projectile design characteristics and characteristics of grain i.e. aerodynamic coefficient as a function of Mach number,  $C_D = f(M_\infty)$ , and values of  $I_{LIM}$ ,  $C_{LIM}$ ,  $a$ ,  $b$  and  $n$ . These quantities we get from experimental testings in wind tunnel and closed vessel, firing testings and theoretical calculations. For trajectory calculations it is also necessary to know values for  $I$ . For calculations  $p_g$  it is necessary to equalize equation (7) with equations (13) or (14) depending on condition (12). Because of nonlinearity of these equations calculation is performed iteratively with checking condition (12).

The calculation procedure is given on figure 5.

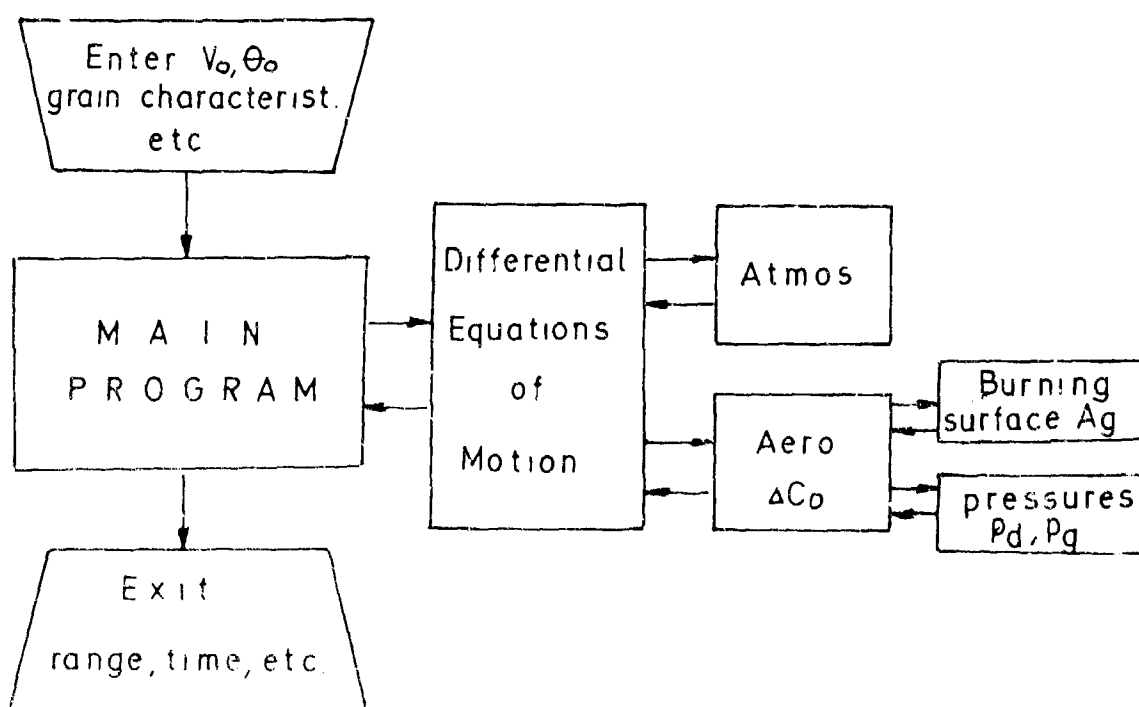


Figure 5 Schematic representation of the calculation procedure

Because the calculation procedure is iterative, the end of burning is reached when the web given by the next expression is burnt.

$$e_0 = \int_{r=0}^{r=R} r dr = R^2 - r_0^2$$

(30) PAGE 9

The time of grain burni is also calculated from the expression (30)

The iterative procedure can be presented on the following way:

- a) assume  $p$  ( $p_{g1} = p_d + \Delta p$ )
  - b) calculation  $r = a + b p_{g1}^n$
  - c) calculation  $e = dr/dt$
  - d) calculation  $Ag = f(e)$
  - e) impuls calculation  $I = \dot{m}_g / \dot{m}_B$
  - f) calculation of decrease of base drag  $\Delta C_D = f(I)$
  - g) base pressure calculation  $p_d = p_\infty [1 - k M_\infty^2 (C_{D80} - \Delta C_D)]$
  - h) ratio calculation  $p_d / p_{g1}$
  - j) calculation  $p_{g1}$  by equations (13) or (14)
- If  $|p_{g1} - p_{g1-1}| < \epsilon_{pg}$  the iterative procedure is finished. If this condition is not satisfied we repeat steps from (h) to (j). After the calculation of burnt web we perform the calculation of next step until we don't satisfy the equation (30).

### 3. Effect of grain characteristic on range

For determining the effect of grain characteristics on range of artillery projectiles with base bleed program, based on the mathematical model which basis is previously given, is subjected to the verification by comparing its results with experimental data for one real projectile. The basic data for projectile and grain are:

#### Projectile

Caliber	155 mm
Mass	46.04 kg
Length	861 mm
Muzzle velocity	897.4 m/s
Elevation	50

#### Grain

Number of segments	3
Mass	1.045 kg
Length	0.0717 m
External diameter	0.117 m
Internal diameter	0.0435 m

The difference between realized and calculated projectile maximum range is 0.09 % which shows that this way of calculation of the range of projectile with base bleed is enough reliable and convenient for determining the effect of grain characteristics on range.

We'll consider the effect of next grain characteristics.

- number of segments
- burning rate
- internal diameter

- length

Beside that we'll consider and effect of the diameter of base bleed orifice and delay of grain ignition. For all these considerations shape of grain will be cylindrical with slots, external and end grain surfaces will be inhibited and external diameter will retained constant.

Number of segments. Number of segments was changed from 2 to 12. The dependance of range on number of segments is presented on figure 6. From the figure it can be seen that maximum ranges are realized with grains which are composed from 6 to 8 segments. For given grain dimensions both burning phases occur when number of segments is greater than 5. Increasing range with grain

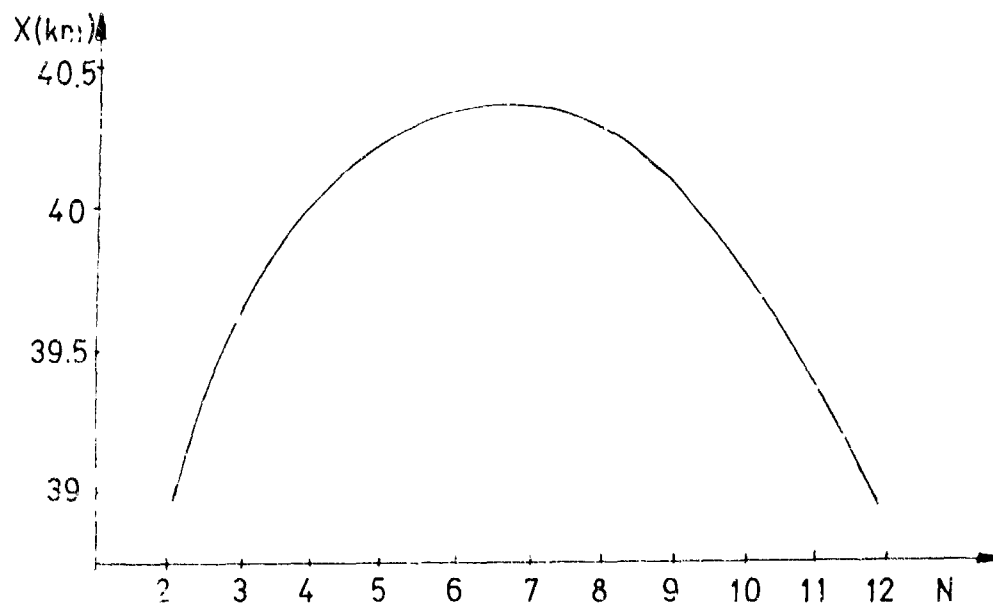


Figure 6. Range dependance on number of segments

consisting of 6 segments comparing with common grain number of segments (3) is 750 m or about 2%. Effect of the others grain characteristics on range is defined for grains with 3 and 6 segments.

Burning rate. Burning rate reflects effect of the grain chemical composition on range. For the grain with common composition constants in the burning law have following values:  $a = 0.00077$  m/s,  $b = 2.12 \cdot 10$  m/(sPa<sup>n</sup>),  $n = 0.66$ . The effect of burning rate on the range is defined by changing value of  $a$  which reflects the effect of exothermic reactions which take place beneath burning surface at low pressures. The dependance of calculated range on the burning rate for grains with 3 and 6 segments is given on the figure 7. From the figure it can be seen that change  $a$  for about 190% increase the range for the grain with 3 segments for 1370 m (3.5%), and for the grain with 6 segments for 435 m (1.1%). At given conditions the dependance of the range on

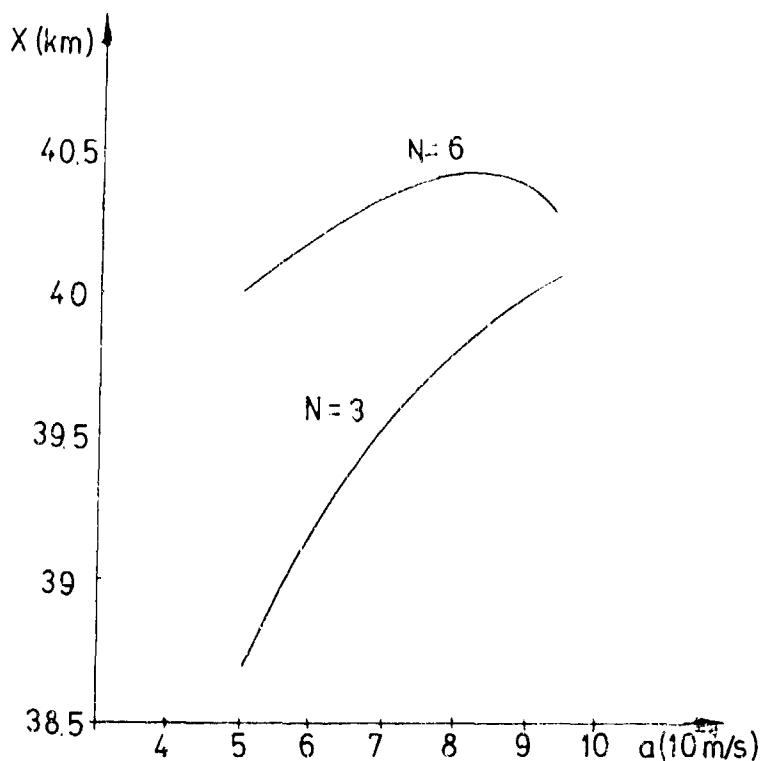


Figure 7. Range dependence on burning rate

for the grain with 3 segments has ever increasing character and for the grain with 6 segments this dependence has maximum.

Internal diameter. The dependence of range on the grain internal diameter is presented on the figure 8. For the grain with

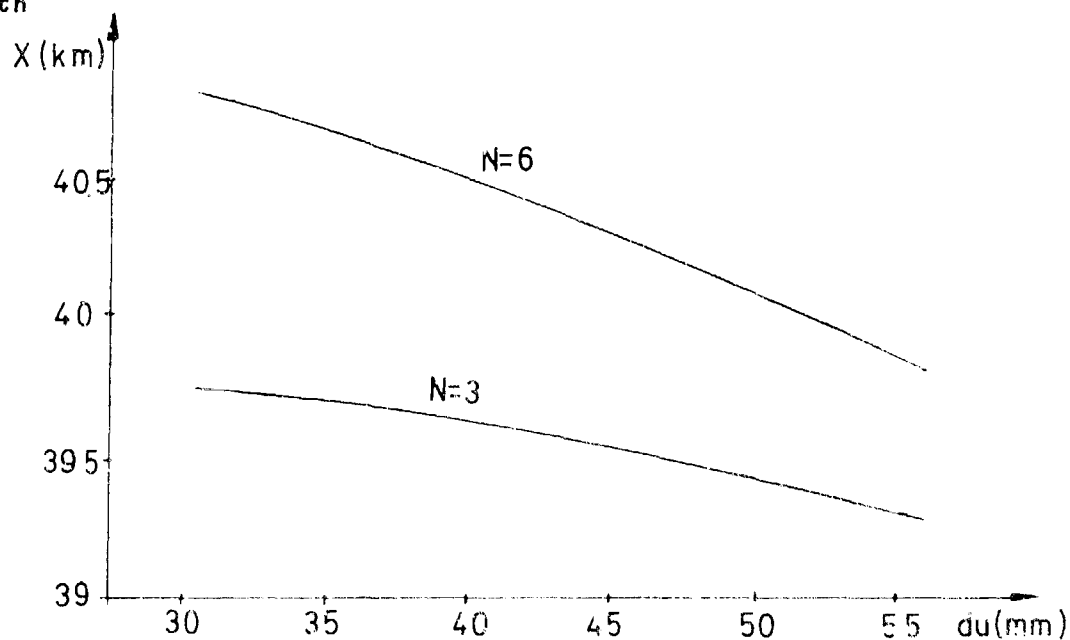
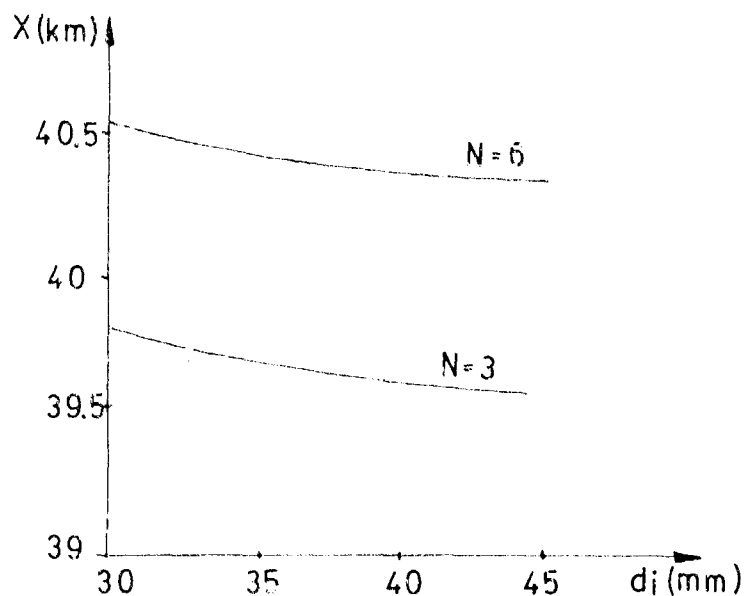
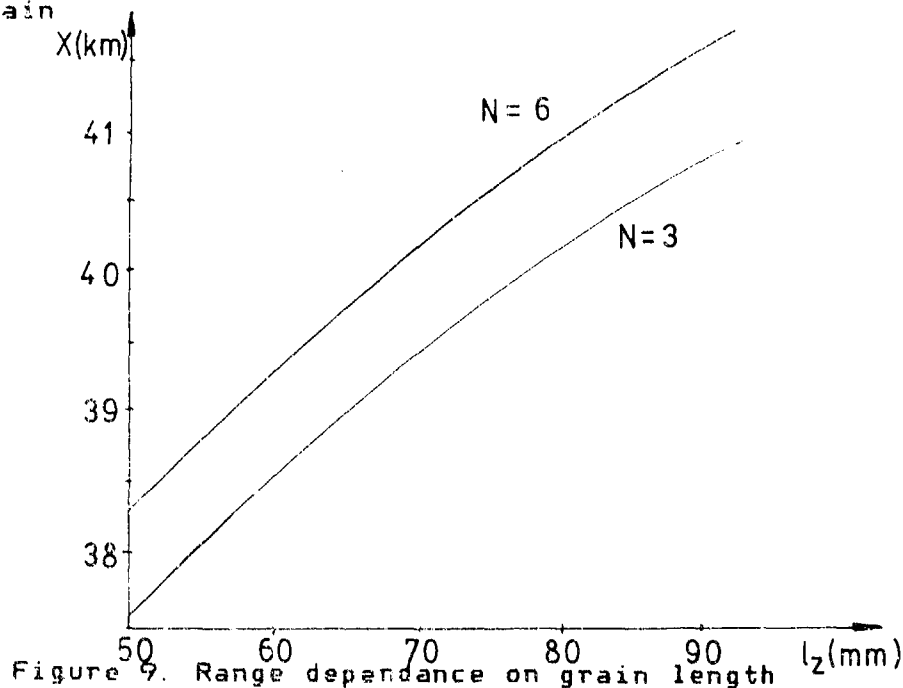


Figure 8. Range dependence on grain internal diameter

3 segments the change of grain internal diameter from 0.03045 to 0.05655 m (85.7%) gives decreasing of range for about 490 m (1.2%) and for grain with 6 segments the same change of internal

diameter gives decreasing of range for about 105 m (2.6%).

Length. The dependance of range on grain length for grains with 3 and 6 segments is given on the figure 9. The change of grain



length from 0.0502 to 0.0932 m (85.7%) gives increasing of range for grain with 3 segments for about 3400 m (8.6%). For the grain with 6 segments the same change of grain length gives increasing of range for 3400 m (8.4%).

Diameter of base bleed orifice. Effect of the base bleed orifice on range is given on the figure 10. With increasing the diameter of base bleed orifice the projectile range is decreasing. So for the grain with 3 segments the change of diameter of base bleed orifice from 0.0435 on 0.03115 m (28.5%) gives increasing of range for about 200 m (0.5%), and for the grain with 6 segments the same change of diameter gives increasing of range for about 180 m (0.45%).

Delay of grain ignition. The range dependance on delay of grain ignition is presented on figure 11. For grains with 3 and

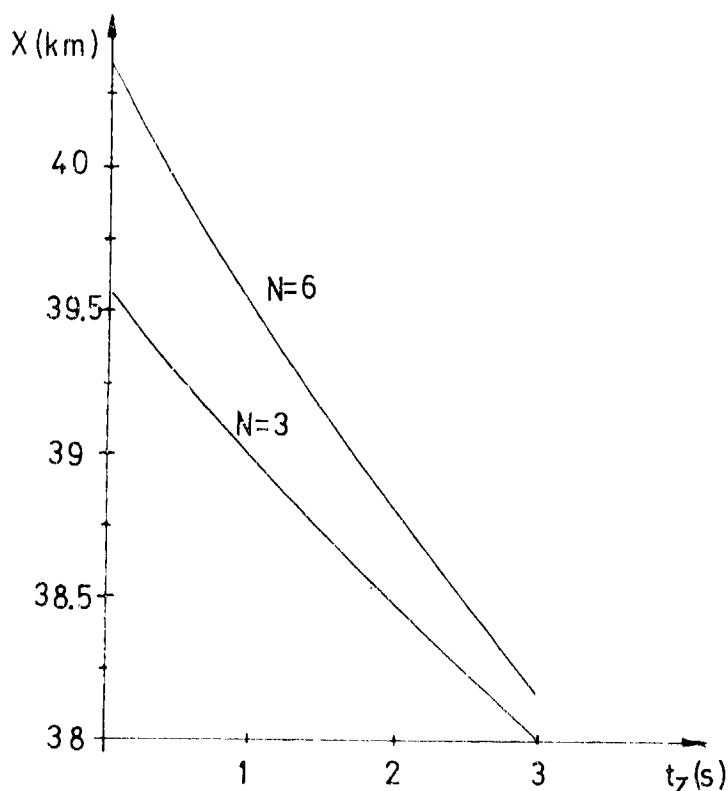


Figure 11. Range dependance on grain delay

6 segments ignition delay of 3 s gives the decreasing of range for 1600 m and 2200 m, t.e 4 and 5.5% respectively. These results show the significance of successful working of base bleed ignitor.

#### 4. Conclusions

On the basis of previously said it can be concluded

1. The developed method for range calculation of artillery projectiles with base bleed enables determining the effect of basic grain characteristics on range



- 2 Using given method it is possible to perform selection of the best grain characteristics and decrease the number of experimental testings for their determining.
- 3 On the basis of considered effects it is pointed on the range in which the characteristics should be kept.

## References:

- [1] Murthy, S.N.B. (ed.). Aerodynamics of Base Combustion, Progress in Astronautics and Aeronautics, Vol 40, New York, 1976.
- [2] Lundhal K, Bartelson N.: Base Bleed, A System to Increase Range and Decrease Ballistic Dispersion, Proceedings of the 3rd International Symposium on Ballistics, Karlsruhe, 1977.
- [3] Hellgren R.V.: Range Calculation for Base Bleed Propellants, Proceedings of the 6th International Symposium on Ballistics, Orlando, 1981.
- [4] Fox J.H.: A generalised Base Flow Analysis with Initial Boundary Layer and Chemistry Effects, AEDC-TR-79-46, ADA 072683, 1979.
- [5] Sahu J.: Numerical Computations of Supersonics Flow over Cylindrical Afterbodies with Base Bleed, Proceedings of the 9th International Symposium on Ballistics, Shrivenham 1986.
- [6] Schilling H.: A simple Theoretical Approach for Base Bleed Calculations, Proceedings of the 9th International Symposium on Ballistics, Shrivenham 1986.
- [7] On the Development of Base Bleed Motors for the SRC-ERFB-MK10 MOD 2 Projectile, SRC-BB-R/D-1710, 1983.
- [8] Hellgren R.V.: Basflodesprojektiler Bonberakningsprogram och Effektivitetsjamforelser (Base Bleed Projectiles: Range Calculation Program and Efficiency Comparisons) Research Inst. of National Defence, 1983, Stockholm
- [9] NATO Surface-to-Surface Artillery Panel the Modified Point Mass Trajectory Model Document AC/225 (Panel IV) D/161.
- [10] Bowman S.E. and Clayden W.A.: Reduction of Base Drag by Gas Ejection, RARDE report 4/69, 1969.

# DISCUSSION FOR TWO IMPORTANT PARAMETERS OF A BASE BLEED PROJECTILE

PROF. XIFU GUO

Dept. Engineering Thermal Physics & Aerodynamics.

East China Inst. of Technology NANJING, CHINA.

## ABSTRACT

The burning rate of a propellant and the ignition time of an igniter are two important parameters of base bleed projectile. They are greatly concerned with the extended range and the dispersion of the projectile. So far there is no reference related in determining the two parameters theoretically. In scientific practice, however the two important problems have been urgently needed to be solved.

Firstly, the paper presents the significance of selecting the burning rate of a propellant, the relationship of the physical essence of reduced drag of the base bleed between bleed parameters. The one-sidedness of analyzing the effect of reduced drag with the burning rate as a mark has been analyzed, and to analyze thoroughly the effect of reduced drag of the base bleed, the concept of the impulse of reduced drag rate is presented. The principle selecting the burning rate is to achieve the maximum rate of extended range on condition that the launch parameters of the projectile are fixed and influence of the spinning effect of the projectile is considered, or, the burning rate when the maximum impulse of reduced drag rate is gained is defined as the optimum.

Secondly, two principles of determining the ignition time of the igniter are given: the time of the igniter is no less than the time of second ignition time of propellant; the range dispersion caused by dispersion of second ignition time does not affect the overall range dispersion of shots. Based on these mentioned above, formulation of determining the ignition time of igniter have been developed.

Finally, examples are given on how to determine those two parameters. This paper provides theoretical basis for the optimum design in the development of base bleed projectile, these formulations have been used to analyze and design, and show satisfactory result.

## 1. DETERMINATION OF BURNING RATE OF PROPELLANT OF BASE BLEED PROJECTILE.

### 1.1 Presentation of Question

In the course of designing a base bleed projectile, we often reference the burning rate obtained to select and design the burning rate of this projectile. This method takes the absolute magnitude of the burning rate as a basis, but does not consider the specific structure and launch condition of the base bleed projectile, therefore it is not all-round. Based on the base flow character of the base bleed projectile and the reducing drag mechanism, this paper describes the selection principle and specific method of burning rate of a base bleed projectile.

### 1.2 Significance of Selecting Burning Rate

The burning rate equation of the base bleed propellant is

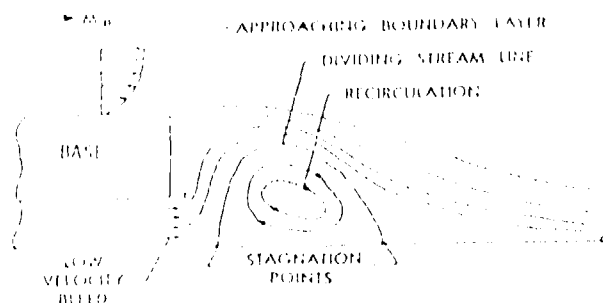


FIGURE 1. Schematic illustration of base flow with base bleed

$$r_f = a_1 + a_2 P_{mot}^{a_3} \quad (1)$$

where  $r_f$  — burning rate;  $a_1, a_2$  — burning equation coefficients;  $a_3$  — exponent of burning equation;  $P_{mot}$  — pressure inside the base bleed motor.

The gas of the base bleed propellant exhausts into the base "dead-air" region with very low velocity, so that the base bleed pressure could be raised and the base drag could be decreased. We measure operation of ejecting gas for raising base pressure with mass flow  $\dot{m}$ , it is

$$\dot{m} = r_f \rho_f A_f \quad (2)$$

where  $\rho_f$  — density of base bleed propellant;  $A_f$  — burning area of the base bleed propellant, as shown in Fig.1, after the gas ejects into dead air region, the flow state in the trailing flow region could be changed, so that the dividing streamline of the dead air region could be extended, flow deflection angle could be diminished, then the base pressure could be raised and the base drag could be decreased. However, the overall effect on raising the base pressure by the base bleed is related to the state of trailing flow region without base bleed. When the structure of the projectile is specified, the state of trailing flow region is related to the state of boundary layer of afterbody and the Mach number of incoming flow. The larger the Mach number of incoming flow, the larger the deflection angle of dividing streamline, the lower the base pressure. Therefore, the base ejecting gas could change the state of flow in trailing flow region, extend the dividing streamline and decrease the deflection angle if the mass flow would be increased. As stated above, the effect of base bleed on increasing base pressure and decreasing base drag depends on not only the mass flow  $\dot{m}$  of the bleed but also the state of flow in trailing flow region without bleed, in other words, it depends on  $M_\infty, v_\infty \rho_\infty$ . We measure the overall influence of the two factors with the bleed parameter  $I$ . It is defined as:

$$I = \frac{\dot{m}}{\rho_\infty v_\infty A_b} \quad (3)$$

where  $A_b$  — base area of the projectile;  $\rho_\infty$  — density of incoming flow;  $v_\infty$  — velocity of incoming flow.

Relationship between  $I$  and  $P_b$  is shown in Fig.2

It is known from above analysis that the effect of bleed is expressed by  $\dot{m}$ . It is related to not only  $r_f$  but also  $\rho_f$  and  $A_f$ . But overall effect of bleed on raising the base pressure depends on the bleed parameter  $I$ . Therefore, we could get the following conclusions:

1. Only if the structure and launch parameters of projectile, as well as the character of bleed propellant are the same, it is significant to consider the effect of burning rate on extended range and compare with each other.
2. For projectiles with different structure (including base bleed unit), bleed propellant and launch conditions, it is not appropriate to compare burning rate. For example, there are two base bleed units, the burning rate of one unit is 1.2 mm/s, the burning area is 100 mm<sup>2</sup>, the burning area of other unit is 200 mm<sup>2</sup>. If their other conditions are the same

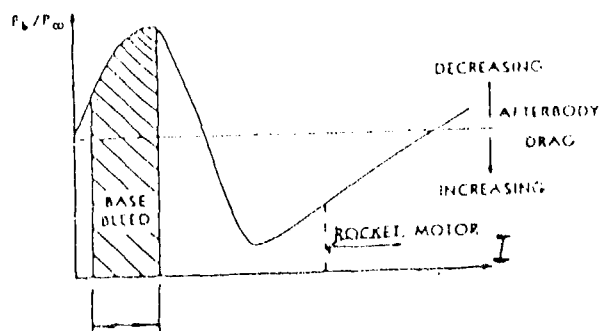


FIGURE. 2 Base pressure vs bleed parameter

and they both keep the same  $\dot{m}$  and  $I$ , then the reduced drag effect of the second projectile would be the same as that of the first one, but its burning rate is only 0.6mm/s. So, it is not all-round to simply compare the burning rate and not to consider other conditions, even it is possible to make mistakes in design.

3. It is reasonable to compare the bleed effect with the value of  $I$  in any case.

### 1.3 Selection Principle of Burning Rate

The selection principle of burning rate should be: in the condition of certain launch parameters, the overall effect of base bleed along the overall trajectory is to obtain the maximum extended range rate. Launch parameters mainly include the initial velocity, and angle of departure. These two parameters influence the velocity, Mach number, air density and pressure along the trajectory, that is,  $v_\infty$ ,  $M_\infty$ ,  $\rho_\infty$  and  $p_\infty$ . At up leg, with time increasing,  $v_\infty$ ,  $M_\infty$  and  $\rho_\infty$  would decrease. Since  $M_\infty$  is changeable along overall trajectory, so that the drag coefficient is changeable along overall trajectory.  $M_\infty$  would influence the effect of reducing drag.

At up leg, in the process of the projectile flying towards the apex of trajectory, air pressure decreases. Since the base bleed is subsonic flow, change of ambient pressure influences the change of the motor pressure. When the former decreases, the latter also decreases. So, the burning rate is reduced.

We know that

$$I = \frac{\dot{m}}{\rho_\infty v_\infty A_b}$$

At up leg,  $\rho_\infty$ ,  $v_\infty$  decrease gradually. If the change of burning area of the bleed propellant is not large that is, the change of  $\dot{m}$  is not large, then in the process of projectile flight, the value of  $I$  would continuously increase, the value of  $p_b/p_\infty$  would be reduced, so that the base drag would be increased. In the process of projectile flight, if we change the burning area, so that, and in  $\rho_\infty$ ,  $v_\infty$ ,  $A_b$  would be changed, but we make the value of  $I$  always be  $(p_b/p_\infty)_{\max}$ , in other words,  $I = I_m$ , then, we can gain the effect maximum extended range. The burning area formula which satisfies this condition is:

$$\frac{\dot{m}}{\rho_\infty v_\infty A_b} = I_m = \text{const} \quad (4)$$

$$A_b = \frac{\dot{m}}{\rho_\infty v_\infty I_m} = \frac{\rho_\infty}{\rho_f} \cdot \frac{v_\infty}{r_f} I_m A_b$$

Since  $\rho_\infty / \rho_f$  and  $v_\infty / r_f$  all decrease,  $I_m A_b$  is constant,  $A_b$  decreases gradually. That is why we design the burning area of the base bleed propellant which reduces along the trajectory. At the trajectory, if the value of  $I$  has some change, in order to get larger extended range effect, we must keep  $I$  is adjacent to  $I_m$ .

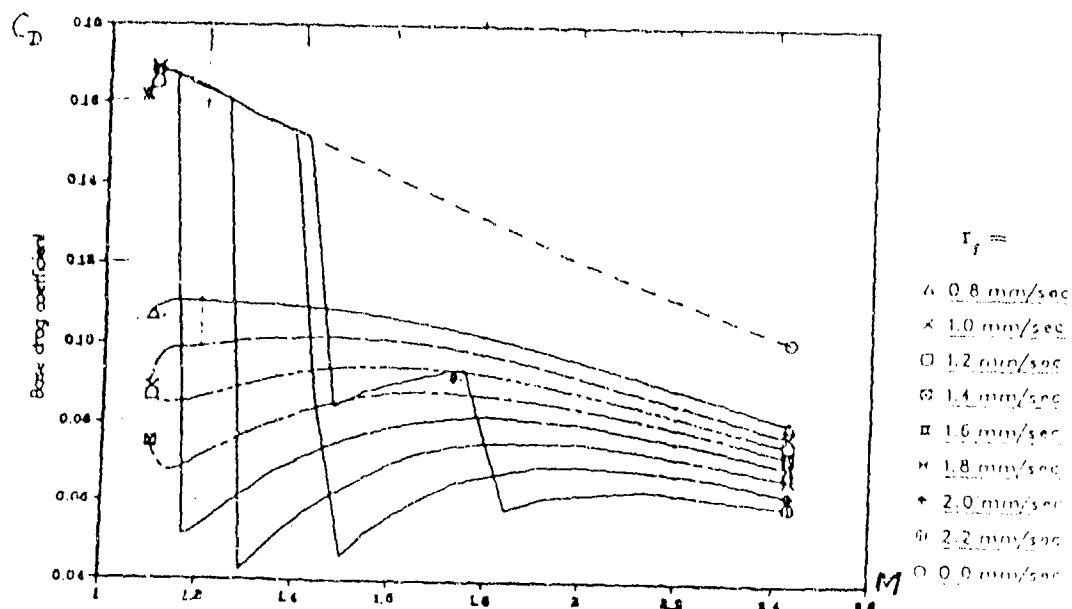


FIGURE 3 Base drag vs flight Mach number

For the bleed propellant with certain weight, the burning rate is related to the burning time of base bleed unit. The higher the burning rate, the shorter the burning time. The lower the burning rate, the longer the burning time. The combined influence of base bleed on the extended range rate is concerned with two parameters, they are the reduced drag rate and burning time, as shown in Fig.3, the burning rate influences the base drag and burning time. Its combined influence on extended range rate is not certain to be large. In order to express this influence, we use the concept of Impulse of reduced drag rate. It is defined as:

$$S_{RI} = \int_0^{t_b} \frac{R_n - R_b}{R_n} dt \quad (5)$$

where  $R_n$  - projectile drag without bleed,  $R_b$  - projectile drag with bleed;  $t_b$  - burning time. Substitute drag expression to Eq. (5), we get

$$S_{RI} = \int_0^{t_b} I_R dt \quad (6)$$

where

$$I_R = \frac{C_{D_n} - C_{D_b}}{C_{D_n}} \quad (7)$$

$C_{D_n}$  - drag coefficient without bleed,  $C_{D_b}$  - drag coefficient with bleed. In approximate calculation, we set

$$S_{RI} = I_{RCP} t_b \quad (8)$$

$$I_{RCP} = \frac{\sum_{i=1}^n I_{R_i}}{n} \quad (9)$$

or we take integrated average value

$$I_{RCP} = \frac{\int_0^{t_b} I_R dt}{t_b} \quad (10)$$

In comparison with schemes, if  $S_{RI}$  reaches maximum, then, this scheme is the optimum one obtaining the maximum extended range effect. In the stage of scheme demonstration and initial design, the influence of the spin effect must be considered in selecting the burning rate. The influence of spin on burning rate is related to the structure of base bleed unit and spin velocity. For general spin stabilized projectile, the spin velocity may increase the burning rate about thirty percent. In a word, the principle of selecting burning rate could be expressed as the following: under the condition of specific projectile launch parameters, considering the influence of spin effect, we acquire the burning rate corresponding to the maximum extended range rate. Mathematically, it can be expressed: we gain the burning rate which corresponds to the maximum impulse of reduced drag rate  $S_{RI}$ .

#### 1.4 Method of Determination of Burning Rate

Method of determination of burning rate may be completed by using electric computer program. In order to understand the calculation procedure clearly, we explain it step by step:

1. Determine the launch parameters of projectile: (1) Initial velocity; (2) Angle of departure; (3) Structure of projectile; (4) Weight of projectile.
2. Determine the structure of base bleed unit initially: (1) Structure size of base bleed unit; (2) Propellant weight; (3) Propellant structure and burning mode; (4) Propellant density.
3. Calculate ballistic elements and meteorological elements of base bleed projectile by given parameters.
4. Calculate  $\dot{m}$  from point to point along trajectory.
5. Calculate  $I$  from point to point along trajectory.
6. Calculate  $p_b/p_\infty \sim I$  curve.
7. Calculate curve of base drag coefficient vs  $M$  or  $t$ .
8. Calculate curve of overall drag coefficient vs  $M$  or  $t$ .
9. Calculate  $S_{RI}$ .
10. Calculate the overall range.
11. Compare schemes and determine burning rate.

Example.

Suppose: projectile length 900 mm, boattail length 90 mm, projectile diameter 155 mm, base diameter 145 mm, projectile mass 43.5 kg, initial velocity 827 m/s. Structure of base bleed propellant: two segments, radial burning, outside diameter of the base bleed unit 120 mm, inside diameter 45 mm. By using procedure mentioned above, obtain the optimum burning rate corresponding the maximum range, which is between 1.8 mm/s and 2.0 mm/s.

## 2. DETERMINATION OF IGNITION TIME OF IGNITER OF BASE BLEED PROJECTILE

### 2.1 Presentation of Question

The propellant of base bleed projectile is ignited by the gas with high temperature and high pressure in bore of a gun. When projectile leaving the muzzle, pressure rapidly drops from hundreds of atmospheres to one atmosphere, the burning propellant blown out is possible. In order to ensure the propellant ignition, we install igniter inside the base bleed unit. It can ignite the propellant once again outside the gun tube to make the propellant burn normal. This is so-called secondary ignition. Based on exterior ballistics and dispersion theory of shot, this paper discusses burning time of igniter as well as theory and method which are used to determine the dispersion scope of the secondary ignition time of propellant.

### 2.2 Principle of Determination of Burning Time of the Igniter

TABLE 1

$E_x$ ( m )	80	100	150
$t_i$ ( s )	0.35	0.41	0.57
$E_{t_b}$ ( s )	0.05	0.063	0.094

The principle of determination of the burning time of igniter is:

1. assure that the propellant can be ignited reliably; 2. decrease the influence of secondary ignition time dispersion of the propellant on overall range dispersion as small as possible. In view of the ignition burning process of the propellant of base bleed projectile, the burning time of igniter must be not smaller than the secondary ignition time of the propellant, otherwise, the propellant can not be ignited once again. That is not assure that the propellant can be ignited reliably. Suppose the maximum secondary ignition time of the propellant is  $t_{b_{2max}}$ , the minimum burning time of the igniter is  $t_{imin}$ , to assure that the propellant is ignited reliably, there must be

$$t_{imin} \geq t_{b_{2max}} \quad (11)$$

Because of the propellant composition, the pressure inside the base bleed unit, performance of igniter, environment conditions and dispersion of initial velocity, the secondary ignition range has certain dispersion. In order to decrease the influence of secondary ignition range dispersion on overall range dispersion, the igniter should assure that the secondary ignition range dispersion for the propellant basically does not influence the overall range dispersion. Suppose the secondary ignition range is  $x_b$ , average velocity in scope of  $x_b$  is  $v_{cp}$ , the secondary ignition time is  $t_{b_2}$ , then

$$x_b = v_{cp} t_{b_2}$$

$$\Delta x_b = \Delta v_{cp} t_{b_2} + \Delta t_{b_2} v_{cp}$$

Suppose the probable error of average velocity dispersion is  $E_{vcp}$ , the probable error of secondary ignition time dispersion is  $E_{tb_2}$ , the probable error of secondary ignition range dispersion is  $E_{xb}$ , then

$$E_{xb} = \sqrt{(t_{b_2} E_{vcp})^2 + (v_{cp} E_{tb_2})^2}$$

Form calculation, we know

$$(v_{cp} E_{tb_2})^2 \gg (t_{b_2} E_{vcp})^2$$

Therefore, when considering the secondary ignition range dispersion, we only need to consider the secondary ignition time dispersion. That is

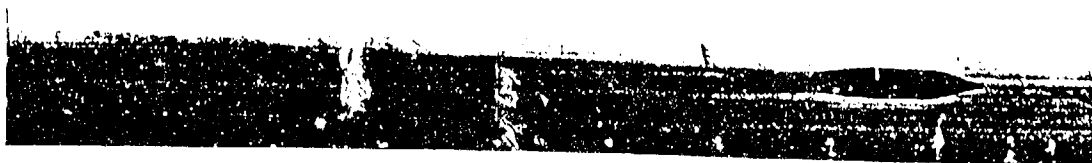
$$E_{xb} = v_{cp} E_{tb_2} \quad (12)$$

### 2.3 Method of Determination of Ignition Time of Igniter.

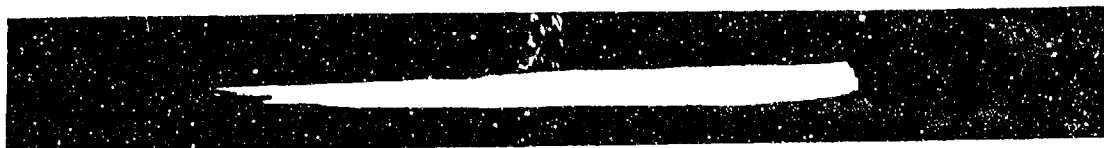
Now, based on two above-mentioned principles, we determine the ignition time of igniter.

1. Determination of maximum burning time of igniter

Suppose the average value of the secondary ignition time of the propellant is  $t_{bcp}$ , probable error of the secondary ignition time dispersion is  $E_{tb_2}$ . So, the maximum ignition time of igniter  $t_i$  is



(a)



(b)

FIGURE 4. Photograph with a burning igniter and inert propellant and photograph with a burning igniter and a burning propellant

$$t_i = t_{bcp} + 5E_{tb_2} \quad (13)$$

where

$$t_{bcp} = \frac{\sum_{i=1}^n t_{b_2 i}}{n} \quad (14)$$

$n$  - number of round;  $t_{b_2 i}$  - secondary ignition time of the  $i$ -th round,  $i = 1, 2, \dots, n$ .

2. Determination of secondary ignition time dispersion of propellant

The probable error of the overall range dispersion of shot is  $E_\Sigma$ . It can be expressed as follows

$$E_\Sigma^2 = E_x^2 + E_{xib}^2$$

Where  $E_x$  - the range probable error of gun,  $E_{xib}$  - the range probable error caused by the secondary ignition range dispersion of propellant. Since the range of base bleed projectile is related to the drag coefficient  $C_D$ , that is

$$X = f_1(C_D) \quad (16)$$

When the secondary ignition time is different, the drag coefficient is also different. That is

$$C_D = f_2(t_b) \quad (17)$$

The relationship between the probable error  $E_{tb}$  of the secondary ignition time of propellant and the range probable error  $E_{xib}$  is



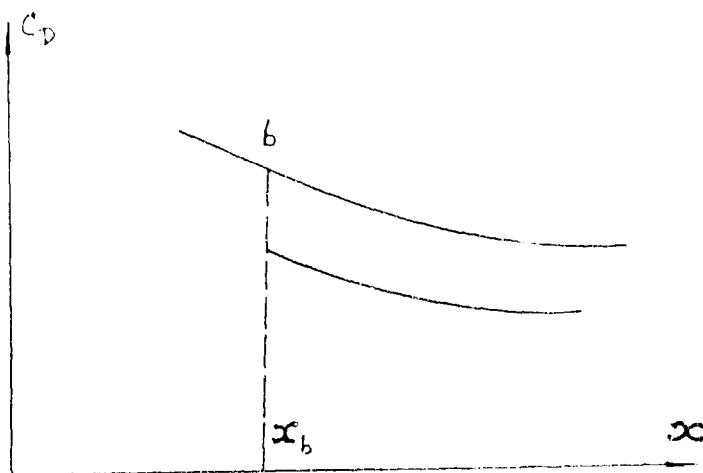


FIGURE 5.  $C_D \sim x$  curve

Point b is the secondary ignition location of the propellant.

$$E_{xib} = \frac{\partial X}{\partial C_D} \frac{\partial C_D}{\partial t_b} E_{ib} \quad (18)$$

where  $\frac{\partial X}{\partial C_D}$  - the sensitivity factor of range on the drag coefficient;  $\frac{\partial C_D}{\partial t_b}$  - the sensitivity factor of drag coefficient on the secondary ignition time. Suppose  $E_{xib} = 0.1 E_x$ , it is ensured that  $E_{xib}$  does not influence  $E_{\Sigma}$ . Substitute it into the formula, we have

$$E_{ib} = \frac{0.1 E_x}{\frac{\partial X}{\partial C_D} \frac{\partial C_D}{\partial t_b}} \quad (19)$$

The formula (19) can be used to calculate the secondary ignition time dispersion. After determination of tactical and technical targets, overall scheme of gun system is also determined.  $E_x$ ,  $\frac{\partial X}{\partial C_D}$ ,  $\frac{\partial C_D}{\partial t_b}$  are all known. Thus, we can determine  $E_{ib}$  by the formula (19).

#### 2.4 Calculation of $\frac{\partial X}{\partial C_D}$ and $\frac{\partial C_D}{\partial t_b}$

##### 1. Calculation of $\frac{\partial X}{\partial C_D}$

###### a. Method based on ballistic equations

Using the motion equations of the projectile, and taking  $C_D$  to change one unit, we can calculate  $\frac{\partial X}{\partial C_D}$

###### b. Method based on correction coefficient

The expression of ballistic coefficient  $c$  is

$$c = \frac{id^2}{G} 10^3$$

we can get

$$\frac{\partial X}{\partial C_D} = \frac{\partial X}{\partial C} \frac{d^2 10^3}{C_{Dn} G} \quad (20)$$

where  $\frac{\partial X}{\partial C}$  - the correction coefficient of range on ballistic coefficient;  $d$  - projectile diameter;  $G$  - projectile weight;  $C_{Dn}$  - drag coefficient under the condition of standard projectile.

$$2. \text{ Calculation of } \frac{\partial C_D}{\partial t_b}$$

we know

$$C_D = f_3(M), \quad M = f_4(t_b)$$

So,

$$\frac{\partial C_D}{\partial t_b} = \frac{\partial C_D}{\partial M} \frac{\partial M}{\partial t_b} \quad (21)$$

By using the above formula, we have two methods to calculate  $\frac{\partial C_D}{\partial t_b}$

$$a. \text{ Direct calculation of } \frac{\partial C_D}{\partial t_b}$$

Based on the aerodynamics of projectile or experiment, we can get  $C_D$ - $M$  curve. By using ballistic equations we can calculate  $M \sim t_b$  at trajectory, thus we can get  $C_D \sim t_b$  curve. From

this curve we obtain  $\frac{\partial C_D}{\partial t_b}$

$$b. \text{ Calculation of } \frac{\partial C_D}{\partial M}, \frac{\partial M}{\partial t_b} \text{ . recalculation of } \frac{\partial C_D}{\partial t_b}$$

By using ballistic equations we calculate  $M \sim t_b$  and  $\frac{\partial C_D}{\partial t_b}$

recalculate  $\frac{\partial C_D}{\partial t_b}$  .

## 2.5 Examples

Suppose diameter of a base bleed projectile  $d=155\text{mm}$ , its weight  $G=45\text{Kg}$ , initial velocity  $v_0=950\text{m/s}$ , departure angle  $\theta_0=45^\circ$ , flight up leg time  $t_1=46\text{s}$ , when range probable error  $E_x=80\text{m}$ ,  $100\text{m}$ ,  $150\text{m}$  find the maximum burning time  $t_i$  of igniter and probably error of its dispersion,  $E_{t_b}$ . Using above - mentioned methods we get  $t_i$  and  $E_{t_b}$  as shown in table 1.

## 2.6 Determination of Secondary Ignition Range of Propellant by Experiment

### 1. Method using smear camera

At the side of departure line, among the distance of 50-60 m, begin with 10 m from the muzzle, we locate smear cameras at 10 m interval. By comparison of photographs one with a burning igniter and an inert propellant and the other with a burning igniter and a burning propellant, we can determine whether the secondary ignition of the propellant would occur, as shown in Fig.4, a is the photograph only with burning igniter, b is the photograph

with both burning igniter and burning propellant.

## 2. Method using Doppler radar

Use a Doppler radar to measure velocity of the base bleed projectile among the range about 300-500m away from the muzzle, draw the  $C_D \sim x$  curve, to the curve, determine the secondary ignition distance of the propellant as shown in Fig.5.

## REFERENCE

1. Xifu Guo Etc, The Exterior Ballistic of Base Bleed Projectile, Ballistic Research Lab. of ECIT 1986
2. Hellgren, R. V., Range Calculation for Base Bleed Projectile, Proc. 6th Intern. Symp. Ball., Orlando, Fla., 1981
3. H. Schilling, A Simple Theoretical Approach for Base Bleed Calculation, Proc. 8th Intern. Symp. Ball., 1985

## A TWO-PHASE BASE BLEED BASE COMBUSTION MODEL AND ITS CALCULATION

Nan-yan Wang  
East China Institute of Technology  
Nanjing, P.R.C.

### 1. INTRODUCTION

The total drag for supersonic projectiles consists of shock wave drag, viscous drag and base drag. The base drag is a major contributor to the total drag and can be as much as 50-70% of the total drag. Thus, it is especially important to minimize this part of the drag. Base bleed is an effective means of reducing the base drag. The structure of the flow in base region is changed by a small quantity of low speed gas injected in to the dead-area.

The best review about base bleed is given by Murthy et al [1]. Bowman and Clayden have reported their experimental studies on supersonic flow over cylindrical afterbodies with gas injection in Ref.[2]. Recently Sahu has developed a new numerical method to compute the base region flow using Azimuthal-Invariant thin-layer N.S. equations, in which an iterative boundary condition procedure has been developed to determine the bleed exit boundary conditions. In Sahu's paper [3], the effects of solid phase fuel particle in the exit jet, fuel enthalpy of combustion and gas molecular weight have not been considered but those factors have shown their very important positions in base bleed function. Recently, Schilling has presented a simple theoretical approach for base bleed calculations in which boat-tail and burning equation of fuel are considered, but solid phase mass ratio, fuel enthalpy of combustion have not been considered.

The present paper describes a new model of base bleed with base combustion in which exit area ratio, flight Mach number, chamber stagnation temperature, jet gas molecular weight, solid mass ratio of exit two-phase mixture gas, enthalpy of combustion etc. have been considered. The predicted results show general agreement with the available experimental curves.

### 2. BASE BLEED GAS DYNAMIC MODEL

For a common projectile without base bleed function, the flow stream pattern

near the base section can be simply sketched out at Fig. 1-a. The dead area is separated by the separation streamline from the outside potential flow. One has plenty of reason to think that there is an interior separation streamline separating the dead area from the base injection flow in the case of the projectile with a base bleed function. See Fig. 1-b. At the end of the dead area, there is section area  $A_2$  which is not equal to zero, so that dead area becomes a hollow head-cut cone. The schlieren photographs from Ref. [2] may support the statement above, see Fig. 2.

The secondary burning phenomenon are observed in the tests very often. Solid-phase fuel in particle form mixed with gas-phase is burning along the jet path. One can consider that dynamic equilibrium has been reached at section  $A_2$ , where  $P_2 = P_s$ , and the burning of solid-phase fuel has been completed already.

Taking a control volume between section  $A_1$  and section  $A_2$ , see Fig. 3 Governing equations as follows. Continuity equation

$$\dot{m}_1 = \rho_{m1} u_1 A_1 = \dot{m}_2 = \rho_2 u_2 A_2 \quad (1)$$

Momentum equation

$$P_b(A_b - A_1) + P_1 A_1 - 2\pi \int_{r_1}^{r_b} r \cdot p_s(r) dr + 2\pi \int_0^L r \cdot \tau(x) dx - P_2 A_2 = \dot{m}_2 u_2 - \dot{m}_1 u_1 \quad (2)$$

Energy equation

$$H_{02} - H_{01} = \varepsilon \cdot \Delta H - \text{Heat lost to surrounding} \quad (3)$$

where solid-phase mass ratio

$$\varepsilon = \rho_p / \rho_m \quad (4)$$

$$\rho_m = \rho_s + \rho_p \quad (5)$$

The following equation can be easily transferred from Eq.(1)

$$\frac{P_1 A_1}{P_s A_2} = \sqrt{\frac{R_{m1} T_{01}}{R_2 T_{02}}} \cdot \frac{M_2 \left[ k_2 \left( 1 + \frac{k_2 - 1}{2} M_2^2 \right) \right]^{\frac{1}{2}}}{M_1 \left[ k_{m1} \left( 1 + \frac{k_{m1} - 1}{2} M_1^2 \right) \right]^{\frac{1}{2}}} \quad (6)$$

It is obvious that the gas-solid phase flow at section  $A_2$  should be in a equilibrium state, so that the following expressions can be quoted from Ref. [7].

$$R_{m1} = (1 - \varepsilon) R_s \quad (7)$$

where

$$R_s = R / \mu \quad (8)$$

and

$$k_{m1} = k_s \left[ \frac{1 - \varepsilon \left( 1 - \frac{C_p}{(C_p)g} \right)}{1 - \varepsilon \left( 1 - \frac{k_g C_p}{(C_p)g} \right)} \right] \quad (9)$$

The viscous term in Eq.(2) is much smaller than another pressure term, so it can be omitted for simplification purpose. Furthermore, the separation streamline can be considered as straight line for the time being. As there exist plenty of reliable methods to estimate pressure distribution in aerodynamics, such as shock expansion method, characteristic method et al.,  $p_s = p_s(x)$  in Eq.(2) can be assured of being solved. Among them, the following equation may be the simplest one [8].

$$\frac{p_s - p_a}{\frac{k}{2} p_a M_\infty^2} = \pm \left( 0.0016 + \frac{0.002}{M_\infty^2} \right) \beta_0^{1.7}$$

it can be rewritten as

$$\frac{p_s}{p_a} = 1 \pm k(0.001 + 0.0008 M_\infty^2) \left[ \left( \frac{57.3}{2L} \left( 1 - \frac{A_2}{A_b} \right)^{\frac{1}{2}} \right)^{1.7} \right] \quad (10)$$

where  $\bar{A}_2 = A_2 / A_1$ ;  $\bar{A}_b = A_b / A_1$ . The length of dead area  $\bar{L} = L / 2r_1$ . Minus or plus sign chosen in Eq.(10) is dependent on whether  $A_2$  less than  $A_b$  or not. For more general case, define

$$P_{s, ave} = \frac{2 \int_{r_2}^{r_b} r \cdot p_s(r) dr}{r_b^2 - r_2^2} \quad (11)$$

where

$$p_s(r) = f(\bar{L}, \bar{A}_b, \bar{A}_2, M_\infty) \quad (12)$$

can be obtained by accurate methods which are available wherever in aerodynamics. Then, Eq. (2) becomes

$$\bar{p}_b = \left( \frac{\bar{A}_2}{\bar{A}_b - 1} \right) \left[ 1 + \bar{p}_s \left( \frac{\bar{A}_b}{\bar{A}_2} - 1 \right) - \frac{\bar{p}_s}{\bar{A}_2} + k_2 M_2^2 - \frac{k_{m1} \bar{p}_s}{\bar{A}_1} M_1^2 \right] \quad (13)$$

where  $\bar{p}_s = P_{s, ave} / p_a$

Considering the specific heat of gas-solid mixture [7]

$$(C_p)_m = (1 - \varepsilon) (C_p)_g + \varepsilon C_p \quad (14)$$

and omitting the radiation heat loss to the surrounding from the control volume, Eq.(3) can be rewritten as

$$T_{02} = \left[ (1 - \varepsilon) + \varepsilon \frac{C_p}{(C_p)_g} \right] T_{01} + \varepsilon \frac{\Delta H}{(C_p)_g} \quad (15)$$

The authors of most available papers on base bleed like to use injection parameter  $I = m_1 / \rho_\infty u_\infty A_b$ , so does the author of the present paper. After simple derivation, one can obtain

$$I = \left( \frac{\bar{p}_s}{\bar{A}_b} \cdot \frac{M_1}{M_\infty} \right) \left[ \frac{k_s}{k_\infty} \cdot \frac{k_{r1}}{k_m} \cdot \frac{T_s}{T_{01}} \left( 1 + \frac{k_m - 1}{2} M_1^2 \right) \right]^{\frac{1}{2}} \quad (16)$$

where  $R$  and  $k$  are 0.287 kJ/kgK and 1.404 respectively for air.

### 3. SOLUTION OF THE EQUATIONS AND ADDITIONAL ASSUMPTIONS

There exist many semi-empirical expressions for estimating the base pressure without base bleed, one of them is from U.S Army BRL in 1981

$$\frac{P_b}{P_a} = \left[ 1 - 0.09 M_\infty^2 (1 - e^{-\bar{L}_{eff}}) \right] \cdot \left[ 1 + \frac{M_\infty^2}{4} \left( 1 - \bar{A}_b^2 \right) \right] \quad (17)$$

The cylinder length  $L_{cyl}$ , boattail shape and flighting Mach number are considered in this expression.

For this case without base bleed, then  $\bar{A}_2 = 0$ . If the contour of the dead area and Mach number are given, taking iteration to Eqs (12), (13) and (17), one can obtain the effective length of the dead area  $\bar{L}_{eff}$ . For the case with base bleed, one can assume the contour of dead area will change only in diameter, but not in the effective length.

According to Eq.(15), one can obtain the stagnation temperature of jet flow at section  $A_2$ .

Since most of the base bleed structures so far contain a subsonic or sonic nozzle, the pressure at exit section  $P_1$  is equal to the base pressure  $P_b$ . As the exit Mach number  $M_1$  is given, the parameters  $\bar{A}_2$ ,  $\bar{p}_1$  and  $\bar{P}_b$  can be solved by iteration method based on Eqs.(6), (12) and (13). For the purpose of comparison with experimental curves, injection flow rate ratio  $I$  is calculated by Eq.(16).

The whole calculating process has been completed by Program BLEED.

### 4. EXAMPLE

A projectile with 5 calibre cylinder without boattail.  $(C_p)_a = 1.0$  kJ/kg K,  $C_p = 0.7$  kJ/kg K, surrounding temperature  $T_a = 200$ K.

Following parameters have been considered as independent parameters in the calculation examples: flight Mach number  $M_\infty$ , jet gas molecular weight  $\mu$ , total temperature in the chamber  $T_{01}$ , solid-phase mass ratio  $\epsilon$ , fuel enthalpy of combustion  $\Delta H$ , and base bleed exit area ratio  $\bar{A}_b$ . The results and the comparisons with experiments are shown as following in sequence.

#### 4.1 The Effects of Exit Area Ratio

Taking  $\epsilon = 0$ , it means that pure gas or no secondary burning is considered. So that,  $T_{01} = T_{02}$ .

$\bar{A}_b = 16, 8$  and  $4$  have been accounted for in this example, the length of dead area  $L$  are obtained 10.296, 7.272 and 5.14 respectively. The results are shown on Fig 4. The pure gas is  $H_2$  whose molecular weight is 4, and total temperature  $T_{01}$  is taken 300K. The results of the wind tunnel test with a center nozzle by Reid and Hastings [2] are shown on Fig.5. Although they did not give the molecular weight and temperature, one can realize that the theoretical model works well indeed.

As the value of  $I$  is less than 0.003, the effect of the exit area on base pressure is negligible, which agrees with the conclusion from Ref. [9], (see Fig.6).

The similar curves can be found from Ref. [1] (see Fig. 62) and Ref.[4] (see Fig.4).

#### 4.2 The Effects of Jet Gas Molecular Weight

Two gases with molecular weight 4 and 28 respectively have been taken in the examples. Taking  $\bar{A}_b = 9$ , pure gas ( $\epsilon = 0$ ),  $T_{01} = T_{02} = 300K$ . The effective length of the dead area,  $L = 7.73$ , is obtained. The numerical results are shown in Fig.7, from which one can see that the lighter jet gas molecular weight will bring a better effect of drag reducing under the condition of flow rate  $I$  is not too large. Many experiment results have been found to support this conclusion. The experiment curves from Ref. [2] are shown in Fig.8 and 9.

#### 4.3 The Effect of Flight Mach Number

Two cases have been calculated. One case is that there is solid fuel particle unburned at the base bleed exit section, as well as the secondary burning phenomenon exists. The other case is under the condition that all the fuel is burnt out at the exit section.

Taking  $\bar{A}_b = 16$ ,  $T_{01} = 3000K$ ,  $T_s = 300K$ , solid mass ratio  $\epsilon = 0.5$ , fuel enthalpy of combustion  $\Delta H = 2000kJ/kg$ , jet gas molecular weight  $\mu = 30$ .

Flight Mach number 1.1, 1.5, 2.0, 2.5 and 3.0 are considered in calculating. Bleed jet Mach number is changed smoothly between zero and 1.0. The higher the flight Mach number, the larger the absolute value of  $(\partial \bar{P}_b / \partial I)_{I=0}$  that one can find from Fig. 10-a. So that the better effectiveness of drag reducing can be accomplished with higher Mach number that has been pointed out by wind tunnel tests.

For the other case,  $\bar{A}_b = 16$ ,  $T_{01} = T_{02} = 3000K$ , jet gas molecular weight  $\mu = 4$ . Four Mach numbers, 1.5, 2.0, 2.5 and 3.0 are calculated, the effective length of dead area are obtained with 11.3, 10.3, 9.8 and 9.4, respectively. Results are shown in Fig. 10-b.

Fig. 11 shows the wind tunnel test results, based on Ref. [9], in which Mach number was taken between 0.96 and 2.525.

Alternative test results one can find from Ref.[2] are quoted in Fig.12. Both Fig.10 of calculating and Fig.12 of experiments show the same tendency.

#### 4.4 The Effect of Stagnation temperature in Burning Chamber

Taking pure gas with  $\mu = 4$  and  $\bar{A}_b = 7$ , flight Mach number  $M_\infty = 2$ ,  $T_s = 200K$ . The stagnation temperatures are 300K, 1000K and 2000K are considered respectively. Fig.13 shows the calculating results in which one can find the higher stagnation temperature in chamber will bring the more effective base bleed function that has been confirmed by plenty of experiments.

The pure Helium gas test results with temperature of 290K and 3000K are given in Fig.14-a. As neither  $M_\infty$  number nor surrounding temperature  $T_s$



is reported in Ref.[2], the comparison with Fig.13 is limited qualitatively, yet it is generally satisfactory. Five different temperatures of Helium gas were taken in the test of which the results are shown in Fig. 14-b.

#### 4.5 The Effects of Solid Phase Fuel Particle Mass Ratio and the Fuel Enthalpy of Combustion $\Delta H$

Taking the first study about the effect of fuel particle mass ratio. In the calculating, taking  $A_b = 16$ ,  $M_\infty = 2.0$ , chamber stagnation temperature 2000K, jet gas molecular weight  $\mu^* = 30$ , adiabatic exponent  $k_g = 1.3$ , fuel enthalpy of combustion  $\Delta H = 3000\text{kJ/kg}$ .

Two cases of solid phase mass ratio  $\varepsilon = 0.5$  and  $0.8$  are considered. The results are given in Fig.15, from which one can find that the increasing of the base pressure will be more obvious for the larger mass ratio case. One can also find that the base pressure may be higher than surrounding atmosphere pressure in the case of certain large value of  $I$  value.

The next calculation is for the case of alternative fuel enthalpy of combustion, taking stagnation temperature  $T_{01} = 1000\text{K}$ , and solid phase mass ratio  $\varepsilon = 0.5$ , and the rest underlying data same as before. Four cases of enthalpy of combustion 1000, 2000, 3000 and 4000kJ/kg are considered in the calculating. (see Fig.16) The case with higher fuel enthalpy of combustion will be followed by better base bleed effectiveness.

Fig.17 is quoted from Ref.[10], whose author has done some tests at No.2 wind tunnel at ECIT. It is obvious that the present theory works well indeed.

#### 5. CONCLUSIONS

A. A practical base bleed combustion model has been given. In the present model the following factors have been considered: base bleed exit area, flight Mach number, stagnation temperature in chamber, solid mass ratio in jet, fuel enthalpy of combustion and jet gas molecular weight etc.

B. In the case of small jet mass flow rate, the effect of exit area on base pressure is negligible. In the case of certain mass flow rate, the larger exit area will be followed by better base bleed effectiveness.

C. The lower jet gas molecular weight of a base bleed instructure will be accompanied by a higher base bleed effectiveness.

D. The acceptance of base bleed instructure is encouraged at higher flight Mach number, in which condition the larger absolute value of  $(\partial \bar{P}_b / \partial I)_{I=0}$  is obtained.

E. When the stagnation temperature in the chamber is rising, the high-performance base bleed will be reached.

F. Either high value of solid particle mass ratio  $\varepsilon$ , or high value of fuel enthalpy of combustion will promote the base bleed function.

#### LIST of SYMBOLS

A Section area  
 $C_p$  Fuel specific heat

$(C_p)_g$	Gas specific heat
$H$	Heat enthalpy (kJ/kg)
$\Delta H$	Fuel enthalpy of combustion (kJ/kg)
$I$	Mass flow rate parameter
$k_{m1}$	Equivalent adiabatic exponent of gas-solid equilibrium mixture
$k_g$	Gas adiabatic exponent
$L$	Length of cylinder; length of dead area
$M$	Mach number
$\dot{m}$	Mass flow rate
$p$	pressure
$R_{m1}$	Equivalent gas constant of gas-solid equilibrium mixture
$R_g$	Gas constant of jet gas at section $A_j$
$r$	Radial coordinate
$u$	Flow velocity
$\varepsilon$	Solid mass ratio
$\rho_p$	Fuel density in gas-solid mixture
$\rho_x$	Gas density in gas-solid mixture
$\rho_m$	Gas-solid mixture density
$\mu$	Gas molecular weight
$\beta$	Semi-angle of conic dead area

#### Subscripts

1	Exit section
2	End section of dead area
a	Atmosphere
ave	Average value, see Eq.(11)
b	Base section
eff	Effective
g	Gas phase
m	Mixture
s	Side surface of dead area
o	stagnation condition
$\infty$	Free stream

#### REFERENCES

1. Murthy, S.N.B. etc. "Aerodynamics of Base Combustion", MIT Press, 1974
2. Bowman, J.E. etc. "Reduction of Base Drag by Gas Ejection", R.A.R.D.E. Report 4/69, 1969
3. Sahu, J. etc. "Numerical Computations Supersonic Flow over Cylindrical Afterbodies with Base Bleed", 9th ISB, 1986
4. Schilling, H. "A Simple Theoretical Approach for Base Bleed Calculations", 9th ISB, 1986
5. PuFa "An Analysis on the Potentiality of Drag-reducing-range-increasing and Its Possible Approach", Ballistics (in Chinese) vol. 3, 1986
6. Guo, Y.F. "Base Bleed Exterior Ballistics" (in Chinese), ECIT, 1986
7. Wang, Nan-yan. "A Analysis on the Impulse Loss of Solid-Propellant Rocket Engines", ACTA ARMAMENTARII (in Chinese) vol. 3, 1987.
8. KLASHOV, N.V. "Aerodynamics of Revolution", Science Press, (translated into Chinese) 1965
9. Qiu, Guang-chun etc. "A Study of Base Combustion Drag-reducing Properties and Aerodynamic Estimate Method", Ballistics (in Chinese) vol. 1, 1987
10. Din, Ze-sheng etc. "An Experimental Study on Supersonic Base Combustion Drag-reducing", Ballistics, (in Chinese) vol. 2, 1985
11. Zhang, Yan-qing "An Interior Ballistic Solution for Base Bleed Installation" Ballistics, (in Chinese) vol. 3, 1985

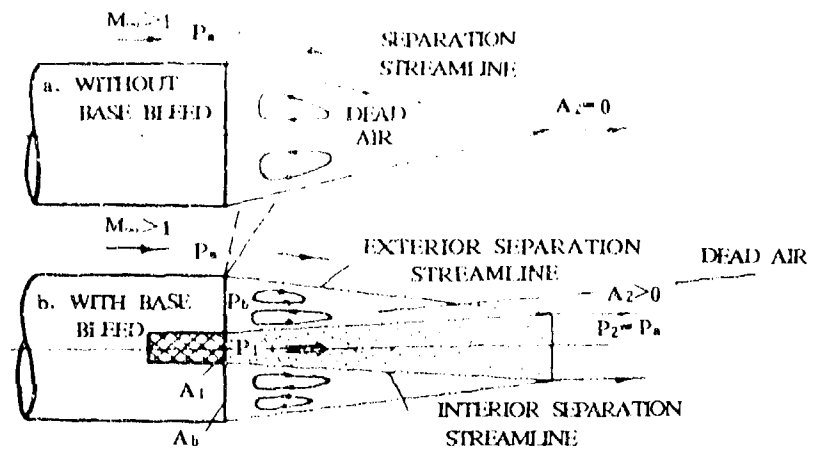


FIGURE 1. Qualitative sketch pattern in the base region

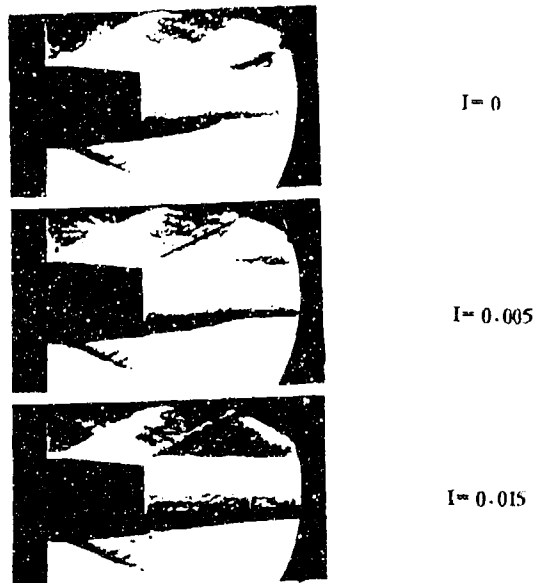


FIGURE 2. Schlieren pictures in the base region

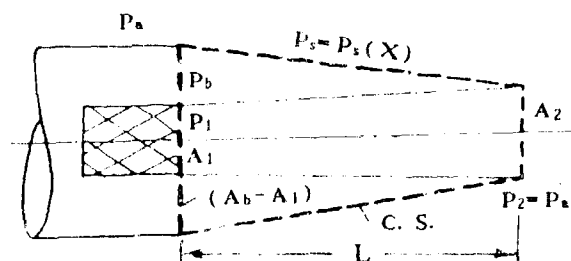


FIGURE 3. Sketch of control volume for base bleed model

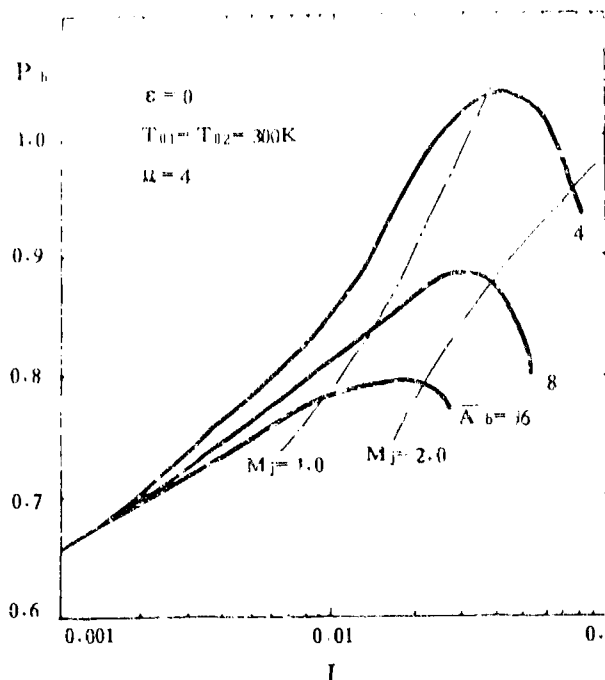


FIGURE 4. The effects of exit area on base pressure

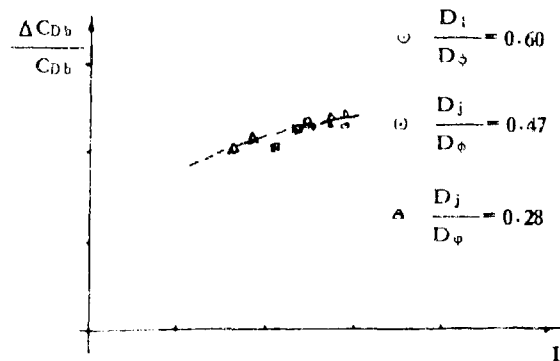


FIGURE 6. Experiment results from Ref. [9]

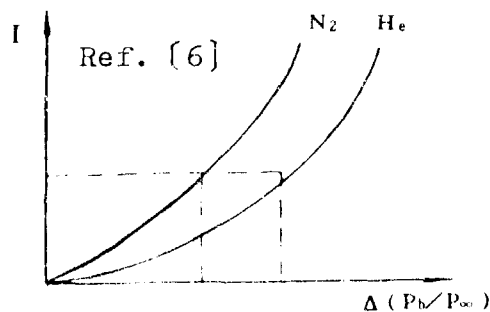


FIGURE 8. Experiment curves of base bleed with N and H

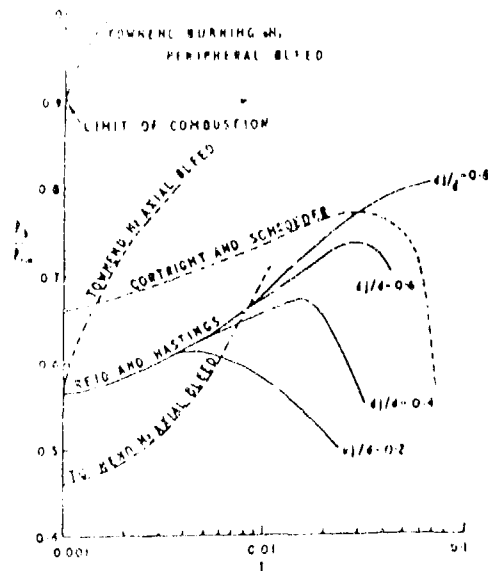


FIGURE 5. Reid and Hastings' experiment curves

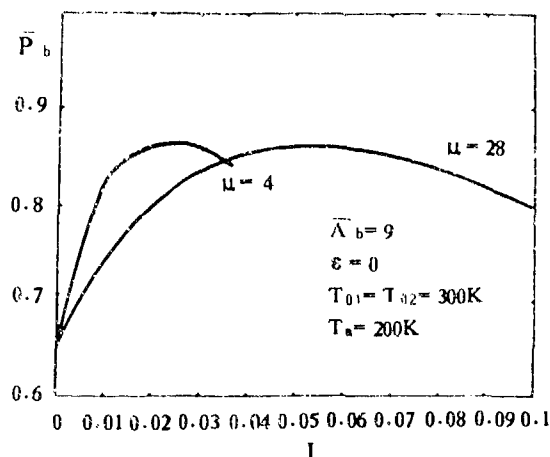


FIGURE 7. The effect of jet molecular weight on base pressure

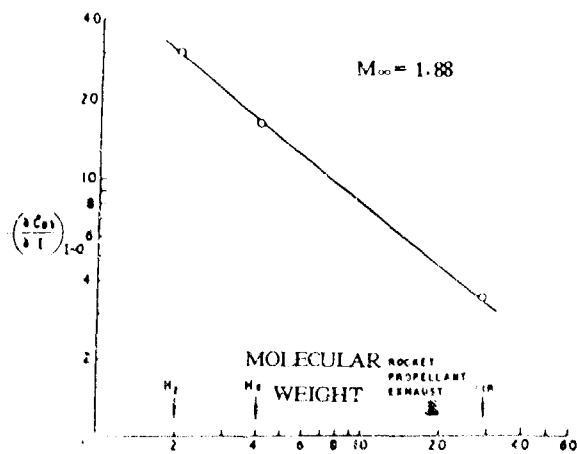
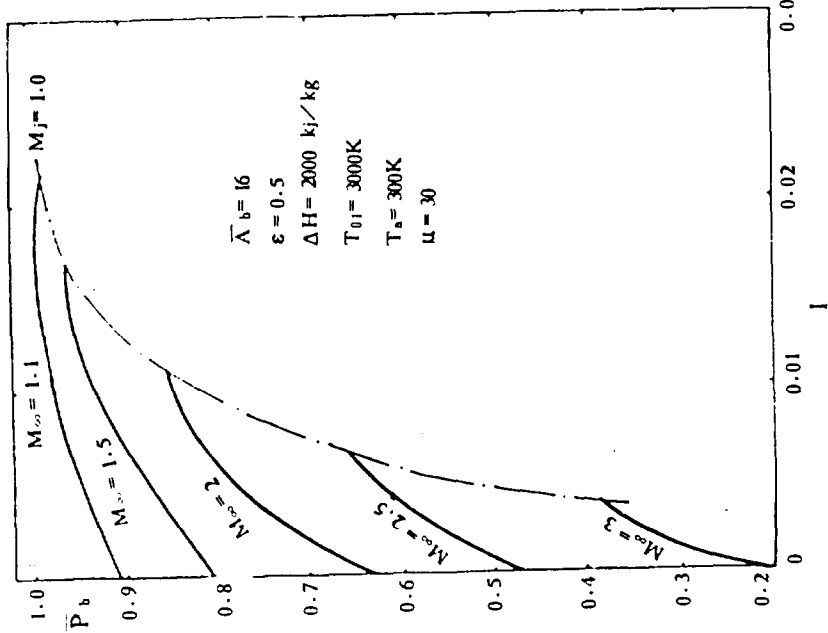
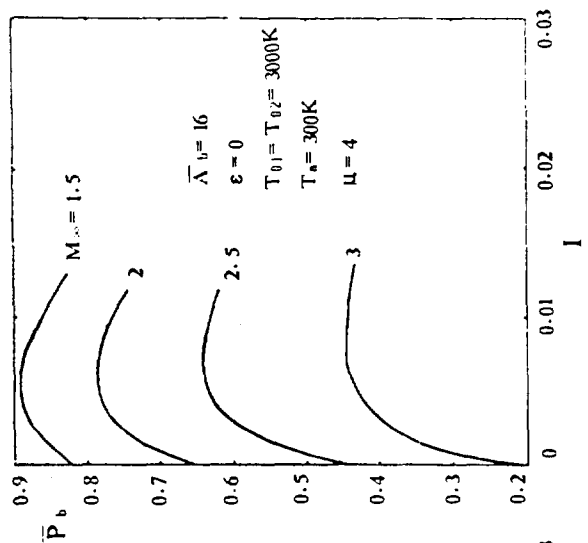


FIGURE 9. The effect of molecular weight, Ref. [2]



a.  $\epsilon = 0.5$  The effect of flight Mach number on base bleed



b.  $\epsilon = 0$

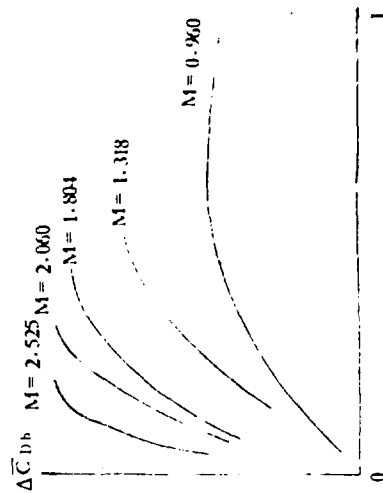


FIGURE 11. The effect of Mach number on drag reduction Ref. [9]

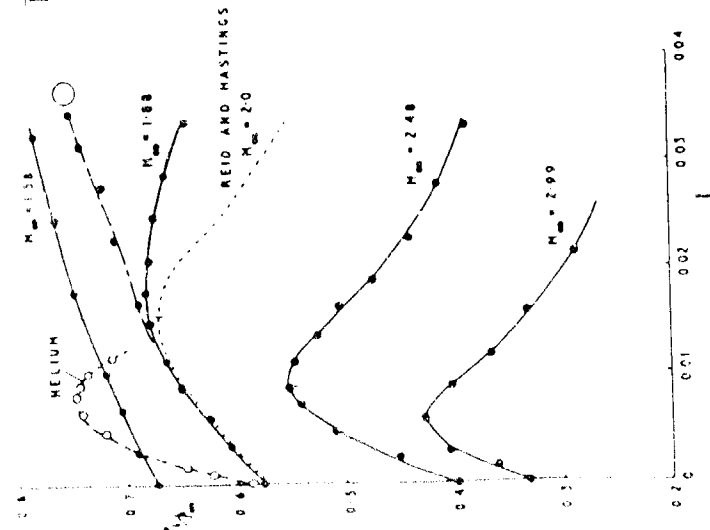


FIGURE 12. The experiment results of the effect of Mach number

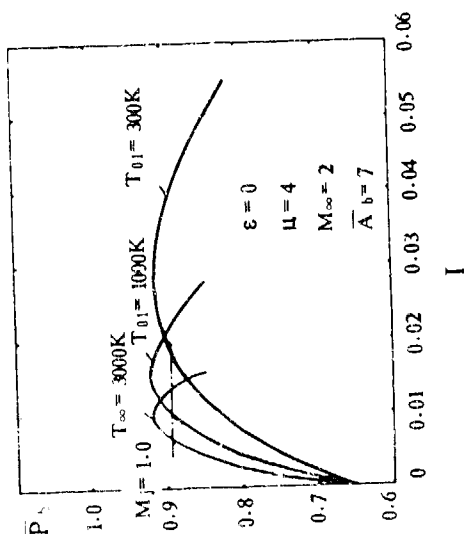
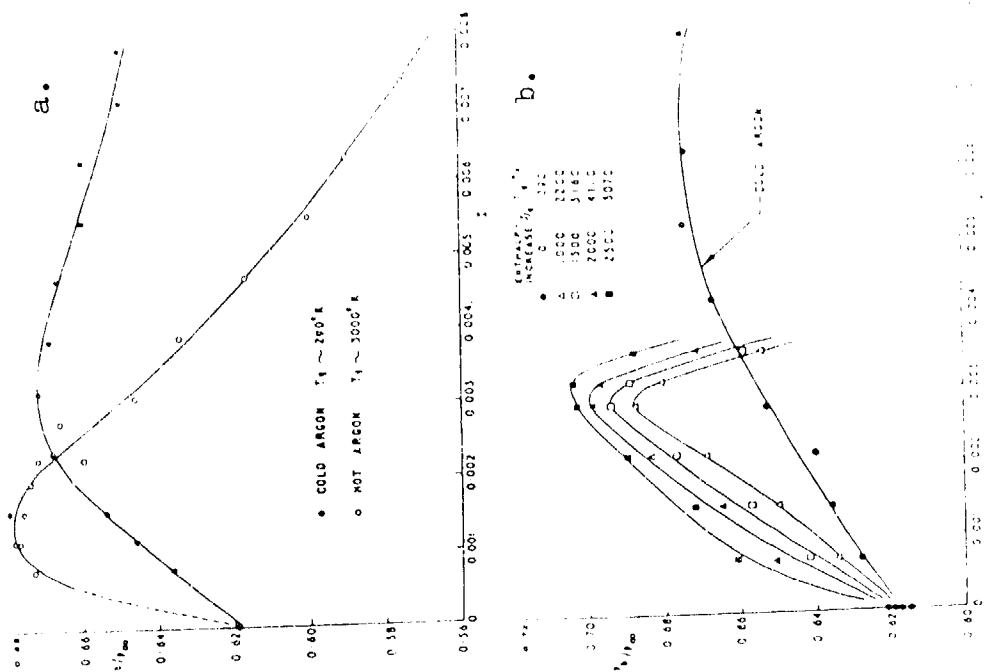


FIGURE 13. The effect of stagnation temperature in chamber on base bleed function



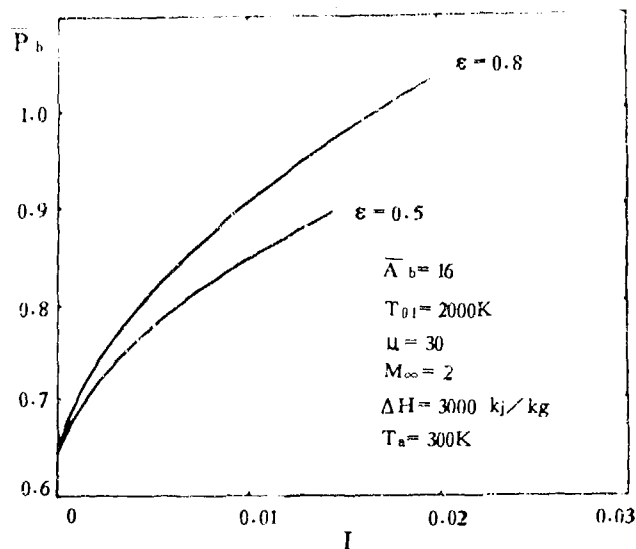


FIGURE 15. The effect of solid phase mass ratio on base bleed function

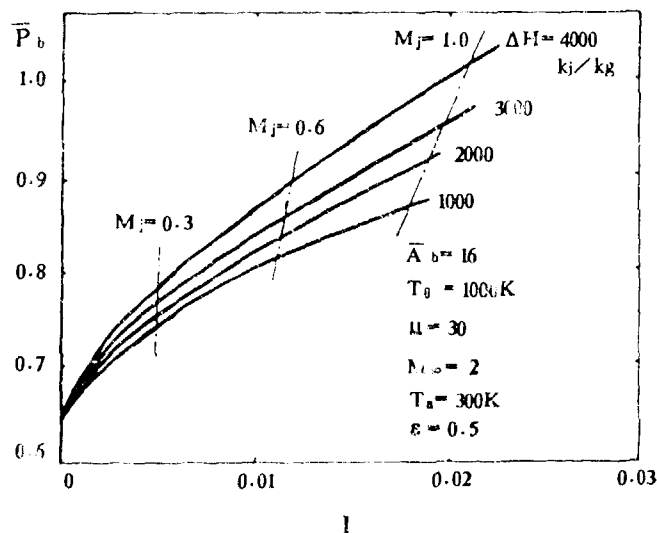


FIGURE 16. The effect of fuel enthalpy of combustion on base bleed function

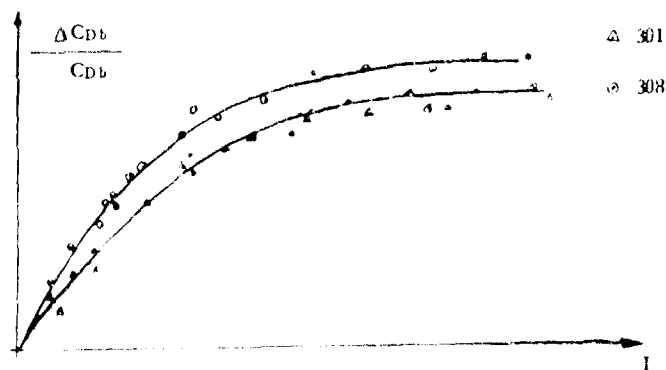


FIGURE 17. Experiment results of two different fuels

# BASE BURN PROJECTILE FRENCH TRAJECTORY MODEL

D.CHARGELEGUE and M.T.COULOUMY

Direction des Armements Terrestres

Etablissement Technique de Bourges

## ABSTRACT

The basic trajectory model is the standardized Modified Point Mass trajectory model where, in the first phase, the base drag reduction and the gas generator mass flow rate are calculated. The burning rate is expressed as a function of the upstream atmospheric pressure and operating generator temperature. The base drag reduction coefficient is expressed as a function of Mach number and characteristic mass flow rate. Following several campaigns, the coherence of the model with firings has been verified.

## 1. INTRODUCTION

Most of the studies on base-burn conducted in France concern special areas such as aerodynamics, constitution and combustion of propellant or interference between combustion and flow in the vicinity of the projectile base. These studies are very interesting in the aim of such projectiles design and development. Our purpose is different, we have to establish firing tables for the users. So we need a trajectory model which include base-burn particularities. This model could be also used by the army in artillery calculators and consequently it must not be too sophisticated.

Hellgren [1] first established such a range calculation program, but it calculates motor pressure and it needs many input data, some of which like base drag coefficient are very difficult to know.

We think that a model more simple can be used. The basic model is a modified point mass trajectory model [2] which is generally used in the preparation of firing tables. This basic model is completed by specific terms which modelise base-burn main aspects : drag reduction and mass flow rate.

Drag reduction and mass flow rate can be written in the following general expression :

$$R_{BB} = 1/2 \rho S V^2 C_{xBB} (M, I, P, \theta_p, \dots) \quad (1)$$



$$dm/dt = V_C (M, I, P, \theta_p, \dots) \rho_p S_C (mcr) \quad (2)$$

The time, for which the burnt propellant mass which is calculated by the equation (2) is equal to the initial mass of propellant, is an output data. This time can be compared to the measured burning time and is also the separation between the two phases of the trajectory. The terms (1) and (2) take part into movement equation system only in the first phase, during which the drag reduction occurs.

From the general formulation, the problem is to identify parameters which affect drag reduction coefficient  $C_{XBB}$  and combustion rate  $V_C$  and finally to determine the functions of these parameters. These functions must be accurate enough to provide calculated trajectories and burning time suitable to measured trajectories and burning time whatever the firing conditions (wind, muzzle velocity, elevation, cannon altitude, etc...) are.

To this end, specific tests and corresponding suitable means of measurement have been set, and are described in §2. Chapters 3 and 4 explain the way of interpreting the results and getting the modelisation of the mass flow rate (chapter 3) and the drag (chapter 4). Finally we have summed up the main characteristics of the model for base-burn projectiles in §5 before concluding.

## 2. TESTS

### 2.1 Tests Planning

To identify the parameters affecting the drag reduction and burning time, the principle of these tests is the following : for two identical values of a single parameter, the other parameters which can affect the drag coefficient or combustion rate are different.

Two French base-burn projectiles have been tested: the first one in June 1986 and the second one in September 1987. The test planning was the same for the two campaigns but the second one took advantage of many means of measurement and especially a trajectory radar.

According to the principle above stated, the test planning is defined as :

- 25 rounds with propellant block at 21°C
  - 5 charges x 5 elevations
- 25 rounds without propellant block
  - 5 charges x 5 elevations
- 24 rounds with propellant block at different temperatures
  - 4 temperatures : -31°C, -5°C, 36°C, 51°C,
  - for each one, 3 charges x 2 elevations.

## 2.2 Means of Measurement

The measures made during firing tests provide all the data used as inputs and as parameters which allow to develop and adjust the model.

Before each firing, the following measurements are made:

- inertial characteristics of each projectile : mass, position of the centre of gravity, moments of inertia
- for each round : elevation and azimuth angles, time of firing, projectile temperature .

It is also very important to know as accurately as possible all the meteorological parameters (air pressure, temperature, humidity, and wind velocity and direction versus altitude). One sounding per hour is required, then wind data are computed by a model of statistic interpolation versus time and distances. So this statistical model can provide sounding as trajectory model input data for each round.

During its flight, the projectile is fully tracked by a trajectory radar, and in addition to that, is tracked by Doppler radar during the beginning of the trajectory (until roughly 20 s of flight).

Each round is also equiped by a radio-electronic fuze to deliver burning time. Some projectiles carry yaw sondes. The muzzle velocity is measured by two independent means of measurement.

## 3. MASS FLOW RATE AND BURNING TIME MODELISATION

### 3.1 Calculation of Mass Flow Rate

The so called "burning time" calculated by the model is the very moment for which the last propellant gramm has been burnt. So it is linked to the mass flow rate which can be expressed by :

$$dm/dt = V_C (M, I, P, \theta_p, \dots) \rho_p S_C (m_{CB})$$

where  $V_C$  is combustion velocity

$\rho_p$  is propellant density

$S_C$  is the area of combustion as a function of mass of burnt propellant ,  $m_{CB}$  :

$$S_C = a_1 + b_1.m_{CB} \quad \text{for } m_{CB_i} \leq m_{CB} \leq m_{CB_{i+1}}$$

At any given time, the mass of burnt propellant is :

$$m_{CB}(t) = m_0 - m(t)$$

where  $m_0$  is the mass of the round when fired

$m(t)$  is the mass of the round at time  $t$

and we know that at initial time i.e.  $t = 0$ ,  $m(0) = m_0 - m_{CB0}$

where  $m_{CB0}$  is the burnt propellant mass in the barrel and depends on the charge.

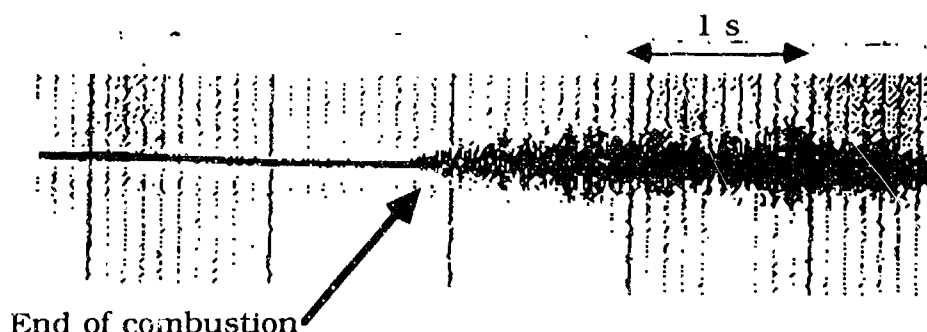
Note that  $\rho_p$  and the function  $S_c(m_{CB})$  is provided by the propellant constructor.

### 3.2 Measurements

First before the campaign, some tests have been conducted on propellant in pyrotechnical laboratory. Particularly we are interested in combustion rate obtained on the stand-burner under several pressures and temperatures. Of course it is not really representative of the combustion during round flight, but these tests allow to determine the combustion rate of reference ( $V_{C0}$ ) for the lot of the tested propellant blocks. This also give some idea about the behaviour of combustion rate with pressure and temperature.

During round flight, the burning time is directly measured by using special fuze. In fact, each projectile with propellant block is equiped with a radio-electronic fuze which emit a signal. As long as the combustion goes on, this signal is perturbed, which permits to obtain the burning time with an accuracy estimated at about 0,1s (see figure 1)

Figure 1 : 155 DTC Measured burning time



### 3.3 Identification of Parameters Affecting Burning Time

We have found good correlation of combustion rate with upstream pressure and also propellant temperature, as shown by the following results obtained through the two firing campaigns.

Correlation with pressure. The rounds with propellant block at 21°C have been exploited with the model where mass flow rate is calculated as :

$$dm/dt = - K(M, I, P, \theta_p, \dots) V_{C0} \rho_p S_c(m_{CB})$$

$V_{C0}$ ,  $\rho_p$ ,  $S_c$  were defined before and  $K$  is an adaptation parameter.

For each round,  $K$  is adjusted to match the measured burning time. Of course the model prints at every step the following data : Mach number  $M$ , characteristic mass flow rate  $I$  ( $I = (dm/dt)/\rho S V$ ), air pressure  $P$ ; it

also calculates the average pressure  $P_{moy}$ , the average Mach number  $M_{moy}$ , and the average characteristic mass flow rate  $I_{moy}$  over the whole base-burn phase.

So we can draw  $K$  as a function of  $M_{moy}$ ,  $P_{moy}$ , or  $I_{moy}$ .

We have only found correlation with upstream pressure as shown on figures 2-1 and 2-2 using a linear scale and figures 3-1 and 3-2 using a logarithmic scale.

Fig. 2-1 155 RTC Combustion rate versus pressure

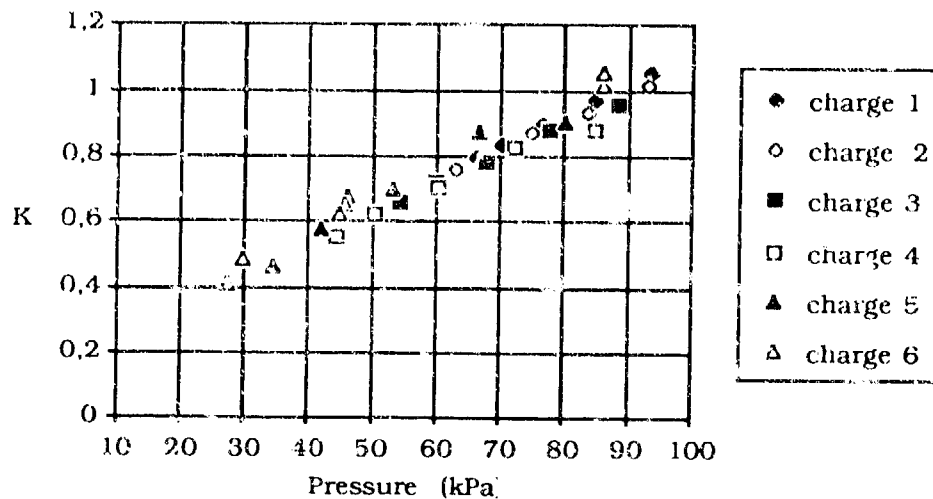


Fig. 2-2 155 DTC Combustion rate versus pressure

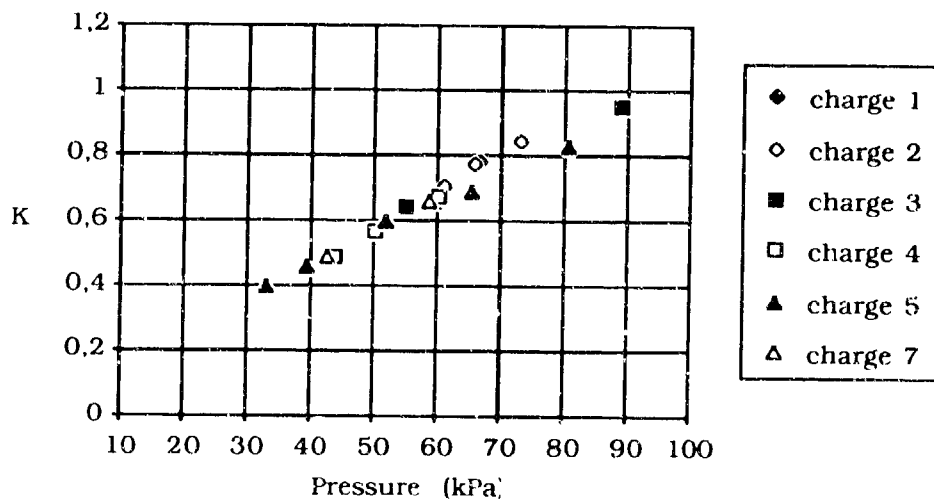


Fig. 3-1 155 RTC Combustion rate versus pressure

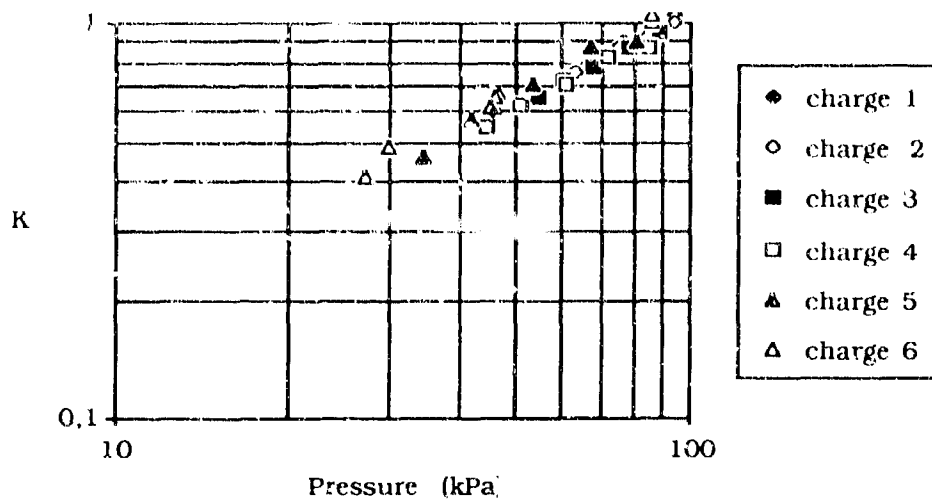
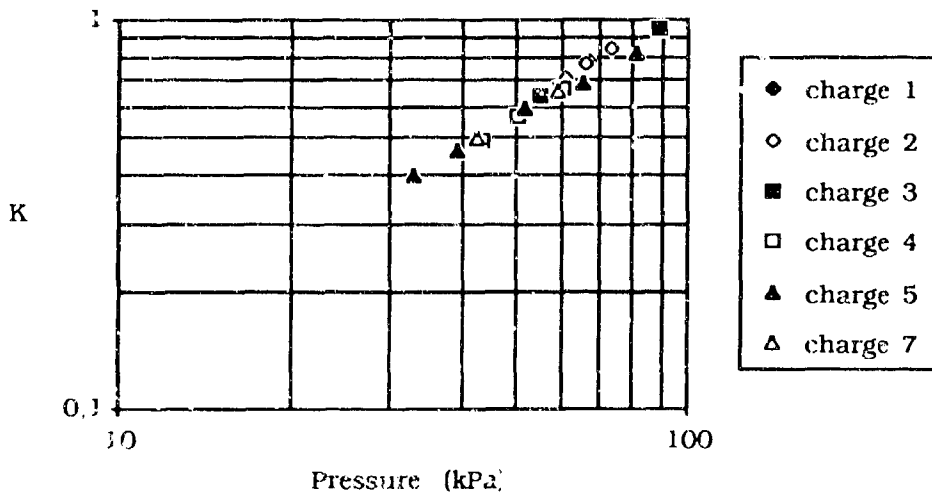


Fig. 3-2 155 DTC Combustion rate versus pressure



The best correlation has been obtained with a law on the form :

$$K = A.P^\alpha$$

Simulations are done with for mass flow rate expression :

$$dm/dt = - A.P^\alpha V_{CC} \rho_p S_C (inCH)$$

Figure 4-1 represents the corresponding computed burning time and figure 4-2 represents the difference between computed and measured burning time. The corresponding difference in combustion rate (in %) and the consequences on the range (in meters) are respectively shown in figure 4-3 and 4-4.

Fig 4-1 155 DTC Computed burning time (s)

Elevation mil. charge	400	600	800	1000	1150
1		30,83	33,26	36,43	38,85
2		31,72	35,25	39,10	41,65
3	29,33	32,61		42,15	45,85
4		34,65	41,40	48,73	55,06
5	31,50	38,20	47,36	60,50	70,97
7		41,76	55,64		

Fig 4-2 155 DTC Difference in burning time (s)

Elevation mil. charge	400	600	800	1000	1150
1		1,33	2,26	2,83	3,05
2		1,62	2,15	3,10	2,15
3	0,23	0,01		0,35	2,45
4		-0,55	0,30	-0,27	-1,14
5	-1,70	-1,10	1,06	1,20	1,97
7		0,46	0,84		

Fig 4-3 155 DTC Difference in combustion rate (%)

Elevation mil. charge	400	600	800	1000	1150
1		4,6%	6,9%	7,4%	7,2%
2		5,4%	5,9%	7,3%	4,5%
3	0,8%	0,0%		0,7%	4,4%
4		-1,5%	0,6%	-0,4%	-1,6%
5	-5,1%	-2,9%	1,9%	1,6%	2,4%
7		1,0%	1,2%		

Fig 4-4 155 DTC Difference in downrange (m)

Elevation mil. charge	400	600	800	1000	1150
1		9	20	24	15
2		16	28	26	12
3	1	0		3	15
4		10	7	0	5
5	23	19	19	14	9
7		22	15		

One may note that for the highest charges the differences are less than 2 s for burning time, 5% for combustion rate, and 22 m for range, which is very satisfactory because it is about the dispersion we can expect with propellant blocks.

For lower charges the differences are larger but this kind of projectiles will be probably used essentially with higher charges.

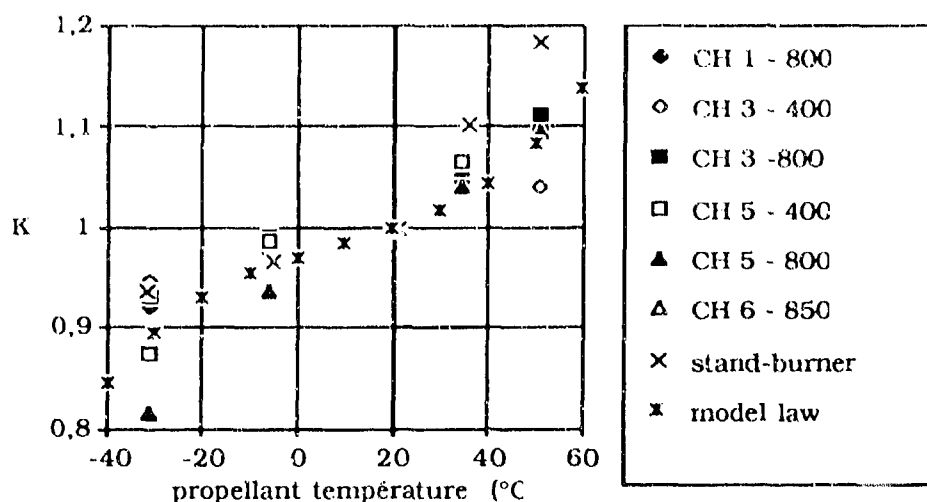
Correlation with propellant temperature. In this case, the rounds with propellant blocks at different temperatures were exploited with the model where mass flow rate is :

$$dm/dt = - K A P^\alpha V_{C0} \rho_p S_c (m_{CB})$$

K is adjusted to meet the measured burning time and drawn versus  $\theta_p$ , this graph represented in figure 5, permits to determine the function of propellant temperature which is a third degree polynome :

$$K(\theta_p) = a_0 + a_1\theta_p + a_2\theta_p^2 + a_3\theta_p^3$$

Fig. 5 155 RTC Combustion rate versus propellant temperature



Then as before, we can compare computed and measured burning times (figure 6).

Fig.6 155 RTC Combustion rate versus propellant temperature  
Difference between computed and measured burning time

Charge	Elevation mil.	Propellant Temperature			
		-31 $^{\circ}\text{C}$	-6,4 $^{\circ}\text{C}$	34 $^{\circ}\text{C}$	50,7 $^{\circ}\text{C}$
3	400	0,36	-0,73	-0,55	-2,55
5	400	-2,98	-0,52	-0,98	-1,86
1	800	2,38	1,62	1,58	1,07
3	800	1,01	0,33	0,27	0,04
5	800	-4,03	-0,67	1,42	1,17
6	850	0,99	---	---	2,13

The difference between computed and measured burning times is generally higher than for 21 $^{\circ}\text{C}$ . The dispersion in combustion rate seems also to be higher, especially for the highest and lowest temperatures tested. So we think that the modelisation of the combustion rate versus temperature is good enough with a third degree polynome but we can expect that the dispersion in range should be higher for very high or very low temperatures.



#### 4. DRAG REDUCTION MODELISATION

The additional term in movement equation due to drag reduction can be written in the following general expression :

$$R_{BB} = 1/2 \rho S V^2 C_{x_{BB}}(M, I, P, \theta_p, \dots)$$

The identification of parameters and their functions which affect drag reduction is allowed by the great diversity of firing conditions and the suitable means of measurements described in §2.

##### 4.1 Measurements

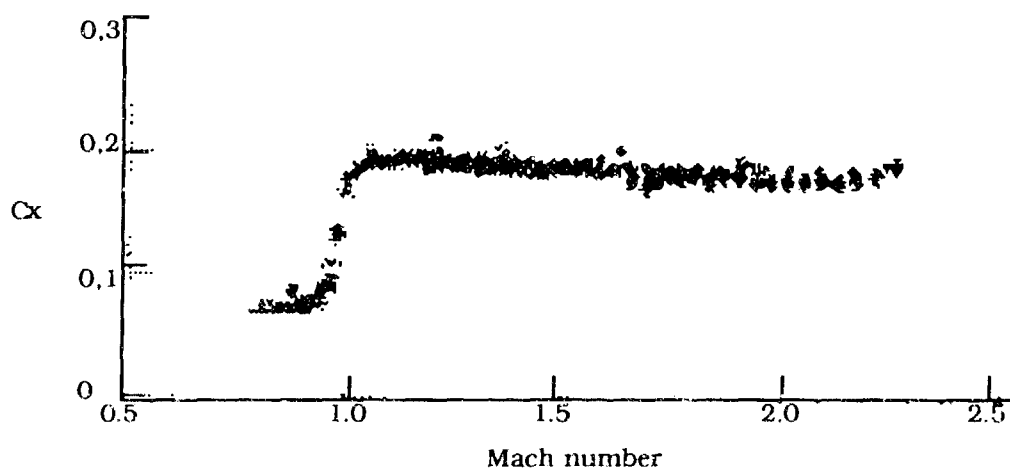
At the beginning of its flight (about 20 s) each projectile is tracked by a Doppler radar which permits to measure velocity as a function of time. Then these data are exploited by a program developed by ETBS [3] which provides drag coefficient  $C_x$  as a function of Mach number. (One value of  $C_x$  is calculated for one Mach number per second, so about twenty values of  $C_x$  are calculated for twenty values of Mach number for each round)

The decrease of the mass flow rate occurs after the end of the Doppler radar tracking. So in order to observe the effects of the mass flow rate on drag reduction at the end of the base-bleed phase, we must use a trajectory radar tracking.

##### 4.2 Identification of Parameters Affecting Drag Reduction

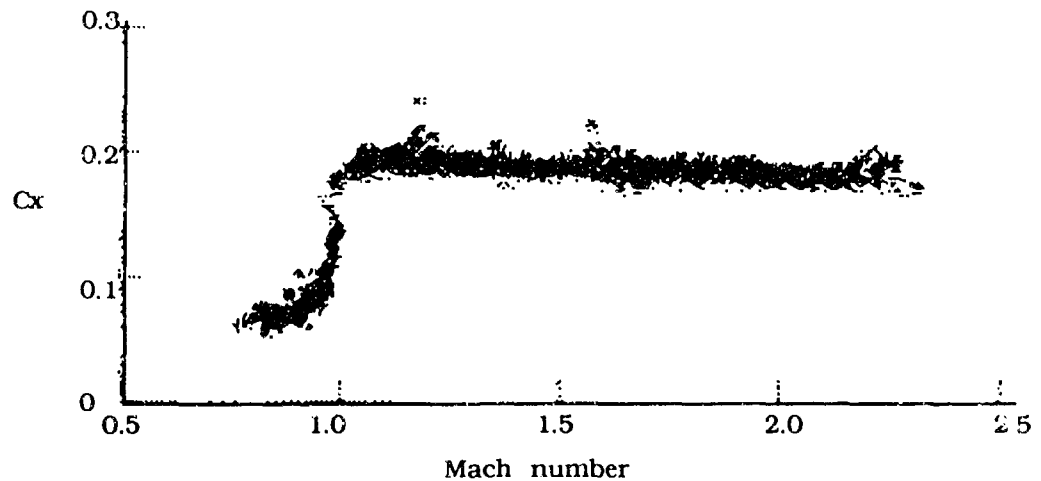
Correlation with Mach number. Figure 7 presents global drag coefficient for DTC projectiles with propellant block at 21°C ( $C_{x_{ABB}}$ ) and shows that  $C_{x_{ABB}}$  only depends on Mach number because the dispersion obtained on this coefficient is not greater than it is for a classical projectile.

Fig. 7 Drag coefficient with propellant block at 21°C



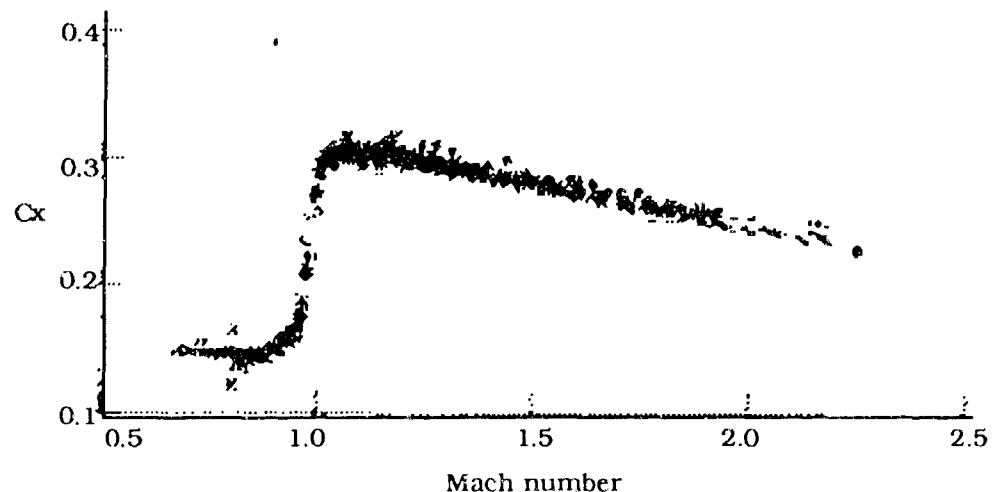
As the propellant temperature affects combustion rate, one may think that drag will be affected. This is not the case as shown on the graph in figure 8 which represents drag coefficient for DTC projectiles with propellant block at different temperatures ( $C_{x_{ABB}}$ ). Temperature effect does not increase the drag dispersion. These two results indicate that an optimal mass flow rate does exist above which the global drag coefficient only depends on Mach number.

Fig. 8 Drag coefficient with propellant block at different temperatures



Drag coefficient for DTC rounds without propellant block ( $C_{x_{SBB}}$ ) is drawn in figure 9.

Fig. 9 Drag coefficient without propellant block



Then the drag reduction coefficient  $C_{x_{BB}}$  used in the formula §4 is calculated as

$$C_{x_{BB}} = C_{x_{SBB}} - C_{x_{ABB}}$$

The three graphs  $C_{xABB}$ ,  $C_{xSBB}$  and  $C_{xBB}$  as functions of Mach number were plotted on figures 10-1 and 10-2 for each of the two tested projectiles.  $C_{xBB}(M)$  is expressed as some polynomial functions of Mach number (degree < 4).

Fig 10- 1 155 RTC Drag coefficients versus Mach number

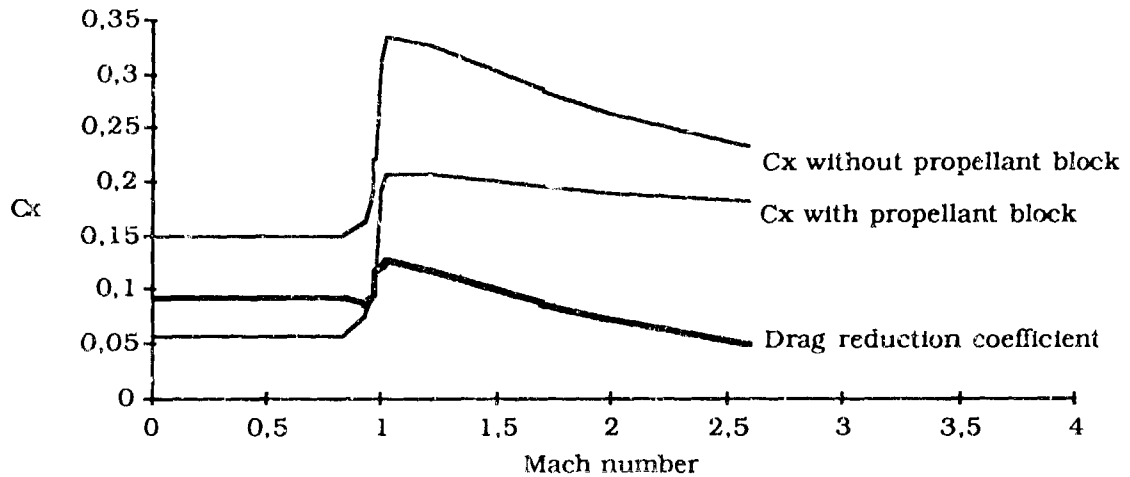
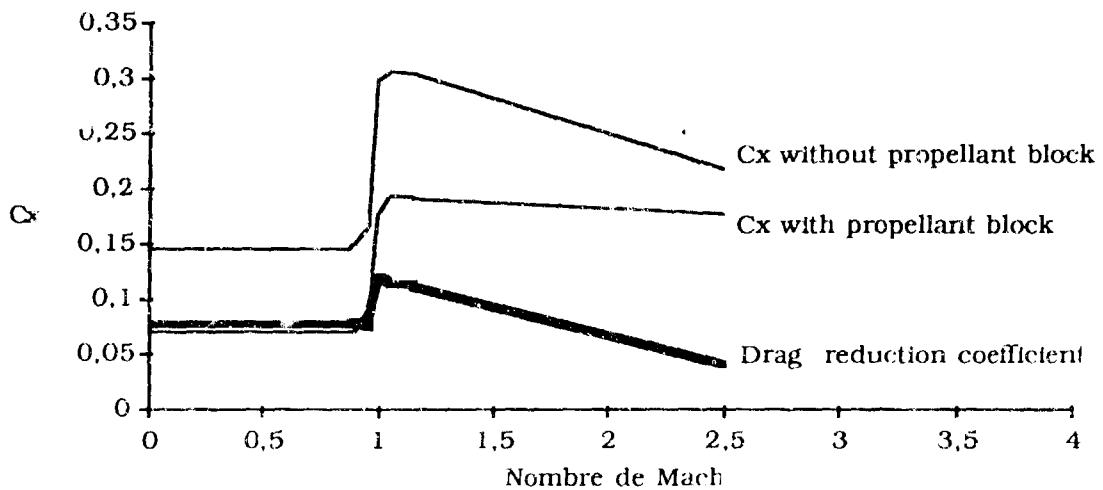


Fig 10-2 155 DTC Drag coefficients versus Mach number



Influence of characteristic mass flow rate. During the emptying phase of base-burn motor, it is clear that drag reduction decreases progressively. As a matter of fact, the projectile drag goes from the  $C_{xABB}$  curve to the  $C_{xSBB}$  curve.

We are trying to define the function of characteristic mass flow rate  $f(I)$  from data obtained by trajectory radar.

The first firing campaign allows us to point out a characteristic flow rate  $I_0$  permitting optimum efficiency of base-bleed motor and the following expression for drag reduction :

$$R_{BB} = 1/2 \rho S V^2 C_{x_{BB}}(M) f(I)$$

$$\text{where } \begin{array}{ll} f(I) = I/I_0 & \text{if } I \leq I_0 \\ f(I) = 1 & \text{if } I \geq I_0 \end{array}$$

## 5. SUMMARY OF THE MAIN ASPECTS OF THE ACTUAL MODELLING FOR BASE-BURN ROUNDS

### 5.1 Additionnal Terms for Base-Burn Rounds

Additionnal term in the center of gravity movement equation :

$$R_{BB} (\vec{V}/V \cos \delta_e + \vec{\delta}_e) / m$$

$$\text{where } R_{BB} = 1/2 \rho S V^2 C_{x_{BB}}(M) f(I)$$

The characteristic flow rate function  $f(I)$ .

$$\begin{array}{ll} f(I) = I/I_0 & \text{if } I \leq I_0 \\ f(I) = 1 & \text{if } I \geq I_0 \end{array}$$

$I$  being the characteristic mass flow rate  $I = (dm/dt) / \rho S V$

$I_0$  being the characteristic mass flow rate permitting optimum efficiency of the base-bleed motor.

### Coefficient $C_{x_{BB}}$

$C_{x_{BB}}$  is the drag reduction coefficient (a function of the Mach number) established for the entire firing envelope, for a given munition and equipment.

$$\text{for } M_1 \leq M \leq M_{1+1} \quad C_{x_{BB}}(M) = a_{01} + a_{11} M + a_{21} M^2 + a_{31} M^3 + a_{41} M^4$$

### 5.2 Calculation of the Mass and Combustion Time

Data.

$m_S$  = standard mass of the complete round  
 $m_0$  = mass of the round when fired  
 $m_C$  = mass of standard burnt substances (propellant, etc...)  
 $m_{CBO}$  = mass of propellant burnt in the barrel.

Calculation of the mass at extinction of the base-bleed motor :  $m_{EBB}$

$$m_{EBB} = m_0 - m_C$$

It is assumed that while  $t \geq t_0$  and  $m \geq m_{EBB}$  the base bleed phase is in progress.

#### Calculation of mass flow.

In this phase, the mass variation law is given by :

$$dm/dt = -K.V_C (M, I, P, \theta_p, \dots) \cdot \rho_p \cdot S_C (m_{CB})$$

where  $K$  is the adaptation parameter enabling the base-bleed time to be found

$V_C$  is combustion rate

$\rho_p$  is propellant density

$S_C$  is the area of combustion as a function of burnt propellant mass,  $m_{CB}$  :

$$S_C = a_i + b_i \cdot m_{CB} \quad \text{for } m_{CB i} \leq m_{CB} \leq m_{CB i+1}$$

At any given time, the mass of burnt propellant is :

$$m_{CB}(t) = m_0 - m(t)$$

where  $m_0$  is the mass of the round when fired

$m(t)$  is the mass of the round at time  $t$

and we know that at initial time i.e.  $t = 0$ ,  $m(0) = m_0 - m_{CB0}$

where  $m_{CB0}$  is the burnt propellant mass in the barrel and depends on the charge.

#### Calculation of the combustion rate.

The combustion rate is expressed as :

$$V_C = V_{C0} \cdot f(\theta_p) \cdot g(P)$$

where  $V_{C0}$  is the combustion rate obtained on the stand-burner

$\theta_p$  is the propellant temperature

$$f(\theta_p) = a_0 + a_1 \theta_p + a_2 \theta_p^2 + a_3 \theta_p^3$$

$P$  is the upstream pressure

$$g(P) = A \cdot P^\alpha$$

## 6. CONCLUSION

These test campaign results have pointed out that one can consider that upstream pressure and propellant temperature are the only parameters which affect the mass flow rate.

By another way, as long as characteristic mass flow rate is greater than an optimal value, drag reduction only depends on Mach number and is independant of propellant temperature. During the emptying phase, characteristic mass flow rate becomes lower than this optimal value. The function of characteristic mass flow rate used for modelling the falling off of the drag reduction, which appears during this phase is still not completely defined. Nevertheless comparisons between computed and experimental trajectories and burning time conducted up to now are very satisfactory.

## REFERENCES

1. Hellgren Rune v., *Range calculation for Base Bleed projectiles* , Proc 6th Int. Symposium on ballistics, Orlando, pp 190-196, 1981.
2. Lieske R.F., and Reiter M.L., *Equations of Motion for a Modified Point Mass Trajectory* , US Army Ballistic Research Laboratory report n°1314, March 1966
3. Runfola Y., *Determination du Cx d'un projectile à partir de mesures de radar Doppler* , Colloque franco-allemand, MEBAL 85, Saint-Louis, rapport R 116/85, pp S.II.9, 1985.

## TRAJECTORY MODELING FOR BASEBLEED PROJECTILES

Gerhard Laube

Defense Technology Agency, Ballistic Division, Thun, Switzerland

### INTRODUCTION

Basebleed projectiles become widely used as an efficient mean of increasing the range of artillery projectiles. Therefore there is a strong need for a trajectory model that fits into existing fire control computers. Such a model should avoid additional integration variables which would lead to longer calculation times and should fit into existing calculation techniques in order to keep software maintenance costs down. Our artillery fire control computer uses trajectory integration within a mass point model [1].

### THEORY

The well known "swedish model" for basebleed calculation, see eg. [2] uses a representation of the effective drag in the form

$$C_{d\text{eff}} = f \cdot C_{d\text{base}} + C_{d\text{frict}} + C_{d\text{front}} \quad (1)$$

where the drag reduction factor depends on the mass flow  $I$ , the Mach number  $M$ , and projectile related geometrical data  $A$ . It is factorized into

$$f(I, M, A) = f_1(I) \cdot f_2(M) \cdot f_3(I, M, A) \quad (2)$$

The mass flow depends on the burning law of the basebleed propellant and therefore on the chamber pressure which may be related to the ambient base pressure. Furthermore, the burning characteristics may be affected by the spin rate. Hence, mass flow calculation is rather complicated.

But, if a suitable initial guess of the burning time is available - depending on muzzle velocity, ambient atmospheric conditions and propellant temperature,  $f_1$  and  $f_3$  in formula (2) may be expressed as functions of time instead as functions of mass flow. Moreover, with

$$g = (f \cdot C_{d_{base}} + C_{d_{frict}} + C_{d_{front}}) / C_{d_{tot}} \quad (3)$$

the total drag  $C_d$  may be used as a reference to the drag reduction factor.

$$C_{d_{eff}} = g(t, M, A) \cdot C_{d_{tot}} \quad (4)$$

Such a representation would conveniently fit into present drag calculation of existing fire control computers. However, the factorisation of  $f$  in (2) will not apply to  $g$  in (4). We have therefore to look for an alternative form.

#### DATA COLLECTION

In order to get data samples covering a wide range of parameters, a test plan was set up covering firings from low zones (380 m/s) to high zones (915 m/s), elevations from 200 mils to 1100 mils. The purpose of using high elevations in the upper register was to expose the active projectile to low ambient pressure conditions which would influence the burning rate and burning time.

ELE  
(A s/oo)

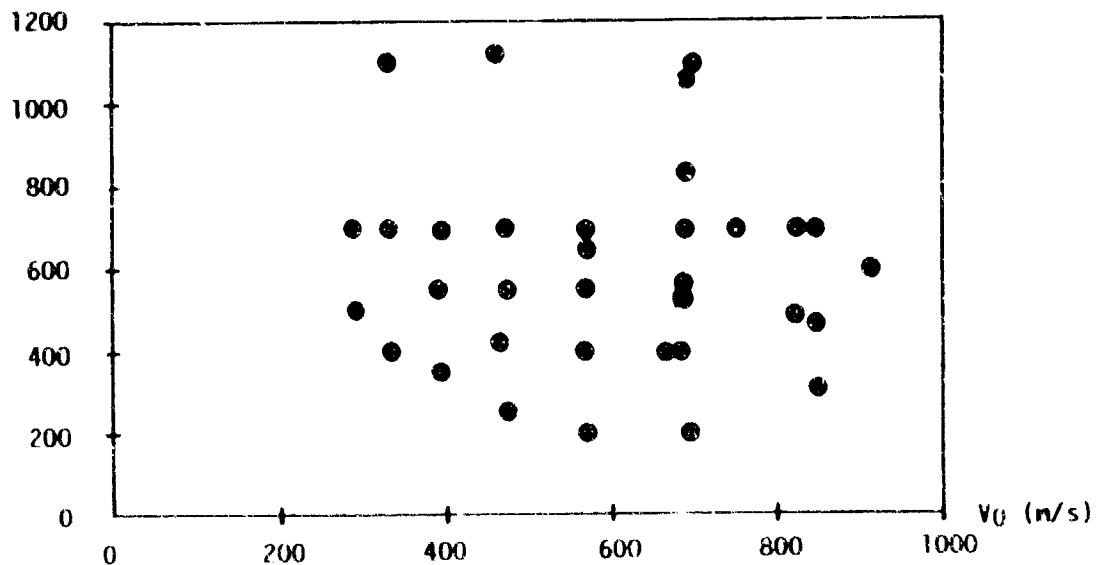


fig 1: summary of the main firing conditions



Unfortunately, low atmospheric pressure and high Mach numbers tend to be correlated, so that the separation of Mach number and atmospheric effects will be difficult. Variation of the mass flow parameter was also achieved by using rounds conditioned at low or high temperatures.

Inert shells, i.e. shells with inactive basebleed units, were used for reference purpose, so that the effectiveness of the drag reduction could be observed in a direct comparison under the same conditions. Due to test site range restrictions, this direct comparison was not always possible, since not always two different target areas were available at the same time which would have been required for rings with both projectiles.

A non-tracking Doppler radar was used to get the velocity data. Met data was collected by standard met sonde technique.

#### DATA REDUCTION

The drag coefficient was calculated from the doppler radar data using a point mass model. It is not necessary to calculate with decreasing mass, the aeroballistic effect of the mass decrease can be incorporated in the efficiency factor  $g$ . fig 2 shows drag data.

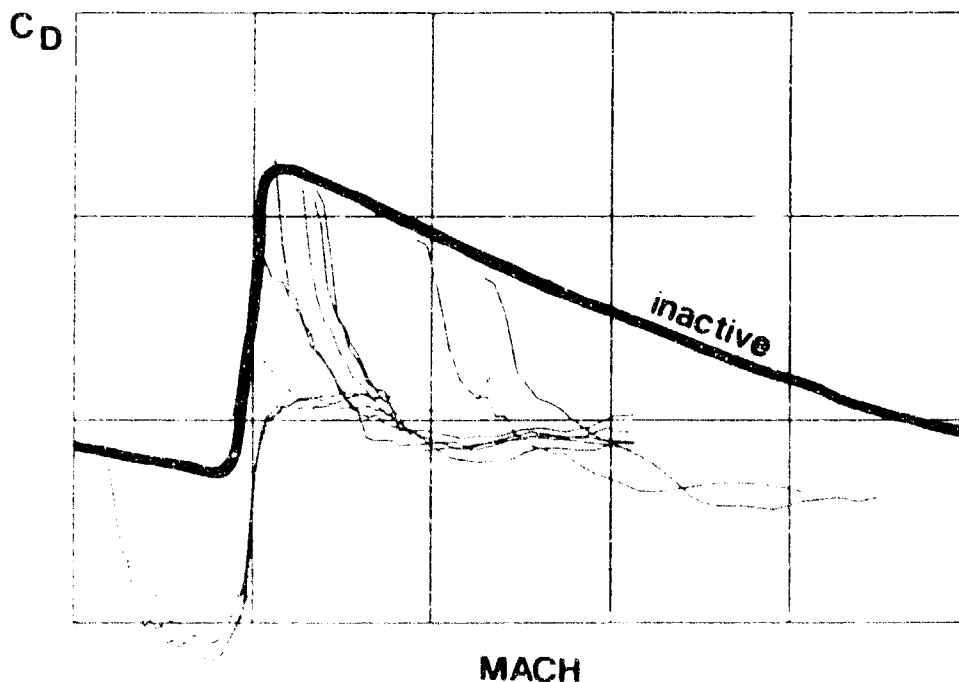


fig 2. measured drag data from basebleed projectiles

In the next step, the drag reduction factor is derived as ratio of  $g = C_{D_{active}}/C_{D_{inactive}}$ , see fig 3.

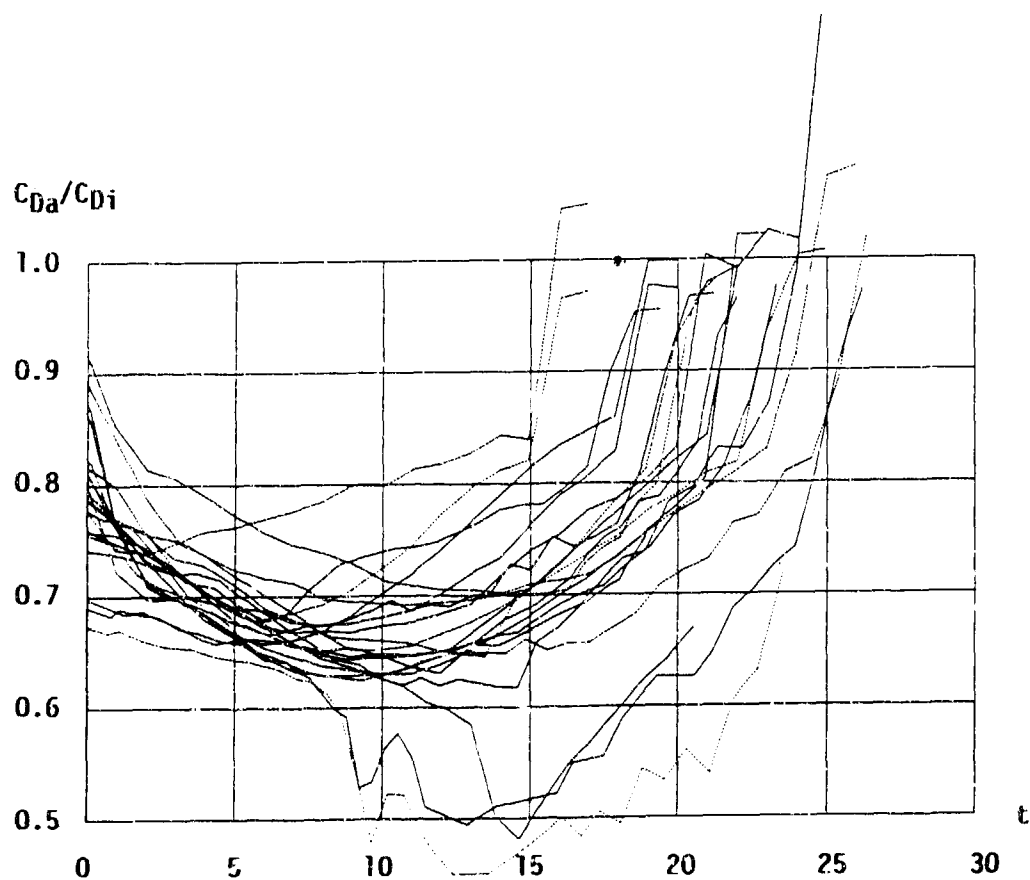


fig 3: drag reduction factor as a function of time, for various Mach numbers.

For the interpretation of the data, burnout time is very important. Optical observation of burnout time turned out to be rather erratic. A still active unit may have no optical signature and, on the other hand, ineffective burnout of remaining propellant may be clearly visible. Therefore we decided to define the burnout time as the end of efficiency, measured by the doppler radar.

Now, having the burnout time  $t_B$  or a suitable guess of it, we are able to rearrange the drag reduction data as a function of the relative burning time  $t/t_B$ . This procedure eliminates the variation of burnout time due to the various influencing factors, such as high propellant temperature and high spin rate which result in an increase of the burning rate, and therefore in a decrease of the burning time. Fig 4 shows the result of this reduction step.

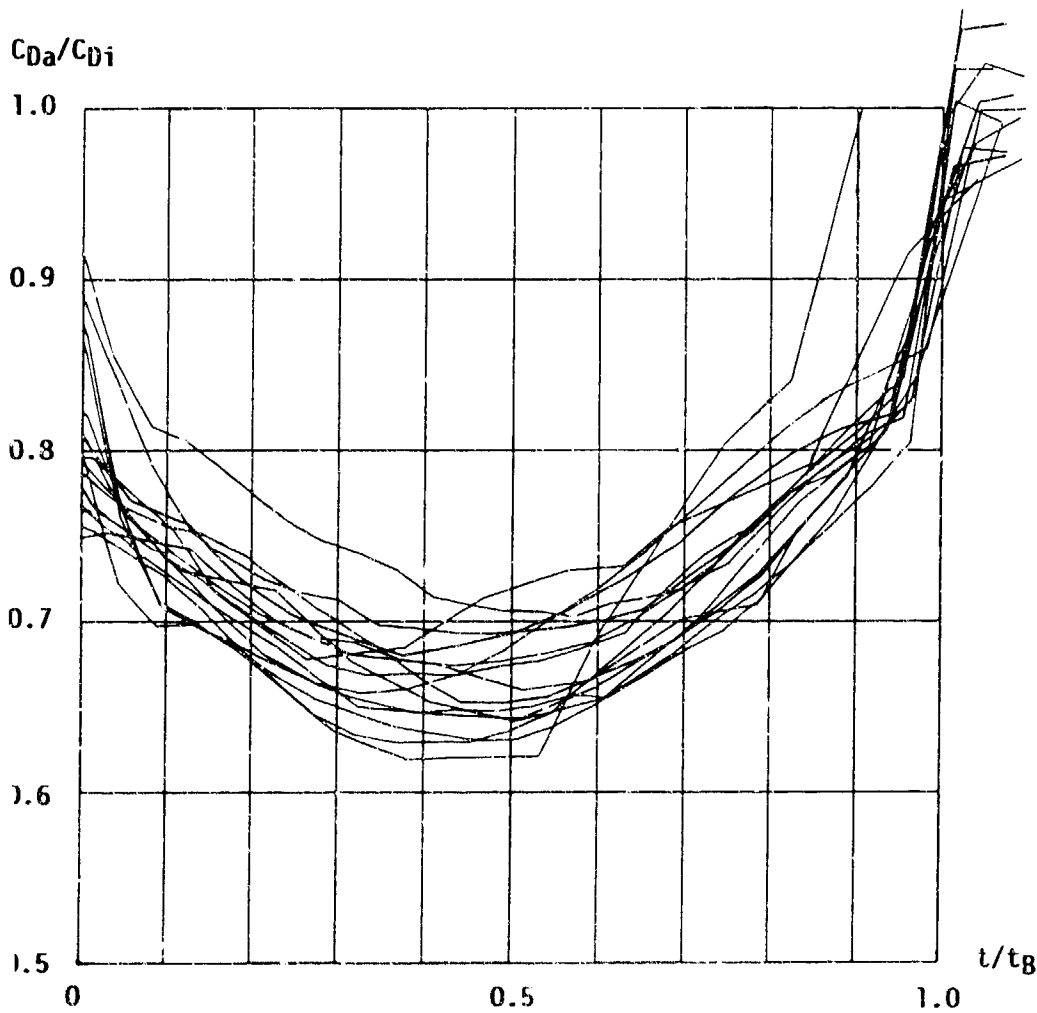


fig 4: drag reduction factor vs relative burning time  $t/t_B$

Obviously, the main effect - the effect originating from the mass flow - has been eliminated. The effectiveness, i.e. the drag reduction factor, of a well designed basebleed unit is not very sensitive to variations in the mass flow. It has to be outlined, that fig 4 contains also measurements on high and low temperature conditioned projectiles, for which the burning time varies more than ten percent. The mass flow will change by approximately the same amount, but the effectiveness varies by far less than ten percent.

Remember that, because of the useage of the total drag as a reference (4), combined effects of mass flow and Mach number have to be expected. It becomes now difficult to identify these remaining effects. Higher spin rates result in higher burning rates. Therefore both Mach number and mass flow correlate with high muzzle velocities. Separating the drag reduction factor curves for different zones gives a separation of Mach number and mass flow parameter simultaneously. The resulting drag reduction curves separated for zones 8 and 10 are shown in fig 5-6.

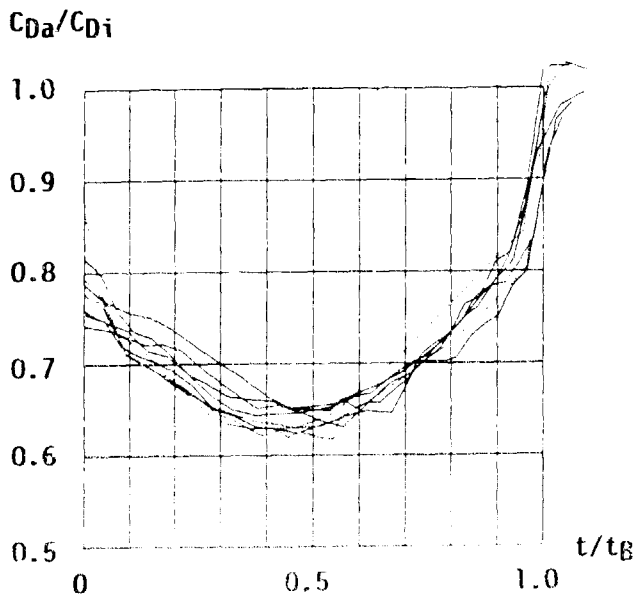


fig 5: drag red for zone 8

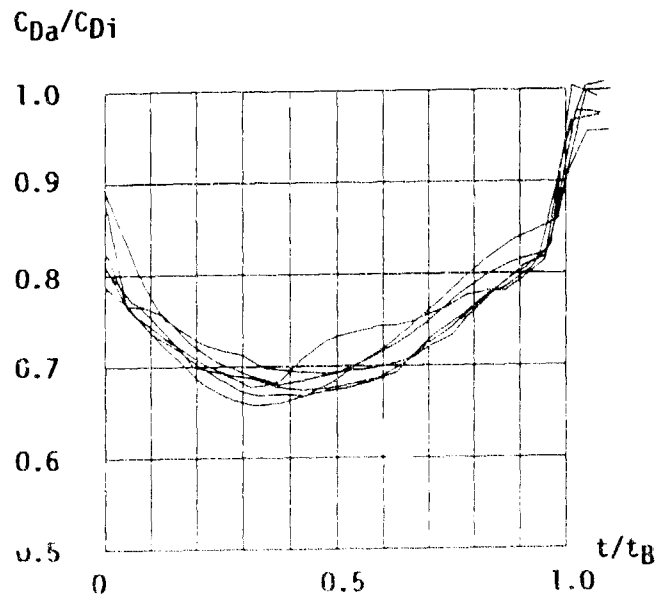


fig 6: drag red for zone 10

## BURNING TIME

Up to now, an empirical formula based on test firing data is used, a function of muzzle velocity and elevation angle. Simple approaches of correlating burning time with free air trajectory data were not successful.

Firing tests, where base pressure and basebleed unit chamber pressure are to be recorded in flight, are in preparation.

## ACCURACY OF THE MODEL

Errors in the burning time (as a result of a bad guess or an inappropriate formula) will result in a range error and a time-of-flight error. It has been calculated, that a ten percent error in burning time, using unaltered drag reduction data results at zone 8 only in a 200 meters range error. Hence, fortunately, the problem of burnout time is not that delicate.

The drag reduction curves of fig 5-6 show some bandwidth. To get a feeling for the yet remaining error, we performed calculations with the lower and upper envelopes of these figures instead of the mean curve, of fig 7. This is a worst case assumption, since no actual curve is lowest or highest over the whole domain.

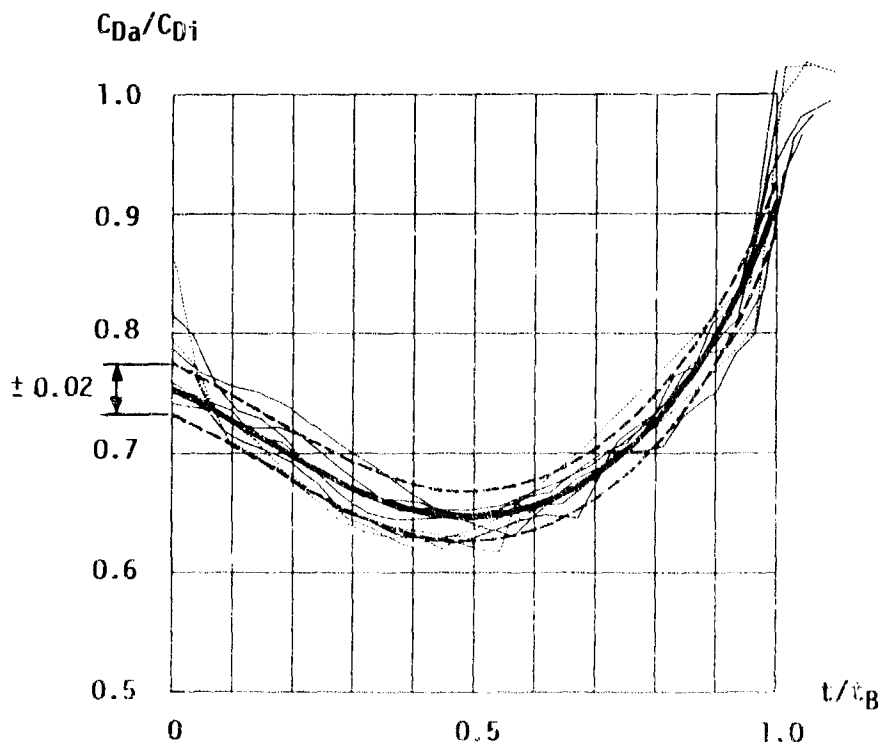


fig 7: drag reduction curves used for range sensitivity calculation

The following table shows the results of this calculation for an example with zone 8. The actual firing distance was 21.9 km, the basebleed unit turning time was 21.7 secs.

Basis: actual firing.	range error	time error
mean drag reduction curve	- 66 m	- .42 s
lower drag reduction curve	+218 m	+ .07 s

Basebleed projectiles are tactically used only over a limited spectrum of the possible parameters. They are used preferably with high zones at long ranges. Therefore usual fitting techniques with heavy weights on high zones and long ranges are applicable and will further improve the accuracy of the calculation.

#### CONCLUSIONS

It was proven that with sufficient accuracy a simple extension of the standard integration formula does the job of trajectory calculation for the purpose of fire control. Further work has to be done, especially in the field of predicting the burnout time.

#### REFERENCES

- 1 G. Laube and B. Kneubühl: A fast running solution of the exterior boundary value problem. Proceedings of the sixth international symposium on ballistics, pp 486-491, Orlando, 1981,
- 2 R.V. Helgren: Rangepcalculation for base bleed projectiles. Proceedings of the sixth international symposium on ballistics, pp 214-220, Orlando 1981.

## BASE BURNING PERFORMANCE AT MACH 3

Warren C. Strahle  
School of Aerospace Engineering  
Georgia Institute of Technology, USA

### INTRODUCTION

Over the past four decades there have appeared spurts of interest in the use of combustion or mass addition either from the side or from the base of a projectile in supersonic flight. The purpose has been for generation of control forces or thrust (drag reduction) for these projectiles or missiles. A brief list of references (not exhaustive) illustrating the chronology is given as Refs. 1-7. This symposium represents a new phase of interest in the problem, but is specialized to the use of base bleed for drag reduction.

Prior work at this laboratory <sup>7,8</sup> has focused on experiments in base bleed for base drag reduction (or elimination) using various injectants, with hydrogen as the combustible. The experiments were limited to a facility of fixed Mach number of 3, but sufficient variables were changed to provide much physical insight into the problem. In particular, this paper will focus on the advantages of using a hot fuel rich bleed gas as the injectant, as opposed to either a pure cold fuel or inert hot gas.

### FACILITY

The facility used was a blowdown windtunnel designed to simulate the base flow for a bluff-base, axisymmetric projectile with a fineness ratio of about 6. The Mach number was 3 at the projectile tailplane. Test section details are shown in Fig. 1.

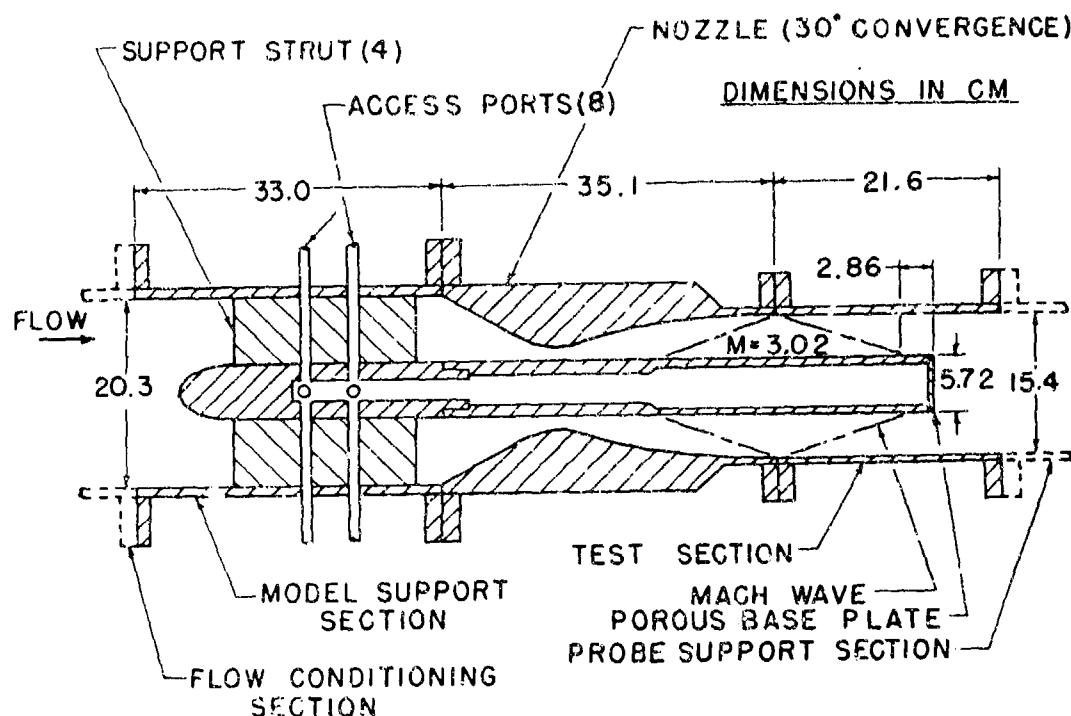


Figure 1. Base burning test section schematic

The windtunnel characteristics are described in Table 1.

Table 1. Wintunnel characteristics

Mach number at base tailplane	3.02
Stagnation pressure	$9.3 \times 10^5$ Pa
Stagnation temperature (drifts during run)	250-280 K
Reynolds number based on base diameter	$3 \times 10^6$
Boundary layer momentum thickness at tailplane	0.67% D
Centerbody base diameter (D)	5.72 cm
Tunnel area at base plane	161 cm <sup>2</sup>
Maximum run time	5 min
Test section static pressure	24600 Pa
Test section static temperature	100 K
Mass flow rate	0.82 kg/s



The hollow cylindrical model extends through the windtunnel nozzle and is supported by four streamlined struts in the upstream portion of the windtunnel where the Mach number is 0.07. Gases for base injection and instrumentation leads were ducted through the support struts.

Two base configurations were used. The plane base shown in Fig. 1 is a plane sintered metal base plate. This plate was used for base bleed with hydrogen injection with diluents of He, CO<sub>2</sub> and H<sub>2</sub>. The second base configuration is shown in Fig. 2. This was used for the combined preburning of pure oxygen with diluted hydrogen before injection into the wake.

#### BASE INJECTION

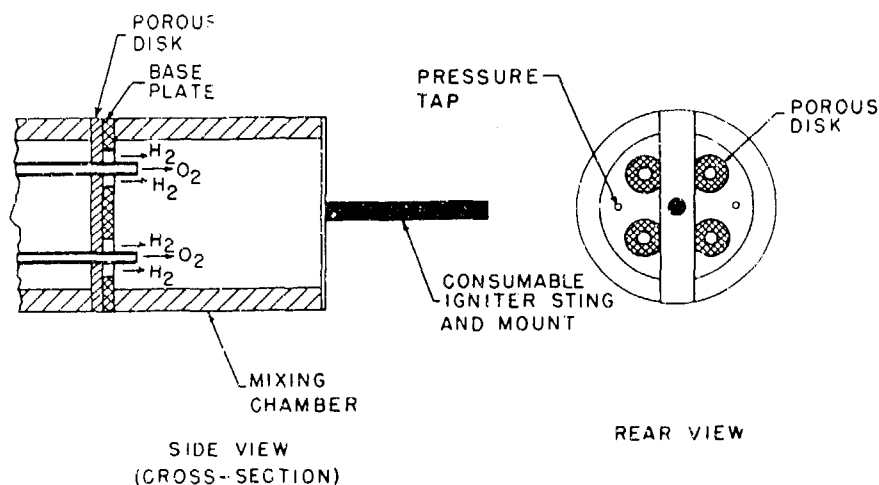


Figure 2. Base configuration for preburning

Ignition for all cases was obtained by igniting a solid propellant consumable igniter sting as shown in Fig. 2. Base pressure was measured as the average of four or five base pressure static taps drilled through the plate nearest the base. In all uses the injectant momentum flux was less than 5% of the base force rise achieved, assuring a base bleed situation as opposed to a thrusting system with the addition of base bleed.

#### PHYSICAL INTERPRETATION

From a variety of sources <sup>7</sup>, both theoretical and experimental, the mean flow field may be expected to look as depicted in Fig. 3. There are many ways to physically reason what may be expected with injection and base burning. The author prefers, for simplicity, arguments based upon injection effects on the streamline passing through the rear stagnation point. This streamline must, by definition, stagnate, so the static pressure plus the dynamic head govern this process. If the Mach number is reduced on this streamline, the stagnation pressure falls so the static pressure must rise. This results in a base pressure rise. The Mach number in combustng flows is primarily determined by the speed of sound because flow speeds are mainly set by the freestream speed. Since the dominant species

in the flow is  $N_2$ , mass diluent effects of various molecular weights will only have a weak effect on the stagnation pressure. Consequently, combustion heating is the dominant cause of base pressure changes.

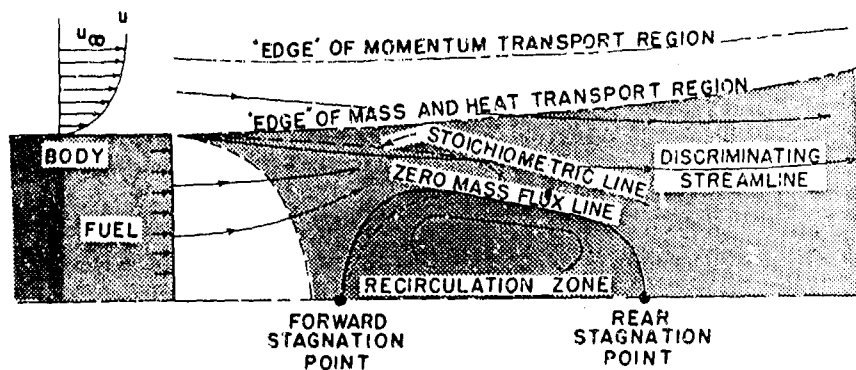


Figure 3. Presumed flow model for base burning

Another source of heating of the subject streamline would be the injection of hot gas, and this is what is accomplished in the preburning case. Control of the injectant temperature, however, alters the entire shape of the flow field and it is not clear what the optimum (if any) mix would be when considering an  $H_2/O_2$  ratio of injectants.

In consideration of the results below, there are two performance parameters of paramount interest. These are the base pressure,  $P_b$ , rise with injection. The no-injection base pressure will be denoted  $P_{b0}$ , and the freestream static pressure at the tailplane will be denoted  $P_1$ . The relevant force change on the base is then  $(P_b - P_{b0})A_b$ , where  $A_b$  is the base area. The overall mass injectant rate is that of  $H_2 + O_2 +$  diluent, denoted  $\dot{m}$ . The effective specific impulse is then

$$I_{sp} = (P_b - P_{b0}) A_b / \dot{m}$$

In order to facilitate comparison of various injectants it is also useful to quote the effective heating value of the fuel plus diluent combination. Pure hydrogen has a value of  $1.21 \times 10^5$  J/g and a typical hydrocarbon has values in the range  $2 - 2.5 \times 10^4$  J/g.

One final parameter used to characterize the injectant rate is the injection parameter  $I$ , defined as the ratio of mass injection rate to the "capture" mass flow rate of the free stream,  $\rho_1 V_1 A_b$ , where  $\rho_1$  is the freestream density and  $V_1$  the freestream velocity. For base bleed situations  $I$  is always a very low number compared with unity.

## RESULTS

Shown first are the results of pure and diluted hydrogen, using the base plate of Fig. 1. In Fig. 4 the  $I_{sp}$  is based upon the flow rate of hydrogen alone, regardless of the diluent. Where diluent was used, the amount was chosen to bring the effective heating value of the mixture to values which

would be practical for a fuel rich gas generator. The reason for presenting the results on the basis of the  $H_2$  flow rate alone are to emphasize the main results of Fig. 4 that the diluent makes little difference. The basic performance depends only upon the amount of fuel poured into the base region (the heat dump into the wake). This result has been qualitatively argued above.

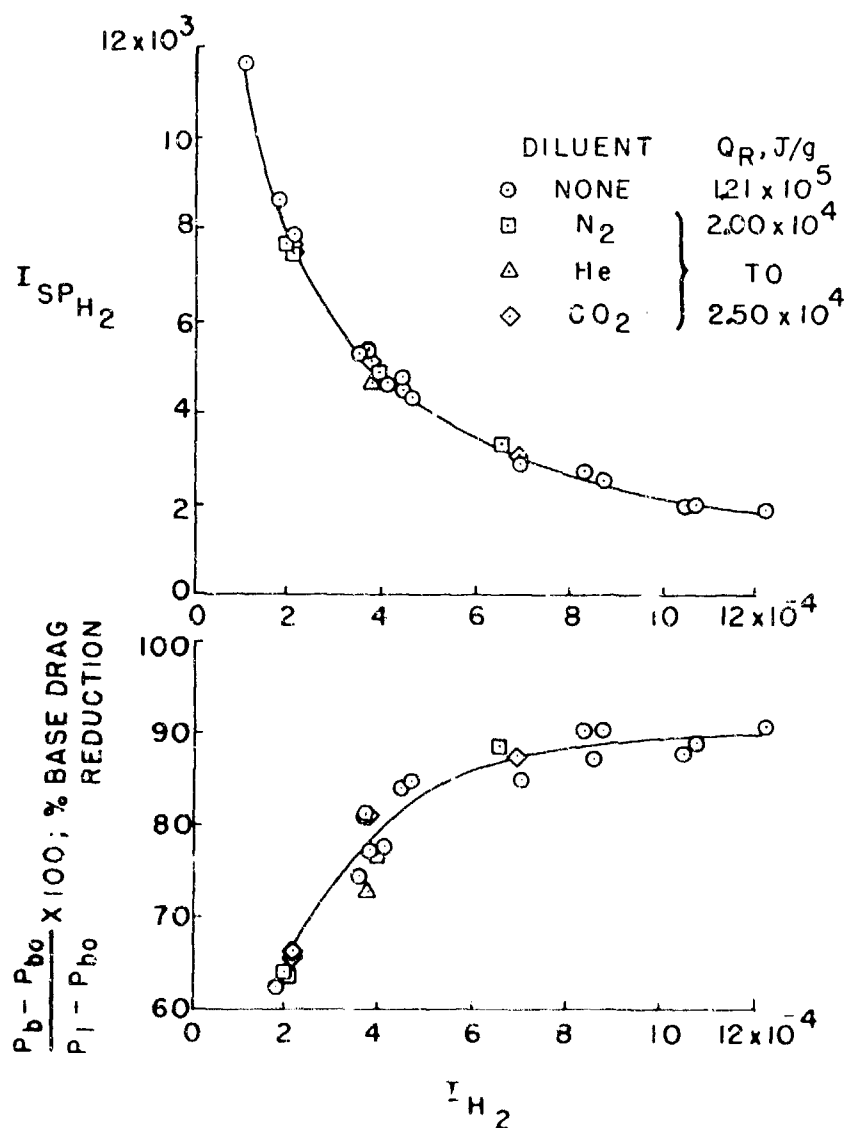


Figure 4. Base burning results with diluted and undiluted hydrogen

An interesting presentation of results occurs when the specific impulse is plotted as a function of the relative base drag reduction, as shown in Fig. 5. Here the true  $I_{sp}$  is shown on the ordinate, but scaled by the effective fuel heating value.<sup>sp</sup> For pure  $H_2$  injection the solid straight line results, which remains, within experimental scatter, a straight line even with diluent. Two major points here are (1) impressive  $I_{sp}$  results may be attained at base pressure reduction values as high as 90%, but (2) with this injection method 100% base drag elimination cannot be achieved.

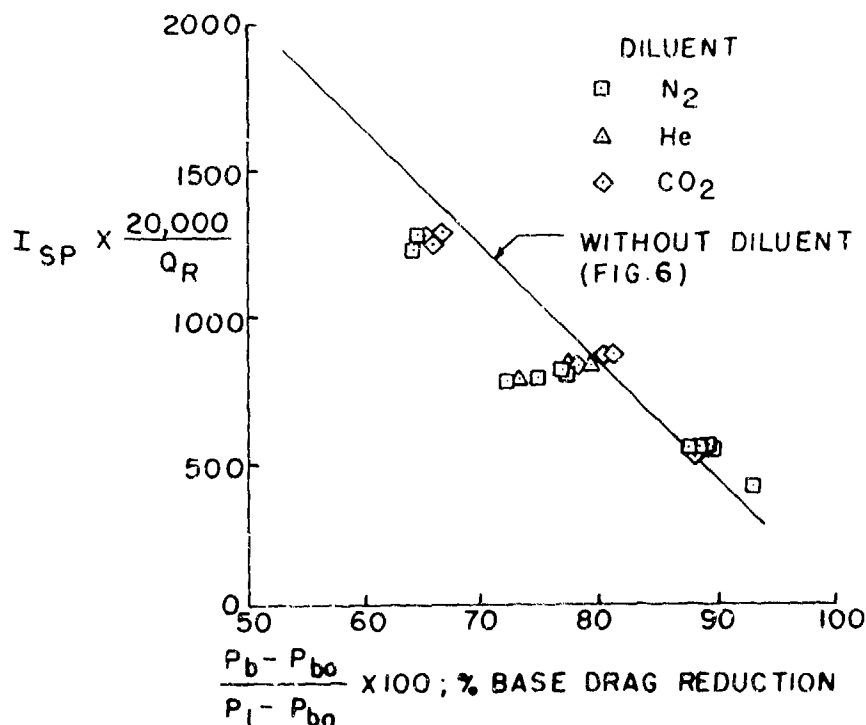


Figure 5. Scaled specific impulse against base drag reduction

The preburner configuration of Fig. 2 was first tested without injection and with pure hydrogen injection to assure results compatible with the Fig. 1 injector at the tailplane. Base pressure results differed by only 1%, which was within experimental scatter. Moreover, with pure  $H_2$  burning, the results for the preburner configuration did not differ from those of Fig. 4.

Figure 6 shows the effect of hydrogen injection rate with various values of  $O_2 + N_2$  maintaining a relatively constant  $O_2 + N_2$  mass flow rate. For comparison the base pressure results of Fig. 4 are also plotted on Fig. 6. The rather startling result is that performance is strongly improved with preburning.

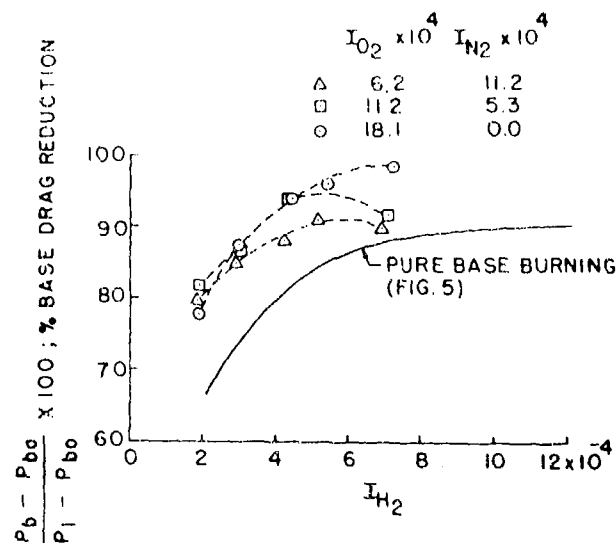


Figure 6. The effect of preburning on base pressure reduction

The net performance gains attainable by preburning are shown in scaled  $I_{sp}$  vs base drag reduction in Fig. 7. The dashed line represents an envelope of upper limit performance attainable. Impressive values of  $I_{sp}$  are attainable with nearly 100% base drag elimination. It was also checked that no effect of inert diluent appeared when the  $H_2/O_2$  ratio was held fixed.

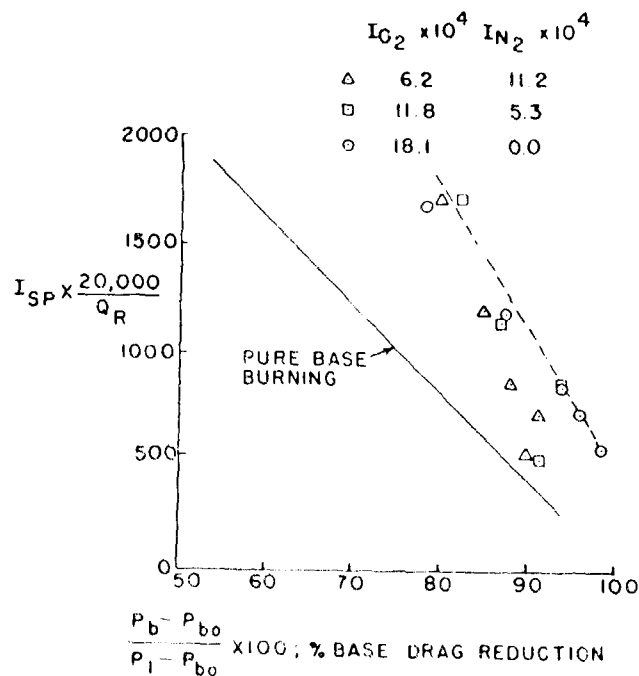


Figure 7. Preburning and pure  $H_2$  injection results compared

It is unclear from a physical viewpoint and without a theoretical model why preburning causes such a large performance increase, as compared with pure or diluted hydrogen injection. Nevertheless, the performance gain is impressive and makes base bleed an extremely attractive propulsive device.

#### CONCLUSION

Pure base burning performance with hydrogen fuel is determined by the hydrogen flow rate and is therefore dependent upon only the heat dump rate into the wake, independent of the diluent used. This has the consequence that the specific impulse for pure base burning (no preburning) is directly proportional to the heating value of the injectant.

Combined preburning and base burning yields considerably higher performance than with pure base burning of a cold injectant. Impressive performance values are attainable. For example, 90% of the base drag can be eliminated with a specific impulse greater than 1000 using an effective fuel heating value of 20,000 J/g.

#### REFERENCES

1. Baker, W. T., Davis, T., and Mathews, S. E., Reduction of Drag on a Projectile in a Supersonic Stream by the Combustion of Hydrogen in the Turbulent Wake, JHUAPL CM-673, June 4, 1951.
2. Sarafini, J. I., Dorsch, H. G., and Fletcher, E. A., Exploratory Investigation of Static and Base-Pressure Increases from Combustion of Aluminum Borohydride. Adjacent to Body of Revolution in Supersonic Wind Tunnel, NACA RM ES7E15, 1957.
3. Townsend, L. H., and Reid, J., in a Supersonic Stream, in Supersonic Flows, Chemical Processes, and Radiative Transfer, ed. D. B. Olfe and V. Zakkay, Mac Millan, New York, 1964.
4. Billig, F. S., External Burning in Supersonic Streams, JHUAPL TG-912, May, 1967.
5. Strahle, W. C., Theoretical Considerations of Combustion Effects on Base pressure in Supersonic Flight, Twelfth Symposium (International) on Combustion, pp. 1163-1173, The Combustion Institute, Pittsburgh, 1969.
6. Schadow, K. C., and Chieze, D. J., Base Drag Reduction by Combined External Burning/Base Burning, CPIA Pub. 315, March, 1980.
7. Strahle, W. C., Hubbarth, J. E., and Walterick R. E., Base Burning Performance at Mach 3, AIAA Journal, Vol. 20, No. 7, pp. 986-991, 1981.
8. Hubbarth, J. E., Strahle, W. C., and Neale, D. H., Mach 3 Hydrogen External/Base Burning, AIAA Journal, Vol. 19, pp. 745-749, 1981.

## Structure and Ballistic Properties of the Rheinmetall RH 49 Base-Bleed Projectile

Dr. Lutz Börngen  
Department of Ballistics

Dr. Ulf Hahn  
Manager-Development Artillery Ammunition

Rheinmetall GmbH, Ulmenstr. 127, 4000 Düsseldorf 30,  
Federal Republic of Germany

### INTRODUCTION

The total drag of an artillery shell consists of several contributions, for example wave drag, friction drag, drag due to lift and base drag. The part of base drag can add up to 75 % of the total drag of the projectile. Figure 1 shows the comparison of the total drag curve with the curve of base drag as function of Mach-number for the RH 49-BB round without base burning. This shows that one possibility to achieve extended ranges for fielded 155 mm gun systems is the reduction of base drag (ref. 1). At Rheinmetall the theoretical basis of the Base Bleed Effect (ref. 2 + 3) was elaborated and the projectile RH 49-BB was developed in the last years. As a result of the theoretical work a simple engineering-type model for base-bleed calculations was developed. Another similar model is known (ref. 4) which is more specialized and bases much more on a great number of wind tunnel measurements.

Next the base-bleed simulation is described. Afterwards the construction and firing results of the RH 49-BB projectile are presented. Finally the methods of trajectory calculation are mentioned.

### BASE BLEED SIMULATION

The supersonic flow around the base of an artillery projectile is rather complicated. The reason for the great base drag is the low base pressure. The base drag is reduced strongly, if a small amount of gas is blown into the afterbody wake. The gas is produced by a pyrotechnical unit placed in the bottom of the projectile (Base-Bleed-Effect). With the definition of a dimensionless gas flow rate,

$$I = \frac{\dot{m}_N}{\rho_\infty v_\infty A_{ref}} = \frac{\Gamma}{\gamma} \frac{p_B}{p_\infty} \frac{M_N}{M_\infty} \frac{a_\infty}{a_N} \left( \frac{d_N}{d_{ref}} \right)^2 \quad (1)$$

it is possible to draw the base pressure as a function of mass flow through a nozzle in the bottom of the round (Fig 2). Only the first part of this curve up to the maximum of base pressure (i. e. minimum of base drag) is important for the Base-Bleed-Effect. In this region where the mass flow rates are in the order of a few percent, the base burn units work.

The Rheinmetall simulation of the Base-Bleed-Effect is based on the theory of the outlet of a jet of gas from a reservoir and the stream tube theory. Figure 3 shows schematically the flow around the base of a boat tail of a artillery shell with base-bleed.

Using these theories it is possible to deduce the following system of equations, describing mass flow  $I$ , dead air angle  $\alpha$ , base pressure ratio  $p_B / p_\infty$ , length of dead air region  $l$ :

$$I = \frac{p_B}{p_\infty} \frac{M_N}{M_\infty} \frac{\Gamma}{\gamma} \left( \frac{d_B}{d_{ref}} \right)^2 \frac{a_\infty}{a_{RES}} \sqrt{1 + \frac{\Gamma-1}{2} M_N^2} \quad (2)$$

$$\alpha = v(M_2) - v(M_1) \quad (3)$$

$$\frac{p_B}{p_\infty} = \left( \frac{2 + (\gamma-1) M_\infty^2}{2 + (\gamma-1) M_2^2} \right)^{\frac{\gamma}{\gamma-1}} \quad (4)$$

$$l = \frac{d_B - \delta}{2} \cot(\alpha + \beta) \quad (5)$$

Input data are the adiabatic exponents  $\gamma$  and  $\Gamma$ , the geometric data  $d_{ref}$ ,  $d_N$  and  $d_B$ , the sound velocities  $a_\infty$  and  $a_{RES}$  the boat tail angle  $\beta$ . The Mach-number  $M_1$  follows from

$$\beta = v(M_1) - v(M_\infty) \quad (6)$$

$v(M)$  is the Prandtl-Meyer-Funktion.  $\delta$  can be calculated by the equations:

$$\delta = d_N \sqrt{M_N} \left( \frac{\Gamma+1}{2 + (\Gamma-1) M_N^2} \right)^{\frac{\Gamma+1}{4(\Gamma-1)}} \quad (7)$$



The gas flow rate is given by the burning law of the Base-Bleed grain. We assume the following burning law for the simulation.

$$R = C P_{RES}^{\mu}$$

$$= C \left( 1 + \frac{\Gamma - 1}{2} M_N^2 \right)^{\frac{\mu \Gamma}{\Gamma - 1}} P_0^{\mu} \quad (8)$$

and now

$$I = \frac{\alpha_{\infty} \rho_{PR} F_{PR}}{M_{\infty} \gamma A_{ref} P_{\infty}} R \quad (9)$$

$\rho_{PR}$  is the constant density of the base-bleed grain. The burning surface  $F_{PR}$  depends on the geometry of the base-bleed unit and the burning rate.

The solution of this system of equation gives the change in base pressure and so also change of base drag by base burning. The connection of this simulation to a ballistic flight programme makes it possible to calculate the trajectories of base-bleed projectiles.

#### PROJECTILE RH 49-BB

The 155 mm RH 49-BB is a long range projectile with bomblet submunition. The round is effective against semi hard targets at ranges up to 31 km fired with the field howitzer FH 70 or 38 km fired with 52 caliber extended range ordnance. The shell carries 49 grenades of the type RH II with self-destruction device. Figure 4 shows the construction of our projectile. The main parts are the one-piece shell, the bottom with the base-bleed motor, the 49 grenades, the expulsion charge and the mechanical time fuze. The base-bleed grain is shown in Figure 5. A summary of the technical characteristics of the RH 49 base-bleed projectile is given in table 1.

TABLE 1. Technical characteristics of RH 49 Base-Bleed

Weight	44.6 kg
Muzzle velocities	
Charge 8: L10A1	823 m/s
Charge 7: L 8A1	678 m/s
Center of gravity	319 mm
Axial moment of inertia	0.15 kg m <sup>2</sup>
Transverse moment of inertia	1.80 kg m <sup>2</sup>
Reference diameter	154.7 mm
Base diameter	146.2 mm

Diameter of base orifice	43.5	mm
Burning law of propellant		
	C =	1.4 mm/sec
	$\mu$ =	0.31
Density of propellant	1.37	g/cm <sup>3</sup>
Weight of BB grain	1.45	kg

#### FIRING RESULTS

The firing results obtained over the last years have demonstrated that the maximum range of the RH 49-BB projectile is greater than 30 km with a muzzle velocity of 823 m/s. The probable errors are  $PE_R < 0.3 \%$  and  $PE_D < 1$  mil. Compared with the inert projectile the base burning produces increasing ranges of 19 - 26 % depending on muzzle velocity and elevation. Thus the base-bleed motor causes a decrease of base drag of about 60 - 80 %.

The burning time was measured statically and in flight by optical and radar methods. The static burning time is 26 s at a temperature of 21°C. Depending on the trajectory the burning time increases up to 36 s. The static burning rate is 1.4 mm/sec. At grain temperature of - 32 °C the burning rate decreases 4 %, at 52°C the burning rate increases 8 %. From these experimental data, it is possible to determine the coefficients of the burning law:  $C = 1.4$  mm/sec,  $\mu = 0.31$ .

From radar measurements the drag coefficient  $C_D$  was calculated as a function of Mach-number for the inert projectile and for the base-burning phase. These curves are shown in Figure 6. The value of  $C_D$  during base-burning is nearly constant ( $C_D = 0.18$ ). The curve deduced from radar measurement is compared with results of the base-bleed simulation. The  $C_D$  curve of the inert projectile has the typical shape of a modern artillery shell. After burn-out the  $C_D$ -value jumps from the base-burning-curve to the inert curve. The Mach-number related to this jump depends on the firing conditions.

#### SIMULATION OF TRAJECTORIES

The simulation programme of the base-bleed effect was linked to a two-degrees-of-freedom trajectory model. The given base drag of the inert projectile, which comes from empirical equations or from tables like DATCOM (Ref. 5), is corrected in the described way. So the drag can be written.

$$D = \frac{\pi \rho_{\infty} v_{\infty} d_{ref}^2}{8 m} (c_B c_D - c_B' f_B c_D) \quad (10)$$

with

$C_D$  - drag coefficient of the inert projectile,  
function of Mach-number

- $C_B$  - Ballistic coefficient of the inert projectile, function of muzzle velocity and elevation
- $f_B$  - Coefficient of base drag reduction
- $C_B'$  - Additional ballistic coefficient of the base burning phase, function of muzzle velocity and elevation

The base drag reduction is calculated by the base-bleed simulation. The ballistic coefficients are used to fit the calculations to the firing results. To reduce the time of calculations we use the results of the flight simulation with base-bleed as input data for a simpler two-degrees-of-freedom trajectory programme with change of the  $C_D$ -curve and ballistic coefficient without gasdynamic base-bleed simulation.

The drags of the base-burning phase and the phase after burn-out can be written

$$D_1 = \frac{\pi \rho_\infty v_\infty^2 d_{ref}^2}{8 m} C_{BB} C_{DB} \quad \text{during base-burning} \quad (11)$$

$$D_2 = \frac{\pi \rho_\infty v_\infty^2 d_{ref}^2}{8 m} C_B C_D \quad \text{after burn-out} \quad (12)$$

- $C_{BB}$  - ballistic coefficient during base-burning, function of muzzle velocity and elevation
- $C_{DB}$  - drag coefficient of the base bleeding projectile, constant value of 0,18

This programme allows very fast calculations of trajectories of the RH 49-BB round. The results of these calculations are presented in Figure 7 - 9. In figure 9 the velocities of the inert and base-burning (burning time 36 s) projectile as a function of time of flight for maximum range are shown.

#### FINAL REMARKS

The long range 155 mm projectile RH 49-Base Bleed with bomblet submunition is presented. With the help of a simple theoretical model for calculating base bleed characteristics methods for range calculation during development are explained. In the next future calculations with the modified point mass trajectory (ref. 6) model are planned.

# LIST OF SYMBOLS

$P$	: Pressure
$\rho$	: Density
$m$	: Projectile mass
$\dot{m}$	: Mass flow
$I$	: Dimensionless mass flow
$A$	: Area
$a$	: Speed of sound
$v$	: Velocity
$M$	: Mach-number
$d$	: Diameter
$\delta$	: Diameter of inner flow throat
$l$	: Axial extension of dead air region
$\alpha$	: Dead air angle
$\beta$	: Boat tail angle
$c$	: Coefficient
$C$	: Burning equation coefficient
$\mu$	: Exponent of burning equation
$R$	: Burning velocity
$F$	: Propellant surface
$D$	: Drag
$\Gamma$	: Ratio of specific heats of combustion products
$\gamma$	: Ratio of specific heats of air

## SUBSCRIPTS

RES	: Reservoir
$\infty$	: Undisturbed flow values
B	: Base
N	: Nozzle
D	: Drag
ref	: Reference value
PR	: Propellant

#### REFERENCES

1. Romer, R., Reichweitensteigerung bei Artilleriegeschossen  
Wahrtechnik. pp. 54-58, October 1976.
2. Schilling, H., Experimental Investigation on the Base-Bleed  
Effect for Body-Tail Combinations, Proc. 8th  
Intern. Symp. Ball., Orlando, Fla., 1984.  
  
Schilling, H., A Simple Theoretical Approach for Base-Bleed  
Calculations, Proc. 9th  
Intern. Symp. Ball., Shrivenham, 1986.  
  
Hellgren, R.V., Range Calculation for Base-Bleed Propellants,  
Proc. 6th Intern. Symp. Ball., Orlando, Fla., 1981.
5. Finck, R.D., et al., USA Stability and Control DATCOM,  
McDonnell Douglas Co., 1972.
6. Lieske, R.F., Modified Point Mass Trajectory Modeling  
for the 155 mm, DPICM, M 864 Base-Burn Projectile,  
BRL, Aberdeen MD 21005-5066.

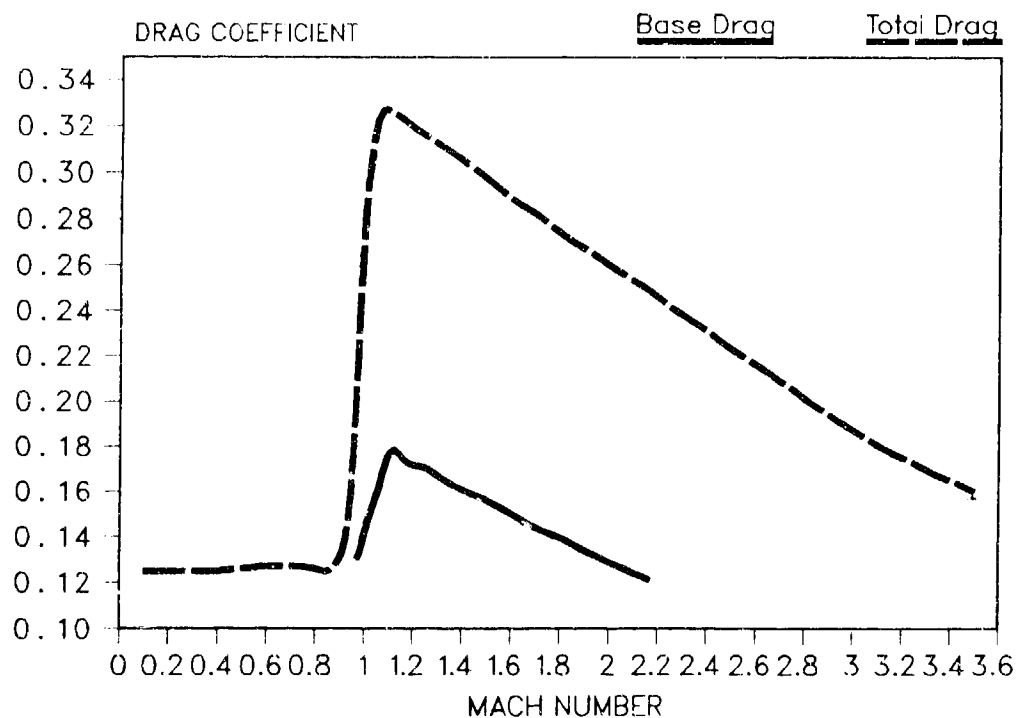


FIGURE 1 Comparison of total drag and base drag of RH 49-BB without Base-burning.

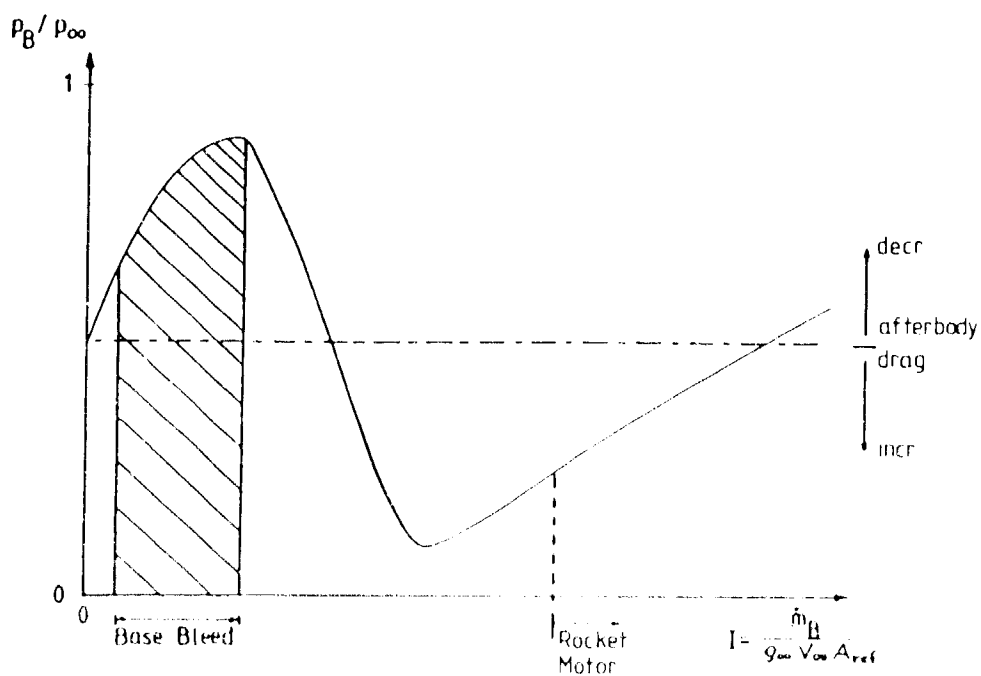


FIGURE 2 Base-bleed characteristics

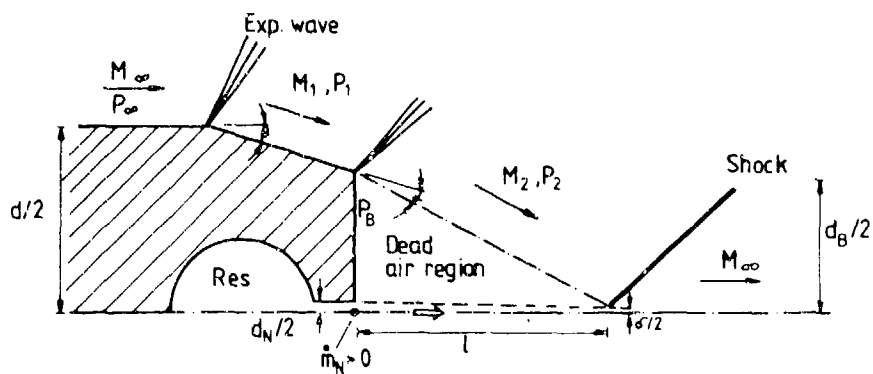


FIGURE 3 Schematic Supersonic base flow pattern

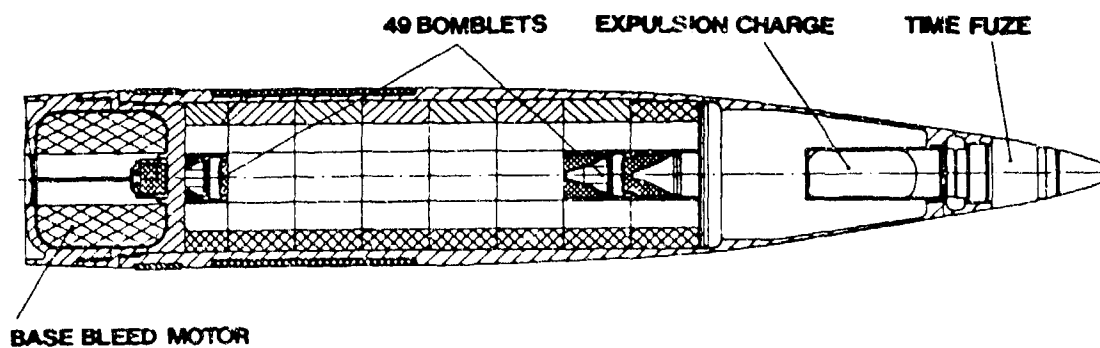


FIGURE 4 Long range projectile 155 mm RH 49-BB

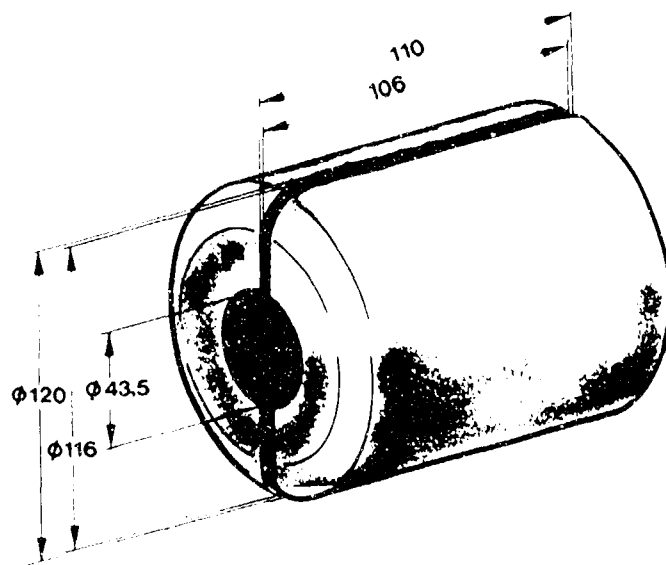


FIGURE 5 RH 49-BB - Base-Bleed-Grain

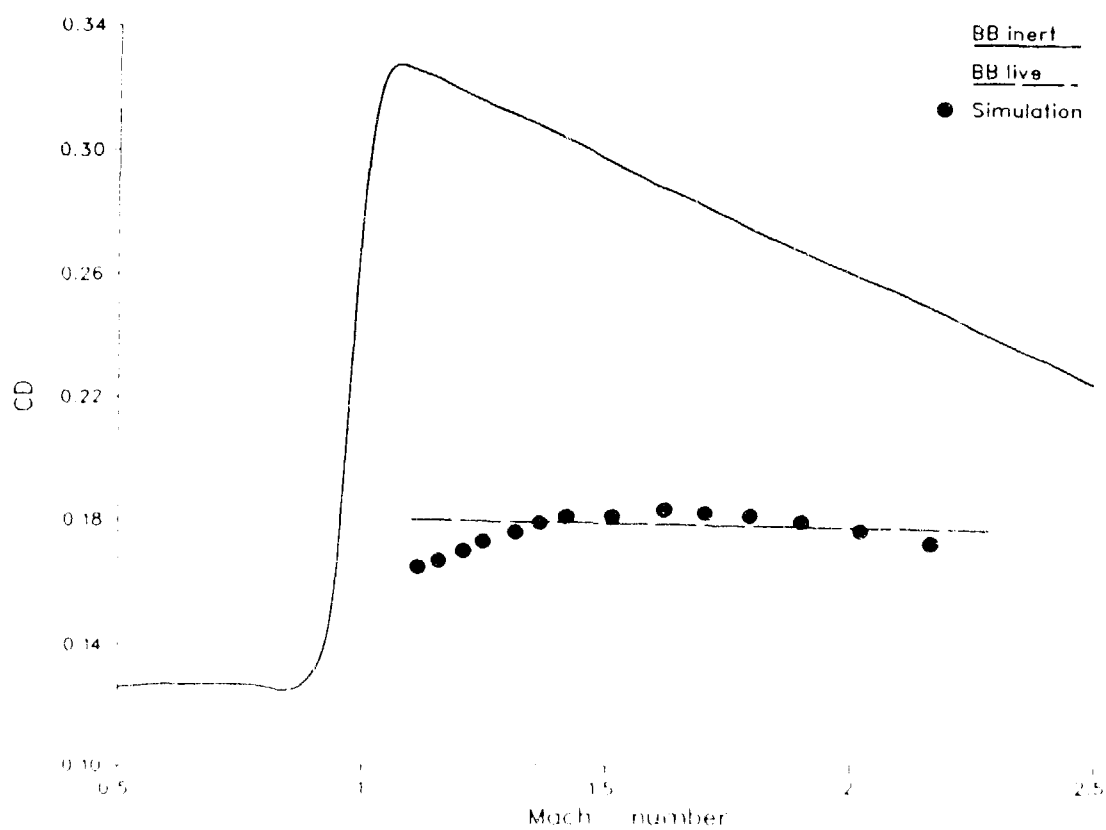


FIGURE 6 RH 49-BB - Base drag vs. flight Mach number



### Charge 7 L8 A1

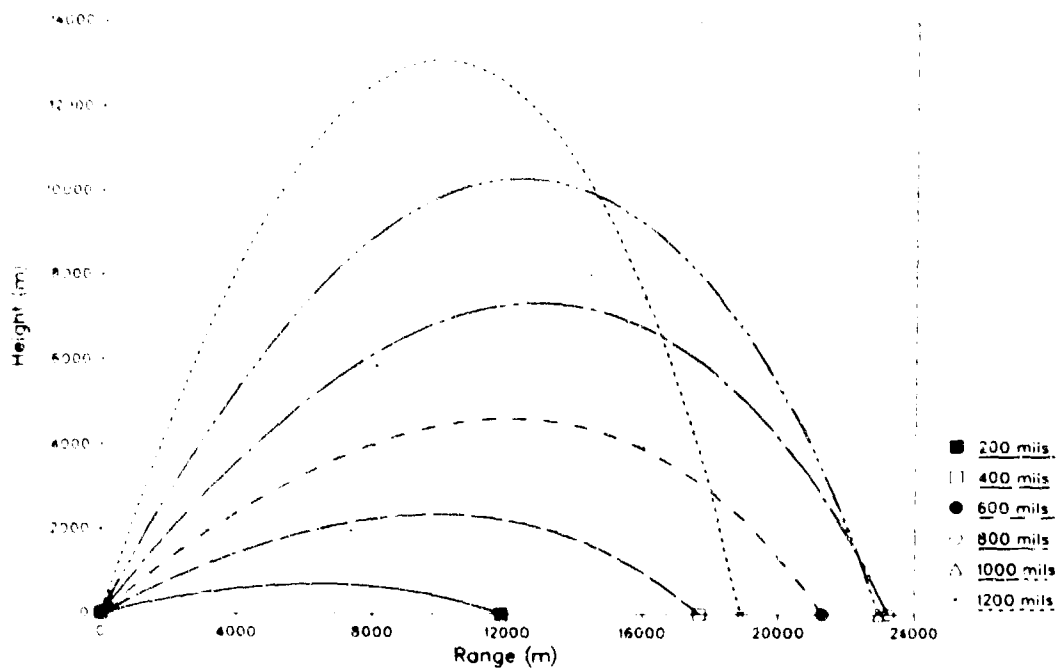


FIGURE 7 RH 49-BB - Calculated trajectories for charge 7 (L8A1),  $v_0 = 678$  m/s

### Charge 8 L10 A1

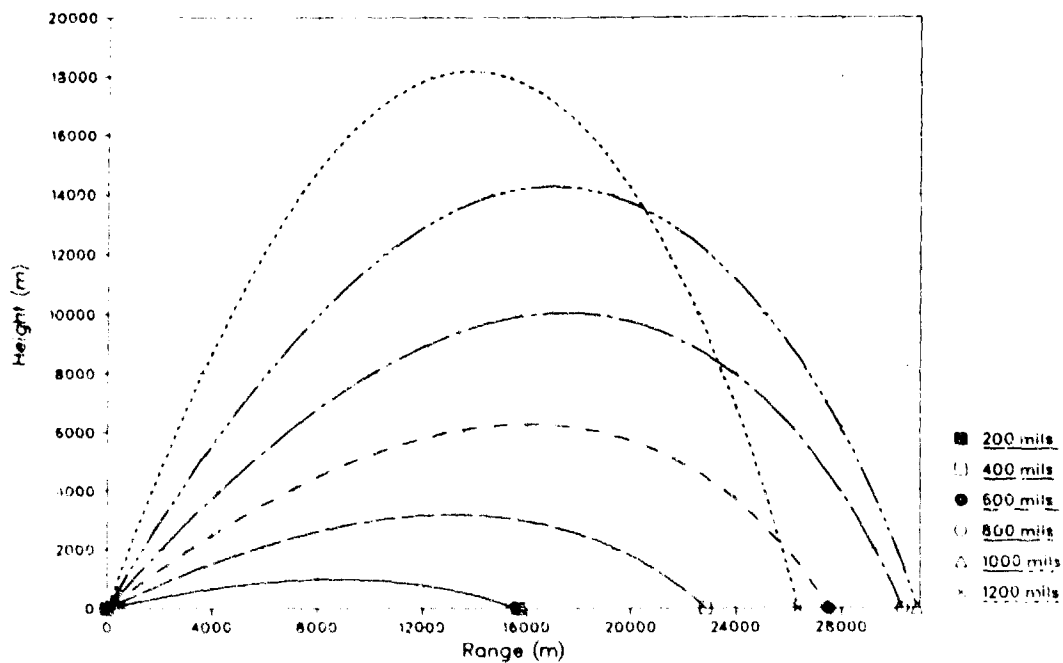


FIGURE 8 RH 49-BB - Calculated trajectories for charge 8 (L10A1),  $v_0 = 823$  m/s

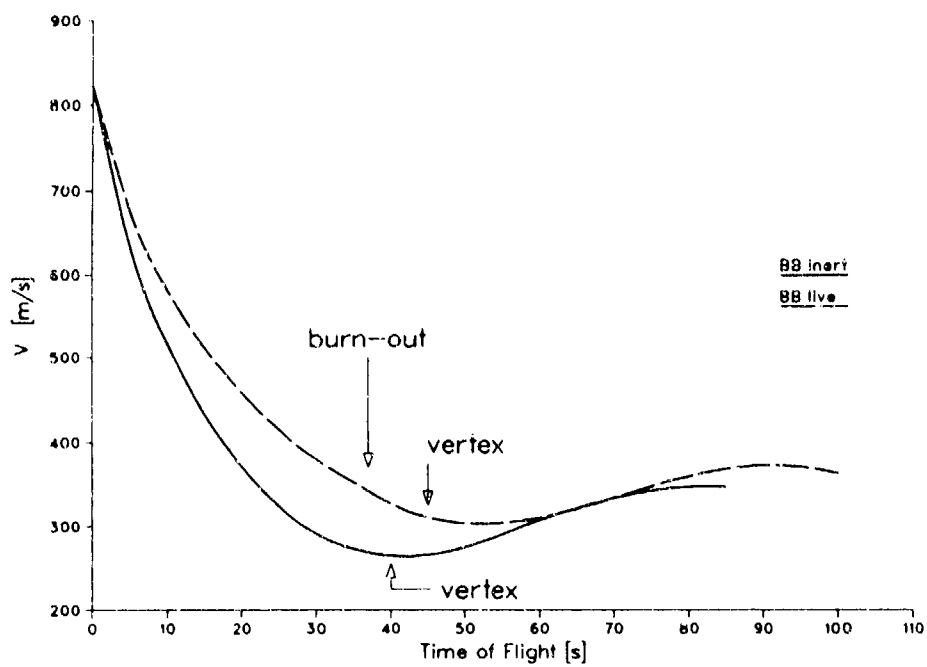


FIGURE 9 RH 49-BB - Velocity curves for maximum range trajectory

# A STUDY OF DRAG REDUCTION BY BASE BLEED AT SUBSONIC SPEEDS

Ding Zeshong, Llu Yafel & Chen Shaosong

East China Inst. of Technology, CHINA.

## 1. INTRODUCTION

Base bleed is accepted now as the most effective technique for reducing drag. Large-caliber, long-range and Low-drag projectile can extend its range by 30% and the gain is quite high. At present, the base bleed technique is mostly used in range of supersonic speed. In accordance with experimental results of cold air bleed, the only research data<sup>(1)</sup> about base bleed of three-dimensional body under subsonic and transonic speeds predict that base drag reduction rate by base bleed is very low in the speed range.

What's the base bleed rate under subsonic and transonic speeds then? It is of great importance to understand the problem in developing base bleed technique and modifying old-fashioned projectile having lower initial velocity.

For this purpose, a wind tunnel test is carried out with real base bleed grain, the base drag reduction rate by base bleed is obtained under subsonic and transonic speeds and compared with results of cold air bleed.

## 2. EQUIPMENT, MODEL AND TEST

### 2.1 Equipment

The test is carried out in base bleed wind tunnel HG-03 in East China Institute of Technology. The tunnel is an open-jet wind tunnel with a centre-body. Mach number varies from 0.6 to 3, and the circumstance pressure on the sea surface can be simulated.

The centre body is supported by four radial struts on the stilling chamber, and the pressure-tube is protruded from the wind tunnel through them, therefore the disturbance of the model support upon the base flow field is eliminated.

The quality of the flow field is high. When  $M = 0.6 \sim 0.8$ ,  $\Delta M_{\max} / M_{cp} < 0.6\%$ , and when  $M = 0.98$ ,  $\Delta M_{\max} / M_{cp} < 1\%$ . The centre-body nozzle is shown in Fig.1.

### 2.2 Model

In this test, a cylindrical tail model is used, which is connected with centre-body end. Its diameter is 0.034m. The ratio of the bleed hole diameter  $D_j$  to the diameter  $D$  of the model base is  $D_j / D = 0.5$ .

### 2.3 Pressure Measurement

The total pressure of the wind tunnel, the static pressure of free-stream and the base pressure are measured in the test. The transducer of base pressure is a  $\pi$ -form beam strain gage

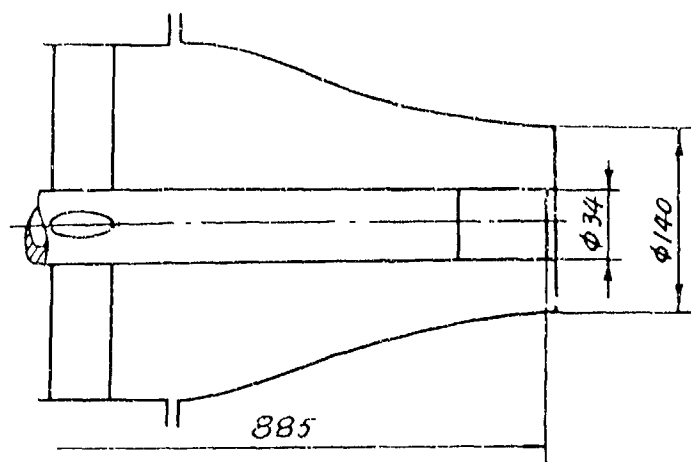
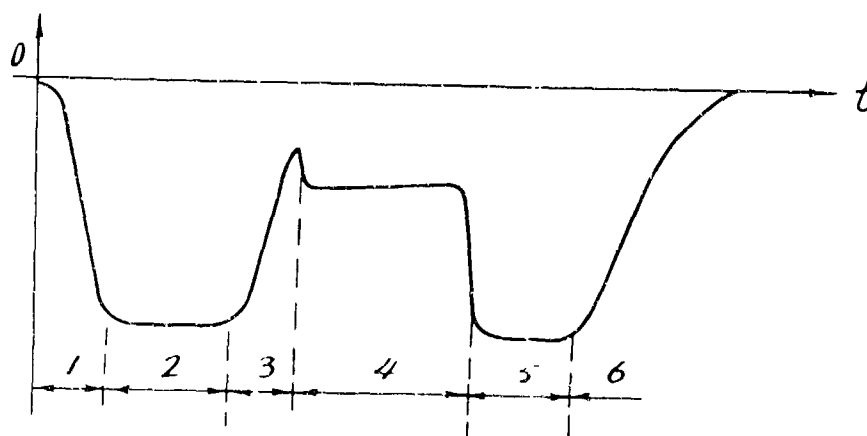


FIGURE 1. Centre body nozzle

transducer, its measurement range is  $\pm 9,810 \text{ N/m}^2$ . All the data are acquired and reduced by computer.

#### 2.4 Base Bleed Grain

Three types of base bleed grains are used in the present test, the burning temperature of number 1 grain is over  $3,000^\circ\text{C}$  and that of number 2 and 3 grain is about  $1,300^\circ\text{C}$ .



- |                        |                   |                      |
|------------------------|-------------------|----------------------|
| 1 start of wind tunnel | 2 flow steady     | 3 ignition           |
| 4 stable burning       | 5 stop of burning | 6 stop of the tunnel |

FIGURE 2. Varied curve of base pressure with time

TABLE 1. Re Number at Each Mach Number

M	Re ( $\times 10^7$ ) / m
0.59	1.64
0.71	2.00
0.82	2.43
0.98	3.26

### 2.5 A Brief Account of Test

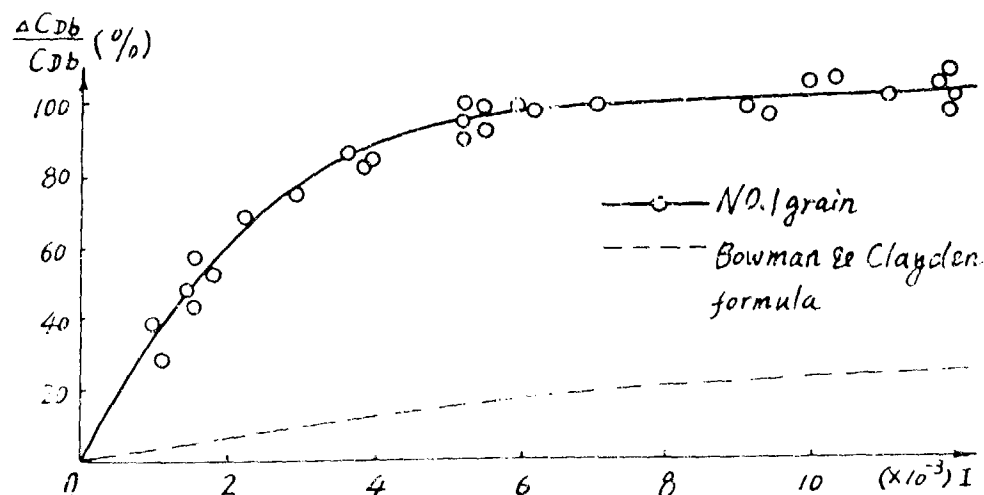
The tests are carried out under four Mach numbers, i. e.  $M=0.59$ ,  $0.71$ ,  $0.82$  and  $0.98$ .

In the whole process of blowing, i. e. before, during and after burning of the grain, the changes of model base pressure are measured, and the time of burning is recorded. Finally,  $P-t$  curve is obtained which is shown in Fig. 2. After processing, the variation of base drag reduction rate with injection parameter  $I$  can be found. Correspondence of  $M$  with  $Re$  is as table 1.

These numbers are far beyond the critical  $Re$  ( $6.5 \times 10^6$ ) of the three-dimensional boundary layer transition, for the practical use the effect of  $Re$  on base pressure can be neglected.

### 3. RESULTS AND DISCUSSION

The experimental data under different Mach numbers are processed into the curves denoting the variation of base drag reduction rate  $\Delta C_{Db}/C_{Db}$  by base bleed with injection parameter  $I$  and shown in Fig.3~Fig.6.

FIGURE 3. Base drag reduction rate curve by base bleed at  $M=0.59$

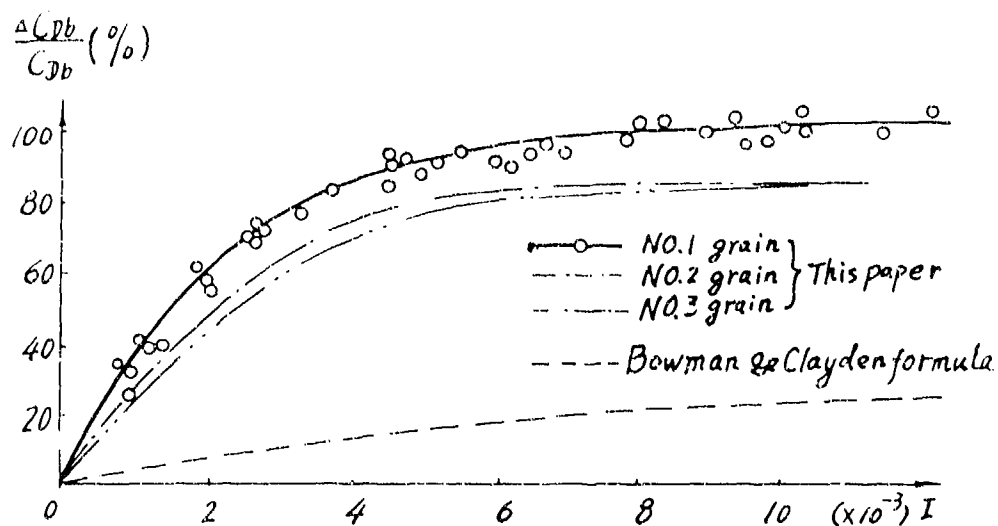


FIGURE 4. Base drag reduction rate curve by base bleed at  $M=0.71$

It can be seen from the figures above that under subsonic and transonic speeds, the whole changed tendency of  $\Delta C_{Db}/C_{Db}$  of all the three grains is identical. It is characterized as follows:

(1) Under small value of  $I$ ,  $\Delta C_{Db}/C_{Db}$  is increased sharply as  $I$  increased. As value  $I$  is small, the velocity and momentum of base bleed are small, and when value  $I$  is increased, the mass of gas entering the wake region and the energy released by burning in a unit of time are quickly increased so that the near wake region is greatly extended, accompanying considerable rise of base pressure and  $\Delta C_{Db}/C_{Db}$ .

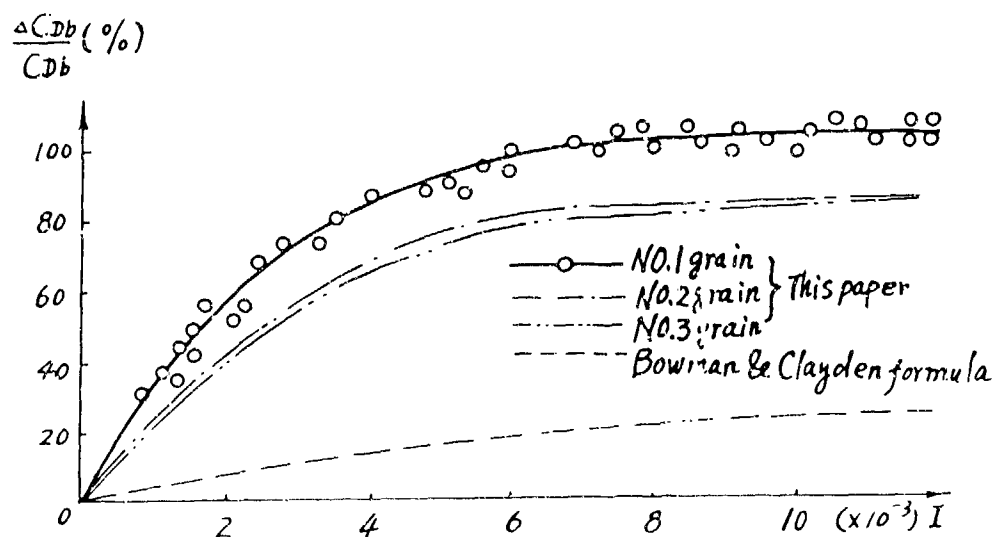


FIGURE 5. Base drag reduction rate curve by base bleed at  $M=0.82$

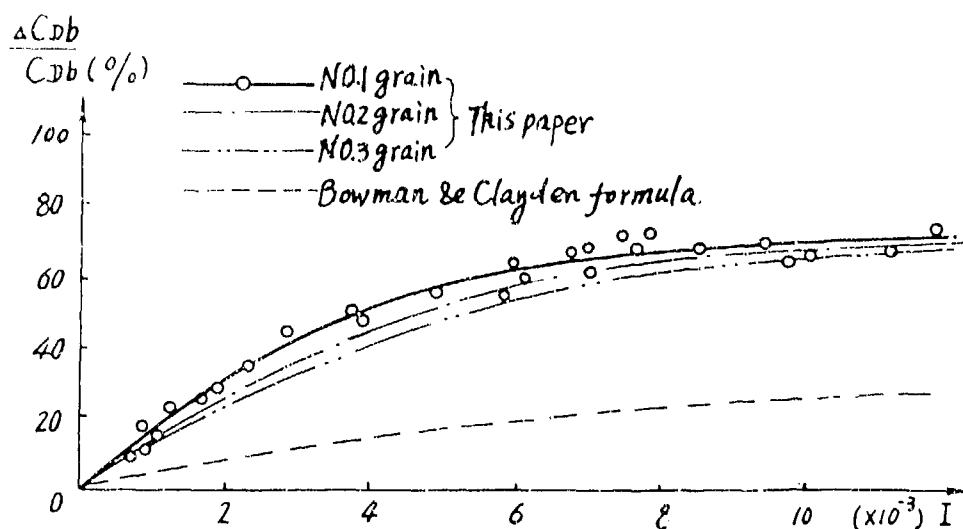


FIGURE 6. Base drag reduction rate curve by base bleed at  $M=0.98$

(2) As value  $I$  is greater, the rise of the curves is gradually flattened. With a greater value  $I$ , the mass entering the wake region in a unit of time is larger, and its velocity and momentum are greater. The strong bleed momentum may destroy the structure of the base recirculation region, reduce the base pressure and cancel the profit from the increase of mass and energy, so that it makes the curve changed smoothly. As value  $I$  is even much greater, the increase of  $\Delta C_{Db}/C_{Db}$  is small.

(3) Under different Mach numbers, the effect of number 1 grain's reduction drag is the best, since its burning temperature is much higher than that of number 2 and number 3 grains.

(4) In the range  $M=0.59\sim 0.82$ , the base drag reduction rate of number 2 and number 3 grains is about 80%, while that of number 1 grain is as high as 100%, i. e. the base drag is completely eliminated.

TABLE 2. The Experiment Results

$M$	point num. of $\frac{\Delta C_{Db}}{C_{Db}} > 100\%$	point num. of $97\% < \frac{\Delta C_{Db}}{C_{Db}} < 100\%$	Total point num. of $I > I_{opt}$
0.59	8	2	10
0.71	9	2	11
0.82	16	3	19

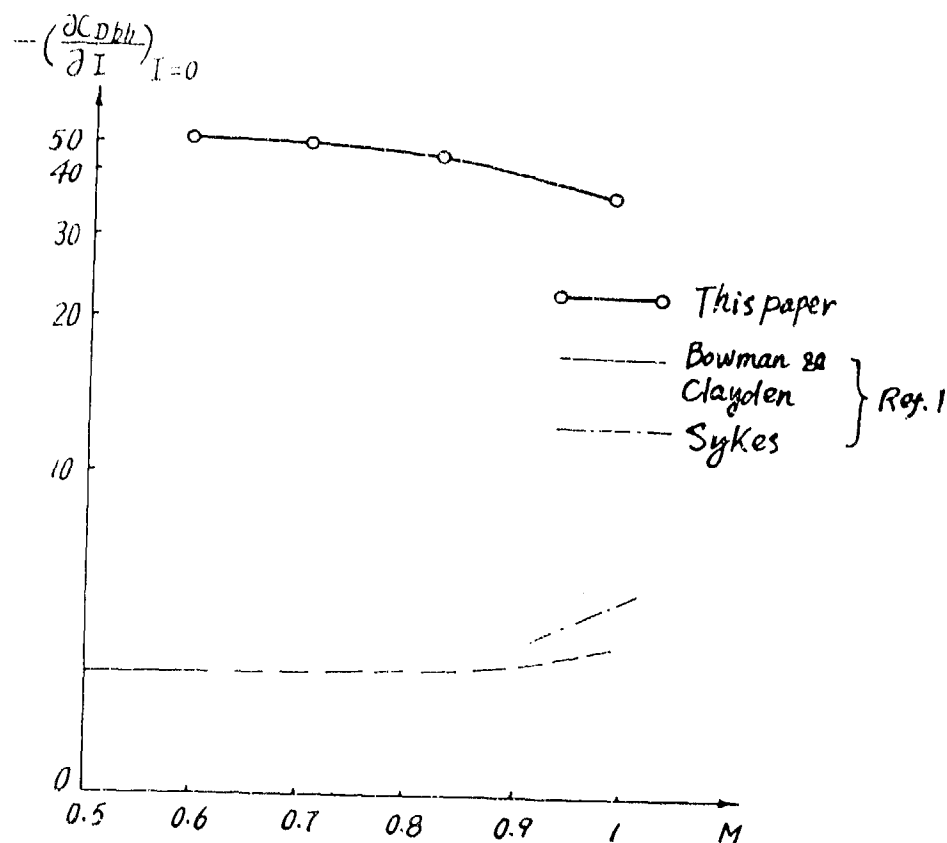


FIGURE 7. Variation of reduction drag efficiency  $-(\partial C_{Dbb} / \partial I)_{I=0}$  with Mach number

The experiments are made repeatedly to prove the reliability of the above-mentioned experimental results. It is shown that under above three Mach numbers, as  $I$  is larger than a definite value, the value of  $\Delta C_{Dbb} / C_{Dbb}$  of most experimental points is slightly higher than 1, and the value of less points is lower than 1 but higher than 0.97. (see table 2). In consideration of the experimental errors, it is regarded that the base drag reduction rate by base bleed of number 1 grain is 100%, the base drag can be completely eliminated. In accordance with base bleed cold air test, Bowman and Clayden derived an empirical formula of reduction drag by base bleed with the use of propellant as a fuel:

$$C_{Dbb} = C_{Dbb} e^{-1/I}$$

The formula was widely quoted. These experiments, however, show that it is not in good agreement with grain's base bleed results. The main difference is as follows:

(1) Under subsonic and transonic speeds, the base bleed reduction drag rate of solid fuel estimated by the formula is much lower than the experimental value. See Fig.3 - Fig.6. In the range of  $M=0.59-0.82$ , the estimated value is only equivalent to  $1/5$  of number 1 grain and  $1/4$  of number 2 and 3 grains.

(2) It can be further understood from Fig.3 - Fig.6 that the variations of real grains base drag reduction rate by base bleed with injection parameter  $I$  does not correspond with the index relation of the empirical formula by Bowman and Clayden. After the value  $I$  is larger than 0.007, the change of reduction drag rate takes place slightly.



Nevertheless, according to the estimation by the empirical formula, when the value  $I$  goes up from 0.007 to 0.012, the reduction drag rate increases almost 50%.

(3) Under subsonic and transonic speeds, the variations of reduction drag rate by real grain's burning with Mach number is different from the expected by reference<sup>[1]</sup>. In that literature, stands for reduction drag efficiency by base bleed. According to the experimental data under  $M=0.11$ , 0.64 and supersonic speeds, the interpolation was made for transonic speed, and the experimental results of transonic speed by Sykes were quoted. See Fig.7. Under subsonic speeds,  $-(\partial C_{Dbb}/\partial I)_{I=0}$  are constant and very low. Under transonic and low supersonic speeds, it goes up steeply, and its maximum is reached about  $M=2.5$ .

But the present experiments of real base bleed grain carried out in wind tunnel show that under subsonic and transonic speeds, the solid fuel-rich grain's base drag reduction efficiency by base bleed is very high, in the range of  $M=0.59-0.82$ ,  $-(\partial C_{Dbb}/\partial I)_{I=0}$  is equivalent to the data with  $M=2-2.5$ . Therefore, the changing tendency of the solid fuel-rich grain reduction drag efficiency by base bleed is high-low-high when Mach number goes up from subsonic, transonic to low supersonic.

Preliminary analysis indicates that the great difference between results by reference<sup>[1]</sup> and real base bleed grain's reduction drag efficiency is caused by the fact that the cold and hot air experiments made by Bowman and Clayden didn't simulated the near wake burning effect of fuel-rich products in the wake region and the influence of different release positions of enthalpy value. It can be concluded that the simulation of solid fuel base bleed with gas (cold or hot) cannot meet the needs of engineering.

#### 4. SUMMARY

The present study uses solid fuel-rich base bleed grain to do the experiment of the base drag reduction rate by base bleed in wind tunnel and the following main results are obtained:

(1). In the range of  $M=0.6-0.8$ , the base drag reduction rate by base bleed of solid fuel-rich grain is very high. Number 2 and 3 grains can reduce base drag by 70-80%, while number 1 grain can completely eliminate the base drag. It is worth developing the technique of the reduction drag by base bleed in the range of subsonic and transonic speeds.

(2). In the range of subsonic, transonic and low supersonic speeds, the variation tendency of grain's reduction drag efficiency with Mach number is as: high-low-high. Sharp changes take place in the range of transonic speeds.

(3). The estimated value by Bowman and Clayden under subsonic and transonic speeds is only 1/4-1/5 of real value of solid fuel-rich grain and so it is not applicable.

#### 5. NOMENCLATURE

$C_{Db}$	base drag coefficient without base bleed
$C_{Dbb}$	base drag coefficient with base bleed
$\frac{\Delta C_{Db}}{C_{Db}} = \frac{C_{Db} - C_{Dbb}}{C_{Db}}$	base drag reduction rate by base bleed
$D$	model diameter
$D_j$	bleed hole diameter
$I = \frac{\dot{m}}{PVS}$	injection parameter
$\dot{m}$	mass burning rate
$M$	Mach number

Re	Reynolds number
S	base area
V	velocity of free stream
$\rho$	density of free stream
$-\left(\Delta C_{Dbb} / \Delta I\right)_{I=0}$	reduction drag efficiency by base bleed

## 6. REFERENCE

1. Bowman, J. E. and Clayden, W. A., Reduction of Base Drag by Gas Ejection, RARDE 4/69

**TESTING OF PARTS AND COMPLETE UNITS OF THE SWEDISH  
BASE-BLEED SYSTEM**

---

Nils-Erik Gunners, Kurt Andersson, Yngve Nilsson  
Swedish Defence Research Establishment  
Box 551, S-147 25 TUMBA, Sweden

**ABSTRACT**

The Swedish Base-Bleed system was invented about twenty years ago. During the research leading to the invention and during the continued development a number of different methods and experimental procedures for testing parts as well as the complete system have been developed.

The paper describes several of these tests in relation to the functioning and the design of the system. Examples of test results and advices on their application are presented.

The first part describes laboratory methods and experimental facilities for testing parts such as propellant grains, igniters and nozzle systems in combustion bombs, spin stand, soft recovery acceleration facility and supersonic wind tunnel.

The second part treats parts and complete base-bleed units functioning and performance testing by means of gun firing in aeroballistic range and in actual free flight trajectories.

## 1. INTRODUCTION

Longer range and greater accuracy are constant objectives when new ammunition is developed or existing ammunition modified. Several methods of achieving these goals may be applied. Most methods can be combined.

Afterbody drag accounts for a substantial part of the total drag, more than 50 % for a slender-nose projectile. Thus, the importance of decreasing the afterbody drag is apparent. By means of a base-pressure-increasing system, such as base-bleed, the base pressure can be increased considerably during an important part of the flight time. This also affects the optimum design of the projectile afterbody.

The Swedish Base-Bleed System was invented in the late 1960-ies, /1/. Characterized by great simplicity and very good performance when correctly designed it has become an internationally adopted prototype for most later designs. It is especially advantageous to modern low drag projectiles. During the research leading to the invention and during the continued development a number of different methods and experimental procedures for testing parts as well as the complete system have been developed. Since these methods and procedures are strongly related to the design and functioning of the system a short resumé of the fundamentals might be of value. Phenomena to which the system is subjected and which give rise to testing will be pointed out.

Environmental tests, such as drop tests, vibration tests, temperature cycling and performance over specified temperature and humidity ranges, are carried out in accordance to actual regulations for conventional ammunition.

Several aging tests are performed of the base-bleed propellant grain and igniter as well as of mechanical parts of the base-bleed unit such as sealings. Aging tests of complete units are also performed. Ultimate tests are gun firings.

In this report neither environmental nor aging tests will be further discussed.

It should be noted that the tests reported here are primarily used for research and development although most of them, with minor alterations, could be used as production tests.

## 2. FUNDAMENTALS OF THE SWEDISH BASE-BLEED SYSTEM

The purpose of the base-bleed system is to eject, or bleed, a suitably low mass flow of under stoichiometric solid propellant combustion products from the body of a flying object, such as a gun projectile, into the near wake where the combustion is completed with ambient air. This affects the wake flow in such a way that the base pressure is increased and the base drag thereby reduced. The base mass flow should be

optimal and should occur during a substantial part of the flight time.

There are many problems associated with the design of base-bleed units for projectiles. The system has to withstand the pressures, temperatures and accelerations in the gun, at the muzzle and during flight. The ignition has to be reliable and consistent and the unit should be designed to work efficiently. Moreover the mass and volume should not adversely affect the lethality or cargo capability of the projectile.

The general design of the Swedish base-bleed unit is shown in fig 1. It is a compromise of efficiency, simplicity and low cost and is based on the fact that a controlled low mass flow of mainly gases can be generated by the combustion of a propellant at low pressures in a combustion chamber within the projectile body.

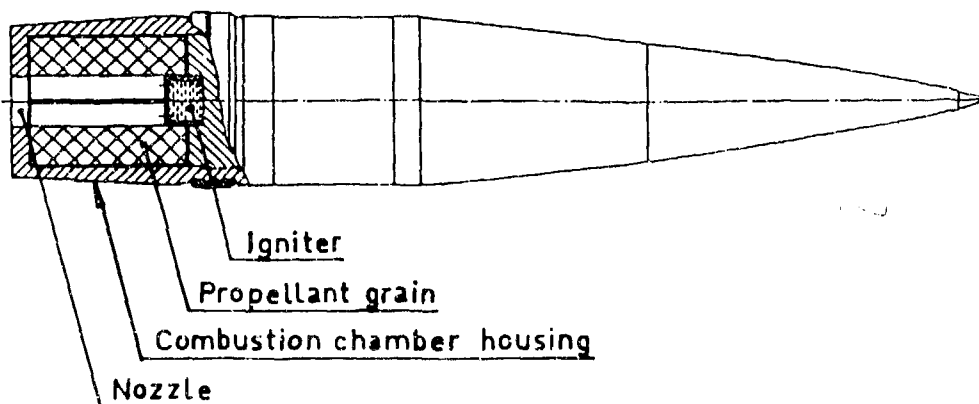


FIGURE 1. Low drag experimental projectile with base-bleed unit.

The main parts of the base-bleed unit are the combustion chamber with the propellant grain, the igniter and the base with a suitable nozzle system. In a sense the entire projectile afterbody is part of the unit since it in most cases constitutes the combustion chamber. The optimum design of the afterbody is very much governed by the performance of the base-bleed unit.

The base-bleed unit is in the course of the interior ballistics subjected to high pressures and pressure changes and to strong axial and angular accelerations. These cause mechanical stresses, strains and deformations of all unit parts.

The propellant compositions should be chosen with great care. A suitable grain design can greatly reduce strains and stresses and the risk of cracks. Spin stand tests and axial acceleration tests are useful for studying mechanical performance.

When the gun is fired, the base-bleed propellant grain, as well as the igniter composition are ignited by the combustion gases in the gun. Due to the very steep pressure drop when the projectile leaves the muzzle, the base-bleed propellant combustion tends to be extinguished. The igniter however has a pyrotechnic composition with very low sensitivity to pressure variations. Thus it is capable of sustaining the combustion of the propellant grain.

It is very important for good range and precision to achieve an instant, reproducible, full effect onset of the base-bleed immediately at the muzzle. Several theoretical and experimental ignition studies and tests have been carried out. These and numerous complete base-bleed projectile firings emphasize the importance of perfect ignition.

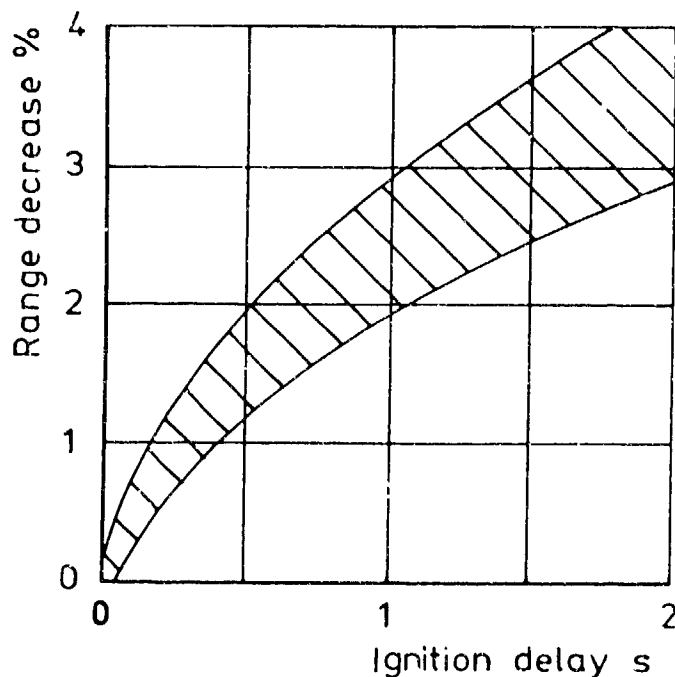


**FIGURE 2.** Calculated range decrease versus ignition delay for a medium caliber low drag base-bleed projectile. Shaded area indicates possible variations due to the size of the base-bleed unit and due to flight conditions.

The conditions are demonstrated in fig 2. Showing calculated range decrease versus effective ignition delay for a medium caliber, low drag base-bleed artillery projectile. An ignition delay of 0.1 sec results in a range decrease of approximately 0.4 %. This is of the same order as the total dispersion at maximum range of good projectiles.

For a normally working unit, full onset of base-bleed occurs, with only small dispersion, within a couple of meters from the muzzle. Consequently ignition should normally not involve any problems but, due to the importance, has to be thoroughly tested and controlled.

Due to high gun pressure the regression of the igniter composition is considerably higher in the course of the interior ballistics than outside the barrel. Several mm of igniter composition length is usually burned in the barrel. This has to be taken into consideration when designing igniters.

The first part of the propellant grain combustion takes place at high pressure while the projectile travels along the barrel. The regression rate is high but the duration very short. The propellant layer burned in the gun is generally relatively thin and usually not determinative for the grain dimensions.

During free flight is the mass flow through the nozzle low and subsonic. The pressure in the combustion chamber exceeds the base pressure only slightly. Due to the effect of the base-bleed the chamber pressure differs very little from ambient pressure. The ambient pressure is degressive along the trajectory up to apex. This results in a degressive regression rate of the propellant. It should be noted that regression rates and thus mass flow and duration of burning are functions of elevation.

The projectile might eventually reach an altitude at which the pressure is so low that propellant combustion is no longer possible. It is vital to determine regression rates and to study propellant combustion from sea level atmospheric pressure down to pressures at which extinction occurs.

### 3. DISPOSITION OF TEST METHODS

The base-bleed unit appears simple in its design. It is however evident that several severe requirements, many with small margins, are to be met. Theoretical calculations may be performed and can elucidate some problems but due to the complexity of the over all process only experimental tests can finally ensure reliable and good performance.

During the research leading to the invention of the Swedish base-bleed system and during the continued development a number of different methods and experimental procedures for testing parts as well as the complete system have been developed and applied.

A summary of some methods is presented in fig 3. In this figure is indicated which tests might be considered as essential or important/of value. As appears, in some cases standard methods already available have been applied, sometimes however with alterations. In some cases new, comprehensive facilities have been designed and built especially for the base-bleed research, development and testing.

METHOD \ OBJECT	OBJECT				
	Propellant	Propellant grain	Igniter	Mechanical parts	Compl base-bleed unit
Combustion bomb tests	●		●		
High/low pressure bomb tests		●	●		
Tensile tests	●				
Spin tests	○	●	●		●
Linear acceleration tests	○	●		●	
Supersonic wind tunnel tests	○	●			●
Aeroballistic range tests		●	●	●	●
Gun firing tests	○	●	●	●	●
Environmental tests		●	●	○	●
Aging tests	●	●	●		●

● essential

○ important/of value

FIGURE 3. Summary of test methods.

#### 4. LABORATORY METHODS AND EXPERIMENTAL FACILITIES

##### 4.1 Combustion Bomb Tests

Subatmospheric to high pressure propellant combustion. As indicated earlier the pressure in the base-bleed unit combustion chamber is normally close to ambient pressure. Starting from gun site atmospheric conditions ambient pressure is decreasing up to apex. An advanced projectile trajectory apex might be as high as 15 km. It is however probable that the optimum end of combustion should occur at a lower altitude. The range of interest for combustion studies is mainly at subatmospheric pressures. Regression rates should



be determined down to the pressure at which extinction occurs. The combustion behaviour such as occurrence of oscillatory combustion should be observed and measured. Although oscillations can be observed in combustion bomb tests, the combustion will tend to be stable in a real base-bleed combustion chamber where the thermodynamic situation is different and usually more favourable. Strand burning regression rates appear to be quite accordant with base-bleed combustion regression provided correction is made for the influence of spin. Combustion tests at subatmospheric pressures are mostly performed in a strand burner window bomb of 500 cm<sup>3</sup> volume connected to a surge tank of 1 m<sup>3</sup> volume as shown in fig 4. The surge tank is connected to a vacuum pump allowing the bomb and tank system to be evacuated to the desired pressure. The system is fitted with valves necessary for operation. Pressures are measured at several locations.

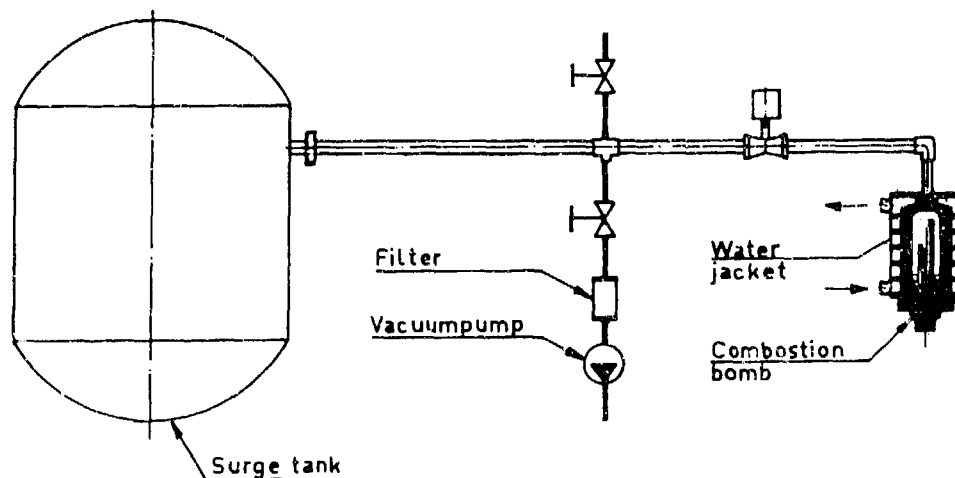


FIGURE 4. Subatmospheric propellant combustion test facility.

A majority of combustion bomb tests have been performed with propellant strands of 5 by 5 mm square cross section and 120 mm length. The strands are inhibited on the sides.

Ignition is accomplished with an electrically heated iron wire. Fine, melting silver wires are used for determination of the average regression rate.

Examples of test results are shown in fig 5 for two different HTPB propellants. Regression rates at pressures higher than atmospheric determined in the same combustion bomb are shown for one of the propellants.

Igniter combustion. During research and development of igniters high pressure combustion bomb tests are valuable. In this case a cylindrical bomb with 100 cm<sup>3</sup> internal volume and maximum 200 MPa pressure is used. The bomb is fitted with transducers for measurements of pressure and light emission.

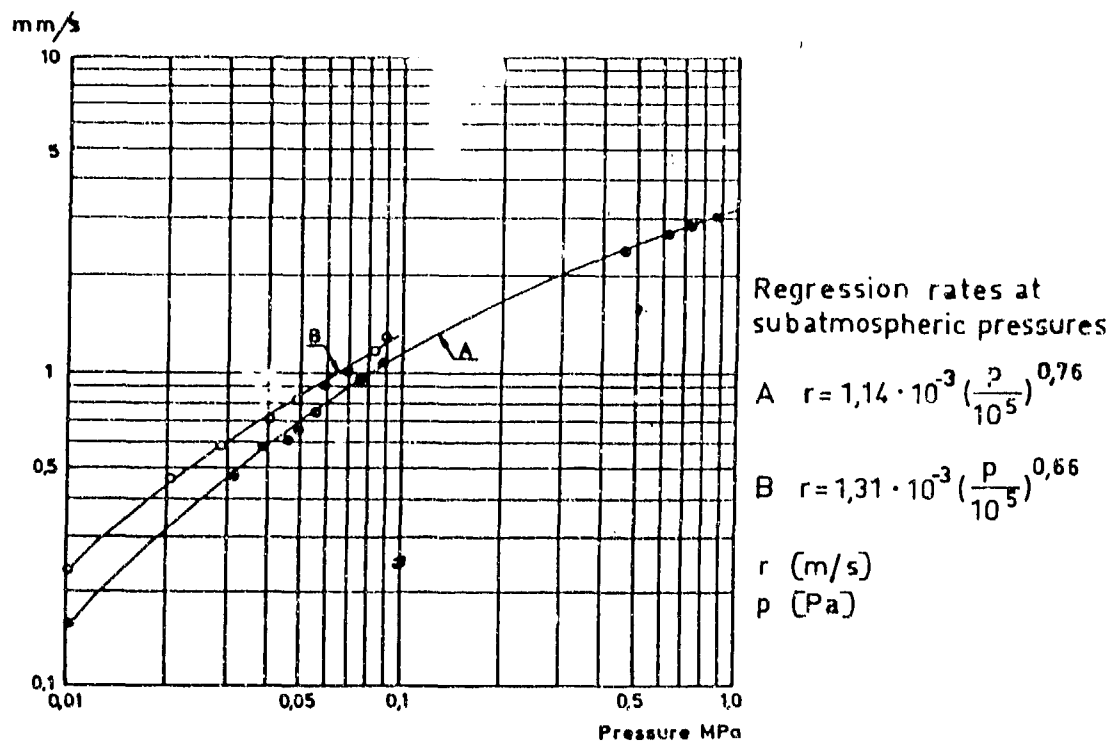


FIGURE 5. Regression rate versus pressure for two different HTPB propellants.

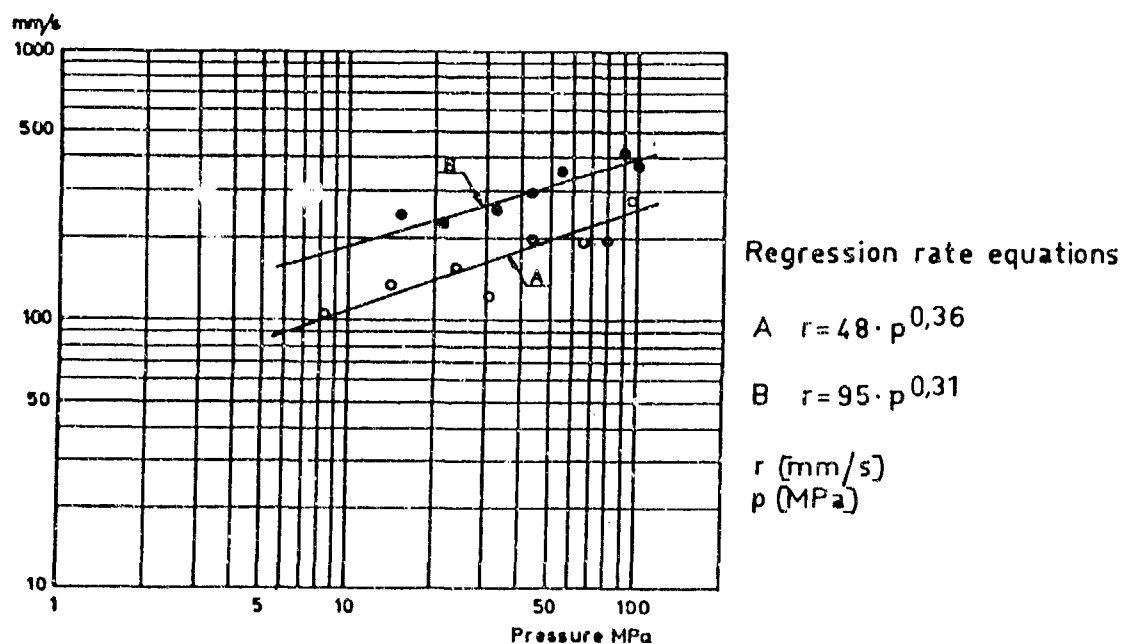


FIGURE 6. Regression rate versus pressure for two different igniter compositions.

It has also connections for the ignition of the igniters to be tested. Test igniters with net diameter 21 mm and length 15 to 20 mm are generally used.

Influences of different variables such as composition, components particle sizes and compacting pressure have been studied in order to find suitable igniters for different designs. As examples regression rates for two igniters are shown in fig 6.

#### 4.2 High/Low Pressure Bomb Tests

The high/low pressure bomb is used for experimental simulation of the conditions the igniter is exposed to during interior, transitional and exterior ballistics.

The bomb in which the igniter to be tested is located, is fitted with a bursting disk. Fig 7. The bomb is loaded with a suitable amount of propellant. When the propellant is ignited the pressure will first increase to a value corresponding to some effective gun pressure. After some ms, corresponding to the duration of the interior ballistics, the disk will burst and the chamber pressure will drop to approximately ambient pressure.

By balancing bomb volume, pressure increasing propellant mass, nozzle area and disk burst conditions an acceptable simulation of the influence on the igniter combustion can be attained.

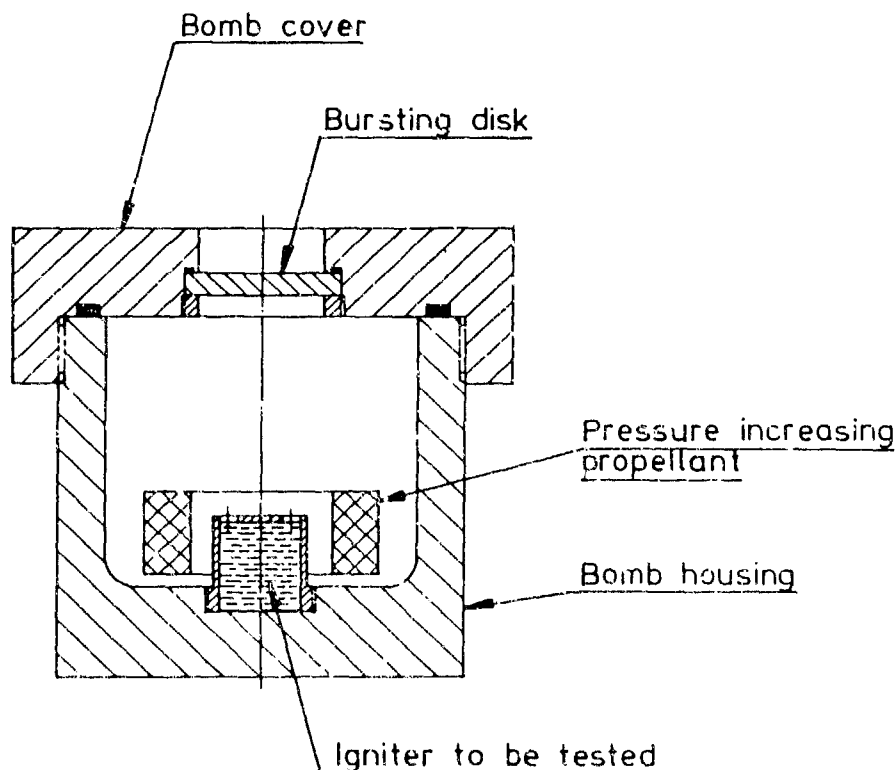


FIGURE 7. High/low pressure igniter combustion test bomb.

### 4.3 Tensile Tests

In the gun the propellant grain is subjected to very strong axial and radial accelerations. In addition the base-bleed system should be working over a wide temperature range, such as  $-40$  to  $+60^{\circ}\text{C}$ . Determination of the mechanical properties of the propellant over the actual temperature range is most important. These properties will in turn determine the maximum grain size. It is convenient to have a series of propellant compositions developed and tested in order to make the optimum choice for each design.

Tensile tests are made with JANAF specimens in a tensile test machine with cross head speeds between 1 and 500 mm/s. Tests are made at different strain rates and temperatures. The results are presented in master curves. Examples of results are shown in fig 8 - 10.

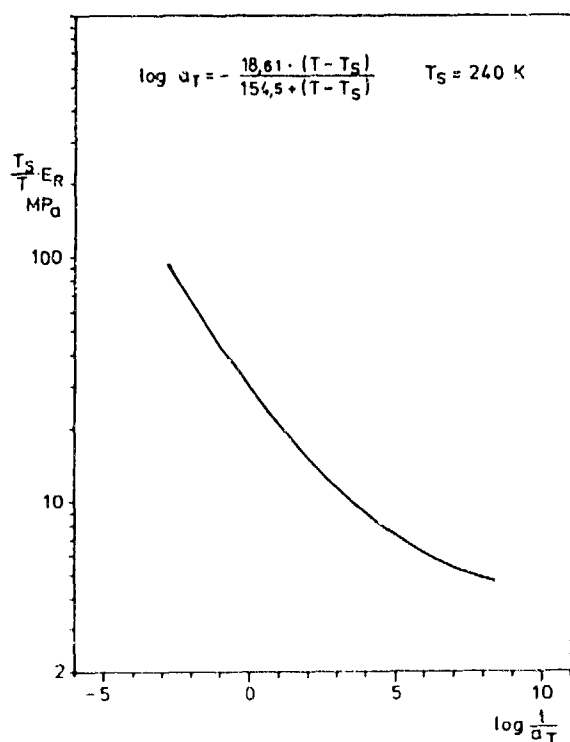


FIGURE 8. Master curve for relaxation modulus

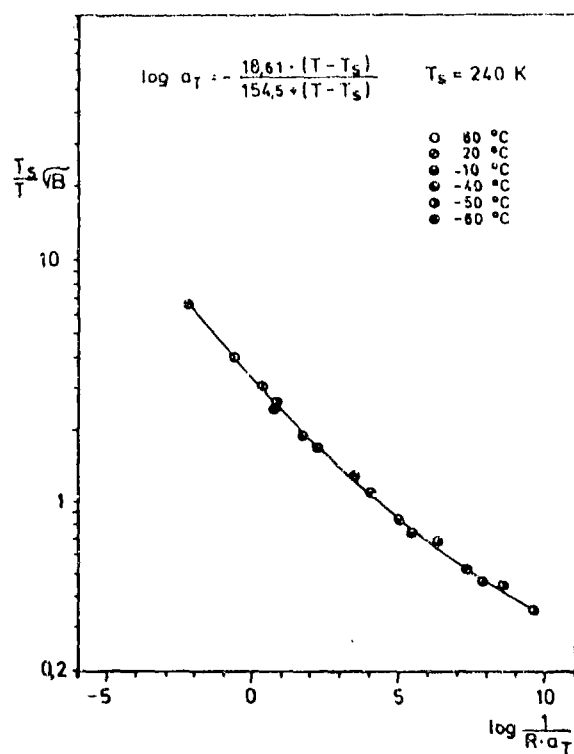
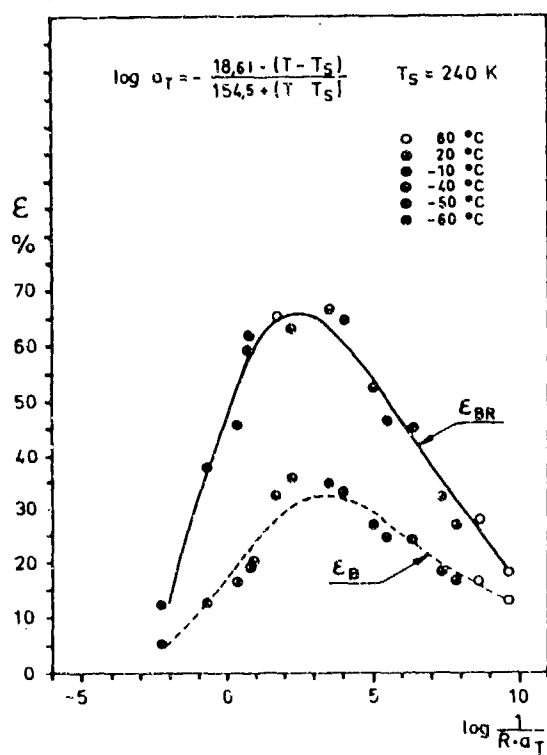


FIGURE 9. Master curve for maximum stress

FIGURE 10. Master curve for strain at maximum stress ( $\epsilon_B$ ) and strain at break ( $\epsilon_{BR}$ )

#### 4.4 Spin Tests

Spinning solid propellant rocket motors perform differently from nonspinning motors and the same applies to spinning base-bleed units with solid propellant grains. The most important consequences of the spin are increased burning rate due to radial acceleration, altered combustion chamber flow and nozzle flow. Spin also influences the ignition process. Consequently spin tests are most valuable.

A spin stand designed and built at FOA (Swedish Defence Research Establishment) is shown in fig 11. An electric motor rotates the shaft by way of a hydraulic drive at variable speeds corresponding to actual projectile rotation, up to about 20 000 rpm. The shaft in which transducers are situated, is journaled by two ball bearings. The main end of the shaft carries the test unit to be spun, the other end is connected to a slip ring assembly. The bearing housing is fixed to a steel plate which rests on two spring blades. Pressures can be measured at different locations through pressure taps. The signals from the pressure transducers are carried via the slip ring assembly to the signal processing equipment. It is also possible to use radio transmission for the signal transfer. Ignition is accomplished via the slip ring assembly or via the combustion chamber nozzle.



FIGURE 11. Spin stand facility

Spin tests are usually performed in full scale to study the effect of spin on propellant grain combustion and on chamber and nozzle flow and blocking. Fig 12 shows a photograph from a spin test. Other spin tests may also be performed such as

igniter spray tests and grain deformation tests. In the first case the actual igniter is used in combination with a dummy propellant grain. The spray pattern of the igniter jet will be clearly marked on the dummy grain surfaces and can be studied after the test.

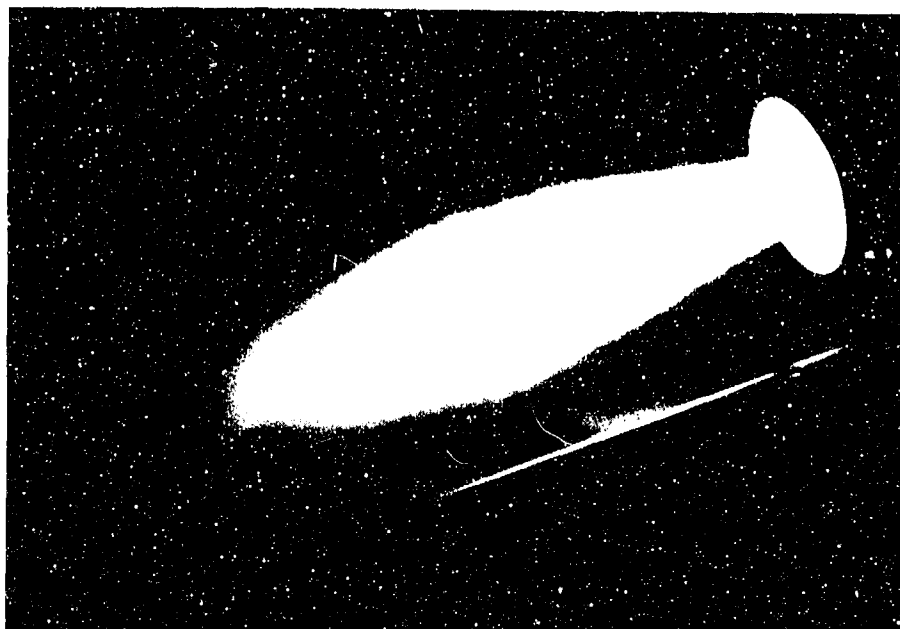


FIGURE 12. Spin stand test of base-bleed unit combustion at 15 000 rpm.



FIGURE 13. Deformation of propellant grain in open ended combustion chamber spinning at 12 000 rpm.

Grain deformation due to spin can conveniently be studied by stroboscopic photographing of a grain in a spinning open ended combustion chamber. The deformation of a segmented grain without central channel is shown in fig 13. External axial flow is generally not provided for in a spin stand of this design. Hence only internal processes of base-bleed units can be studied. On the other hand this can readily be made in full scale.

The interaction of base-bleed and external ambient flow is ordinarily studied in supersonic wind tunnels. At FOA a spinning experimental base-bleed unit has been designed and built for this purpose.

#### 4.5 Linear Acceleration Tests

Soft recovery of gun fired projectiles has always been an interesting and important task. In 1966 was at the proving ground of FOA designed and built a very special linear acceleration and soft recovery facility. It has performed excellently over the years and is still in current use.

The basic element is a recoilless 84 mm caliber smooth-bored gun in a heavy experimental version. This gun is fixed to a long support and the barrel is elongated to 275 m by means of pipes. Fig 14. When the gun is fired an increasing pressure is built up in front of the projectile as it travels along the barrel. The pressure behind the projectile is continuously decreasing. The projectile is softly retarding and will come to a stop after about 100 m. Compressed air is used to move the projectile out of the barrel.

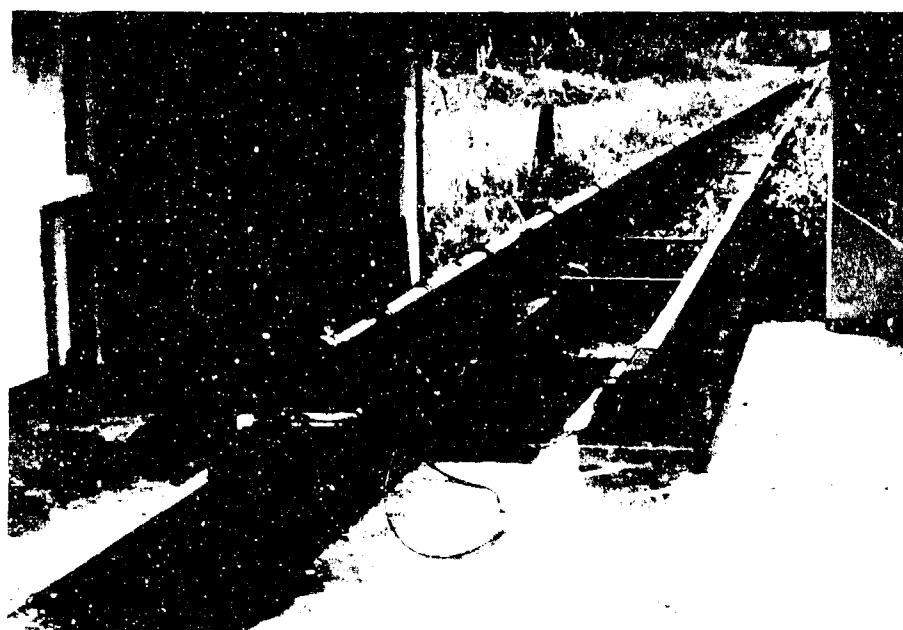


FIGURE 14. Linear acceleration test facility



By changing projectile mass and gun propellant mass, linear accelerations up to  $400\,000\text{ m/s}^2$  ( $40\,000\text{ g}$ ) can be obtained. Numerous tests with propellant samples and grains have been carried out in order to obtain data on mechanical properties of the propellant as well as to study deformation, occurrence of cracks etc of the grains.

Mechanical behaviour of igniters subjected to strong accelerations has also been studied. The facility is well suited to acceleration tests of mechanical parts and electronics.

#### 4.6 Supersonic Wind Tunnel Tests

The supersonic wind tunnel at FOA, used for base-bleed studies, is a blow down type of tunnel with fixed nozzles for  $M = 1.81$  and  $M = 2.65$ . Fig 15. The nozzle test section diameters are 125 mm and 170 mm respectively. The afterbody model is supported by a central cylindrical tube extending from upstream the tunnel nozzle. Thus no problems with support interference will occur. Model external diameters are mostly 50 mm.

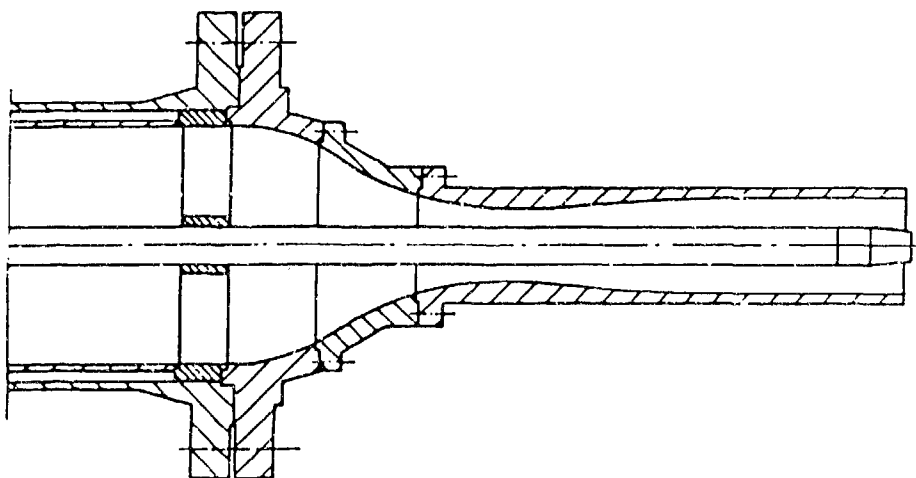


FIGURE 15. Supersonic wind tunnel test section. Nozzle with central support tube and after body model with base-bleed unit. Test section can be open or closed for tests at subatmospheric pressures corresponding to flight at high altitudes.

Several non spinning models of different base-bleed unit designs have been built and tested. The unit is located within the afterbody model and consists of the combustion chamber with the propellant grain and the base with the nozzle system to be tested.

Ignition of the propellant grain is accomplished through the base nozzles by means of the jet from a pyrotechnic igniter mounted on a retractable support.

Pressures in the combustion chamber and on the after-body surface are measured by means of a large number of taps connected to scanning transducers. Lines from the transducers are fed through the support tube.

In a typical test, the tunnel is run some seconds after the base-bleed has ceased. Thus data with as well as without base flow are obtained during the same test run.

A support device for wind tunnel testing of spinning base-bleed units has also been designed and built. The device is mounted to the central axial support tube. Air bearings are used. Spin rates up to about 40 000 rpm are brought about by means of an air turbine and spin rates are measured with a photo-cell system. By measuring the pressure in the chamber stabilising the axial position, total axial force and base drag can be calculated.

Several hundreds of base-bleed tests have been carried out with variables such as propellant composition, grain configuration, nozzle configuration, nozzle area and afterbody configuration. Also further advanced systems related to base-bleed, such as external burning, have been investigated.

The large number of test results have made possible the formulation of very reliable performance data which in turn have been introduced into our exterior ballistics code. Very good agreement between calculated and complete gun firing results are demonstrated over a large range of calibers, sizes and applications.

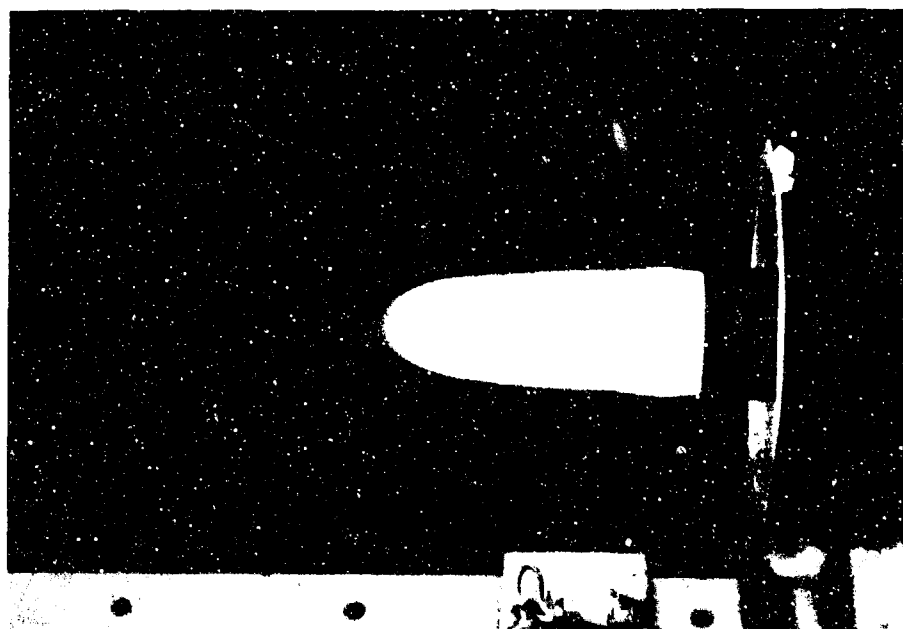


FIGURE 16. Supersonic wind tunnel test of base-bleed unit combustion at  $M=1.81$ .

## 5. GUN FIRING TESTS AND FACILITIES

### 5.1 Aeroballistic Range Tests

The purpose of aeroballistic range tests is mainly to determine aerodynamic coefficients and stability factors of projectiles in free flight. The flow around free flying projectiles with and without base-bleed can be studied. Since range tests concern the very first part of the trajectory the base-bleed ignition process may be observed simultaneously.

In Sweden is a 240 m long, 11.5 m wide and 6 m high covered aeroballistic range named Nordbanan at the proving ground of FFK in Karlsborg. In this range it is possible to fire rounds of up to 155 mm calibre.

The range of measurements extends over 230 m and includes 93 yaw-cards and 10 photographic stations. Fig 17. Each station is equipped with two Hasselblad 500 EL cameras for horizontal and vertical photographs perpendicular to the trajectory, and flashes of very short duration. By focusing the cameras on white back ground screens the projectile attitude, and the shadowgraph of the flow field can be registered. The camera shutters open shortly before the projectile passes and closes shortly afterwards. The actual exposures are brought about by the very short flashes. When applying the method with open cameras and flashes the strong light from the base-bleed combustion might interfere with the shadowgraph. However there seems to be no difficulties in using yaw-cards for base-bleed projectile firings.



FIGURE 17. Indoor picture of the aeroballistic range at Karlsborg proving ground.

## 5.2 Ballistic Firing Tests

Ballistic firings offer the ultimate tests of the performance of the complete base-bleed projectiles. The fundamental tests concern range and dispersion at different angles of elevation and muzzle velocities. In Sweden this kind of firings are often made over water. The impact is usually measured by radar and/or cine-theodolites.

Firings in darkness with good visibility offer excellent conditions for studying the performance of base-bleed units during flight. The ignition process as well as the combustion process - duration, stability etc - can be observed and recorded. Registrations are made with open shutter cameras.

During most ballistic test firings Doppler radar measurements are performed. The results are generally presented as drag coefficients,  $C_D$ , versus Mach-number and versus flight time and provide important data for use e.g. in aeroballistic calculations.

In general all malfunctions and disturbances of importance of the base-bleed process will cause observable divergences of the drag coefficient from normal values.

In fig 18 is shown measured  $C_D$  versus Mach number for an experimental 155 mm base-bleed projectile. As can be seen the base-bleed unit of round 3 is not working correctly. The ignition is retarded, causing high  $C_D$  at start. The base mass flow is displaced towards the later part of the process.

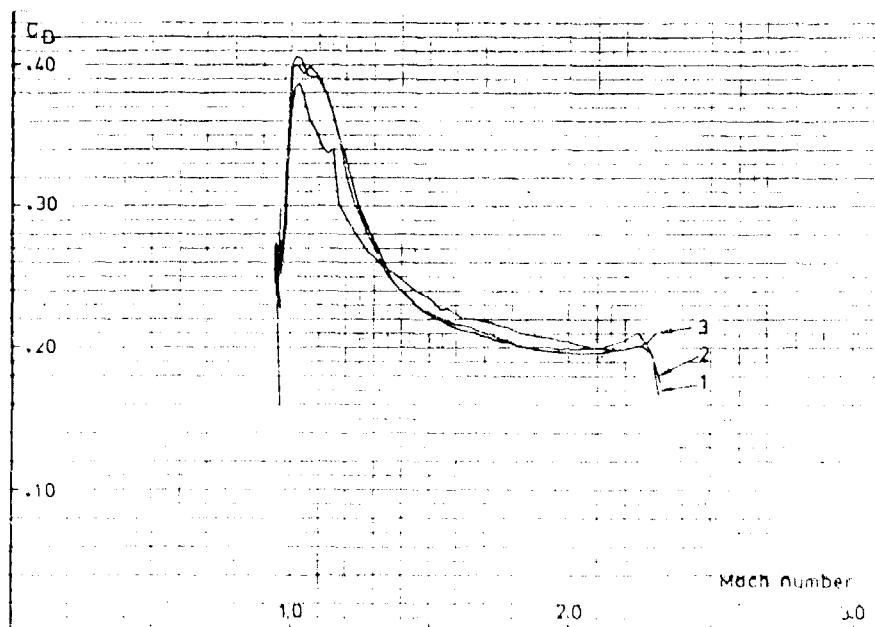


FIGURE 18. Measured drag coefficients versus Mach number for an experimental 155 mm base-bleed projectile.

## 6. CONCLUSIONS

The base-bleed unit is an apparently simple system with no moving parts. It is however evident that the over all process is very complex and that several severe requirements are to be met. Analytic design methods and data are still insufficient. Thus experimental tests for research and development of parts and subsystems as well as complete base-bleed units are of utmost importance. Experiments are also necessary for obtaining basic data such as regression rates, mechanical properties and aeroballistic coefficients. However good theories might be developed testing will still be needed for proving reliable and efficient performance.

In this report some of the more important test methods and experimental procedures now in use have been presented. New methods are however currently being developed. In later years several laser based methods have been introduced. Fiber optics and micro electronics render possible new transducers, data transfer and data processing technique. Larger computers and computer codes will be developed.

## 7. REFERENCES

1. Gunners N-E, Hellgren R V, Liljegren T  
Kanonprojektill med anordning för ökning av dess skottvidd  
(Gun projectile arranged with a base drag reducing system)  
Swedish Patent 340076, 1969
2. Andersson K, Gunners N-E, Hellgren R  
Swedish Base-Bleed - Increasing in Range of Artillery  
Projectiles through Base Flow  
Propellants and Explosives 1, Oct 1976
3. Bartelson N and Lundahl K  
Base-Bleed - A System to Increase Range and Decrease  
Ballistic Dispersion  
Proceeding of the 3rd International Symposium on  
Ballistics, March 23-25, 1977, Karlsruhe, Deutsche  
Gesellschaft für Wehrtechnik
4. Andersson K, Bartelson N and Gunners N-E  
Afterbody Drag of Projectiles with Base Drag Reducing  
Systems  
4th International Symposium on Ballistics,  
October 17-19, 1978
5. Gunners N-E, Hellgren R, Liljegren T and Nilsson Y  
Basflödesaggregat för 155 mm sgr m/77 för havbits F  
FOA rapport C 20305-De, May 1979
6. Liljegren T  
Erfarenheter från tillverkning av krut för basflödes-  
laddningar till 105 mm stgr m40/74  
FOA rapport C 20350-D1, April 1980

7. Hellgren R V  
Range Calculation for Base-Bleed projectiles  
6th International Symposium on Ballistics  
Orlando, Florida, Oct 1961
8. Englund C-E  
Sammanställning av teori och resultat från undersök-  
ningar av stabilitet och aerodynamiska koefficienter hos  
friflygande projektiler  
FOA rapport C 20690-2.1, Dec 1987
9. Gunners N-E, Andersson K, Hellgren R  
Base-Bleed Systems for Gun Projectiles  
Gun Propulsion Technology  
AIAA Progress in Astronautics and Aeronautics  
Vol 109, 1988

# ANALYSIS OF DISPERSION OF BASE BLEED PROJECTILE

PROF. XIFU GUO

Dept. of Engineering Thermal Physics & Aerodynamics.

East China Inst. of Technology NANJING, CHINA.

## [ ABSTRACT ]

The dispersion of shot is an important performance index of a base bleed projectile. Correct estimation the characteristic quantity of dispersion of the base bleed projectile, effective reducing the dispersion of the projectile, reasonable determining the dispersion index are problems of great concern for projectile designers and ballisticians.

In this paper, the dispersion of the base bleed projectile has been estimated, and the methods for reducing the influence of nutation, and the drag dispersion with base bleeding and the highaltitude wind on the dispersion of projectile have been introduced. Then, the effects of various factors on the dispersion of projectile have been analyzed, and it is pointed out that the initial velocity dispersion, nutation dispersion, gusty wind and drag dispersion with base bleeding are the main factors affecting dispersion of projectile. Because the drag of base bleed projectile is so weak that the effect of the drag dispersion on over all - dispersion will be more sensitive. Factors affecting dispersion of the base drag with base bleeding and the influence of the dispersion of ignition time on over all - dispersion have been discussed. The methods of reducing dispersion have been stated, and the methods of determining the index of dispersion and of making reasonable distribution have been demonstrated. The firing test have proved that the theory and methods given in this paper are verified.

## 1. INTRODUCTION

A base bleed projectile can increase range efficiently, and the increase of range rate is normally about 20~30%. Under the condition of high initial velocity, the less the wave drag of the projectile, the more the proportion of the base drag to total drag, and also the more noticeable the effect of the increasing range of base bleeding. Hence, the increasing range of base bleeding especially suitable for the low drag projectile with the shape of high fineness ratio head.

Owing to the structure characteristic of the base bleed projectile, it is very probable that slight carelessness in design causes excess large dispersion of shot. The reasons of large dispersion can be summed up in following respects: 1. For large calibre and long-range projectile, charge weight is more, the ignition and flame tranger are not uniform, it is easy to cause the large dispersion of initial velocity; 2. Due to rather large fineness ratio of the projectile, long gun barrel, high bore pressure, spin rate of projectile, it is not easy to centre the projectile in bore so that the considerable yaw dispersion of projectile during launch period is caused; 3. Due to extended range, high altitude and large time of flight, a long-range projectile is easy to be affected by random change of meteorological elements; 4. Because of the additional base bleed unit, the stability of propellant gas flow and dispersion of ignition, etc, which are related to the base bleed unit immediately, will cause dispersion of base drag; 5. Because base bleed projectile has the shape of low

drag, the sensitivity of projectile for the initial velocity and drag dispersion increases as drag decreases. But the relative variation of drag dispersion increases, so that the dispersion of shot further increases.

In this paper, based on theoretical analysis and test data, the estimating method of the dispersion of base bleed projectile has been researched, the factors causing dispersion have been analyzed, the ways of decreasing dispersion have been pointed out, the dispersion index have been discussed. Theoretical foundations and actual methods of reducing the dispersion of base bleed projectile have been provided, in order to realize the overall optimum design of base bleed projectile, and estimate the dispersion elements of the firing table of base bleed projectile.

## 2. ESTIMATION OF DISPERSION PROBABLE ERROR OF BASE BLEED PROJECTILE

The flight stability of the base bleed projectile is a necessary condition to meet the dispersion index. In estimating the dispersion of shot, the gyroscopic stability, dynamic stability and trailing stability of the base bleed projectile must meet the requirement along overall trajectory. Under these conditions, the dispersion probable error of the falling point of base bleed projectile can be calculated by following formulas:

$$\begin{aligned} E_x^2 &= \sum_{i=1}^n \left( \frac{\partial X}{\partial \alpha_i} E_{\alpha_i} \right)^2 \\ E_z^2 &= \sum_{i=1}^n \left( \frac{\partial Z}{\partial \alpha_i} E_{\alpha_i} \right)^2 \end{aligned} \quad (1)$$

where  $E_x$  - probable error in range;  $E_z$  - probable error in deflection;  $\alpha_i$  - factors related with the range and the deflection, such as the initial velocity,  $v_0$ , the ballistic coefficient,  $c$ , the weight of the projectile,  $G$ , the range wind,  $W_x$ , the cross wind,  $W_z$ , the ignition time of base bleed unit,  $t_H$ , etc.  $E_{\alpha_i}$  - the probable errors of dispersion of factors ( $\alpha_i$ ), such as  $E_{v_0}$ ,  $E_G$ ,  $E_c$ ,  $E_{W_x}$ ,  $E_{W_z}$ , etc.  $\frac{\partial X}{\partial \alpha_i}$  - the sensitivity of the factors  $\alpha_i$  for range,  $\frac{\partial Z}{\partial \alpha_i}$  - the sensitivity of the factors  $\alpha_i$  for deflection. Hence the dispersion of range and deflection caused by the dispersion of factor  $\alpha_i$  can be written as

$$\begin{aligned} E_{x_i} &= \frac{\partial X}{\partial \alpha_i} E_{\alpha_i} \\ E_{z_i} &= \frac{\partial Z}{\partial \alpha_i} E_{\alpha_i} \end{aligned} \quad (2)$$

this is, the dispersion of falling point caused by factor  $\alpha_i$  is a product of its sensitivity factor with its probable error. When the dispersion is analyzed, the two respects - the sensitivity factor and dispersion amount must be considered.

## 3. TREATING METHOD OF FALLING POINT DISPERSION CAUSED BY NUTATION DISPERSION, DRAG DISPERSION WITH BASE BLEEDING AND GUSTY WIND

### 3.1 Falling Point Dispersion by Nutation



The nutation dispersion causes not only the range dispersion but also the deflection dispersion. They are discussed respectively as follows:

3.1.1 Estimation of range dispersion caused by nutation dispersion. Several methods are described as follows: a. Method of ballistic equation

Using equation of motion for a modified mass point or ballistic equation of six degrees of freedom, the range  $X_i$  corresponding to the individual nutation amplitude  $\delta_{ni}$  can be calculated and the  $E_{X\delta_i}$  can be written as

$$E_{X\delta_i} = 0.6745 \sqrt{\frac{\sum_{i=1}^n (X_i - \bar{X})^2}{n-1}} \quad (3)$$

$$\bar{X} = \frac{\sum_{i=1}^n X_i}{n}$$

b. Method of equivalent initial velocity

The influence of nutation on range can be considered as the influence on the initial velocity,  $v_0$ , if the change of initial velocity caused by nutation  $\delta_{ni}$  is  $\Delta v_{oi}$ , the their relation is

$$\Delta v_{oi} = a \left( \frac{\delta_{ni}}{10} \right)^2 \quad (4)$$

then, the probable error of initial velocity caused by the nutation dispersion is given by

$$E_{v_0\delta} = 0.6745 \sqrt{\frac{\sum_{i=1}^n \left[ \Delta v_{oi} - \left( \frac{\sum_{i=1}^n \Delta v_{oi}}{n} \right) \right]^2}{n-1}} \quad (5)$$

The range dispersion caused by the nutation dispersion is given by

$$E_{X\delta_i} = \frac{\partial X}{\partial v_0} E_{v_0\delta} \quad (6)$$

c. Method of ballistic coefficient

Under the condition of existing the nutation, the ballistic coefficient of projectile is given by

$$c_i = c_0 (1 + K \delta_{ni}^2) \quad (7)$$

$$\delta_{ni}^2 = \frac{\int_0^{t_i} v \, dt}{T} \quad (8)$$

where  $c_0$  is the ballistic coefficient when nutation is zero;  $K$  is the coefficient related with the projectile shape and Much number  $M$ ;  $t_i$  is the time when nutation is damped to zero;  $T$  - total time of flight.

The dispersion of the ballistic coefficient caused by the nutation dispersion is given by

$$E_{C\delta} = 0.6745 \sqrt{\frac{\sum_{i=1}^n (C_i - \bar{C})^2}{n-1}} \quad (9)$$

$$\bar{C} = \frac{\sum_{i=1}^n C_i}{n}$$

The probable error in range is given by

$$E_{x\delta_1} = \frac{\partial X}{\partial C} E_{C\delta} \quad (10)$$

d. Method of nutation deviation

Firstly, calculate

$$\frac{\partial X}{\partial \delta_m} = \sqrt{\frac{\sum_{i=1}^n \left( \frac{\partial X}{\partial \delta_{mi}} \right)^2}{n}} \quad (11)$$

Secondly, calculate

$$E_{\delta_m} = 0.6745 \sqrt{\frac{\sum_{i=1}^n (\delta_{mi} - \bar{\delta}_m)^2}{n-1}} \quad (12)$$

$$\bar{\delta}_m = \frac{\sum_{i=1}^n \delta_{mi}}{n}$$

finally, calculate

$$E_{x\delta_1} = \frac{\partial X}{\partial \delta_m} E_{\delta_m} \quad (13)$$

3.1.2 Dispersion of aerodynamic jump caused by nutation dispersion. The aerodynamic jump caused by the nutation is

$$\psi_i = \frac{\delta_{oi}}{v_{oi}} \frac{R_A^2}{h} \quad (14)$$

$$E_\psi = 0.6745 \sqrt{\frac{\sum_{i=1}^n (\psi_i - \bar{\psi})^2}{n-1}}$$

$$\bar{\psi} = \frac{\sum_{i=1}^n \psi_i}{n}$$

where  $\delta_{oi}$  - the initial nutation angle velocity;  $R_A$  - the equator radius of the gyration of projectile;  $h$  - the distance of drag centre to mass centre of the projectile. The range and deflection dispersion caused by  $E_\psi$  is respectively given by

$$E_{x\delta_2} = \frac{\partial X}{\partial \theta_0} E_\psi \quad (16)$$

$$E_{z\delta} = X E_\psi \quad (17)$$

finally, the falling point dispersion caused by the nutation is yielded by

$$E_{x\delta} = \sqrt{E_{x\delta 1}^2 + E_{x\delta 2}^2} \quad (18)$$

$$E_{z\delta} = X E_\psi$$

### 3.2 Range and Deflection Dispersion Caused by Gusty Wind

To calculate the influence of the gusty wind of every point on trajectory on the falling point dispersion, firstly, the method of calculating the falling point dispersion caused by the gusty wind of every point on trajectory need to be discussed. For the point  $i$ , the mean wind  $W_i$  and the mean square error of the gusty wind  $\sigma_{wi}$  have a relation in the following

$$\sigma_{wi} = \psi_{wi} \bar{W}_i \quad (19)$$

where  $\psi_{wi}$  - the relative intensity of wind.

If the falling point dispersion caused by the gusty wind of every point on trajectory is equal to the mean square error of the gusty wind, that is considered the same along all-over trajectory, hence, following formula can be yielded

$$\left( \frac{\partial X}{\partial W} \sigma_{wb} \right)^2 = \sum_{i=1}^n \left( \frac{\partial X}{\partial W_i} \sigma_{wi} \right)^2$$

$$\sigma_{wb} = \sqrt{\sum_{i=1}^n (q_i \sigma_{wi})^2} \quad (20)$$

$$q_i = \frac{\partial X}{\partial W_i} / \frac{\partial X}{\partial W}$$

where  $\sigma_{wb}$  - mean square error of ballistic gusty wind;  $\frac{\partial X}{\partial W}$  - the change of range caused by a unit wind all-over the trajectory;  $\frac{\partial X}{\partial W_i}$  - the change of range caused by unit wind of point  $i$ ;  $q_i$  - the layer-weight of layer  $i$ .

If  $\psi_{wi}$  is constant all-over the trajectory, or  $\psi_{wi} = \psi$ , hence

$$\sigma_{wb} = \psi \sqrt{\sum_{i=1}^n (q_i W_i)^2} \quad (21)$$

generally,  $\psi \approx 0.1$   
for the range wind,

$$\sigma_{wxb} = \sqrt{\sum_{i=1}^n (q_i \psi_{wi} \bar{W}_{xi})^2} \quad (22)$$

for the cross wind,

$$\sigma_{wzb} = \sqrt{\sum_{i=1}^n (q_i \psi_{wi} \bar{W}_{zi})^2} \quad (23)$$

The probable errors of ballistic range wind and cross wind are respectively given by

$$E_{wxb} = 0.6745 \sigma_{wxb} \quad (24)$$

$$E_{wzb} = 0.6745 \sigma_{wzb} \quad (25)$$

Hence, the probable errors of the falling point caused by the gusty wind are given by

$$E_{xwx} = \frac{\partial X}{\partial W_x} E_{wxb} \quad (26)$$

$$E_{zwz} = \frac{\partial Z}{\partial W_z} E_{wzb}$$

### 3.3 Falling Point Dispersion Caused by Dispersion of Base Bleed Drag

The influence of the drag dispersion of the base bleed projectile with base bleeding on the falling point dispersion is concerned with different times and positions on trajectory. To simplify calculating procedure, the concept of ballistic probable error of the base bleed drag coefficient has been presented. Based on following principle: the falling point dispersion caused by the ballistic deviation of the base bleed drag coefficient is equal to that caused by the dispersion of the drag coefficient of every point on trajectory with base bleeding, the ballistic deviation of drag coefficient can be determined by

$$\left( \frac{\partial X}{\partial C_D} E_{C_{Db}} \right)^2 = \sum_{i=1}^n \left( \frac{\partial X}{\partial C_{Di}} E_{C_{Di}} \right)^2 \quad (27)$$

$$E_{C_{Db}}^2 = \sum_{i=1}^n q_i^2 E_{C_{Di}}^2 \quad (28)$$

$$q_{C_{Di}} = \frac{\partial X}{\partial C_{Di}} / \frac{\partial X}{\partial C_D}$$

TABLE 1. Falling point dispersion caused by factors of dispersion

$\alpha_i$	$E_{x\alpha_i} (m)$	$E_{z\alpha_i} (m)$
$v_0$	184	6.6
$G$	28.1	0
$W_x$	58.65	2.14
$W_z$	0	22.5
$\rho$	0	0
$\tau$	0	0
$h$	0.046	0.022
$A$	0.118	0.43
$B$	0	0
$t_H$	2.56	0.23
$\delta_M$	280.6	33.6
$C_{DBB}$	436.5	1.1
$Z$	0	39
$\psi_0$	6.31	3.9
$\omega_{BB}$	6.31	0
$E_{\Sigma}$	544.4	59.6

where  $E_{CDB}$  - the ballistic probable error of the drag coefficient with base bleeding;  $\frac{\partial X}{\partial C_D}$  - the change of range caused by an unit change of the drag coefficient with base bleeding;  $\frac{\partial X}{\partial C_{D_i}}$  - the change of range caused by an unit change of the drag coefficient of point  $i$  with base bleeding;  $q_{CD_i}$  - the layer weight of drag coefficient at point  $i$ . During base bleeding, if  $E_{CD_i}$  is constant ( $\bar{E}_{CD}$ ), then

$$E_{C_D}^2 = E_{C_D} \sum_{i=1}^n q_{C_{D_i}}^2 \quad (29)$$

The range dispersion caused by the dispersion of drag coefficient with base bleeding is given by

$$E_{x_{c_D}} = \frac{\partial X}{\partial C_D} E_{C_D} \quad (30)$$

TABLE 2. Compare of theoretical result with experimental result

	$E_x$ (m)	$E_z$ (m)	$E_x/X$
theoretical result	544.4	59.5	1/72
experimental result	505.8	65.6	1/77

#### 4. ESTIMATION AND ANALYSIS OF INFLUENCE OF DISPERSION FACTORS ON DISPERSION OF BASE BLEED PROJECTILE

##### 4.1 Step of Estimating Dispersion of Base Bleed Projectile

- Calculate sensitivity factors;
- Calculate dispersion;
- Calculate falling point dispersion caused by dispersion factors;
- Composition of probable error of dispersion.

##### 4.2 An Example

For a projectile, the diameter is 155mm, the weight is 47.8Kg, the initial velocity is 850 m/s, the angle of depardure is  $52^\circ$ , the burning time is 24s, how to estimate the dispersion of the projectile.

Based on above-mentioned formulas and steps of calculation, the probable error of falling point dispersion by the dispersion of factors can be calculated, the results are shown in table 1.

TABLE 3. Falling point dispersion in proportion to overall dispersion caused by the dispersion of any factor

$\alpha_i$	$E_{\alpha_i}^2 / E_x^2 \cdot 100\%$	$E_{\alpha_i}^2 / E_z^2 \cdot 100\%$
$v_o$	11.4	1.2
G	0.266	0
$W_x$	1.16	0.12
$W_z$	0	14.17
$t_H$	0.02	0
$C_{DBB}$	64.29	0.003
$\delta_M$	26.57	41.16
$\psi_o$	0.013	0.042
Z	0	42.44

TABLE 4

change of factor	change of range ( m )
$\omega_B$ ( 1g )	5.34
$T_B$ ( 1°C )	0.12
$\rho_B$ ( 1% )	32.74
$r_f$ ( 1% )	22
$A_f$ ( 1% )	75
$S_B$ ( 1% )	7.5

### 4.3 Example Analysis

Above-estimated theory results and test results are shown in table 2. They are in very good agreement. The falling point dispersion in proportion to overall dispersion caused by the dispersion of any factor is shown in table 3.

From table 3, main factors that cause the range dispersion of base bleed projectile can be shown. They are the drag dispersion with base bleed, nutation dispersion, dispersion of initial velocity and the dispersion of range wind, main factors that cause the deflection dispersion are drift dispersion, nutation dispersion and the dispersion of cross wind. The law obtained by lots of calculations and tests from this example is of universal significance. The formulas of the probable error of falling point considering above main factors are given by

$$E_x^2 = E_{x_{BB}}^2 + E_{x_d}^2 + E_{x_{v_0}}^2 + E_{x_{w_x}}^2 \quad (31)$$

$$E_z^2 = E_{z_z}^2 + E_{z_d}^2 + E_{z_{w_z}}^2$$

Next, the causes of formation of main factors will be further analyzed, and the key points are the drag dispersion with base bleeding, nutation dispersion and drift dispersion.

(1) Drag dispersion with base bleeding. By using wind tunnel and flight test, it has been known that the drag dispersion with base bleeding is larger its order of magnitude is close to that of the drag dispersion of common high explosive projectile, and some time is larger. In the wind tunnel test, the relative drag dispersion of base bleed projectile is around 1.5%, the relative drag dispersion measured by Doppler radar is 1.6 to 1.7%, the corresponding relative deviation of ballistic drag coefficient is 0.6% to 0.7%, the value of common high explosive projectile is mostly less than 0.5%, and the value of 175mm M483 high explosive projectile is only 0.2%. To analyze the cause of forming above phenomenon, the influence of each factors of base bleeding on the range has been calculated, and concrete data is shown in table 4.

TABLE 5

spin rate ( RPM )	$r_t$ ( mm / s )	$r_t / r_{t0}$
0	1.29	1.0
6000	1.47	1.14
7200	1.48	1.15
9000	1.51	1.17
10200	1.56	1.21
10800	1.60	1.24

It is shown from calculated results that the dispersion of burning rate and burning surface are two main factors that affect the drag dispersion of base bleed projectile, and the reasons of forming such phenomenon can be divided into interior and external factors, the stability of burning and ejecting of propellant, burning law of burning surface, spin rate and velocity dispersion of projectile, random swashing effect of gas flow of ignition propellant on bleed propellant, and sudden disturbance of meteorologic elements on trajectory, etc, all these would randomly affect the burning of bleed propellant and flowing of gas, and cause base drag dispersion, these have been proved by tests, it is shown from firing test that the dispersion of falling point is also large when the dispersion of burning time is large, the burning test is 28s and that in firing test is 24s, even decreases to 13s. In ground spin test, the burning rate would increase when the spin rate increases, the data is shown in table 5. Based on above tests and analysis, it is shown that the controlling of stability of burning rate and surface is very important to reduce the drag dispersion of base bleed.

(2) The nutation dispersion. Factors that cause the nutation dispersion are very complicated. From the moment when a projectile is charged into bore to the end after effect period, or, in overall launch process, factors that cause the nutation would exist all along. The malalignment of band-engraving, imbalance of projectile, the clearance between bourrelet and tube, non-stableness of in bore motion of projectile, the jump of pressure in bore and the vibration of barrel, etc, all these would cause random yawing of projectile in bore. For the low drag high explosive projectile of extended range with bourrelet nub, the position of nub on bod, shape of nub, canted angle of nub would all affect greatly the motion of projectile in bore. For example, for some projectile, the initial maximum extent of the nutation is  $15^\circ$ , after improving the condition of the motion of projectile in bore, it is reduced to  $5^\circ$ . By using firing test and theoretical calculation, it is proved that the precision would be improved if the nutation angle is controlled to be less than  $5^\circ$ .

(3) Drift dispersion. For a spin-stabilized projectile, the drift is caused by the repose angle, the dispersion of repose angle is the reason that affects directly the drift dispersion, and the dispersion of spin rate velocity would also cause the drift dispersion, the setting error of nub, especially the error of canted angle of nub would affect the dispersion of spin rate, and cause the drift. Dispersion formula of the drift dispersion is give in the form,

$$E_{zz} = \gamma_z X t g \theta_0 \quad (32)$$

where  $E_{zz}$ - the probable error of drift dispersion;  $X$ - range;  $\theta_0$ - the angle of dequardure;  $\gamma_z$ - drift coefficient, its value is 0.0005 to 0.002, generally adopted 0.001.

## 5. DISPERSION CHARACTER OF LOW DRAG PROJECTILE



TABLE 6

projectile	ballistic coefficient
M107 155	0.51
M46 130	0.472
M62 152	0.529
ERFB 155	0.38
ERFB - BB 155	0.28

To extend range, the drag must be reduced in a large extent. The drag of low drag extended range projectile is about half as large as that of old common high explosive projectile. If the ballistic coefficient is used as standard, its variation is shown in table 6.

To extend range, initial velocity also must be increased, however, sensitivity factors are increased largely, the data is given in table 7.

Compare with M107155mm projectile,  $\frac{\partial X}{\partial v_0}$  and  $\frac{\partial X}{\partial C}$  of ERFB 155 and ERFB - BB 155 respective  $v_0$  is increased 2.2 times and 3.1 times.

Secondly, the relative change of the drag coefficient or the ballistic coefficient of low drag projectile is increased largely. Define relative change as

$$E_c = \frac{E_{c1}}{C} 100\% \quad (33)$$

where  $E_{c1}$  - the probable error of ballistic coefficient;  $c$  - ballistic coefficient;  $E_c$  - the relative change of the dispersion of ballistic coefficient.

Because the ballistic coefficient  $c$  of base bleed projectile is reduced, even if  $E_{c1}$  is maintained constant,  $E_c$  would be reduced, besides, because of the base bleed unit, the drag dispersion of base bleed is increased,  $E_{c1}$  of base bleed projectile is also larger than that of common high explosive projectile, and  $E_c$  would be still larger.

$$E_{xc} = \frac{\partial X}{\partial C} E_c \quad (34)$$

$$E_{xv_0} = \frac{\partial X}{\partial v_0} E_{v_0}$$

From above formulas, because the low drag projectile is added the base bleed unit,  $E_{v_0}$ ,  $\frac{\partial X}{\partial C}$  and  $\frac{\partial X}{\partial v_0}$  are increased. This problem is caused by the low drag projectile itself, designers must correctly deal with the relation of extended range with dispersion, otherwise, they would attend to one and neglect the other.

## 6. DEMONSTRATION AND DISTRIBUTION OF INDEX OF PRECISION OF BASE BLEED PROJECTILE

Under the condition of strict controlling precision test, the influence of natural error must be about the same. For the extended range high explosive projectile, the definition

TABLE 7

projectile	$\frac{\partial X}{\partial v_0}$	$\frac{\partial X}{\partial C}$
M107 155	28.5	99.5
M46 130	39	107
M62 152	29	116
ERFB 155	62	220
ERFB - BL - 155	92	310

dispersion is not main, at the stage of preliminary design main attention must be paid to the range dispersion. Use following formula

$$E_x^2 = \left( \frac{\partial X}{\partial v_0} E_{v_0} \right)^2 + \left( \frac{\partial X}{\partial C} E_c \right)^2$$

6.1 Under the Condition of Precision Index of Common High Explosive Projectile Known, Determination of the Index of Precision of Base Bleed Projectile.

For example, following data of common high explosive projectile:  $E_{v_0a}$ ,  $E_{ca}$ ,

$\left( \frac{\partial X}{\partial C} \right)_a$ ,  $\left( \frac{\partial X}{\partial v_0} \right)_a$ ,  $X_a$ ,  $E_{xa}$ , and the data of base bleed projectile:  $\left( \frac{\partial X}{\partial v_0} \right)_b$ ,  $\left( \frac{\partial X}{\partial C} \right)_b$ ,  $X_b$ , are known. how to determine  $E_{xb}/X_b$  of base bleed projectile.

adopt:

$$\left( \frac{\partial X}{\partial C} \right)_b = K_1 \left( \frac{\partial X}{\partial C} \right)_a$$

$$\left( \frac{\partial X}{\partial v_0} \right)_b = K_2 \left( \frac{\partial X}{\partial v_0} \right)_a$$

$$E_{cb} = K_3 E_{ca}$$

$$E_{v_0b} = K_4 E_{v_0a}$$

$$X_b = K_5 X_a$$

(35)

yield

$$\frac{E_{xb}}{X_b} = \frac{\sqrt{\left[ K_1 K_2 \left( \frac{\partial X}{\partial C} \right)_a E_{ca} \right]^2 + \left[ K_2 K_4 \left( \frac{\partial X}{\partial v_0} \right)_a E_{v_0a} \right]^2}}{K_5 X_a} \quad (36)$$

For convenience to discussion, firstly, assume:  $K_1 = K_2$ ,  $K_3 = K_4 = K_5 = 1$ , then

$$\frac{E_{xb}}{X_b} = \frac{K \sqrt{\left[ \left( \frac{\partial X}{\partial C} \right)_a E_{c_a} \right]^2 + \left[ \left( \frac{\partial X}{\partial v_0} \right)_a E_{v_{0a}} \right]^2}}{K_s X_a}$$

$$\frac{E_{xb}}{X_b} = \frac{K}{K_s} \frac{E_{xa}}{X_a} \quad (37)$$

from (37), it is shown that

$K = K_s$ ,  $\frac{E_{xb}}{X_b} = \frac{E_{xa}}{X_a}$ , or, the precision index of base bleed projectile is same as that of high explosive projectile.

$K > K_s$ ,  $\frac{E_{xb}}{X_b} > \frac{E_{xa}}{X_a}$ , or, the precision index of base bleed projectile is larger than that of high explosive projectile.

$K < K_s$ ,  $\frac{E_{xb}}{X_b} < \frac{E_{xa}}{X_a}$ , or, the precision index of base bleed projectile is less than that of high explosive projectile.

where,  $K$  denotes the amplification of sensitivity factors  $\frac{\partial X}{\partial v_0}$ ,  $\frac{\partial X}{\partial C}$ ;  $K_s$  denotes extended range rate;  $K_3$  and  $K_4$  denote amplification of  $E_{v_0}$  and  $E_c$ . Hence, some conclusions can be obtained. Under the condition that  $E_{v_0}$  and  $E_c$  of two kinds of projectile are kept constant, if the amplification of sensitivity factors is equal to the extended range rate, the precision index may be kept constant. Taking ERFB155 and ERFB-BB155 for

example,  $K = 1.5$ ,  $K_s = 1.3$ , or,  $K > K_s$ , yield  $\frac{E_{xb}}{X_b} > \frac{E_{xa}}{X_a}$ . Above-mentioned discussion is made under  $E_{v_{0a}} = E_{v_{0b}}$ ,  $E_{c_a} = E_{c_b}$ . In fact,  $E_{v_{0a}} = E_{v_{0b}}$  may be received, but  $E_{c_b}$  is not equal to  $E_{c_a}$  generally, its reason has been discussed above. When demonstrating, correct estimating  $E_{c_b}$  is very important. In terms of wind tunnel tests and experience, it is reasonable to assume  $E_{c_b} = (1.2 \sim 1.4) E_{c_a}$  for preliminary design, hence

$$E_{c_b} = (1.2 \sim 1.4) \frac{C}{C_s} E_{c_a} \quad (38)$$

take ERFB155 for example,  $\left( \frac{\partial X}{\partial v_0} \right)_a = 62$ ,  $\left( \frac{\partial X}{\partial C} \right)_a = 220$ ,  $C_a = 0.38$ ,  $E_{v_{0a}} = 1.62$ ,  $E_{c_a} = 0.5$ ,  $X_a = 30000m$ ,  $\left( \frac{\partial X}{\partial C} \right)_b = 310$ ,  $\left( \frac{\partial X}{\partial v_0} \right)_b = 92$ ,  $C_b = 0.28$ ,  $X_b = 39000m$ , result are given by calculation as follows:

$$\frac{E_{x_a}}{X_a} = \frac{1}{201}, \quad \frac{E_{x_b}}{X_b} = \frac{1}{131}$$

## 6.2 Distribution of Precision Index and Design

Next, put main factors that affect precision as standards, to distribute the precision index, and to design structure under the condition of ensuring precision index.

If  $E_{v_0}$ ,  $E_c$ ,  $c$ ,  $v_0$ ,  $\theta_0$ ,  $X$  are known, steps to distribute the index and to design are given as follows:

(a) Distribution of index and determination of dispersion probable error  $E_{x_{01}}$ ,  $E_{x_{02}}$  caused by every factor, Or.

$$\begin{aligned}
E_{XBB}^2 &= C_1 E_X^2 & E_{ZZ}^2 &= C_3 E_Z^2 \\
E_{X\delta_m}^2 &= C_2 E_X^2 & E_{Z\delta}^2 &= C_6 E_Z^2 \\
E_{Xv_0}^2 &= C_3 E_X^2 & E_{ZW_Z}^2 &= C_7 E_Z^2 \\
E_{XW_X}^2 &= C_4 E_X^2
\end{aligned}$$

where, coefficient  $C_1 \cdots C_7$  can be determined by lots of statistic data and experience. So  $E_{XBB}$ ,  $E_{X\delta_m}$ ,  $E_{Xv_0}$ ,  $E_{XW_X}$ ,  $E_{ZZ}$ ,  $E_{Z\delta}$ ,  $E_{ZW_Z}$  can be yielded.

(b) Determination of sensitivity factors of every factor. With  $c$ ,  $v_0$ ,  $\theta_0$ , sensitivity factors  $\frac{\partial X}{\partial C}$ ,  $\frac{\partial X}{\partial \delta_m}$ ,  $\frac{\partial X}{\partial v_0}$ ,  $\cdots$  of every factor can be yielded via ballistic tables and equations.

(c) Determination of probable error of dispersion factors.

$$\begin{aligned}
\frac{\partial X}{\partial C} E_{CBB} &= E_{XBB} & \frac{\partial Z}{\partial \delta_p} E_{\delta_p} &= E_{ZZ} = Z \chi \operatorname{tg} \theta_0 \\
\frac{\partial X}{\partial \delta_m} E_{\delta_m} &= E_{X\delta_m} & \frac{\partial Z}{\partial \psi} E_{\psi} &= E_{Z\delta} \\
\frac{\partial X}{\partial v_0} E_{v_0} &= E_{Xv_0}
\end{aligned} \tag{39}$$

from above,  $E_{CBB}$ ,  $E_{\delta_m}$ ,  $E_{v_0}$ ,  $v_Z$ ,  $E_{\psi}$ , can be determined.

(d) Determination of probable error of dispersion of every factor assumed to satisfy needs, and determination of the structure of gun system, or, presentation as advanced index such as  $E_{v_0}$ ,  $E_{CBB}$ . According to the probable error of the dispersion of every factor, when the base bleed unit, propellant structure, projectile/gun structure, etc, are considered, as the result of respective error of every factor is reached,  $E_{X/X}$  and  $E_Z$  that satisfy needs would be obtained. This is the process of combining theory and experiment, among other some theoretical problems are not completely solved and satisfactory results would be obtained when modified design and test are taken again and again.

## REFERENCE

1. Pu Fa, Exterior Ballistics, National Defence Industry Publishing House, 1980.
2. Guo, Xifu Etc, the Exterior Ballistics of Base Bledd Projectile, Ballistic Research Lab. of EICT, 1986.

# A B S T R A C T

## " Solutions to Base Bleed Projectile Hardware Manufacturing Challenges "

By L.L. CROWSON, Jr., Morton Thiokol Inc., Louisiana Division,  
P.O. Box 30058, Shreveport, Louisiana, 71130, U.S.A.

Carbide tooling inserts cannot machine this material at optimum rates and costs. It was known that ceramic tooling theoretically would permit higher metal removal rates per unit time and increase productivity by increasing tool life. However, a good data base of information on the use of ceramic tooling was not available. The Louisiana Division initiated an 18&0 project to establish the needed data base. Work was again performed in conjunction with

Turning tests demonstrated metal removal rates of 18 cubic inches per minute while performing standard profile machining. This is double stated data bank values. In this demonstration, typical 155mm XM864 Projectile parts were turned. The AISI 4340 Steel Test specimens had hardnesses from Rc36 to Rc48. Typical machining conditions were:

1. Feed rate 0/1000th of an inch per revolution
2. Depth of cut 1/10 inch
3. Speed 1,250 surface feet per minute

Speeds of 1,500 surface feet per minute were demonstrated. Published literature data gives maximum speeds in the 400 to 500 surface feet per minute range. This paper will discuss details of ceramic tool tests. The resulting tool geometries, tool holders, work holding methods, and turning sequences will be presented.

This investigation produced positive results in both areas of concern:

1. The application of a CAD analysis surfaced problem areas early in the TDP development cycle.
2. The use of ceramic tooling instead of carbide will reduce the number of production machines required by one-third. This will save \$2-5 million in initial facilitation costs, and significantly reduce ongoing manufacturing costs.

The 155mm XM864 HE, Base Bleed (BB) Projectile is the newest addition to the Army's family of Improved Conventional Munitions (ICM). The Base Bleed feature adds a small solid propellant gas generator to the aft or base end of the projectile. The gas generator grain ignites shortly after gun launch. Gases generated flow into the low pressure area normally found in the wake of an artillery projectile. Eliminating this low pressure region decreases aerodynamic drag, thus increasing range. The range of the XM864 is 23 km vs. 18 km for the M83A1 Projectile, a gain of 30%. Timing of the ignition of a base bleed grain is less critical than that of the rocket motor on a rocket assisted projectile (RAP). This decreases round to round performance variability and increases accuracy.

In the fall, 1985, the Louisiana Division, Morton Thiokol, Inc. (Contractor Operator of Louisiana Army Ammunition Plant) was asked by the Army Research Development and Engineering Center (ARDEC), Dover, New Jersey, to review the embryonic XM864 Technical Data Package (TDP) with regard to producibility of the projectile hardware. A preliminary review by Division Engineering and Quality Control personnel surfaced several possible areas of dimensional or tolerance incompatibility. The Louisiana Division was funded by ARDEC to fully evaluate the existing Technical Data Package (TDP) from the standpoint of producibility. The services of the Advanced Manufacturing Technology Center, University of Southwest Louisiana, were used to perform a complete CAD analysis of 1) the projectile dimensions and stated tolerances, 2) the ability to manufacture the parts using CNC machines, standard tooling, and proven work holding techniques. That study disclosed several areas of incompatibility between the body, ogive, and base closure and contours which could not be readily generated with standard cutting tool inserts. This data was presented to ARDEC for consideration. Engineering changes have eliminated these problem areas. This paper will discuss the details of major findings from the CAD study and how problem areas were resolved.

A second challenge which was addressed was optimizing the machining operation through the application of ceramic tooling. The ogive, base, and base closure (gas generator case) are made from AISI 4340 Steel and heat treated to Rc42 minimum in order to achieve required physical properties.

# SOLID FUEL RAMJET, SELF-PROPELLED GUN LAUNCHED PROJECTILES

Alon Gany  
Faculty of Aeronautical Engineering  
Technion - Israel Institute of Technology  
Haifa 32000, Israel

## ABSTRACT

The feasibility and performance of self propelled, gun launched projectiles by means of solid fuel ramjet (SFRJ) motor is studied. It is demonstrated that the SFRJ can provide remarkable improvement of the projectile performance without changing the weapon itself. Consuming amount of fuel which is comparable to that of base bleed round, the SFRJ can generate thrust-equal-drag situation resulting in more than doubling the effective range compared to the modest range increase of the order of 20%, offered by base bleed. The much higher terminal velocity and kinetic energy along with shorter flight time and flatter trajectory can make the SFRJ projectile significantly more effective, particularly for air defense systems.

## INTRODUCTION

Increasing the terminal velocity and the range of a projectile can be done by several methods: (a) by increasing the muzzle momentum of the projectile, (b) by reducing the aerodynamic drag, and (c) by providing active propulsion to the projectile during its flight. Increased muzzle momentum can be achieved by either increasing the muzzle velocity and/or the projectile mass. Both imply changes in the gun system to accommodate the higher pressure and propellant amount involved, which actually mean a new design of the weapon. Drag reduction can be achieved by either the use of smaller cross-section, high density material, sub-caliber projectile, or by raising the base pressure closer to the ambient pressure using injection of fluid (burning or non-burning) near the projectile base zone (so called "base bleed"). Base drag is a significant portion of the total aerodynamic drag, (whose other components are skin friction drag and form or wave drag), and the most amenable to change. Nevertheless, a maximum reduction of about 25% of the total drag can be achieved due to the use of base bleed, hence the projectile range increase is typically limited to approximately 5 to 20%.

Data and correlations on the total projectile drag and the different drag components exhibit quite a spread although reflecting similar typical behavior. The total drag

coefficient  $C_D$  (based on the free stream dynamic pressure and the maximum cross-section of the projectile) has a relatively low value (approximately 0.1) in the subsonic range which increases sharply to reach a maximum of 0.3-0.4 in the transonic range (around  $M=1.2-1.3$ ) and then decreases monotonically in the supersonic flight range. The base drag coefficient  $C_{Db}$  demonstrates similar behavior. Hudgins Jr. [1] gives the following empirical correlation for  $C_{Db}$  versus Mach number

$$C_{Db} = 0.306 e^{-0.353 M} \quad M = 1-8 \quad (1)$$

while Murthy and Osborn [2] correlate some experimental data in the Mach number range of 1.5 to 3. using another approximation:

$$C_{Db} \approx \frac{0.7}{M^2} \quad M > 1.5 \quad (2)$$

Summarizing the data and analyses in Refs. [1]-[5] one can see that the base drag component is indeed a large portion of the total drag (of the order of one third). See Fig. 1. The correlation used in this work to represent the (total) aerodynamic drag coefficient is shown in Eq. (3):

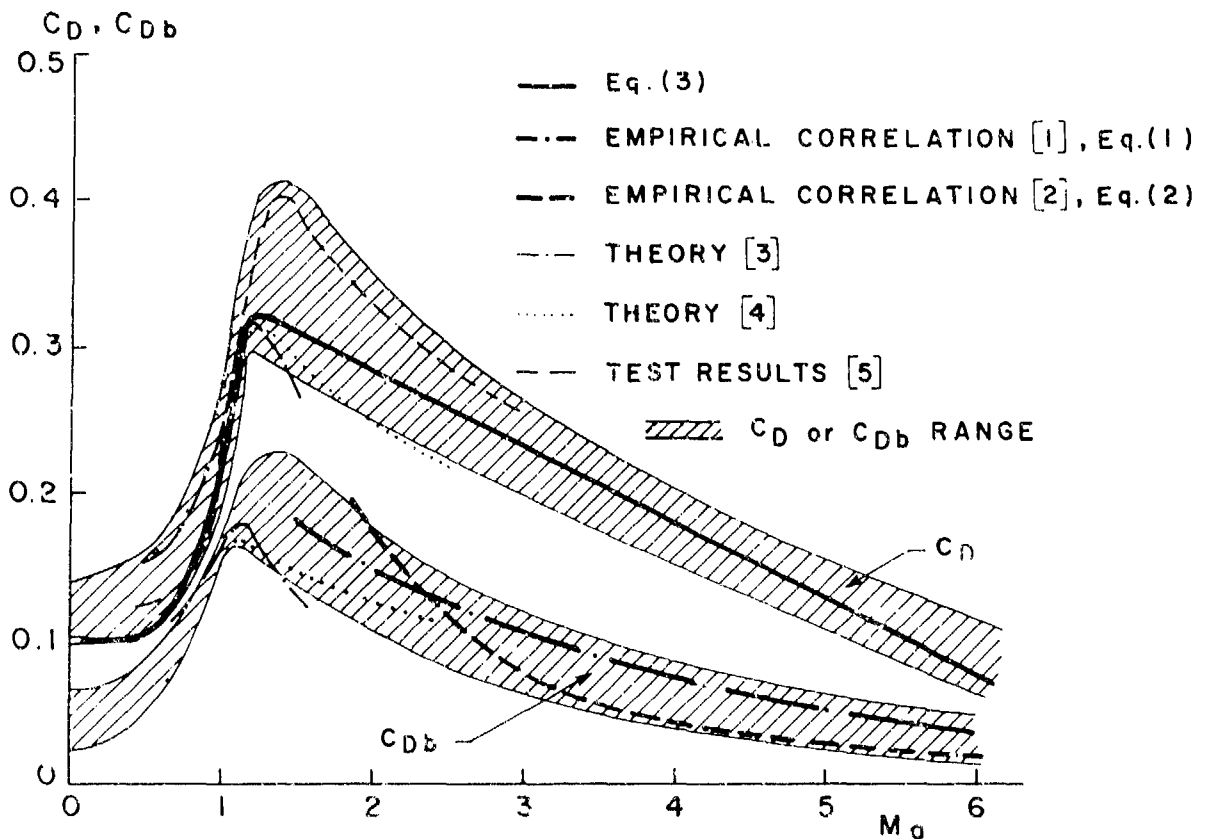


FIGURE 1. Typical variation of the total and base drag coefficients of projectiles with Mach number.

$$C_D = 0.35 M^2 - 0.27 M + 0.14 \quad M < 1.2$$

$$C_D = 0.32 \quad 1.2 \leq M \leq 1.3 \quad (3)$$

$$C_D = 0.3876 - 0.052 M \quad M > 1.3$$

Investigations on base drag reduction by base bleed (usually by means of a solid propellant gas generator, so-called "fumer"), have shown a decrease in the value of  $C_{Db}$  to 50% and even less compared to its original value [1], [4], [5]. The effect is more pronounced for the supersonic flight range ( $M > 1.5$ ). The optimal situation (maximum base drag reduction) requires, however, an injection of gas amounting to 0.030 of the reference flow rate  $\dot{m}_{ref}$  for cold gas (air) and to about  $0.013 \cdot \dot{m}_{ref}$  for hot gas [1].  $\dot{m}_{ref}$  is defined as

$$\dot{m}_{ref} = \rho_a u_a A_{max} \quad (4)$$

Illustration of a projectile with base bleed is shown in Fig. 2.

Active propulsion for projectiles can be done by two main methods: rocket motor (rocket assisted projectile, RAP) or solid fuel ramjet (SFRJ) motor. The rocket motor is a simple and reliable propulsion means, which is independent of flight conditions. Its main disadvantage is its high propellant consumption rate and low specific impulse, resulting in a limited total momentum that can be provided for the projectile and, hence, limited improvement in the overall performance. In addition, the RAP operation inherently introduces larger trajectory errors and inaccuracies. The RAP concept is shown in Fig. 3.

The solid fuel ramjet seems to be "naturally tailored" to the specific use of propelling projectiles. Muzzle conditions provide the necessary high velocity needed for the aerodynamic compression, which is essential for the SFRJ operation. This way the gun system serves as an economical, high accuracy accelerator, avoiding the need for a special rocket-type booster stage. The ramjet motor then starts to operate upon leaving the gun barrel. The main advantage of ramjet over rocket is in its much higher specific impulse (of the order of 800-1000 seconds versus 200 seconds approximately) resulting in a much smaller fuel consumption rate. Hence, it can provide much higher total impulse to the projectile, applied as a certain thrust for the required amount of time.

The SFRJ is the simplest air breathing engine. It does not contain any moving parts, valves, storage tanks, or injection systems. It consists of a diffuser, a combustion chamber, and a nozzle. The solid fuel grain, typically of a hollow cylinder shape, is placed in the combustion chamber, and the incoming air flows through its port. It should be



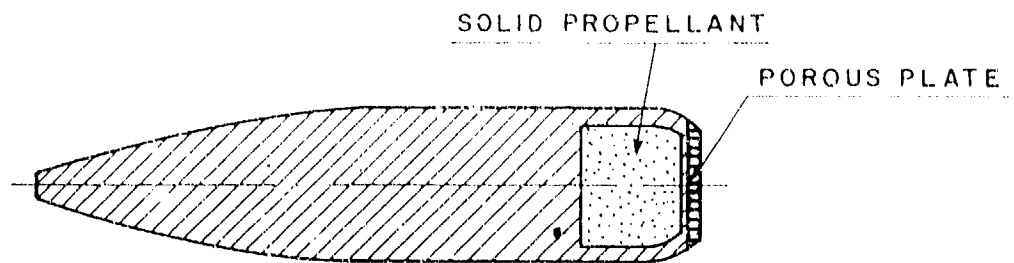


FIGURE 2. Projectile with base bleed.

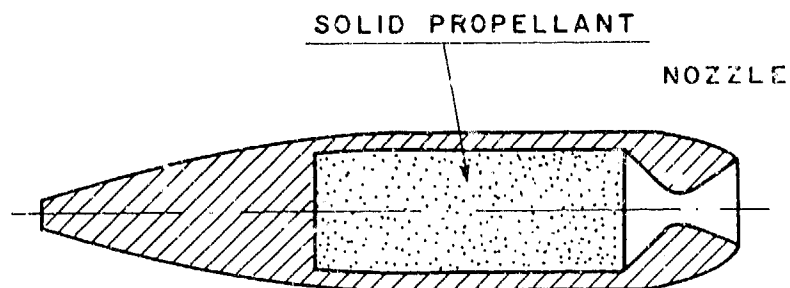
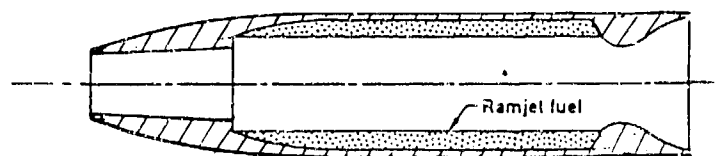
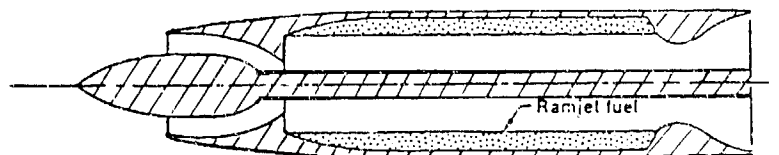


FIGURE 3. Rocket assisted projectile (RAP).



(a) Pitot (normal shock) inlet



(b) Center body (external compression) inlet

FIGURE 4. Solid fuel ramjet (SFRJ) projectiles.

noted, however, that the SFRJ is a more complex motor than rocket, and its operation depends on several factors that do not affect the rocket motor, such as flight Mach number, density and temperature of the atmosphere, and the angle of attack. Figure 4 presents the concept of an SFRJ projectile with two different inlet types: a simple pitot diffuser and a higher performance, external compression center-body diffuser.

It is desirable that a self propelled projectile operates at thrust-equal-drag situation. Such conditions imply a pure (vacuum) ballistic trajectory, enabling high precision and self correcting action against winds. In general, the SFRJ motor compensates for variations in the atmosphere density as a result of the similar effect of the density on the drag and the thrust.

The objective of this work is to present the operation characteristics of SFRJ self-propelled gun launched projectiles. It will be shown that for an amount of fuel similar to the amount of propellant needed for base drag reduction by base bleed, the superiority of the SFRJ system in terms of projectile performance is essential. The thrust-equal-drag condition implies a constant flight velocity, more-or-less, equal to the muzzle velocity. This situation results in a number of significant advantages: (a) the terminal kinetic energy of the projectile remains equal to that at the muzzle exit implying the maximum penetration potential. The improvement is more pronounced in the case of small caliber projectiles because of the larger ratio between drag and mass. (b) The trajectory is flatter than in regular rounds, causing easier aiming and better precision. (c) The time in flight may be much shorter, a major advantage particularly for air defense systems, also reducing wind effects. (d) The range may be increased by a factor of 2 and even more [6], compared to a maximum range increase of about 20% expected for based bleed projectiles.

Figure 5 demonstrates the striking superiority of a thrust-equal-drag operation, which is supposed to be achieved for an SFRJ projectile, compared to regular and base bleed rounds, regarding the velocity, kinetic energy, and time along the path. Calculation and data [7], [8] are presented for a 5.56 mm, 3.6 gram projectile, with a muzzle velocity of 990 m/s.

#### THE SFRJ PROJECTILE - GENERAL CHARACTERISTICS

Detailed configuration and notation characterizing an SFRJ projectile having a pitot-type inlet are shown in Fig. 6.

An  $\dot{m}_a$  mass flow rate of air at supersonic flight speed  $u_a$  and Mach number  $M_a$  enters the diffuser through a normal shock wave. The resulting subsonic flow is then expanding from the inlet cross section  $A_{in}$  into the combustion chamber, flowing through the cylindrical port (cross section

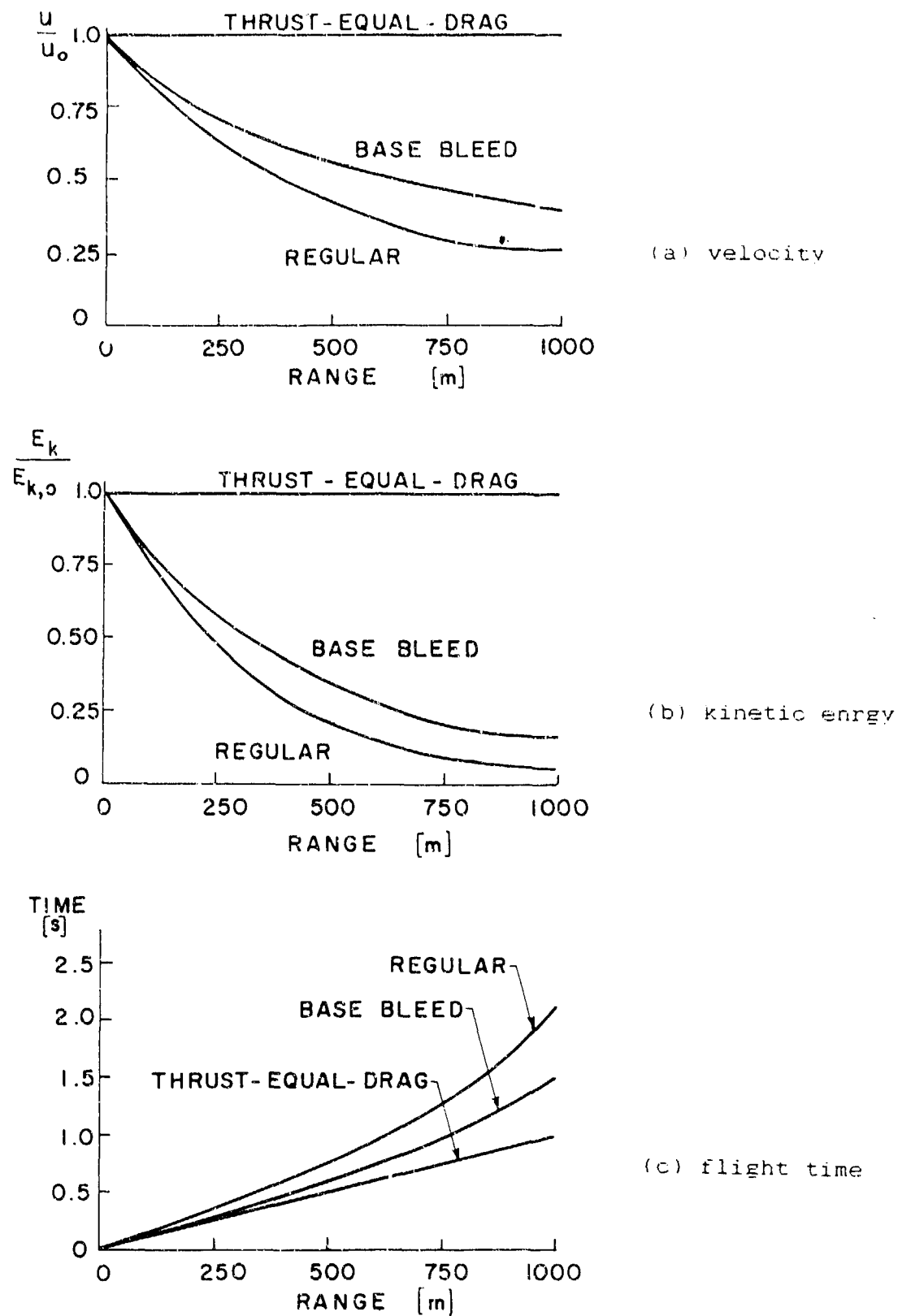


FIGURE 5. Variations of the (a) velocity, (b) kinetic energy, and (c) flight time along the path of regular, base bleed, and thrust-equal-drag, 5.56 mm projectiles.

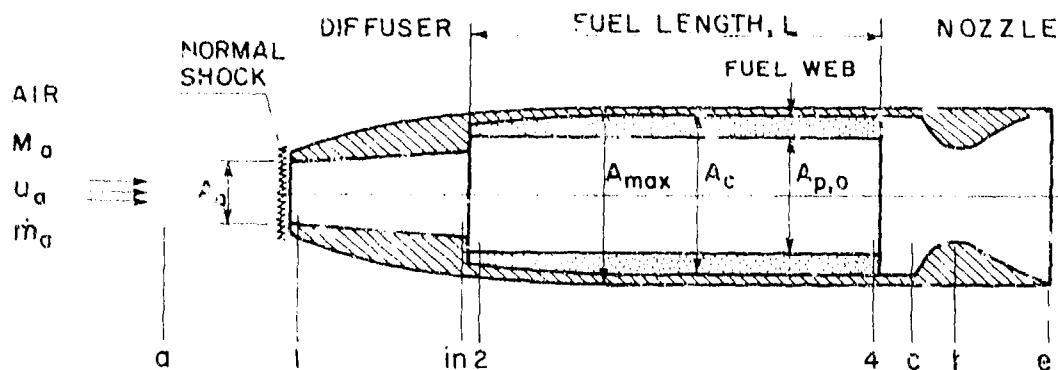


FIGURE 6. Geometry and notation of an SFRJ motor with a pitot diffuser.

$A_p$ ) of the fuel grain. The inlet step, represented by the area ratio  $A_p/A_{in}$ , is essential for flame stabilization, especially at low air temperature corresponding to low flight Mach number (up to about  $M_a=3$ ) [9]-[11]. The fuel, typically a hydrocarbon (HC) polymer, burns with the air, heating the gas mixture to its stagnation combustion temperature  $T_c$ , while the surface regresses radially at a typical regression rate,  $\dot{r}$ , affected by the air mass flux through the port, the inlet air temperature, the fuel type, and some other operation parameters (e.g., combustor geometry).

Optimal operation implies that the exit pressure  $p_e$  is equal to the ambient pressure  $p_a$  (adapted nozzle). Maximum thrust at given flight conditions results from a stoichiometric fuel/air ratio (equivalence ratio,  $\phi=1$ ).

A general theoretical plot of the specific thrust  $F/\dot{m}_a$  and the specific drag  $D/\dot{m}_a$  versus Mach number can be drawn, using the ratio between the air capture area ( $A_a=A_1$ ) and the maximum projectile cross-section area  $A_{max}$  as a parameter.

The effect of combustion efficiency on the thrust can be shown too (see Fig. 7). In the calculation of Fig. 7, a hydroxyl-terminated polybutadiene (HTPB) fuel was assumed at sea level flight conditions with a pitot (normal shock) diffuser. Stagnation pressure losses resulting from the normal shock wave in addition to 5% losses from other processes (e.g. heat addition) were assumed as well. Somewhat better performance can be obtained from an improved (center-body) diffuser (Fig. 8). The stagnation pressure losses of a pitot (normal shock) diffuser and a typical improved diffuser [12] are shown in Fig. 9.

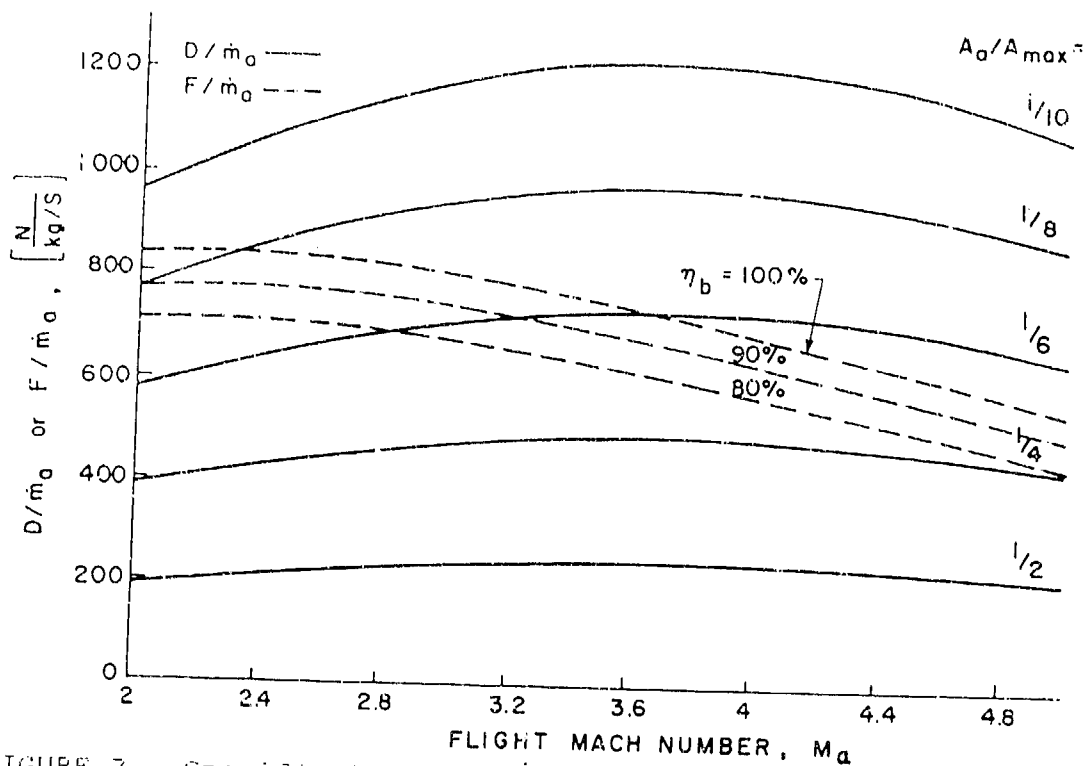


FIGURE 7. Specific thrust  $F/\dot{m}_a$  and specific drag  $D/\dot{m}_a$  of a pitot (normal shock) diffuser SFRJ motor versus flight Mach number  $M_a$  for different  $A_0/A_{\max}$  ratios and combustion efficiencies  $\eta_b$ . Sea level. HTPB fuel.

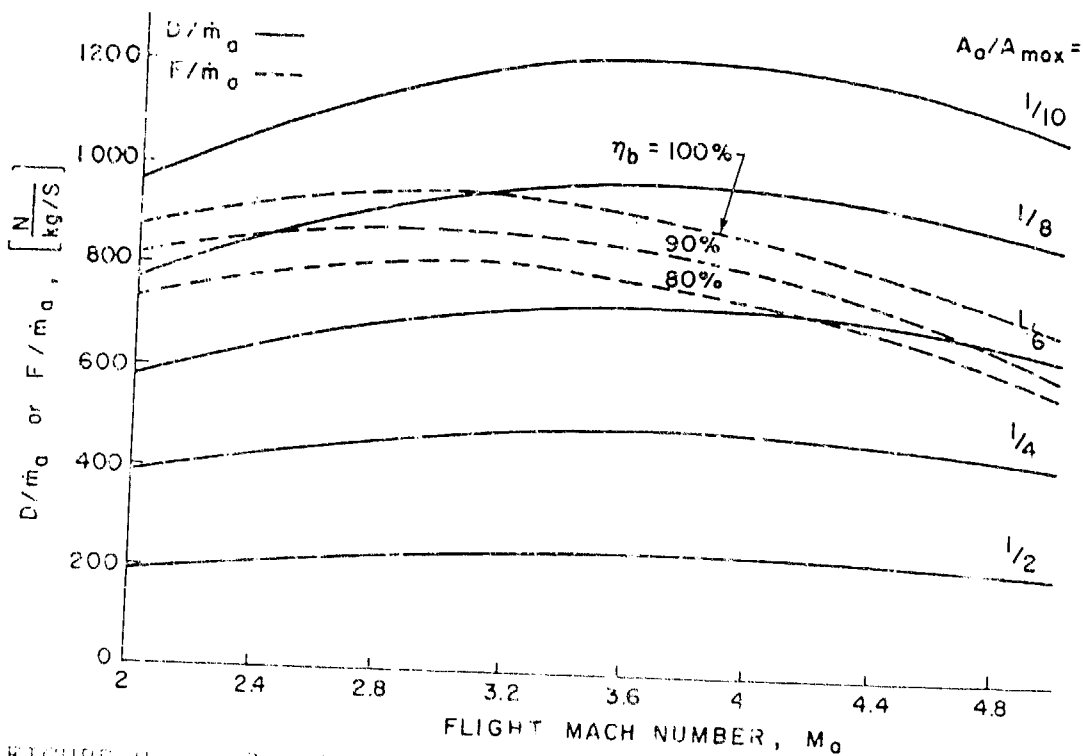


FIGURE 8. Specific thrust  $F/\dot{m}_a$  and specific drag  $D/\dot{m}_a$  of an improved (center body) diffuser SFRJ motor versus flight Mach number  $M_a$  for different  $A_0/A_{\max}$  ratios and combustion efficiencies  $\eta_b$ . Sea level. HTPB fuel.

The thrust equation (adapted nozzle conditions) is:

$$F = \dot{m}_a [(1+f)u_e - u_a] \quad p_e = p_a \quad (5)$$

where  $f$  is the fuel-to-air ratio:

$$f = \frac{\dot{m}_f}{\dot{m}_a} \quad (6)$$

The exit jet velocity was calculated from

$$u_e = \sqrt{2c_p T_c \left[ 1 - \left( \frac{p_e}{p_c} \right)^{\frac{\gamma-1}{\gamma}} \right]} \quad (7)$$

$p_c$  is the stagnation pressure at the end of the combustion chamber, calculated from the ambient pressure, flight Mach number, and stagnation pressure losses, as described above.  $T_c$  is the stagnation chamber temperature obtained from the theoretical flame temperature calculated by a thermochemical computer code [13] (along with other gas properties such as  $c_p$  and  $\gamma$ ), and the combustion efficiency defined as

$$\eta_b = \frac{T_c - T_{oa}}{T_{c,th} - T_{oa}} \quad (8)$$

where

$$T_{oa} = T_a \left[ 1 + \frac{\gamma-1}{2} M_a^2 \right] \quad (9)$$

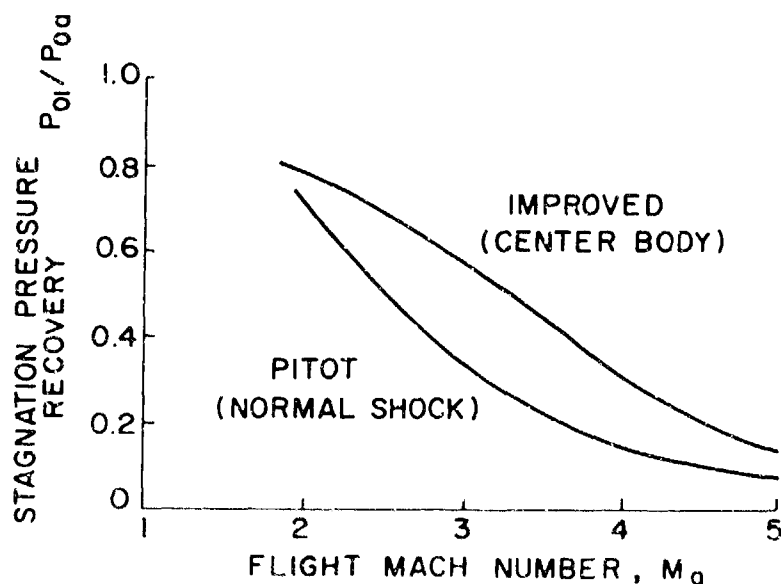


FIGURE 9. Stagnation pressure recovery in a pitot (normal shock) diffuser and in a typical improved diffuser.

Aerodynamic drag was calculated by

$$D = C_D \cdot \frac{1}{2} \rho_a u_a^2 \cdot A_{\max} \quad (10)$$

where the value of  $C_D$  was obtained from Eq. (3).

From Figs. 7 and 8 one can draw the minimum  $A_a/A_{\max}$  ratio necessary to obtain thrust-equal-drag conditions at each Mach number (Fig. 10). Note that lower combustion efficiency implies larger  $A_a/A_{\max}$  ratio. Figure 10 demonstrates the superiority of an improved (center-body) diffuser compared to a pitot diffuser

Constraints on  $A_a/A_{\max}$  ratio may be relieved to some extent by adding some amount of oxidizer to the SFRJ fuel, thereby reducing the required amount of air. Between the two limiting cases, pure SFRJ (only fuel) and pure rocket (no air), i.e. RAP, lie the different (increasing) oxidizer percentages implying decreasing  $I_{sp}$  values. Figure 11 shows the variations of the minimum  $A_a/A_{\max}$  ratio required for thrust-equal-drag operation versus  $M_a$  for different fuel (or propellant)/air ratios associated with different oxidizer fractions in the fuel, maintaining overall stoichiometric fuel(+ oxidizer)/air ratio. HTPB fuel and ammonium-perchlorate (AP) oxidizer as well as pitot-type diffuser were used in the calculations.

As has been mentioned before, along with increasing the specific thrust  $F/m_a$ , the use of oxidizer in addition to the fuel results in a penalty of a reduced specific impulse

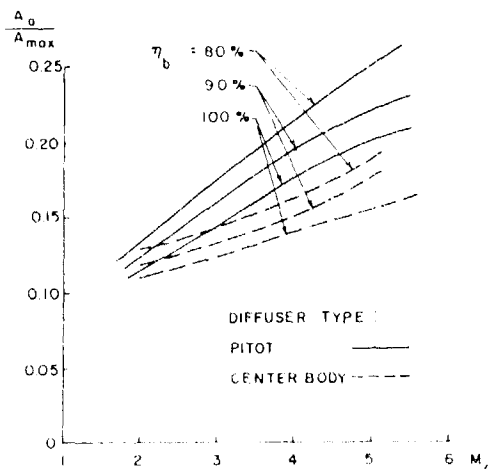


FIGURE 10. Minimum ratio of air capture to maximum cross section area,  $A_a/A_{\max}$ , necessary to achieve thrust-equal-drag conditions versus flight Mach number.

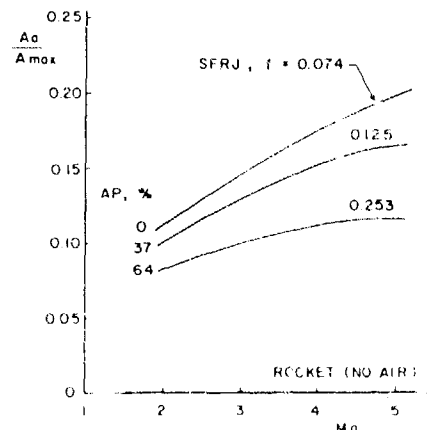


FIGURE 11.  $A_a/A_{\max}$  ratio required for thrust-equal-drag operation versus Mach number demonstrating decrease with increasing fraction of AP oxidizer in the fuel. Pitot diffuser.

defined as:

$$I_{sp} = \frac{F}{\dot{m}_f g_0} \quad (11)$$

Figure 12 demonstrates the variations in  $F/\dot{m}_a$ , in  $I_{sp}$ , and in  $f$  with the oxidizer fraction in the fuel for the specific flight conditions of  $M_a=3$  at sea level with a pitot diffuser and  $\eta_D=90\%$ .

One should be aware of the fact that higher specific impulse means more economical use of the fuel (or propellant), i.e., smaller fuel consumption rate  $\dot{m}_f$  for the same thrust level.

For a given mission, say, thrust-equal-drag operation, it means longer burn time (and range) per given amount of fuel. The fuel flow rate necessary to maintain thrust-equal-drag operation of a projectile at Mach number of 3 is given in Fig. 13 (normalized by a reference flow rate) as a function of the oxidizer mass fraction in the fuel or propellant. The two extreme cases, SFRJ with pure fuel (zero oxidizer) and pure rocket (no air) are obvious. A more complete idea on the fuel (or propellant) flow rate necessary to maintain thrust-equal-drag, can be revealed by Fig. 14, showing the variation of the fuel (or propellant) flow rate (normalized

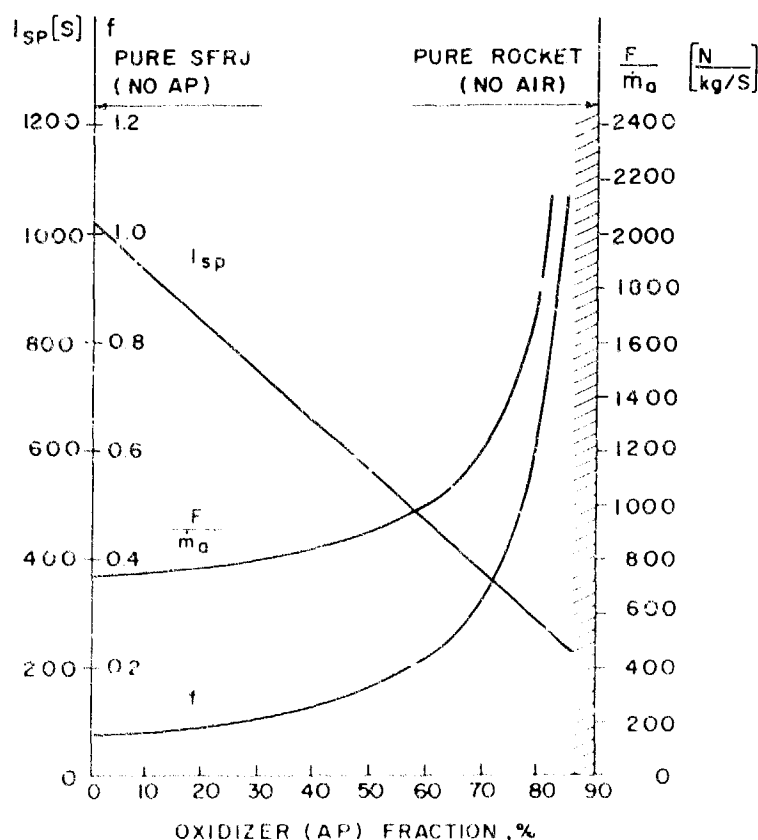


FIGURE 12. Variation of  $I_{sp}$ ,  $F/\dot{m}_a$ , and  $f$  with the oxidizer (AP) mass fraction in the solid propellant. Pitot diffuser,  $M_a=3$ ,  $\eta_D=90\%$ .



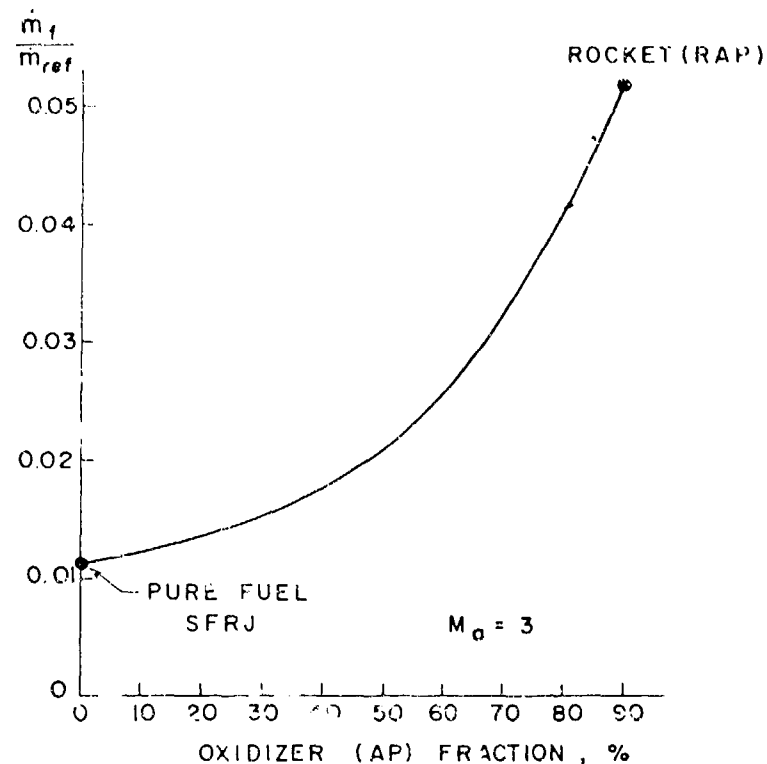


FIGURE 13. Variation of the fuel (or propellant) flow rate necessary for thrust-equal-drag operation as a function of the oxidizer mass fraction at flight Mach number of 3. Pitot diffuser,  $\eta_b = 90\%$ .

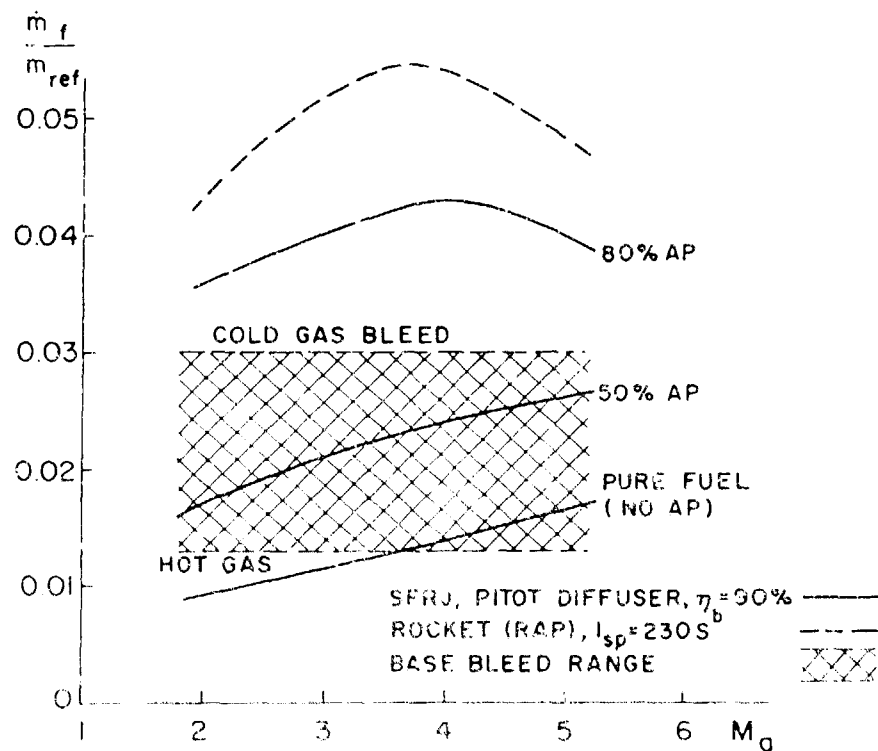


FIGURE 14. Fuel (or propellant) flow rate versus flight Mach number for thrust-equal-drag rocket (RAP) or SFRJ projectiles and for base bleed rounds.

by a reference flow rate) with the flight Mach number for different fuel-oxidizer combinations between pure SFRJ ( $f=0.074$ , zero oxidizer) and a pure rocket (RAP), having specific impulse of 230 s. For comparison, the typical base bleed operation range (which does not even come close to thrust-equal-drag conditions) is also shown in Fig. 14. The figure demonstrates the remarkable superiority of the SFRJ projectile versus RAP with regard to fuel consumption rate (factor of approximately 4). In addition, it reveals that the fuel flow rate of an SFRJ projectile giving thrust-equal-drag, is comparable and even lower than typical base bleed flow rates, whose improvement with regard to projectile performance is only a small fraction of the SFRJ's.

#### INTERNAL BALLISTICS AND CONSTRAINTS

The general requirements from an SFRJ projectile, as presented in the previous chapter, should be examined in the light of the internal ballistics of the SFRJ motor. The internal flow, combustion process, heat addition, and flameholding characteristics, in addition to geometric, construction and other constraints may, in some cases, contradict the mission requirements (such as certain thrust at given velocity and burning time), hence, questioning the SFRJ as a practical solution for self propelled projectiles in certain conditions.

The basic operation limit is due to flow choking in the combustion chamber ( $M_4=1$ ) as a result of the heat addition.

This should set the lowest value of the ratio between the fuel port area and the air capture area,  $A_p/A_a$ . The operation limit can be found from the continuity equation:

$$\dot{m}_4 = (1+f)\dot{m}_a \quad (12)$$

taking into account the heat addition in the constant cross section combustor, and the stagnation pressure losses resulting from the inlet shock waves and from the combustion process. The calculations were made for a pitot (normal shock) diffuser, using thermochemical code [13] to compute the theoretical stagnation combustion temperature. Combustion efficiency of 90% was assumed [14].

Table 1 shows calculated values of temperatures and pressures for a pitot diffuser SFRJ motor operating at sea level with ambient temperature of 288 K, and  $M_4=1$ . HTPB fuel at stoichiometric ratio was assumed.

TABLE 1. Stagnation Air and Combustion Temperatures and Stagnation Pressure Ratio Versus Flight Mach Number.

$M_a$	$T_{oa}$ (K)	$T_{c.th}$ (K)	$T_c(\eta_b=90\%)$ (K)	$P_c/P_{oa}$
2	518	2471	2276	0.59
3	806	2623	2441	0.27
4	1210	2856	2691	0.12
5	1728	3077	2942	0.054

Figure 15 presents the operation limits of the SFRJ motor in terms of the minimum  $A_p/A_a$  ratio versus the flight Mach number  $M_a$ , based on the data of Table 1. As can be seen from Fig. 15, the operation limit may be even narrower for small caliber projectiles at the lower Mach number range due to the deteriorating flameholding capability, requiring larger inlet step height under these conditions, as reported by Netzer and Gany [11]. Note that, in general, smaller ratio  $A_p/A_a$  is desirable, since it means that a larger amount of solid fuel can be placed in the combustor volume.

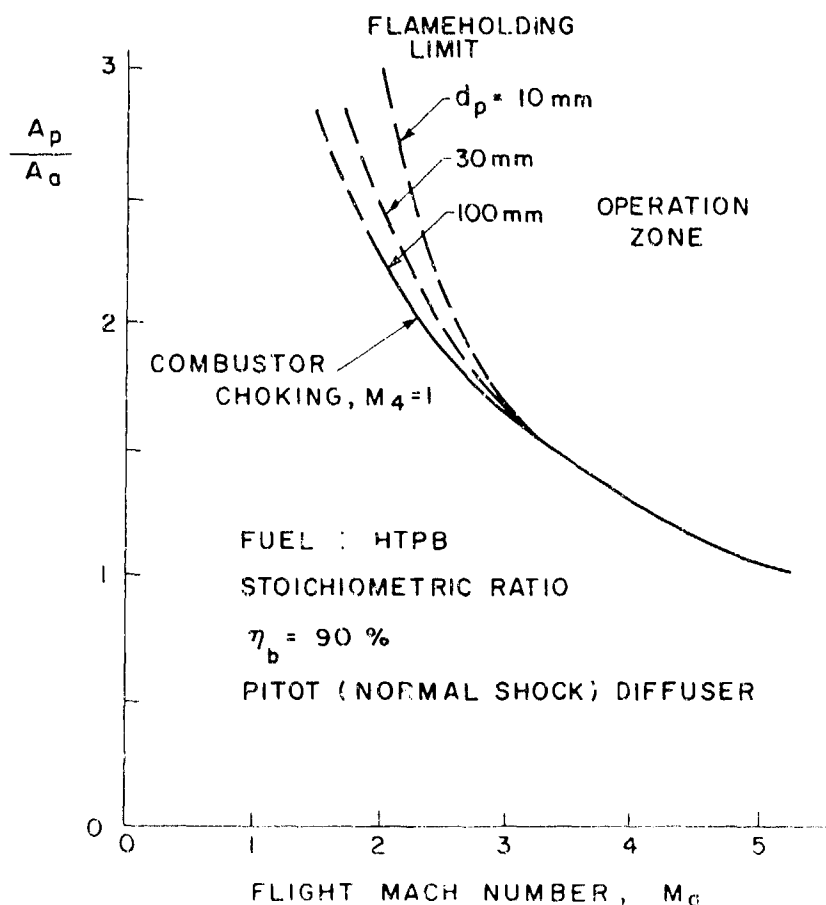


FIGURE 15. Operation limits of an SFRJ motor due to combustor's flow choking and flameholding requirements.

The operation limit in terms of  $A_p/A_a$  can determine the fuel burning rate and burning time and, hence, the projectile range with active, thrust-equal-drag propulsion, provided that some geometric parameters are given.

Substituting

$$\dot{m}_f = f \cdot \rho_a \quad (13)$$

and

$$\dot{m}_f = \rho_f \pi d_p L \dot{r} \quad (14)$$

one obtains

$$\dot{r} = \frac{f \cdot \rho_a \cdot u_a \left( \frac{A_a}{A_{\max}} \right)}{4 \rho_f \left( \frac{d_p}{d_{\max}} \right) \cdot \left( \frac{L}{d_{\max}} \right)} \quad (15)$$

It is convenient to relate the fuel length  $L$  and the different diameters to the projectile diameter,  $d_{\max}$ , as a basis for geometric similarity.

The requirement for constant thrust at constant flight speed implies fixed fuel consumption rate, i.e.,

$$\dot{r} \cdot d_p = \text{const} = \dot{r}_o d_{p.o} \quad (16)$$

The fuel burning time can then be found from the web thickness, by integrating Eq. (16) for  $d_p$  from  $d_{p.o}$  to  $d_c$  (external fuel diameter):

$$t_b = \frac{d_c^2 - d_{p.o}^2}{4 \dot{r}_o d_{p.o}} \quad (17)$$

It should be noted that Eqs. (15) and (17) contain two free parameters:  $L/d_{\max}$  and  $d_c$  (or by some manipulations,

$d_c/d_{\max}$ ). Those are design, geometric (construction) parameters. For given flight Mach number and similar geometric ratios, the initial value of  $r$  is found to be independent of the projectile diameter, and inversely dependent on  $L/d_{\max}$ :

$$\dot{r}_o = \frac{K_1}{(L/d_{\max})} \quad (18)$$

where  $K_1$  is a constant. In the specific conditions of  $M_a=3$  and  $d_c/d_{\max}=0.8$  (namely, the combustor metal wall thickness is 10% of the projectile diameter  $d_{\max}$ ), when using HTPB fuel of  $\rho_f=0.95$  g/cc and  $\eta_b=90\%$ , the value of  $K_1$  is found to

be approximately 8 mm/s.  $\dot{r}_0$  can be controlled by changing the ratio of  $L/d_{\max}$ . For instance,  $L/d_{\max}=4$  gives  $\dot{r}_0=2$  mm/s. The value of  $\dot{r}_0$  should increase when increasing the flight Mach number (up to about 5 mm/s at  $M_a=5$  for the same geometry and fuel). The experimental results and empirical correlations of the regression rate of an HTPB-based fuel [11] indicate that the required regression rates mentioned above are achievable in the typical conditions, particularly for small caliber projectiles (e.g. 20 mm). Furthermore, data on small port diameter SFRJ combustors [15] reveal fixed fuel consumption rate (according to the desirable situation presented by Eq. (16)) and, hence, constant fuel/air ratio  $f$  during the combustion, permitting optimal performance throughout the combustor operation. Fuel regression rate was found to be lower for larger port diameter combustors [15], hence, fast burning fuels should be used in such cases. In addition, regression rate correlations for large port diameter fuels [9], [16] indicate that the fuel consumption rate as well as the fuel/air ratio may vary a little during the combustion, because of the increase in the port diameter, thus some deviations from optimal operation conditions may be expected.

The burning time  $t_b$ , which is equivalent to the duration of the propelled stage of the flight, is one of the most important factors for evaluating the SFRJ projectile system. For a given flight speed,  $t_b$  determines the propelled stage range. In the case of projectiles flying at a given Mach number and having geometric similarity,  $t_b$  is found to be directly proportional to  $L/d_{\max}$  and to the projectile diameter  $d_{\max}$ :

$$t_b = K_2 \left( \frac{L}{d_{\max}} \right) \cdot d_{\max} \quad (19)$$

$K_2$  is a constant which, under the specific conditions giving  $K_1=8$  mm/s has a value of 0.023, approximately, when  $t_b$  is in seconds and  $d_{\max}$  in millimeters. Table 2 presents some examples of calculated burn time results based on the combustor operation limit shown in Fig. 15.

Equation (19) suggests that under the same conditions, where the firing angle is relatively small, the propelled stage range,  $R$ , is approximately:

$$R \cong K_3 \left( \frac{L}{d_{\max}} \right) \cdot d_{\max} \quad (20)$$

The specific conditions of  $M_a=3$  and  $d_c/d_{\max}=0.8$  yield  $K_3 \cong 23.5$ , where  $R$  is in meters and  $d_{\max}$  in millimeters.

TABLE 2. Example of Calculated Burn-Times of SFRJ Propelled Projectiles at Different Mach Numbers and Normalized Fuel Lengths.

caliber $d_{\max}$ [mm]	burn-time, $t_b$ [s]			
	$M_a=3$		$M=5$	
	$L/d_{\max}=4$	$L/d_{\max}=6$	$L/d_{\max}=4$	$L/d_{\max}=6$
20	1.8	2.8	1.0	1.5
40	3.7	5.5	2.0	3.0
105	9.7	14.5	5.2	7.9

Although the burn-time is significantly affected by the flight Mach number, the effect of Mach number on the range is only secondary, as the range is a product of  $t_b$  and  $u_a$ .

Note that more severe constraints are imposed on the SFRJ combustor for  $d_p < 10$  mm because of flameholding deterioration in smaller port diameter motors [11]. In such cases shorter burn-time and range are expected.  $d_p$  of 10 mm corresponds to projectile caliber of about 20 mm (it was found that  $d_{p,\min} \approx 0.5 d_{\max}$ ). Flameholding constraints associated with the inlet air temperature effect could also cause difficulties in achieving the performance predicted by the combustor choking limit in the lower Mach number range. For instance, at Mach 2, even combustors with fuel port diameter as large as 100 mm may yield somewhat lower performance.

Figure 16 presents the predicted propelled flight range versus the projectile caliber for SFRJ projectiles of

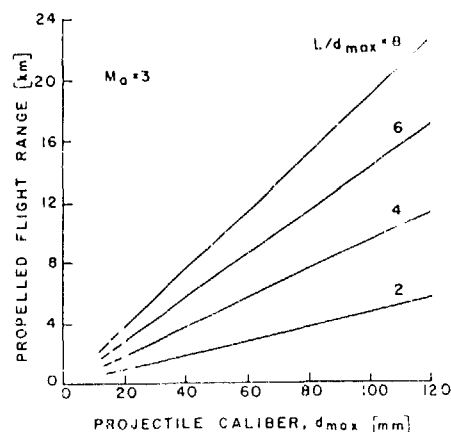


FIGURE 16. Calculated propelled stage range of SFRJ projectiles having geometric similarity versus projectile caliber  $d_{\max}$  for different fuel length to projectile diameter ratios.  $M_a=3$ , pitot diffuser,  $\eta_b=90\%$ .

different  $L/d_{\max}$  ratios flying at Mach 3 (see Eq. (20)). Note that operation constraints can be eased when using larger  $L/d_{\max}$  ratios. Both propelled stage time and range grow linearly with the fuel length to projectile diameter ratio. In this respect it is desirable that SFRJ projectiles have as large as possible length to diameter ratio.

#### CONCLUDING REMARKS

Solid fuel ramjet (SFRJ) propulsion can offer a remarkable improvement in projectile performance in terms of terminal velocity, kinetic energy, and range. It can also shorten the flight time and flatten the trajectory for a given range, thus making aiming easier and increasing hit probability, particularly in air defense operations. The SFRJ propulsion can provide thrust-equal-drag operation for much longer flight time and range than those encountered in rocket assisted projectiles (RAP). The performance superiority of the SFRJ is especially striking when being compared to base bleed projectiles. For approximately the same fuel (or propellant) mass flow rate, the former can double or even triple the effective projectile range, while the latter can only cancel approximately 25% of the overall drag by reducing the base drag, thus can offer a modest increase of about 20% in the projectile range.

It should be noted, however, that the SFRJ projectile is not only more complicated, but also has some inherent operation constraints resulting in poor volumetric efficiency of the fuel. This is due to the empty port volume required as well as because of the much lower fuel density in the SFRJ. As a result the effective fuel volume in the SFRJ will be about three times larger than that of a base bleed propellant having similar mass. This may require projectiles of length to diameter ratios larger than usual.

One should also bear in mind, that more severe operation constraints may be encountered in small caliber SFRJ projectiles due to deterioration of the combustor's flameholding capability.

#### ACKNOWLEDGMENT

The author thanks Miss Meira Ben-Zaken for assisting in the thermochemical calculations.

#### NOMENCLATURE

A	cross section area
$c_p$	specific heat at constant pressure
$C_D$	drag coefficient
d	diameter
D	drag force

$E_k$  kinetic energy  
 $f$  fuel/air ratio  
 $F$  thrust  
 $g_0$  standard gravity acceleration  
 $I_{sp}$  specific impulse  
 $K_1$  constant (Eq. (18))  
 $K_2$  constant (Eq. (19))  
 $K_3$  constant (Eq. (20))  
 $L$  fuel grain length  
 $\dot{m}$  mass flow rate  
 $M$  Mach number  
 $p$  pressure  
 $\dot{r}$  fuel regression rate  
 $R$  range  
 $t$  time  
 $u$  velocity  
 $\gamma$  specific heat ratio  
 $\eta_b$  combustion efficiency  
 $\rho$  density  
 $\phi$  equivalence ratio

#### Subscripts

1 station behind inlet normal shock  
 2 station at the beginning of combustor  
 4 station at the end of fuel grain  
 a ambient (or flight) conditions: air  
 b base conditions: burning  
 c stagnation conditions at combustor end  
 e nozzle exit plane  
 f fuel  
 in combustor inlet  
 max maximum; largest projectile cross section  
 min minimum  
 c stagnation (total) conditions: initial  
 p fuel port  
 ref reference (Eq. (4))  
 th theoretical

#### REFERENCES

1. Hudgins, Jr., H. E., Range Increase of Projectiles by Heat and/or Mass Addition to Base or External Flow, in *Aerodynamics of Base Combustion, Progress in Astronautics and Aeronautics*, Vol. 40, eds. S.N.B. Murthy, J.R. Osborn, A.W. Barrows, and J.R. Ward, pp. 495-521, AIAA, New York, NY, 1976.
2. Murthy, S. N. B. and Osborn, J. R., Base Flow Phenomena With and Without Injection: Experimental Results, Theories and Bibliography, in *Aerodynamics of Base Combustion, Progress in Astronautics and Aeronautics*, Vol. 40, eds. S.N.B. Murthy, J.R. Osborn, A.W. Barrows and J.R. Ward, pp. 7-210, AIAA, New York, NY, 1976.



3. Chow, W. L., Base Pressure of a Projectile within the Transonic Flight Regime, *AIAA J.*, Vol. 23, No. 3, pp. 388-395, March 1985.
4. Schilling, H., A Simple Theoretical Approach for Base Bleed Calculations, *Proc. 9th Int. Symposium on Ballistics*, pp. 2-59 to 2-66, 1986.
5. Elmendorf, T. A. and Trifiletti, R. A., Gas Generators for Base Drag Reduction (Fumers), in *Aerodynamics of Base Combustion, Progress in Astronautics and Aeronautics*, Vol. 40, eds. S.N.B. Murthy, J.R. Osborn, A.W. Barrows and J.R. Ward, pp. 471-486, AIAA, New York, NY, 1976.
6. Fink, M.R., Aerodynamic Properties of an Advanced Indirect Fire System (AIFS) Projectile, *Journal of Spacecraft and Rockets*, Vol. 19, No. 1, pp. 36-40, 1982.
7. Barrows, A. W., Drag Reducing Fumers, in *Aerodynamics of Base Combustion, Progress in Astronautics and Aeronautics*, Vol. 40, eds. S.N.B. Murthy, J.R. Osborn, A.W. Barrows and J.R. Wood, pp. 1-6, AIAA, New York, NY, 1976.
8. Kwatnoski, R., Drag-Reducing Fumer as a Tool in Ammunition Design, in *Aerodynamics of Base Combustion, Progress in Astronautics and Aeronautics*, Vol. 40, eds. S.N.B. Murthy, J.R. Osborn, A.W. Barrows and J.R. Ward, pp. 487-494, AIAA, New York, NY, 1976.
9. United Technologies Chemical Systems, Solid Fuel Ramjet.
10. Schulte, G., Fuel Regression and Flame Stabilization Studies of Solid Fuel Ramjets, *Journal of Propulsion and Power*, Vol. 2, No. 4, pp. 301-304, July-Aug. 1986.
11. Netzer, A. and Gany, A., Burning and Flameholding Characteristics of a Miniature Solid Fuel Ramjet Combustor, AIAA Paper 88-3044, 24th Joint Propulsion Conference, July 1988.
12. Kinroth, G. D. and Anderson, W. R., *Ramjet Design Handbook*, CPIA Publication 319, p. 2-17, 1980.
13. Cruise, D. R., Theoretical Computations of Equilibrium Compositions, Thermodynamic Properties, and Performance Characteristics of Propellant Systems, NWC-TP-6037, Naval Weapons Center, China Lake, CA, 1979.
14. Zvuloni, R., Levy, Y. and Gany, A., Investigation of a Small Solid Fuel Ramjet Combustor, *Journal of Propulsion and Power*, vol. 5, 1989 (in press).
15. Zvuloni, R., Gany, A. and Levy, Y., Geometric Effects on the Combustion in Solid Fuel Ramjets, *Journal of Propulsion and Power*, Vol. 4, 1988 (in press).
16. Mady, C.J., Hickey, P.J. and Netzer, D.W., Combustion Behavior of Solid Fuel Ramjets, *Journal of Spacecraft and Rockets*, Vol 15, No. 3, pp. 131-132, 1978.

**BASE BLEED SOLID PROPELLANT  
PROPERTIES AND PROCESSIBILITY FOR INDUSTRIAL SOLID PROPELLANT**

**GAUCHOUX Jacques - COUPEZ Dominique - LECOUSTRE Max**

**S.N.P.E St Médard  
33160 St MEDARD en JALLÈS**

**ABSTRACT**

Composite solid propellants were studied in order to obtain optimized propellant with good properties and processibility required for base bleed applications. HTPB propellant with Ammonium Perchlorate oxydizer ratio from 70 up to 80 % loading is selected after thermodynamical calculations.

This paper describes the mechanical and ballistic properties of the optimized propellant and the importance of each parameter.

**INTRODUCTION**

The base bleed effect increases the shell range by reducing the projectile base drag. The system consists in injecting hot and reductive propellant gases at the shell base.

Before experimental investigations, the propellant specialist determines the burning gas theoretical composition and the temperature with the help of classical thermodynamical calculations.

During the following experimental propellant optimization, he looks more particularly :

- To obtain a propellant grain with appropriated mechanical properties in order to ensure structural integrity during gun firing tests.
- To give the required burning rate under sub-atmospheric pressure.
- To reduce production costs due to mixing time and tooling immobilization.

Then, the optimized propellant is incorporated into an industrial context to satisfy technical and economical requirements in order to get a base bleed generator with the best performances at the best cost.

## THEORETICAL EVALUATION

Propellant formulation evaluations were performed initially with thermodynamical program. Optimum oxidizer loadings were determined with the used polymeric binder system. The optimization was based on the heat of combustion, density, and fuel ratio.

Propellants based on initial formulations were mixed, and Strand Burning rate, mechanical properties, and density determined.

From these initial formulations, additional modifications were introduced to evaluate the burning rate range capability and mechanical properties improvement. Working life evaluations were also performed.

## THERMODYNAMICAL PROPERTIES

The type of composite propellant is composed of a polymeric binder (here a HTPB) loaded with an oxidizer, the ammonium perchlorate. Some additives like bonding agent, ballistic catalyst and curing agent and generally an amount of heat allow to obtain the final propellant material.

Composition of base bleed propellant (ex : Filler AP : 80 wt %)

Ingredient	Weight %
Binder, HTPB	18
Antioxydant	0,4
Bonding agent	0,1
Curing agent	1,4
Catalyst	0,1
Oxydizer	80

The propellant combustion delivers some gaseous, liquid and solid species that we are able to compute with a good level of accuracy.

The thermodynamical characteristics are :

- C : 13,63 At.G/kg
- H : 49,75
- O : 28,08
- N : 6,81
- Cl : 6,81

These significant products of combustion are gaseous and characterized by :

- Heat of combustion :  $T_b$  : 2370° (in chamber)
- Density :  $\eta_l$  : 1593 G/cm<sup>3</sup>

The program delivers also some other parameters more communly used for ballistic requirements :

- Isentropic coefficient :  $\gamma$
- Flow coefficient :  $C_D$
- Characteristic velocity :  $C^*$

$$\text{Where : } C_D = F(\gamma) \sqrt{\frac{R \cdot T_b}{\eta_l}} = \frac{1}{C^*}$$

with  $F(\gamma)$  : function of the isentropic coefficient  $\gamma$

R : perfect gaz constant

All these parameters mainly depend on the percentage of oxidizer and binder.

### VISCOSITY OF COMPOSITE SOLID PROPELLANT SLURRY

The viscosity of composite solid propellant slurry is an important parameter to the processability and castability behaviours. It is affected not only by the binder, but also by the size, content, shape and surface properties of solid fillers in propellant.

Brookfield viscosimeter is used to measure the slurry viscosity. First it was evaluated for process temperature specified for end-of-mix.

The viscosity of the selected propellant is less than 15 Kp at the end of mix, for 40°C temperature. These low viscosity is remained over a eight hour period.

Figures 1 and 2 shows these results.

The viscosity of propellant slurry is significantly affected by the end-of-mix temperature, the ratio of particle size and the ratio of content between coarse and fine particles.

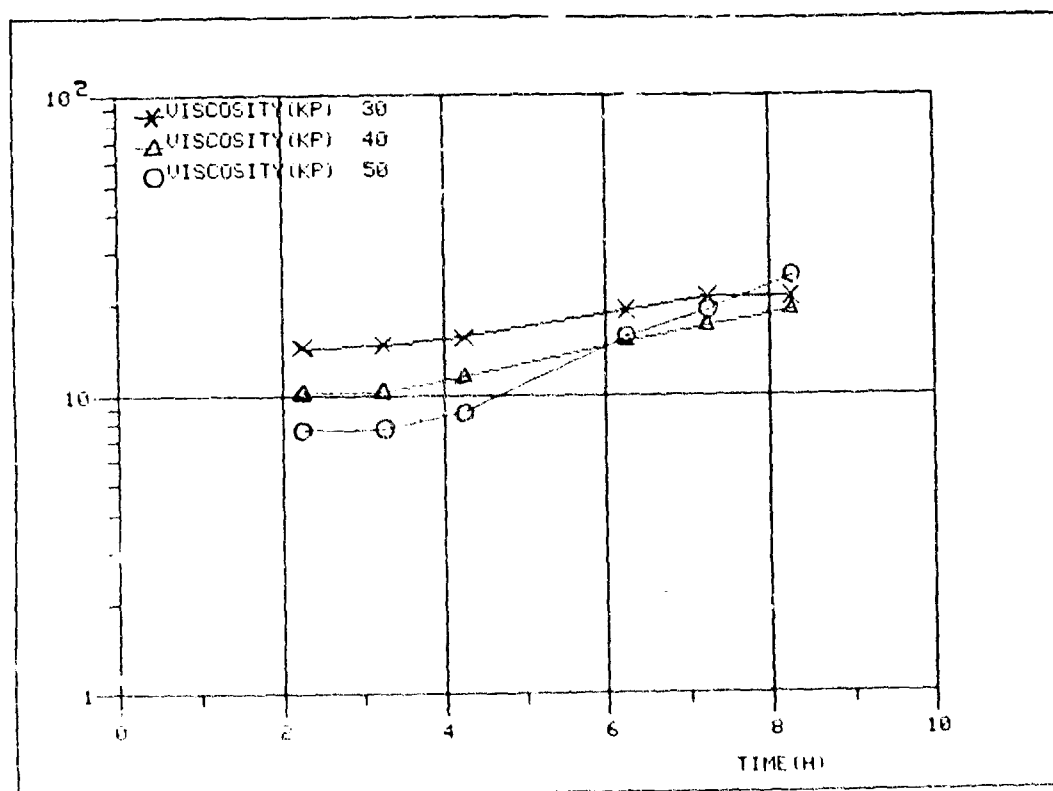


FIGURE 1 - Viscosity of the uncured propellant slurry versus time and different temperatures

$$A = 400 \text{ } \mu\text{m}$$

$$D = 100 \text{ } \mu\text{m}$$

$$F = 10 \text{ } \mu\text{m}$$

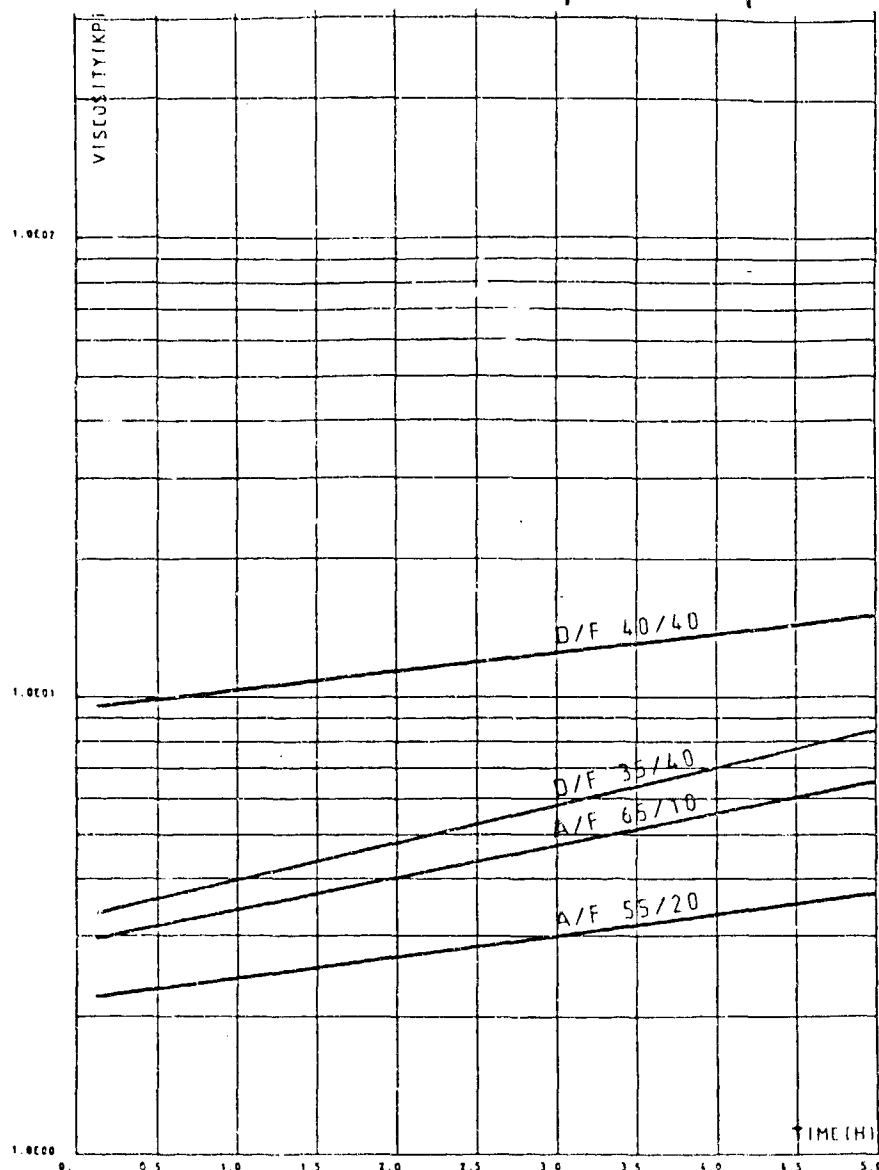


FIGURE 2 - Viscosity of propellant slurry for different filler ratio and AP distributions

## MECHANICAL PROPERTIES

Due to the high acceleration of the projectile longitudinal strains are developed in the bore of the grain. The propellant must therefore have a high flexibility and ultimate tensile strain limit.

Mechanical characteristics mainly depend on the binder but also on the particle size and on the adhesion between particles and binder.

They vary with temperature and stress rate or strain in such a way that a time temperature equivalence has been determined for each type of binder. A shift factor  $aT$  gives mechanical characteristics at every temperature  $T$  if they are known in standard conditions at  $20^{\circ}\text{C}$ . All mechanical properties (ultimate strength,  $S_m$ , elastic modulus,  $E$ , deformation at maximum strength,  $\epsilon_m$ ) are related to the number  $t/aT$  which takes into account the time of application of stress  $t$  and the shift factor  $aT$ .

The tensile tests are carried out with JANAF specimen and the properties defined according to Figure 3.

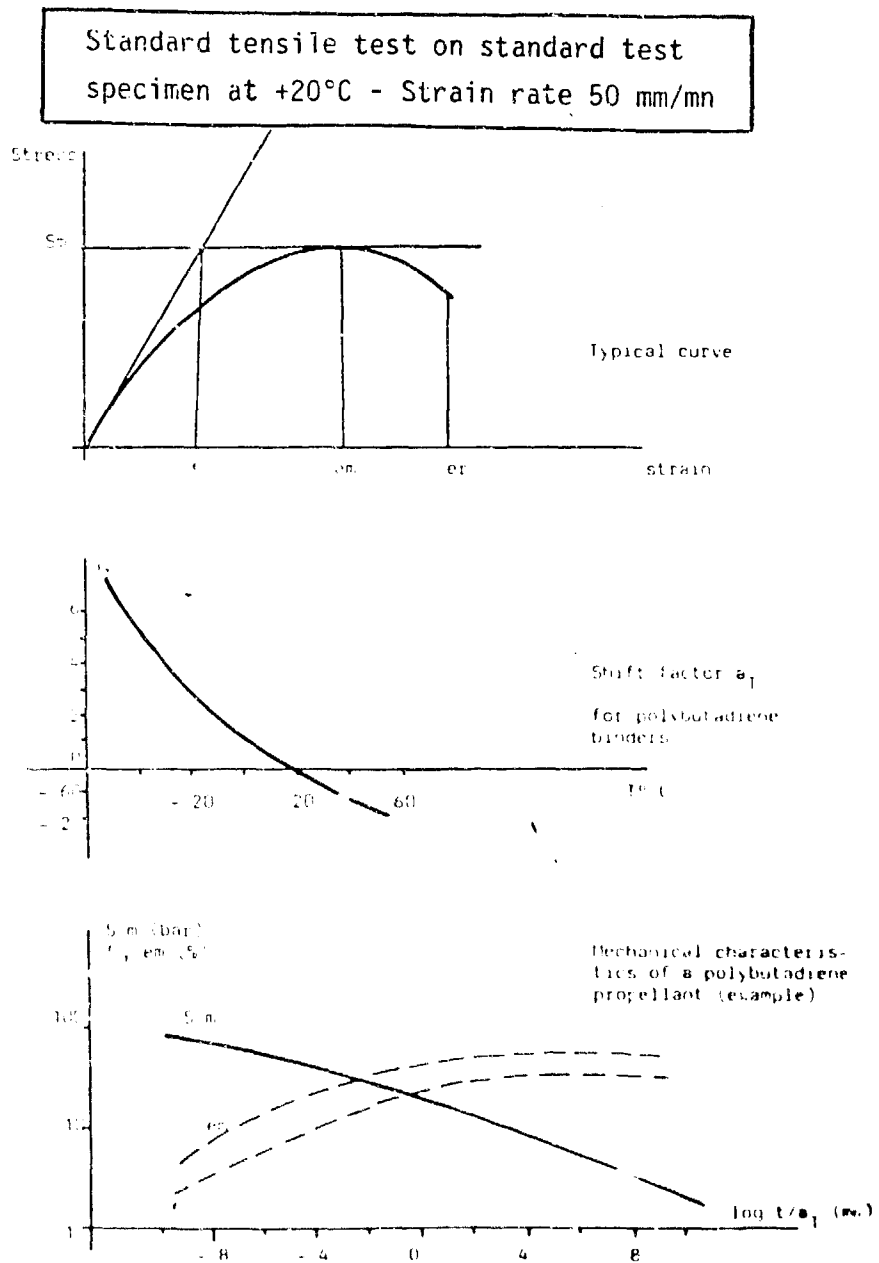


FIGURE 3 - Example for mechanical behaviour of propellant

## MECHANICAL CHARACTERISTICS OPTIMIZATION

The combination of HTPB/AP is a current composite propellant composition, giving high performance, long service life and low cost. The nature of the fuel-binder allows high concentration of solid filler and good anti-aging characteristics has greatly extended the solid rocket technology. Therefore, the addition of a bonding agent is essential to ensure the improved interaction at the binder-filler interface and to have best mechanical property behaviour.

HTPB binder is hydroxylated polymeric material and, as such, is curable using isocyanates. To reduce the moisture sensitivity of the curing reaction, isophorone diisocyanate (IPDI) was selected as the primary curing agent to be evaluated. To achieve sufficient mechanical properties of the propellant the curing ratio (NCO/OH) ranging from 0,85 : 1 up to 0,95 : 1 were evaluated.

Laboratory testing resulted in the selection of the effects of :

Binder variation, including bonding agents.

Curing agent and AP oxidizer distribution.

Burning rate catalyst.

A series of formulations having the required burning rate were developed, and selected for evaluation in intermediate-scale propellant mixes. All these parameters were varied to assure selection of the formulation with the highest possible strain capability and optimum processing characteristics.

Propellant from this effort have been successfully scaled up to the 300 Gallon mixer, and the effect of mixer size and process on propellant processing, mechanical properties and ballistic properties have been evaluated.

Some examples : optimization for some parameters. Effects of oxidizes particle size, curing ratio and bonding agent ratio. Tables 1, 2, 3.

We present also the mechanical properties versus temperatures and stress or strain rate on selected propellant. Table 4.

Characteristics	Curing ratio, NCO : OH			
	0,91	0,90	0,89	0,88
Maximum tensile strength : Sm (MPa) at + 20°	1,4	1,4	1,4	1,4
Elastic modulus : E (MPa)	4	4	3,3	1,6
Strain at maximum tensile (%) : em	40	20	80	140

TABLE 1 - Curing ratio effects on mechanical characteristics

Characteristics	Oxidizer loading (%)					
	70	75			80	
Particule size distribution	D:30 F:40	D:35 F:40	A:65 F:10	A:55 F:20	b:53 F:27	D:40 F:40
Curing ratio (NCO : OH)	0,90	0,90	0,90	0,95	0,94	0,85
Maximum tensile strength : Sm (MPa)	1,4	2	1,1	1	1,4	1,8
Elastic modulus : E (MPa)	4	8	8	8	11	7
Strain at maximum tensile (%) : em	90	50	50	24	31	42

**TABLE 2 - Oxidizer loading and particule size distribution on mechanical characteristics**

Characteristics	Bonding agent ratio (%)			
	0,5	0,3	0,1	0
Maximale tensile strength : Sm (MPa) at + 20°C	2	1,6	1,4	1,2
Elastic modulus : E (MPa)	8	7	8	8
Strain at maximum tensile (%) : em	50	47	36	32

**TABLE 3 - Bonding agent ratio on mechanical characteristics**

Temp. (°C)	R (mm/mn)	Sm (MP <sub>a</sub> )	Eps (%)	E.tg (MP <sub>a</sub> )	em (%)	er (%)
- 60	1	6,46	8,3	77,76	16,9	20,3
- 60	50	8,30	6,2	133,71	11,8	12,3
- 60	500	9,77	4,0	243,76	8,0	8,7
+ 20	1	1,40	30,3	4,64	38,1	38,9
+ 20	50	1,93	31,6	6,10	52,2	56,2
+ 20	500	2,36	28,9	8,16	56,5	66,8
+ 40	1	1,07	29,8	3,59	39,2	40,0
+ 40	50	1,51	32,7	4,62	52,1	55,2
+ 40	500	1,84	30,9	5,97	54,5	66,2

**TABLE 4 - Mechanical characteristics versus temperatures and strain rate for a selected propellant**

### BALLISTIC PROPERTIES

Ballistic properties are defined by the burning rate of the propellant which depend mainly on the particles ratio and sizes and on the quantity of ballistic additives (accelerators).

Besides, the burning rate is also proportionnal to the initial temperature of the propellant.



The equation of the burning rate is :

$$V_b = ap^n$$

Where  $a$  and  $n$  are the characteristics of the propellant.

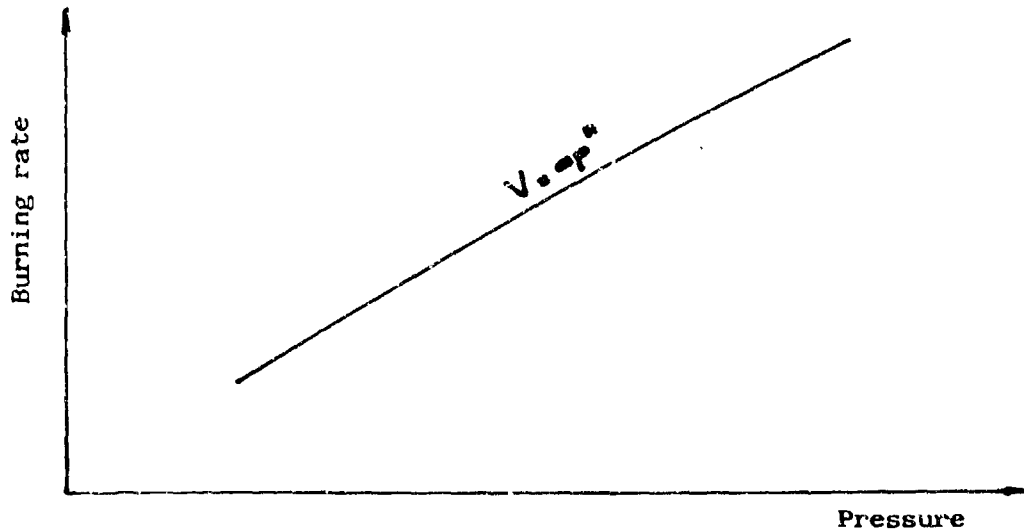


FIGURE 4 - Burning rate versus pressure

The burning rate of the propellant, in our case, is measured by the "Strand Burner" method, in nitrogen, and in a large range of atmospheric and subatmospheric pressures.

At the ambient temperature, the range of the burning rate must be

$$0,9 < V_c < 1,5 \text{ (mm/s)}$$

This range is optimized for different propellant grain dimensions.

The experimental propellant, in atmospheric pressure and  $T^\circ = 20^\circ\text{C}$ , is selected for  $V_c = 1,22 \text{ mm/s}$ .

Figure 5 shows experimental results burning rate versus pressure.

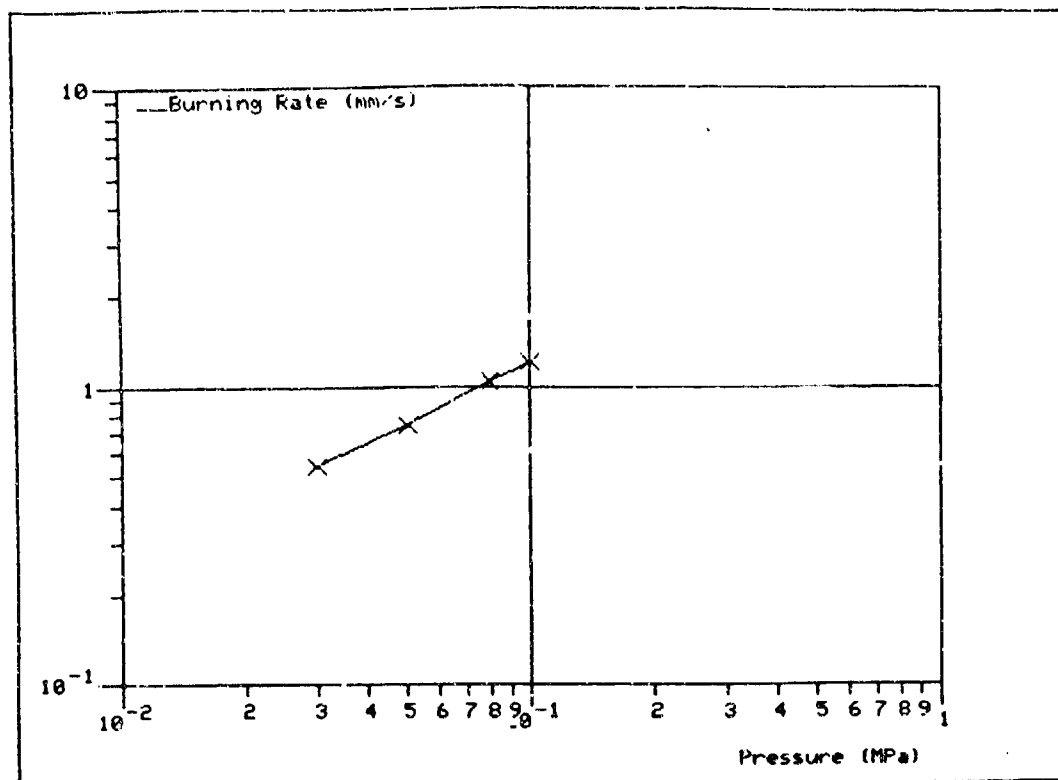


FIGURE 5 - Burning rate versus pressure

#### BURNING RATE OPTIMIZATION

In general, the binder has a relatively small influence on the burning rate.

The burning rate is governed more particularly by the ammonium perchlorate (AP) oxidizer.

The investigations on the oxidizer are :

- oxidizer ratio (Filler ratio)
- particle size distribution
- particle size diameter ( $\phi_m$ )

Some additives govern also the burning rate :

- Ballistic catalyst
- Carbon Black

If the ballistic catalyst is a burning rate adjuster, the carbon black is an opacifier, which decreases reflectivity and increase radiative absorption at propellant surface. He cannot be recognized to be an active catalyst particularly at subatmospheric pressures.

. Effect of the filler ratio

Filler ratio is chosen, essentially, on the base of the thermodynamical calculations. To obtain the required burning rate it is necessary to optimize the other parameters.

Particle size distribution

Ballistic catalyst ratio

Table 5 shows the results for constant burning rate.

Characteristics	Filler ratio (%)					
	70	75		80		
Particule size distribution	D:30 F:40	D:35 F:40	A:65 F:10	A:55 F:20	b:53 F:27	D:40 F:40
Burning rate (mm/s)	1,25	1,26	1,22	1,27	1,25	1,22
Ballistic catalyst ratio (%)	0,75	0,2	4	2,5	0,5	0

TABLE 5 - Effects of filler ratio, particle size distribution and ballistic catalyst ratio at constant burning rate

. Effect of particle size distribution

Particle size distribution is optimized for give the required burning rate, in first, but also for a good processability. For a constant burning rate if it is directly dependant of the average particle size, it is also in relation with ballistic catalyst ratio. See results table 5.

. Effects of ballistic catalyst ratio versus particle size distribution

Particle size distribution used in this propellant is a bimodal blend using 10 and 90  $\mu$  or 10 and 200  $\mu$ .

The results are shown on figure 6.

For the required burning rate, all these parameter were correiated and used to determine along the constant burn line the best distribution which gives the minimum mix viscosity and longer pot life for better casting of the grain.

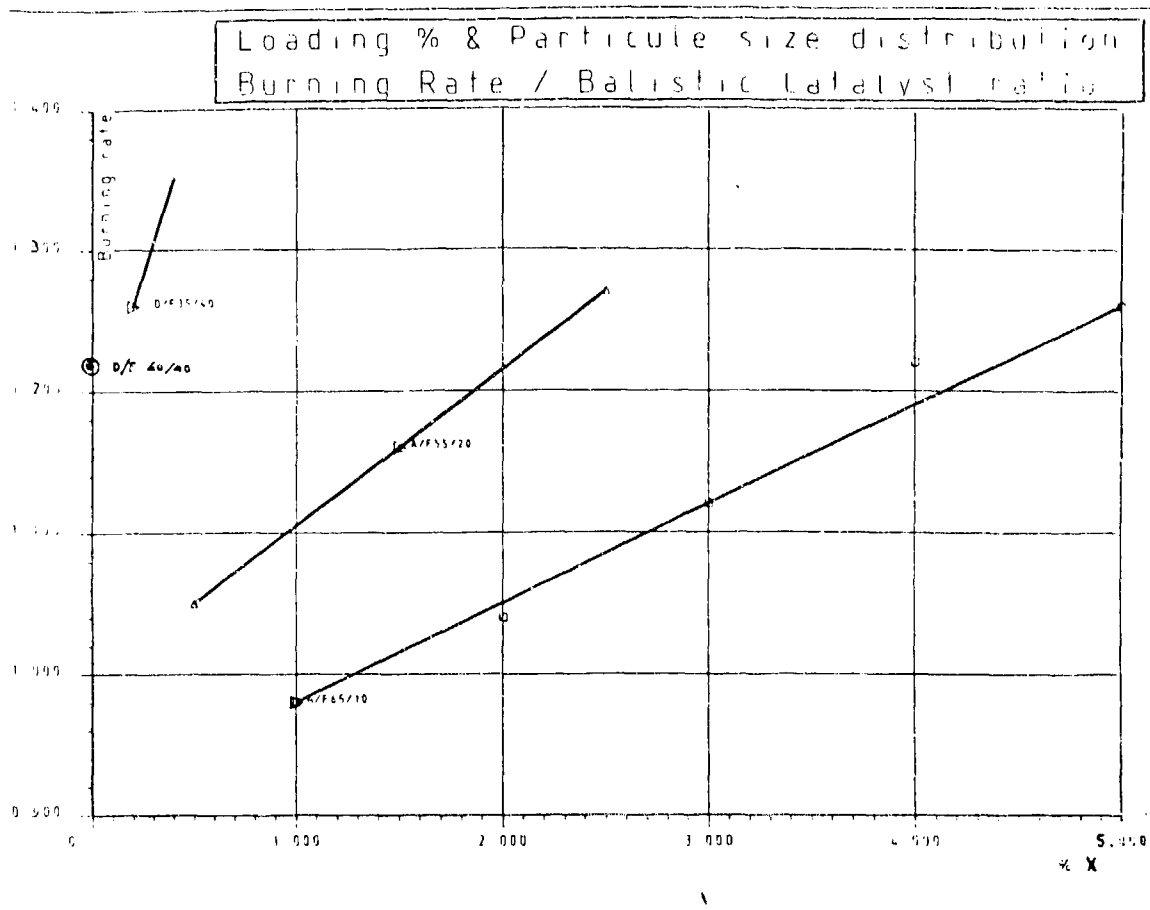


**FIGURE 6 - Effects of particle size distribution and ballistic catalyst ratio on burning rate**

### HAZARDS AND SAFETY

The identification and evaluation of hazards and pyrotechnic effects in manufacturing solid propellants are necessary.

Consideration of the ignition consequences suggests modifications of process conditions or plant instruction to minimize risk to personnel, facilities, and product. Attempts to estimate the probable hazards of handling a new propellant were based on correlation of available test data with that of materials which had been processed successfully.

The results of different tests made on the optimized propellant are shown in table 6.

. Autoignition temperature	278°C
. Impact sensitivity (High energy Shock)	> 4 meters
. Impact sensitivity (Julius Peters Appartus)	11 Joules
. Friction sensitivity	203 Newton
. Regression Speed (burning rate) at Patm	< 1,6 mm/s
. Detonability	< 1 card
. Electrostatic sensitivity	No sensitive

#### . Process and processability

The composite solid propellant manufacturing system is shown in table 7. It is a typical block flow diagram. Noting that processability is an important factor in propellant formulation which processability determination is a function of the rheology of the propellant.

The different steps in propellant processing are binder preparation, oxidizes preparation, propellant mixing, casting and curing. Processing differences between size mixes are a source of propellant variation. Frequently a new mixing cycle is optimized for each size mixer or type (Sigma or Vertical). After optimization of the required specifications propellant, for one mixing cycle adapted to one size mixer, the propellant processing parameters are selected.

In our application and with different size industrial mixes since 5. Gallons to 300 Gallons we have developed and demonstrated the feasibility of an HTPB propellant for Base-Bleed applications, and with a low cost owing to the fact that we obtain many thousand grains by batch.

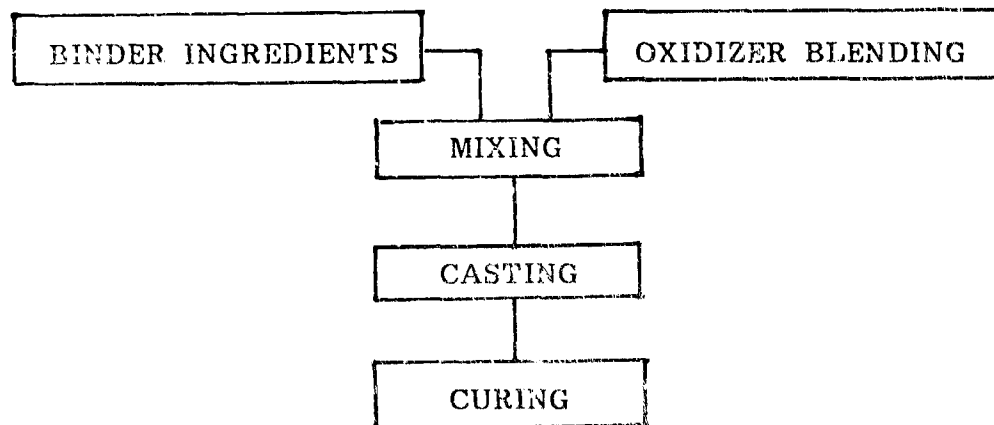


TABLE 7 - Composite solid propellant processing

#### CONCLUSION

Based on the initial formulations and the success of their foregoing evaluations a large-scale mix was prepared from horizontal mixer for 1000 kgs and Vertical "DAY" mixer for 2400 kgs.

From these initial formulations, additional modifications were introduced to evaluate process and processability of the propellant. Rheological properties, burning rate range capability and mechanical properties improvement were evaluated.

High volume manufacturing have been conducted to provide reproducible process required for the production of large quantities of base-bleed composite grain at low cost.

## REFERENCE

- [1] Computer program for calculation of complex chemical equilibrium composition - rocket performance - incident and reflecting shocks and CHAPMAN JOUGET detonation  
S. Gordon, B.G Mac Bride  
NASA Lewis research center (1971)

# COMPUTER CODES FOR BALLISTIC PERFORMANCE CALCULATIONS OF BASE BLEED PROPELLANT GRAIN

FABIGNON Yves

S.N.P.E C.R.B

91710 Vert le Petit

COUPEZ Dominique

S.N.P.E St Médard

33160 St Médard en Jalles

## ABSTRACT

Concerning shell external ballistics, different technical solutions are studied in order to improve aerodynamic performance of a shell. The solution named base bleed consists in injecting a hot gas at a low velocity into the depressional flow area.

Preliminary design of a base bleed propellant grain has to satisfy requirements generally expressed as a shell range increase regarding available grain volume. In order to adapt the propellant grain ballistic performance to the shell trajectory conditions, two different investigations have been developed. The first investigation is essentially theoretical and consists in computer simulations of the flowfield near the shell base with and without effect of subsonic injection.

The second investigation is more empirical and consists in analysing the shell velocity evolution by means of radar measurements in order to determine drag reduction factor due to the base bleed effect. The organization of the developed ballistic computer codes and some results are described in this paper. The results of the two studies give ballistic data necessary for simulations of base bleed shell trajectories.

## NOMENCLATURE

Theoretical approach :

$C_D, C_1, C_2$	: turbulence model parameters
$C$	: specific heat at constant pressure
$D^p$	: diameter of projectile
$D_b$	: diameter of exhaust port
$f^b$	: mixing ratio
$H$	: total enthalpy
$k$	: turbulent energy
$M_\infty$	: projectile Mach Number
$M_K$	: molar mass of specie K
$p_K$	: base pressure
$p_c$	: local pressure
$p_\infty$	: ambient pressure
$Q_b$	: mass flow rate

$R$	: constant of perfect gases
$S_\phi$	: source term
$T$	: temperature of gas
$T_b$	: stagnation temperature of base bleed gas
$u, v$	: cartesian velocity components
$x, r$	: cylindrical coordinates
$x_K$	: molar concentration of specie K
$Y^K$	: altitude
$Y_K$	: mass fraction of specie K
$\epsilon_K$	: dissipation rate
$\rho$	: density of gas
$\phi$	: dependent variable
$\Gamma_\phi$	: turbulent exchange coefficient
$\mu_t$	: eddy viscosity
$\mu_l$	: laminar viscosity
$\sigma_k, \sigma_\epsilon$	: turbulent Prandtl number
Empirical approach :	
$C_D$	: total drag coefficient
$C_{DTOT}$	: total drag coefficient without base bleed effect
$C_{DBASE}$	: base drag coefficient without base bleed effect
$C_{RED}$	: base drag reduction factor
$g$	: acceleration of gravity
$I$	: injection parameter
$m$	: projectile mass
$M$	: mach number of projectile
$r_b$	: burning rate
$S_b$	: propellant burning area
$S_{REF}, S_{BASE}$	: reference area and base area of projectile
$V$	: projectile velocity
$x, y$	: range, altitude
$\rho_\infty$	: air density
$\rho_p$	: propellant density
$\theta$	: trajectory angle

## 1 . INTRODUCTION

When a shell manufacturer designs a new projectile with a base bleed device, the requirements are expressed as a shell range increase according with the available grain volume. The first step in the preliminary design of a base bleed grain is to derive propellant grain configuration from shell performance. The designer has first to select a grain internal shape and a propellant. Figure 1. shows general architecture of a new base bleed grain analysis.



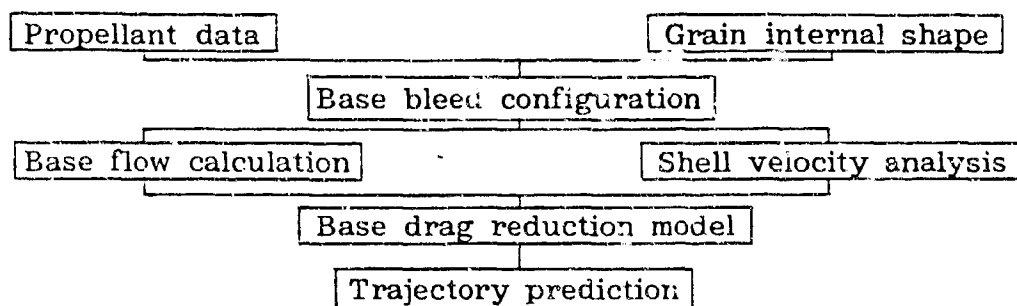


FIGURE 1. Main flow chart

This paper presents the work performed in our company on different methods to establish and to complete a base drag reduction model.

The theoretical approach starts with calculation of propellant thermochemical properties [1]. These calculated data are input data to simulate afterwards base flows with base bleed effect.

The computer code used to simulate base flow solves Navier-Stokes equations in cylindrical coordinates including a  $(k-\epsilon)$  turbulence model. A combustion model has also been developed in order to analyse the effect of propellant gas afterburning in ambient air. To simulate operating conditions of a base bleed gas generator, calculations are performed with and without a reactive injected flow. Results show the effect of propellant gas on the shell base pressure and the dead air area location. This approach is described in more details in the chapter 2.

The empirical approach is based on gun firing test results and consists in analysing the shell velocity evolution during base bleed operating time. The computer code uses a simple external ballistic model. After some gun firing tests, radar velocity measurements are performed in order to evaluate total aerodynamic drag coefficient with and without base bleed effect. Results allow to determine base bleed grain efficiency according with a shell configuration. This approach is described in the chapter 3.

Computed results of these two investigations are used to compare ballistic performances of different base bleed configurations.

Further objective of this project is to establish a base bleed system data base by means of results obtained with these computer codes.

## 2 . THEORETICAL APPROACH OF THE PROJECTILE BASE FLOW

The complexity of base pressure calculation for an axisymmetric body even without stabilizing fins or spinning is well known.

In the case of a projectile with base injection of chemically reactive gas, afterburning leads to additional problems. The objective of the present work is to compute the steady reactive flow behind the rear projectile (Figure 2). To solve this problem, a numerical integration of Navier Stokes equations has been used. In fact, this computer code initially developed to simulate Rocket Motor Plumes has been modified to introduce projectile base flow concept.

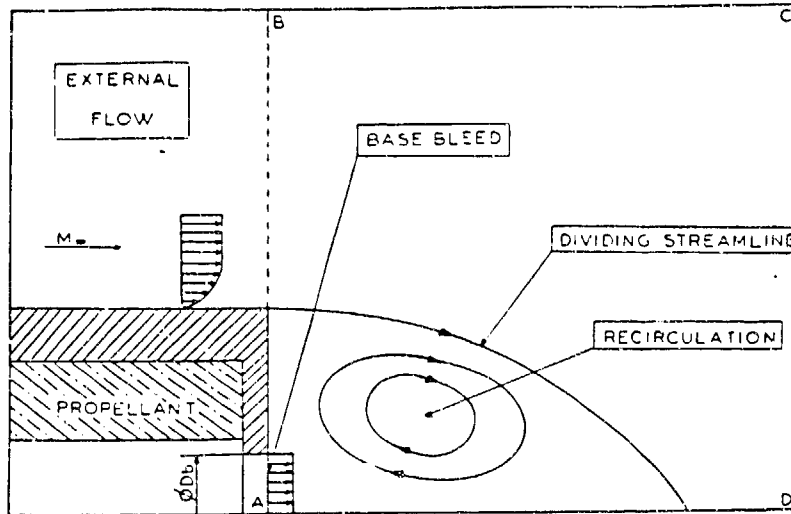


FIGURE 2 . Schematic of base area flowfield.

## 2.1. Governing equations

The original Navier Stokes equations are averaged and completed by a  $(k-\epsilon)$  turbulence model and a simplified combustion model. For a two dimensional, axisymmetric, steady, turbulent flow the governing equations may be written in the general form :

$$\frac{\partial \rho u \phi}{\partial x} + \frac{1}{r} \frac{\partial}{\partial r} (\rho r v \phi) - \frac{1}{r} \left[ \frac{\partial}{\partial r} (\Gamma \phi \cdot r \frac{\partial \phi}{\partial r}) + \frac{\partial}{\partial x} (\Gamma \phi \cdot r \frac{\partial \phi}{\partial x}) \right] = S \phi \quad (1)$$

Where  $\phi$  represents the dependent variable,  $\Gamma \phi$  is the appropriate effective exchange coefficient for turbulent flow and  $S \phi$  is the corresponding source term. The definitions of  $\Gamma \phi$  and  $S \phi$  for the different dependent variables ( $\phi$ ) are listed in table 1.

The local pressure is determined using the equation of state :

$$p = \rho R T \sum_{k=1}^{k=7} \frac{Y_k}{M_k} \quad (2)$$

Where  $R$  is perfect gas constant and  $Y_K$  the mass fraction of specie  $K$  and  $M_K$  its molar mass.

The relation between enthalpy ( $H$ ) and temperature ( $T$ ) is given by

$$H - \frac{1}{2} (u^2 + v^2) - k = h^* + \int_{T^*}^T C_p \cdot dT \quad (3)$$

$C_p$ ,  $h^*$  and  $\int_{T^*}^T C_p \cdot dT$  are given by tables from Ref. [2].

The gas contains seven species ( $CO$ ,  $CO_2$ ,  $H_2$ ,  $H_2O$ ,  $HCL$ ,  $N_2$ ,  $O_2$ ) and the combustion model is based on the following reaction :



Conserved property	$\Phi$	$\Gamma_\Phi$	$S_\Phi$
Mass	1	0	0
x momentum	u	$\mu_t$	$-\frac{\delta p}{\delta x} + \frac{\delta}{\delta x} \left( \mu_t \frac{\delta u}{\delta x} \right) + \frac{1}{r} \frac{\delta}{\delta r} \left( \mu_t \cdot r \cdot \frac{\delta v}{\delta x} \right)$
r momentum	v	$\mu_t$	$-\frac{\delta p}{\delta r} + \frac{\delta}{\delta x} \left( \mu_t \frac{\delta u}{\delta r} \right) + \frac{1}{r} \frac{\delta}{\delta r} \left( \mu_t r \frac{\delta v}{\delta r} \right) - \frac{2\mu_t}{r}$
total enthalpy	H	$\frac{\mu_t}{\tau_H}$	0
turbulent energy	k	$\frac{\mu_t}{\tau_k}$	$\mu_t G - \rho \epsilon$
dissipation rate	$\epsilon$	$\frac{\mu_t}{\tau_\epsilon}$	$(C_1 \mu_t G - C_2 \rho \epsilon) \frac{\epsilon}{k}$

$G = 2 \left[ \left( \frac{\delta u}{\delta x} \right)^2 + \left( \frac{\delta v}{\delta r} \right)^2 \right] + \left( \frac{\delta u}{\delta r} + \frac{\delta v}{\delta x} \right)^2 + \frac{2v^2}{r}$			
$\mu_t = \mu_e + \rho \frac{C_D k^2}{\epsilon}$			
$C_D = 0,09$	$C_1 = 1,14$	$C_2 = 1,12$	$\tau_H = 1 \quad \tau_k = 1 \quad \tau_\epsilon = 1,3$

TABLE 1 - Definition of terms

The atomic conservation equations and two linear relations between a passive scalar  $f$  and the mass fraction  $Y_{O_2}$  and  $Y_{CO} + Y_{H_2}$  provide the gas composition  $f$  can be defined as the "mixing ratio" and it is convenient [3] to assume the values zero and unity as boundary conditions.  $f$  is given by :

$$F = \frac{H - H_{\infty}}{H_b - H_{\infty}} \quad (5)$$

Where the subscripts  $\infty$  denote values in the external flow and  $b$  the flow through exhaust port.

## 2.2. Solution procedure

A numerical code is used to solve the elliptic partial differential system of equations given by (1) and table (1) with the appropriate boundary conditions.

This code uses a numerical scheme due to Patankar [4] with a modification to include gas compressibility effects. In the numerical code, the flow area ABCD (Figure 2) is divided in a rectangular grid.

## 2.3. Predictions

Different data are necessary to calculate the flowfield :

- Two geometrical parameters, the diameter of the projectile ( $D$ ) and the diameter of the exhaust port ( $D_b$ ) (Figure 2).
- The altitude ( $Y$ ) and the Mach Number ( $M_{\infty}$ ) of the projectile.
- Gas composition ( $CO$ ,  $CO_2$ ,  $H_2$ ,  $H_2O$ ,  $HCL$ ,  $N_2$ ), mass flow rate ( $Q_b$ ) and stagnation temperature ( $T_b$ ).

A series of computations have been carried out for 105 mm projectile at Mach Number 1,66 and 1,28 for altitude  $Y = 1210$  m and  $Y = 3000$  m, respectively. The calculations simulate operating conditions of an experimental base bleed gas generator. The injection of mass flow is provided by the combustion of composite propellant, and a chemical equilibrium calculation near the ambient pressure gives stagnation temperature (flame temperature) and combustion product composition.

For the present case the results are :

$$T_b = 2290 \text{ K}$$

$$x(CO) = 0,248 \quad x(CO_2) = 0,0534 \quad x(H_2) = 0,217$$

$$x(H_2O) = 0,256 \quad x(HCL) = 0,147 \quad x(N_2) = 0,075 \quad (\text{molar concentration for one mol of gas})$$

To estimate the base bleed effect, we have computed the base pressure ( $p_c$ ) with the following assumption :

$$p_c = \frac{1}{S} \int_0^R 2\pi r p \cdot dr \quad (6)$$

Where  $p$  is the pressure given by predictions near the projectile,  $S$  its section.

First calculation has been performed without injection for  $M_\infty = 1,28$  and  $M = 1,66$ . In this case, Figure 3 shows the stream function contours and Figure 4 the pressure function contours in  $MP_a$ . The results are presented in an adimensionalized coordinate system ( $X/D$ ,  $Y/D$ ).

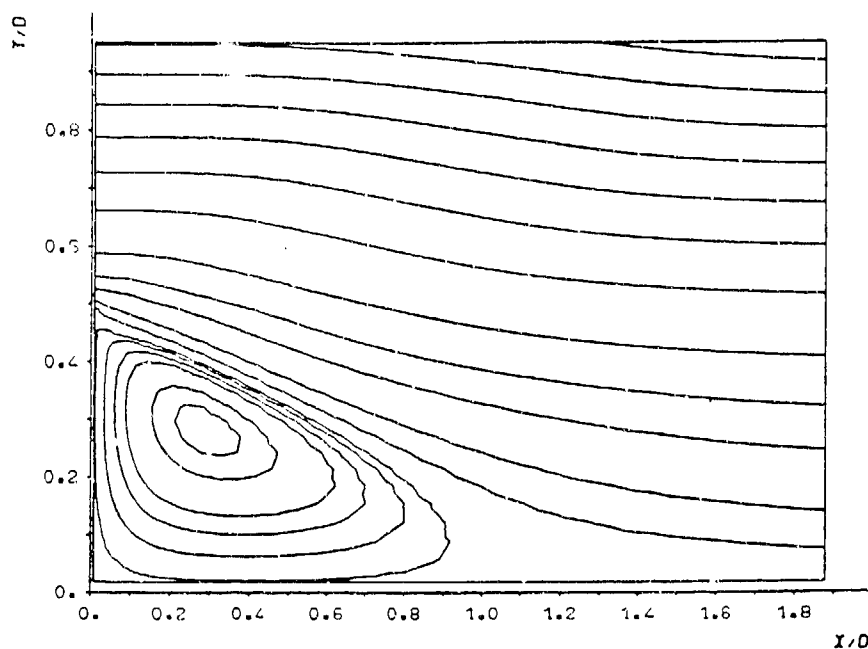


FIGURE 3 - Stream function contours without injection. Mach = 1,66

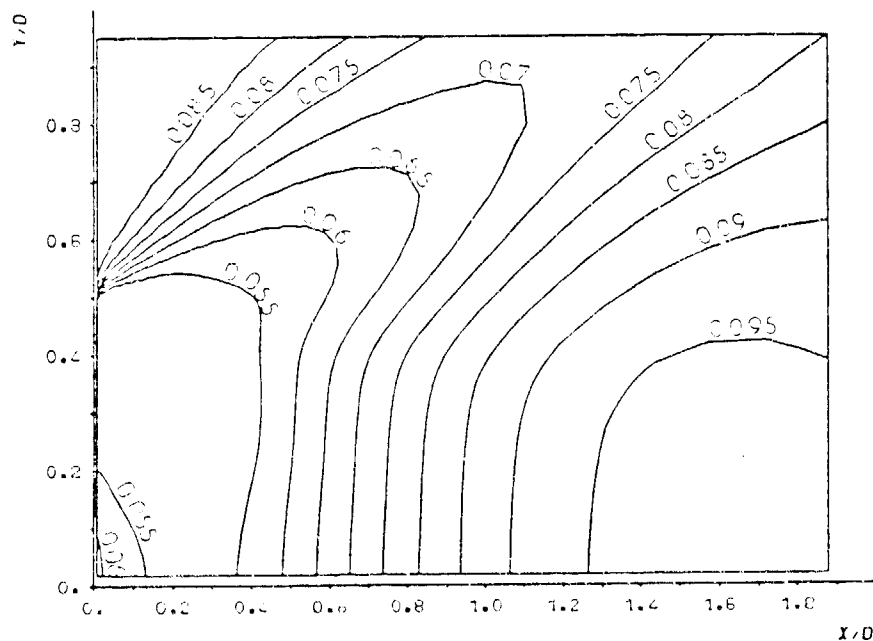


FIGURE 4 - Pressure function contours without injection. Mach = 1,66

Now, an injection is specified ( $D_b = 30$  mm) with  $Q_b = 18,5$  g/s for  $M_\infty = 1,28$  and  $Q_b = 25,8$  g/s for  $M_\infty = 1,66$ . To examine the afterburning effect on the base pressure, we have considered at first an inert flow (without reaction (4)) and then a reactive flow. For the case  $M_\infty = 1,66$



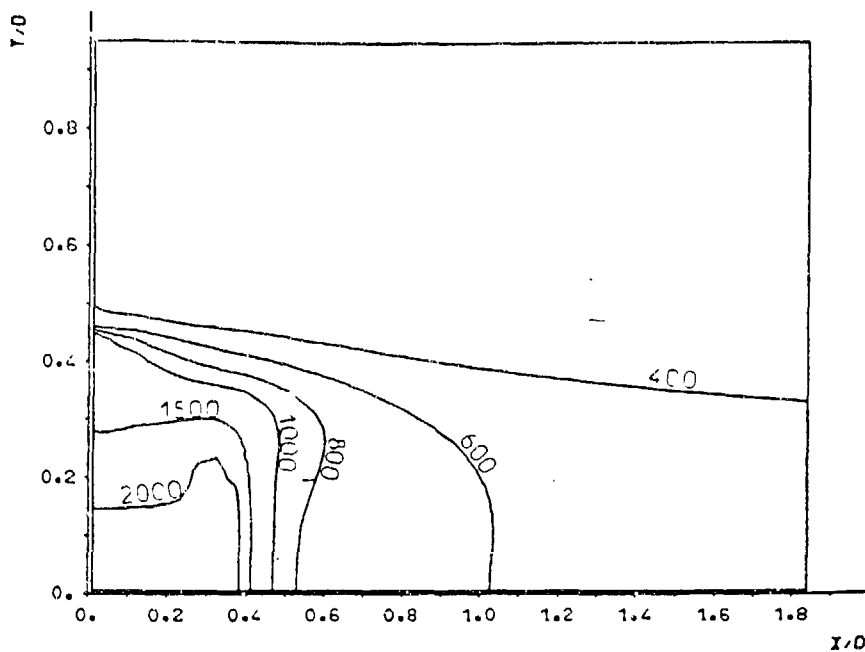


FIGURE 7 - Temperature function contours with inert flow  
Mach = 1,66  $Q_b = 25,8 \text{ g/s}$

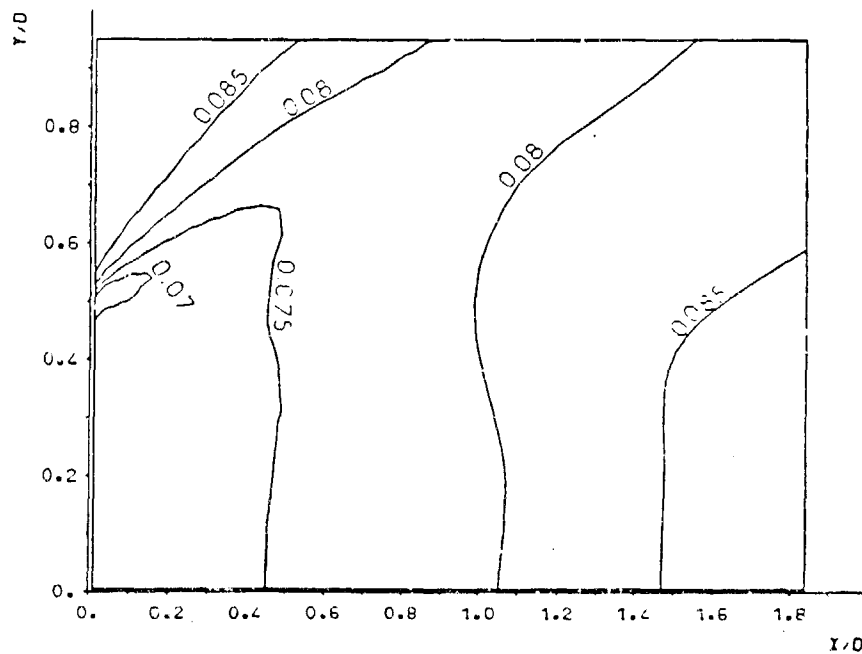


FIGURE 8 - Pressure function contours with reactive flow  
Mach = 1,66  $Q_b = 25,8 \text{ g/s}$

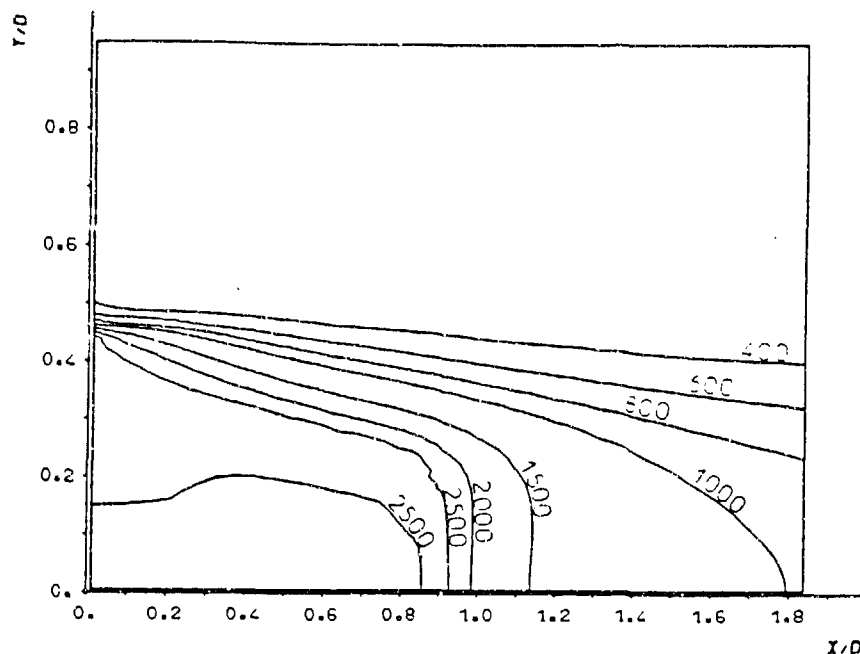


FIGURE 9 - Temperature function contours with reactive flow  
Mach = 1,66  $Q_b = 25,8 \text{ g/s}$

Table 2 gives the pressure ratio ( $p_c/p_\infty$ ) for the different cases studied with this computer code

	Without injection $Q_b = 0$	With injection	
		inert fluid	reactive fluid
$M_\infty = 1,28$ $Y = 3000 \text{ m}$ $Q_b = 18,5 \text{ g/s}$	0,68	0,77	0,85
$M_\infty = 1,66$ $Y = 1210 \text{ m}$ $Q_b = 25,8 \text{ g/s}$	0,57	0,69	0,80

TABLE 2 - Pressure ratio ( $p_c/p_\infty$ ) for different calculated cases.

### 3 . EXPERIMENTAL INVESTIGATION : GUN FIRING TEST ANALYSIS

#### 3.1. Description of the method

The method used for the gun firing test analysis is divided in two main steps.

Step 1. We determine total drag coefficient vs Mach Number from projectile velocity on its trajectory.



Step 2. Comparing total drag coefficient with and without base bleed effect enables to calculate base bleed reduction efficiency. For each total drag coefficient calculation the block diagram of modules is the same as the one presented in Figure 10.

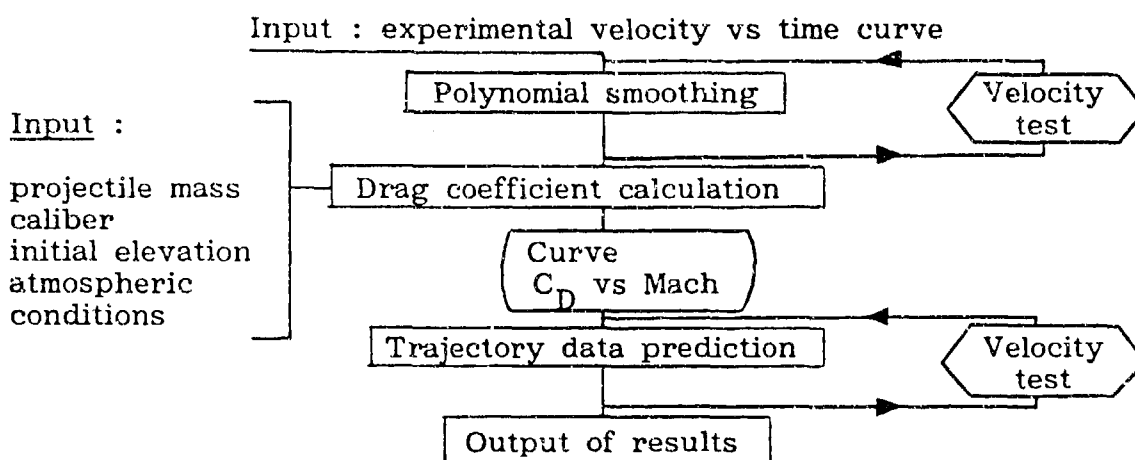


FIGURE 10 - Block diagram of modules

The function of each module is briefly described.

Polynomial smoothing module : Experimental velocity curve is smoothed by means of polynomial functions. At each time step in the curve, we calculate smoothed velocity and its derivative versus time (t). Changing the degree of polynomial functions allows to respect a given criterion between calculated velocity and experimental velocity.

Module of total drag coefficient calculation : total drag coefficient may be calculated from the equations of an external ballistic model. The projectile motion is confined to the XY-plane and is given by the equations of motion :

$$\text{Drag equation } m\dot{V} = -mg\sin\theta - \frac{1}{2}\rho_{\infty}\cdot S_{REF}\cdot V^2\cdot C_D(M) \quad (7)$$

$$\text{Lift equation } mV\dot{\theta} = -mg\cos\theta \quad (8)$$

Kinematical relations and an equation of projectile mass balance for base bleed configuration complete this model.

$$\dot{x} = V \cos\theta \quad (9)$$

$$\dot{y} = V \sin\theta \quad (10)$$

$$\dot{m} = \rho_p \cdot S_B \cdot r_b \quad (11)$$

Initial conditions are given by gun firing test conditions (elevation and muzzle velocity measurements).

The calculation procedure is as follows. Equations (8) (9) and (10) are solved using a Runge-Kutta scheme and determine x,y and  $\theta$  variables. These data and polynomial smoothing results are used to compute total drag coefficient vs Mach Number using equation (7). Note that the projectile mass with a base bleed gas generator is estimated by means of propellant mass flow calculation (11).

Module of trajectory data calculation : then the calculated total drag coefficient curve is an input data. Equations (7) (8) (9) and (10) are solved using a Runge-Kutta scheme and give V,x,y and  $\theta$  variables. By an iterative procedure we adapt total drag coefficient in order to respect a given criterion between predicted and observed velocity.

The comparison of total drag coefficient with and without base bleed effect is based on the Swedish approach of Ref. [5]. The drag coefficient of the projectile during base bleed operating time is :

$$C_D = C_{DTOT} - C_{RED} \times C_{DBASE}$$

Where  $C_D$  = total drag coefficient with base bleed effect.  
 $C_{DTOT}$  = total drag coefficient without base bleed effect.  
 $C_{RED}$  = base drag reduction factor.  
 $C_{DBASE}$  = base drag coefficient without base bleed effect.

$C_{RED}$  is considered as a polynomial function of Mach Number and of an injection parameter I defined as the ratio of the propellant mass flow through exhaust port to the mass flow of air through the section of the shell base.

Then, base pressure (pc) may be calculated from the expression given by Ref. [5].

$$p_c = p_\infty \left[ 1 - \frac{(1 - C_{RED}) C_{DBASE}}{S_{BASE}/S_{REF}} \cdot 0,7 \cdot M^2 \right]$$

Where p = free stream pressure

$S_{REF}$ ,  $S_{BASE}$  = reference area and base area of the projectile

$C_{RED}$ ,  $C_{DBASE}$ , M = ballistic data from the range calculation

### 3.2. Some examples

These results are proposed to illustrate code capabilities.

Table 3 shows an example of velocity comparison for a 155 mm projectile.

Time of flight (s)	Experimental velocity	Smoothed velocity	Calculated $C_D$ (M)	Predicted velocity (m/s)
0	783.1	783.0	0.241 (2.30)	783.1
5	610.2	610.2	0.274 (1.82)	609.3
10	499.3	499.4	0.290 (1.51)	493.2
15	423.1	423.2	0.311 (1.29)	421.7

TABLE 3 - Velocity comparison

Figure 11 and Figure 12 show experimental velocity and calculated total drag coefficient for a 105 mm projectile with and without base bleed effect.

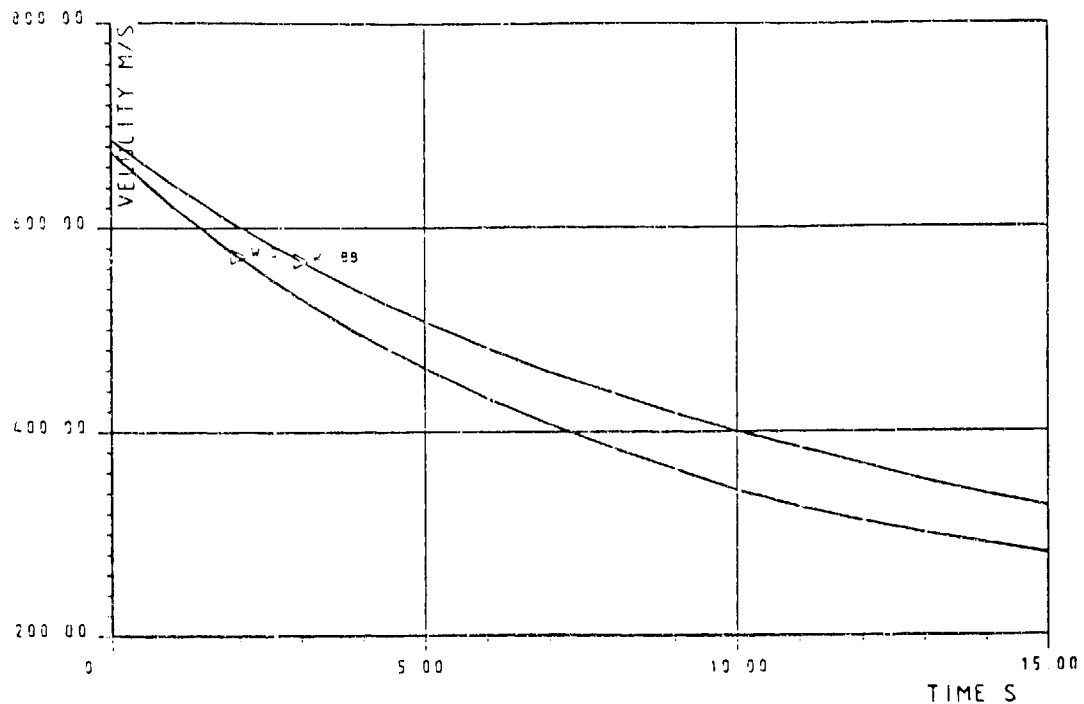


FIGURE 11 - Experimental velocity versus time

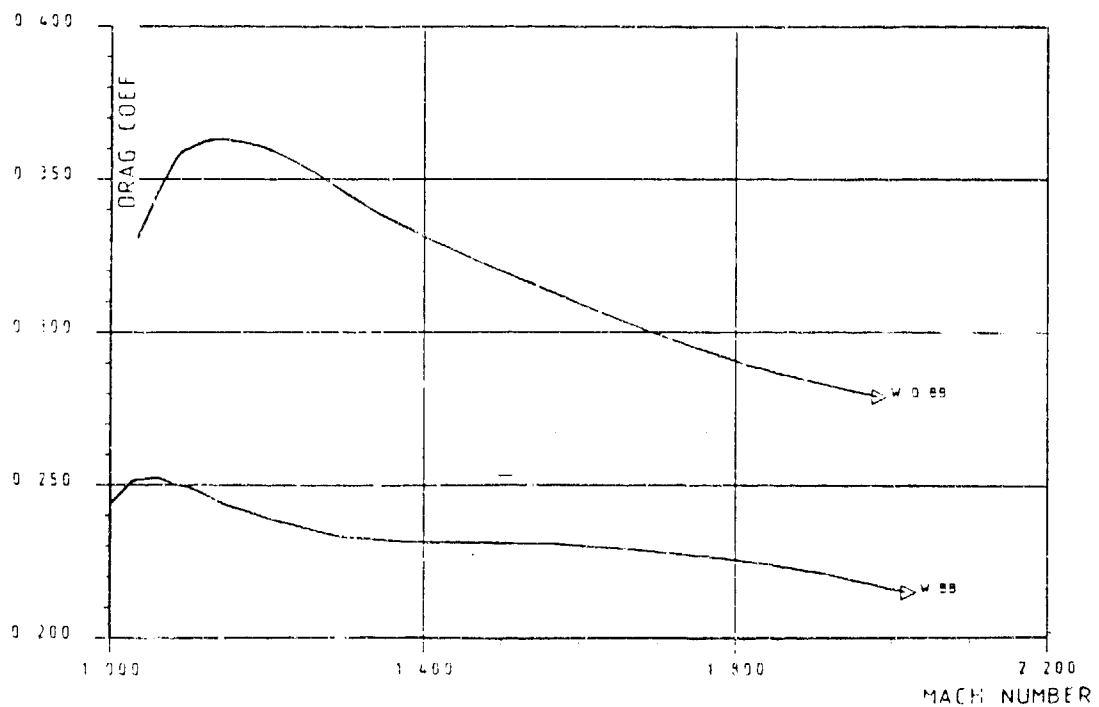


FIGURE 12 - Calculated total drag coefficient versus Mach Number

Figure 13 shows pressure ratio ( $p_c/p_\infty$ ) and base drag reduction factor ( $C_{RED}$ ) as a function of injection parameter (I) and Mach Number (M). The method to determine ( $C_{RED}$ ) is to suppose that base drag coefficient without base bleed effect ( $C_{DBASE}$ ) is 40 % of ( $C_{DTOT}$ ).

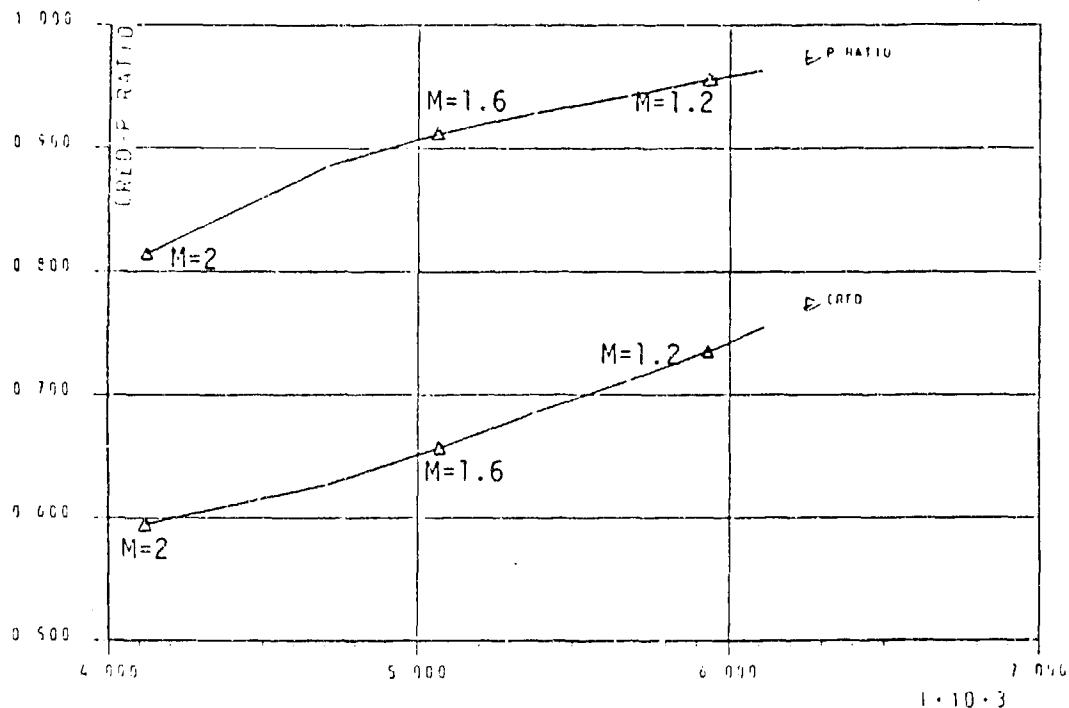


FIGURE 13 - Pressure ratio and base drag reduction factor versus injection parameter and Mach Number

#### 4 . CONCLUSION

Different computer codes have been developed in order to study effectiveness of base bleed systems. An intensive use of these programs will allow to quickly perform preliminary design of base bleed grains. Calculations are computed now to analyse tendencies or to compare results of different base bleed configurations by acting on injected mass flow rate, propellant gas composition. Pressure ratio results ( $p_c/p_\infty$ ) show a good concordance between the two presented methods.

Further studies will consist in improving conditions of simulation.

1 - Theoretical approach : boat-tail cone effect, comparison with wind tunnel tests.

2 - Empirical approach : good knowledge of aerodynamical data such as base drag coefficient.

## REFERENCES

- [1] Computer programm for calculation of complex chemical equilibrium composition - rocket performance - incident and reflecting shocks and CHAPMAN JOUGET detonation.  
S. Gordon, B.G Mac Bride  
NASA Lewis research center (1971)
- [2] JANAF thermochemical tables (second edition)  
D.R. STULL and H. PROPHET  
NSDRS - NBS 37
- [3] The modelling of turbulent premixed and diffusion combustion in the computation of engineering flows.  
F.C. Locwood  
Combustion and Flame 29, p. 111-122 (1977)
- [4] Numerical heat transfer and fluid flow  
S.V Patankar  
Hemisphere publising corporation  
MC Graw hill book company
- [5] Basfloedesprojektiler. Banberaekningsprogram och Effeektivitetsjaemfoerelser (French translation)  
Rune Hellgren  
Foersvarest Forskningsanstalt Stockholm (1983)